Gas Adsorption
on
Suspended Carbon Nanotubes and Graphene

Boris Dzyubenko

A dissertation
submitted in partial fulfillment of the
requirements for the degree of

Doctor of Philosophy

University of Washington

2017

Reading Committee:

David Cobden, Chair

Oscar Vilches

Xiaodong Xu

Program Authorized to Offer Degree:
Physics

University of Washington

Abstract

Gas Adsorption
on
Suspended Carbon Nanotubes and Graphene

Boris Dzyubenko

Chair of the Supervisory Committee:
Professor David Cobden
Physics

Rare gas adsorption was studied on suspended individual single walled carbon nanotubes and graphene. The devices were fabricated as field effect transistors. Adsorption on graphene was studied through two-terminal conductance. On nanotube devices adsorption was studied through conductance while the coverage (density) of the adsorbates was determined from the mechanical resonance frequency shifts.

The adsorbed atoms modified the conductance of the nanotube field effect transistors, in part through charge transfer from the adsorbates to the nanotube. By tracking the shifts of conductance as a function of gate voltage, $G = G(V_g)$, and comparing these shifts with the periodicity of the Coulomb blockade oscillations we quantified the charge transfer to the nanotubes with high accuracy. For all studied gases (He, Ar, Kr, Xe, N_2, CO, and O_2) the charge transfer had a similar magnitude and was rather small, on the order of 10^{-5} to 10^{-3} electrons per adsorbed atom.

The nanotube devices displayed two classes of adsorption behavior. On some devices the monolayers exhibited first-order phase transitions analogous to those that occur in adsorbed monolayers on graphite. On other devices phase transitions within the adsorbed monolayers were absent. We present evidence that a highly uniform layer of contaminants deposits on the surface of suspended nanotube devices either upon cooldown in the cryostat or at room

temperature from air. These contaminants modify the adsorption behavior preventing the adsorbed monolayers from exhibiting the first order phase transitions expected to occur on a clean surface. A similar type of contamination leading to virtually identical effects occurs on suspended graphene.

In the low coverage regions of isotherms on nanotubes we observe Henry's law behavior, demonstrating a high uniformity of the surface and allowing us to accurately determine the single particle binding energy to this surface. The determined binding energies were $(776 \pm 10)\,\mathrm{K}$ for Ar, and $(997 \pm 37)\,\mathrm{K}$ for Kr.

In the second part of the dissertation we present the first measurements of adsorption on a pristine graphene surface, exposed through aggressive electric current annealing. On graphene the rare gas adsorbates form monolayers with phases analogous to those on graphite, but with phase transitions occurring at slightly higher pressures due to a reduction of binding energy. The condensations of monolayers with phases not commensurate with the graphene lattice resulted in a slight shift of the charge neutrality point of monolayer graphene corresponding to a change of carrier concentration on the order of $1 \times 10^9\, e/\mathrm{cm}^2$.

Adsorption of N_2 and CO, which formed a $\sqrt{3}\times\sqrt{3}$ commensurate solid monolayer, produced a dramatic reduction of the two-terminal conductance of graphene by as much as a factor of three. This effect is possibly connected with the opening of a band gap expected to occur in such structures. We observe hysteretic behavior in the adsorbed $\sqrt{3}\times\sqrt{3}$ commensurate monolayers on freestanding graphene, which is likely due to the interaction of two adsorbed monolayers on opposite surfaces of the graphene sheet.

TABLE OF CONTENTS

LIST OF FIGURES

LIST OF TABLES

ACKNOWLEDGMENTS

While working on my PhD thesis in Prof. Cobden's group I was lucky to have an opportunity to learn the physics of nanodevices, the fabrication techniques, and receive lots of hands on experience of working with various scientific equipment. At the same time I learned a great deal about the physics of gas adsorption. I am very grateful to Prof. Cobden for his interest in my work, his support, and guidance. I would like to thank Prof. Oscar Vilches for his vast knowledge and expertise in the physics of gas adsorption. We have had many interesting and motivating discussions.

I would like to thank several people, former and current graduate students in Cobden's group, who contributed to this project. Hao-Chun Lee worked with me on the nanotube part of the project. Joshua Kahn provided help with the graphene part of the project, especially with drafting the schematics for the new adsorption gas cell, with device structure fabrication, and with data analysis. I would like to thank Bosong Sun for helping fabricate the etched trench structures used for suspended graphene at the UW Nanofabrication Facility.

I would also like to thank several undergraduates who worked on this project. Denise Schmitz performed extensive coverage measurements on nanotubes which we used for binding energy determination. Reece Henry and Ryan Foster were a substantial help in fabricating the suspended graphene devices.

I would also like to thank Harold Cai, a postdoc in Prof. Xu's lab for helping perform Raman measurements to determine the thickness of my suspended graphene devices.

I would like to acknowledge the NSF and the UW Physics Department for providing funding during my PhD work.

Chapter 1

BACKGROUND AND LITERATURE OVERVIEW

1.1 Introduction

In this dissertation we are reporting our results of rare gas adsorption of both noble gases and diatomic molecules on the surfaces of suspended single walled nanotubes and graphene field effect transistors. The effects of gas adsorption and their various 2D phases on the electrical subsystem of these devices are studied through electrical transport measurements in the case of graphene and through both electrical transport and vibrational mass detection techniques on nanotubes.

The motivation for this work is a controlled study of the interactions of physisorbed gases with the electron subsystem of pristine nanotubes and graphene devices under controlled conditions. Field effect transistors made out of suspended nanotubes and graphene are the perfect substrates for studying such interactions. In these devices the electron wave functions are confined entirely at the surface. At the same time virtually defect free, ultra clean devices can be made with these materials [8, 13, 52, 83]. The adsorption of rare gases on bulk graphite was a very large and active research field with thousands of published papers, see the monographs [10, 23, 58] and the literature cited therein. This allowed us to refer to the large amount of both theoretical and experimental literature to help us understand the structures and behaviors of the adsorbed layers on the graphite-like surfaces of suspended nanotubes and graphene.

The basic understanding of interactions of gases with the electron subsystem of carbon based materials is important in many applications. At the same time the behavior of the adsorbed layers are interesting in their own right. It is important to note here that the

measurements of gas adsorption on graphene and nanotube devices presented in this dissertation are basic research. The studied suspended devices are delicate and become easily contaminated when exposed to air. This precludes their direct use for application purposes such as gas sensors.

In this chapter I will present only the physical pictures, data, and theory relevant to our experimental studies.

1.2 Graphene band structure

Graphene is a single layer of sp^2-bonded carbon atoms with a hexagonal lattice, see Fig. 1.1. The nearest neighbor distance of carbon atoms in graphene is 1.42 Å and so the areal density is approximately 38.2 atoms per nm^2. Graphene is one plane of a graphite crystal and can thus be mechanically exfoliated from it.

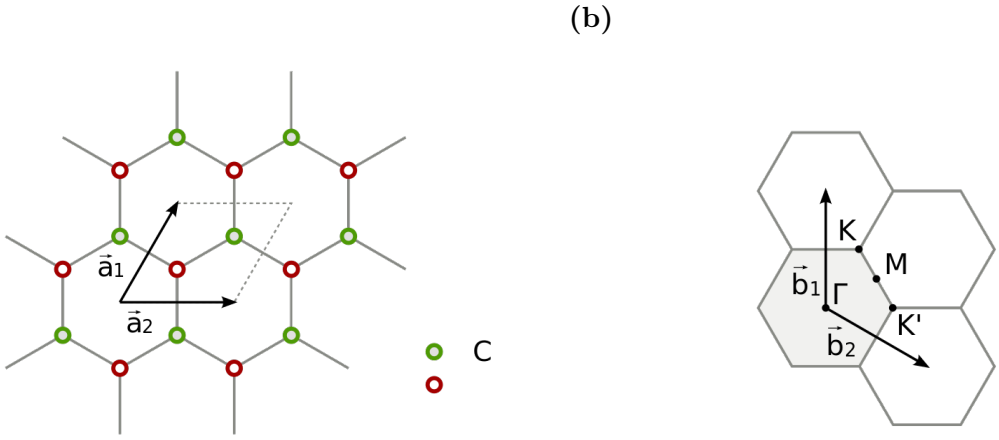

Figure 1.1: (a) Graphene lattice in real space. The two carbon atoms in the unit cell are colored red and green. (b) The Brillouin Zone of graphene in reciprocal space. The high symmetry points are labeled. A particular choice of the primitive vectors $\boldsymbol{a_1}$, $\boldsymbol{a_2}$ and $\boldsymbol{b_1}$, $\boldsymbol{b_2}$ are shown for the direct and reciprocal lattices. The figure is adapted from reference [73].

The band structure of graphene can be calculated using tight binding, which was first

done by P.R. Wallace back in 1947 [82]. If only nearest neighbor hopping is taken into account the dispersion is given by:

$$E(\boldsymbol{\kappa}) = \pm t\sqrt{3 + f(\boldsymbol{\kappa})} \ , \tag{1.1}$$
$$f(\boldsymbol{\kappa}) = 2\cos(\sqrt{3}\kappa_y a_0) + 4\cos(\frac{3}{2}\kappa_x a_0)\cos(\frac{\sqrt{3}}{2}\kappa_y a_0) \ ,$$

where t is the nearest neighbor hopping energy. The wave vector κ is measured from the Γ point of the Brillouin zone. A plot of the band structure is shown in Fig. 1.2. There are two inequivalent Dirac cones with linear dispersion $E_{\pm}(\boldsymbol{k}) = \pm\hbar v_F|\boldsymbol{k}|$ at the corners of the Brillouin zone. Here $\boldsymbol{k} = \boldsymbol{\kappa} - \boldsymbol{K}$ and $\boldsymbol{k} = \boldsymbol{\kappa} - \boldsymbol{K'}$ for the two Dirac points. The tight binding parameter t can be chosen to match Fermi velocity, which is given by $v_F = 3ta_0/2 \approx 1 \times 10^6\,\mathrm{m\,s^{-1}}$ [15].

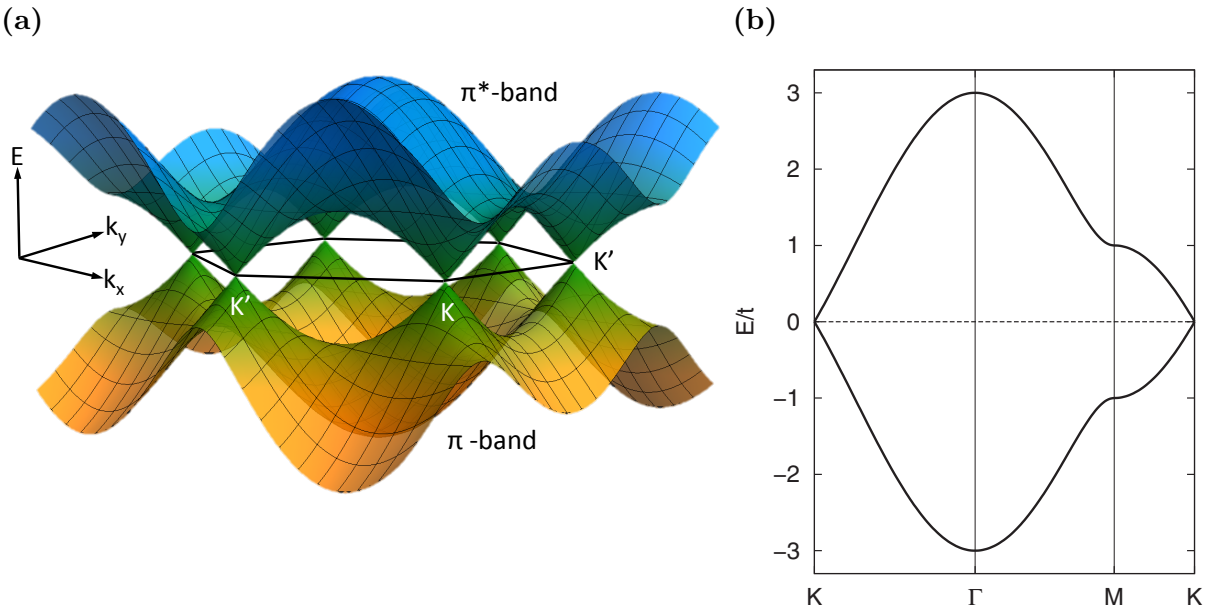

Figure 1.2: (a) Band structure of graphene from nearest neighbor tight binding, using Eq. (1.1). (b) The dispersion relation along high symmetry directions, adapted from reference [31].

1.2.0.1 *Effect of $\sqrt{3}\times\sqrt{3}$ superlattice on the band structure of graphene*

It is known that several gases such as Kr, N_2 and CO form a commensurate $\sqrt{3}\times\sqrt{3}$ solid monolayer on the surface of graphite [17, 27, 32]. In such a structure the adsorbed atoms sit on top of the centers of every third hexagon. The formation of such a superlattice on graphene leads to the modification of its band structure, and is predicted to open a bandgap in the single particle spectrum [31, 68]. The $\sqrt{3}\times\sqrt{3}$ superlattice on graphene is also called a Kekulé pattern or distortion [38]. The name arises because the superlattice is expected to produce slight bond distortions, which appear similar to the Kekulé structure of Benzene.

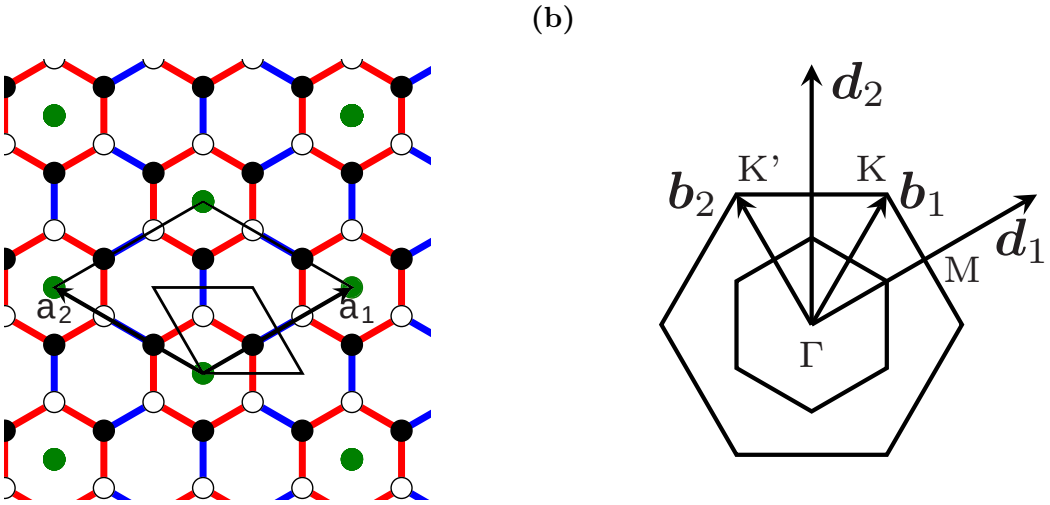

Figure 1.3: (a) A commensurate $\sqrt{3}\times\sqrt{3}$ lattice on top of graphene. The positions of the adsorbed atoms are shown with green circles. The adatoms cause a perturbation of the bonds in graphene, the two types of bonds are shown in blue and red color. (b) The Brillouin zone of graphene in the presence of the $\sqrt{3}\times\sqrt{3}$ superlattice. The reciprocal lattice vectors of the superlattice $\boldsymbol{b_1}$ and $\boldsymbol{b_2}$ connect the $\boldsymbol{K}$ and $\boldsymbol{K'}$ points of graphene. The figures are adapted from reference [31].

A $\sqrt{3}\times\sqrt{3}$ superlattice on graphene is shown in Fig 1.3. In real space the lattice vectors

of the $\sqrt{3}\times\sqrt{3}$ commensurate solid (CS) monolayer are $\sqrt{3}$ times longer than the graphene lattice vectors and are rotated by 30°. This results in Brillouin zone folding in reciprocal space. It so happens that the reciprocal lattice vectors exactly match the $\boldsymbol{K}$ and $\boldsymbol{K'}$ points of graphene in reciprocal space. Due to zone folding the $\boldsymbol{K}$ and $\boldsymbol{K'}$ points of graphene end up at the Γ point of the new folded Brillouin zone, see Fig. 1.4a.

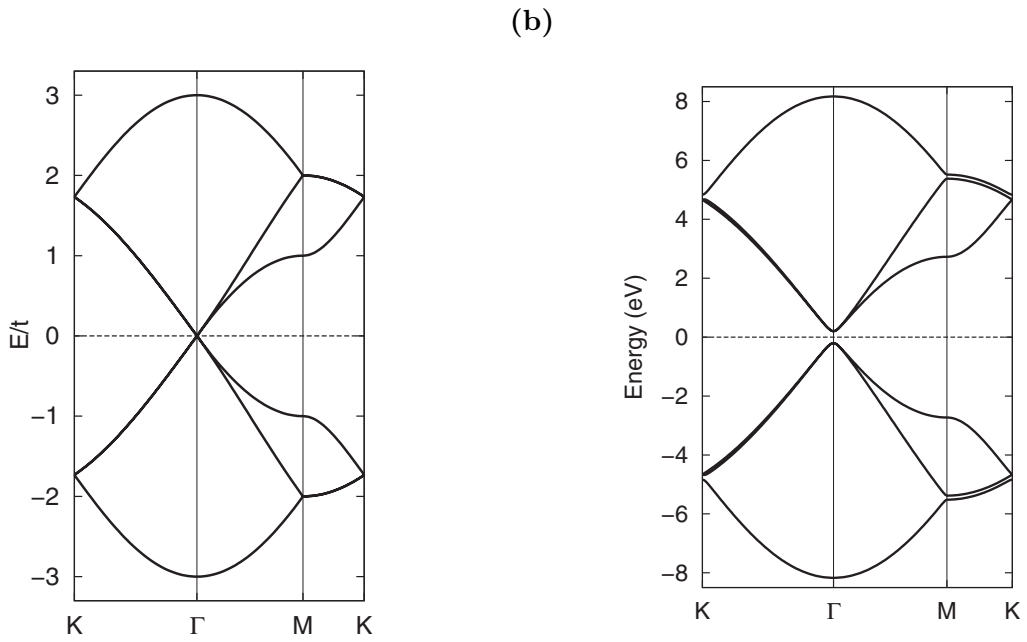

Figure 1.4: (a) The tight binding band structure of graphene artificially zone folded with a periodicity of the $\sqrt{3}\times\sqrt{3}$ superlattice. (b) The band structure of $\sqrt{3}\times\sqrt{3}$ coated graphene with the hopping amplitudes $t_1 = 2.79\,\text{eV}$ and $t_2 = 2.59\,\text{eV}$. The figure is adapted from reference [31].

In the simplest model the opening of a gap due to the formation of the $\sqrt{3}\times\sqrt{3}$ adsorbed monolayer can be calculated using tight binding [31]. In this model the adsorbed atoms are expected to slightly perturb the bonds between the surrounding carbon atoms. This gives rise to two types of bonds with two slightly different hopping amplitudes t_1 and t_2. The two types of bonds are colored red and blue in Fig. 1.3a. In this case the new dispersion relation

becomes

$$E_{\pm}(\boldsymbol{k}) = \pm\sqrt{\hbar^2 v_F^2 \boldsymbol{k}^2 + \frac{E_g^2}{4}} \ , \tag{1.2}$$

with the size of the gap given by $E_g = 2|t_2 - t_1|$ [31].

In reference [31] the formation of a $\sqrt{3}\times\sqrt{3}$ commensurate solid monolayer of lithium on graphene was considered. The band gap estimated in this case was fairly large, $E_g \approx 0.39\,\mathrm{eV}$. We note that the formation of the $\sqrt{3}\times\sqrt{3}$ solid monolayer of lithium on graphene is highly unlikely, as there is a tendency of lithium atoms to covalently bond into clusters. There are no estimates in the literature for the possible values the band gap E_g due to the formation of the $\sqrt{3}\times\sqrt{3}$ commensurate monolayer of physisorbed rare gases.

In our experiments we see a large reduction of the two-terminal conductance of graphene due to the formation of the $\sqrt{3}\times\sqrt{3}$ commensurate solid monolayer of N_2 and CO, see section 4.2.3.4.

1.3 Gas adsorption on graphite

The rare gas atoms and molecules that we studied in this dissertation bind weakly to the nanotube and graphene surface. The surfaces of our devices are closely related to the surface of graphite so the adsorption to graphite can be used as a starting point for understanding the behavior of the adsorbed monolayers on our devices. The relevant physics of gas adsorption to graphite is reviewed in this section.

The rare gas atoms are attracted to the graphite surface through Van der Waals interactions, which are due to induced dipole interactions of the gases with the substrate due to polarizability. The single particle binding energies of the gases we studied to graphite are small, $\epsilon_b < 0.2\,\mathrm{eV}$, see table 1.1, so the adsorption is easily reversible. The larger the adsorbed atom or molecule, the more easily polarizable it is thus the binding energy to the surface increases with the size.

At cryogenic temperatures the rare gases condense into a monolayer on the surface of graphite, followed by multilayer condensation. These monolayers are quasi-2D states of matter. The condensation occurs at pressures lower than the 3D saturation pressure, which

Gas	Binding to graphite, ϵ_b (K)	2D T_c (K)	2D T_{tr} (K)
Noble gases			
Ne	350	15.8	13.6
Ar	1100	55	49
Kr	1450	85	—
Xe	1845	117	99
Diatomic Molecules			
N_2	1160	48	—
O_2	1050	64	—
CO	1270	50	—

Table 1.1: Single particle binding energies of gases to graphite. The values are from reference [81]. The 2D critical T_c and triple T_{tr} point temperatures for the gases on graphite are from reference [74]. The gases labeled in blue form a $\sqrt{3}\times\sqrt{3}$ commensurate solid (CS) monolayer. These gases do not have liquid-vapor-solid coexistence and thus lack a triple point. The T_c temperatures listed for these gases are temperatures at which the fluid in coexistence with the CS monolayer undergoes a crossover from low to high density, see discussion in text.

is the pressure at which a bulk crystal of the adsorbates can form; this is due to the fact that the binding to the graphite surface is higher than the adsorbate-adsorbate interatomic interactions.

If the monolayer is in equilibrium with the 3D gas, the chemical potentials of the two systems are equal: $\mu_{2D} = \mu_{3D}$. Thus as the 3D gas pressure increases, it causes an increase of μ_{2D}. This leads to the increase of the monolayer density or coverage ϕ. The adsorbed monolayer undergoes phase transitions between various 2D phases. For the gases we study

there are two main types of 2D phase behavior within the monolayers.

The monolayer phase diagrams depend mainly on whether the equilibrium nearest neighbor spacing of the adsorbate in their 3D solid match closely the periodicity of the underlying graphite lattice. More specifically, the centers of the graphite hexagons are the high binding sites of the graphite surface. It is matching this periodicity that is critical to the formation of the CS phase [10]. As an example, the interatomic equilibrium spacing for Kr is 0.400 nm [76], which is only 6 % less than the centers of the graphite hexagons in a $\sqrt{3}\times\sqrt{3}$ superlattice, 0.426 nm. Thus it is energetically favorable for a Kr monolayer to expand slightly and lock into the centers of the hexagons. For the same reason the monolayers of molecular adsorbates N_2 and CO form an identical CS structure. In fact the phase diagrams of these three gases are almost identical [51].

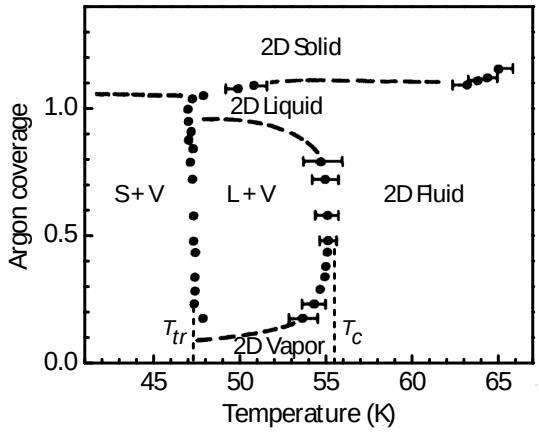

Figure 1.5: The argon coverage temperature phase diagram. The data is taken from A. Migone et al. [54]. The positions of the 2D critical point, $T_c = 55.5\,\mathrm{K}$ and 2D triple point $T_{tr} = 47\,\mathrm{K}$ are shown.

If the periodicities do not match well, the adsorbates form monolayers which average over the graphite surface potential corrugations and behave as if the monolayer is adsorbed on an almost smooth surface. The phases formed in the monolayers of such adsorbates are mostly 2D analogues of bulk 3D phases. These phases are 2D gas (G), 2D liquid (L), and 2D solid

(S). At different temperatures T and pressures P the monolayers exhibit phase coexistence and have critical and triple points, see table 1.1 and Fig. 1.5. This behavior is analogous to the behavior of 3D rare gases. Adsorbates that we have studied on our devices with such phase diagrams within the first layer on graphite are Ne, Ar, and Xe. It is important to note that the 2D solid phases of these monolayers are still sensitive to the periodicity of the graphite substrate and thus exhibit epitaxial rotation with respect to the graphite lattice, which minimizes the energy of the solid monolayer [21, 22, 60].

Adsorbates that match the periodicity of the centers of the graphite hexagons form a $\sqrt{3}\times\sqrt{3}$ commensurate solid (CS) phase. Gases that we have studied that have such a phase diagram on graphite are N_2, CO, and Kr as discussed above. All three of the gases have very similar phase diagrams [51]. For our work this phase is interesting and important as when formed on graphene it is expected to open a bandgap in the electronic structure, see previous section. On graphite, at low pressures the monolayer first forms a 2D fluid phase. As the pressure is increased the monolayer undergoes a first order phase transition into the $\sqrt{3}\times\sqrt{3}$ CS phase. At even higher pressures there is a complicated phase transition into an incommensurate solid (ICS) phase [51, 59]. The ICS phase is a close packed solid monolayer which is epitaxially rotated with respect to the graphite lattice.

The adsorbed monolayers on graphite have been studied by a wide variety of techniques. The most important ones were volumetric isotherm measurements, heat capacity studies, and various form of diffraction, such as low-energy electron diffraction (LEED) and X-ray diffraction. All of the techniques produced complimentary data on the structures and behaviors of the adsorbed monolayers, and were used to produce the adsorbate phase diagrams. A comprehensive review of the experimental works is provided in the book by Mulero and Caudros [58].

1.3.1 Phase diagram of N_2, description of the $\sqrt{3}\times\sqrt{3}$ CS phase

In this dissertation we present extensive measurements of N_2 adsorption on graphene, so a review of the relevant behavior of the N_2 monolayer on graphite is presented in this section.

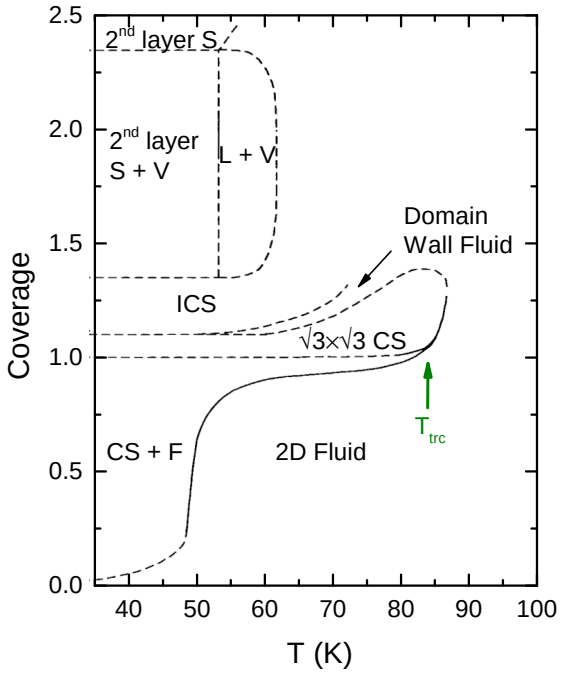

Figure 1.6: The N_2 on graphite coverage-temperature phase diagram in the high temperature regime. The phase diagram shows the monolayer and bilayer phases. See text for discussion. The figure is adapted from reference [51].

For a more comprehensive review see the publication by Marx and Wiechert [51]. For the discussion of domain wall behavior at the commensurate-incommensurate transition see the publication by den Nijs [59].

The N_2 monolayer on graphite has a very rich phase diagram with a multitude of different phases. The main feature of the monolayer phase diagram is the $\sqrt{3}\times\sqrt{3}$ CS phase, which is present up to temperatures $T \approx 87\,\mathrm{K}$. The coverage-temperature phase diagram is shown in Fig 1.6. At low pressures N_2 first condenses into a 2D fluid. As the 3D pressure increases the density of the fluid changes continuously. The 2D fluid undergoes a first order phase transition into the $\sqrt{3}\times\sqrt{3}$ CS monolayer. The 2D liquid and 2D gas phases with phase coexistence between them is absent in the N_2 monolayer on graphite at all temperatures [51]. It is assumed that in the vicinity of the first order phase transition between the 2D fluid

and CS phase the CS monolayer has a defect free lattice. The structure of a defect free CS monolayer is shown in Fig 1.3a. The coverage of one is assigned to this monolayer density in Fig 1.6. In the CS phase the adsorbed N_2 molecules occupy the high binding sites at the center of the graphite hexagons. The N_2 molecules cover every third hexagon, so the CS phase has 3 equivalent domains.

At temperatures $T > 30\,\mathrm{K}$, the N_2 molecules are not in their rotational ground state and are rotating freely. Below $T < 30\,\mathrm{K}$ the N_2 molecules undergo an orientational ordering phase transition into a herringbone structure with the doubling of the unit cell along one direction. The low temperature $T < 30\,\mathrm{K}$ and high density region of the N_2 monolayer phase diagram hosts a rich number of different phases [51]. We were not experimentally interested in this region of the phase diagram because of the low 3D gas pressures in equilibrium with the monolayer at these temperatures [28], although we do cool CS N_2 coated graphene devices through this temperature range, see section 4.2.3.5.

At temperatures $T < 50\,\mathrm{K}$ the density of the 2D fluid in coexistence with the CS phase is low. At $T > 50\,\mathrm{K}$ the density of the fluid at the phase transition quickly increases. The phase transition from the 2D fluid into the CS phase is first order up to the tricritical point at T_{trc}. As $T \to T_{\mathrm{trc}}$ the densities of the fluid phase in coexistence with the CS phase become equal. Above T_{trc} the phase transition between the fluid and the CS phase is continuous. The literature consensus is that the tricritical point occurs at $T_{\mathrm{trc}} \approx 85\,\mathrm{K}$, but the exact temperatures are uncertain due to experimental challenges at these hight temperatures, see discussion in reference [51]. The phase transition between the fluid and CS phase is expected to fall into the 3-state Potts model university class because the CS phase is described by three equivalent domains [59].

It is important to note that in the vicinity of T_{trc} in the accepted phase diagram the coverage of the CS monolayer at the CS-F phase boundary is slightly higher than one [56]. This implies that there is an excess of N_2 atoms adsorbed in the monolayer compared to a defect free CS phase. This is important to our work, as it turns out that the conductance of our monolayer graphene devices is highly sensitive to the formation of the defect free CS N_2

phase, which still persists at these temperatures on our devices, see section 4.2.3.10.

1.3.1.1 Domain wall phase

At gas pressures before the condensation of the second layer, the high density N_2 monolayer is in an incommensurate solid (ICS) phase. This phase is an isotropic close packed monolayer that is epitaxially rotated with respect to the graphite lattice [10, 51]. At coverages between the CS solid monolayer and the ICS solid there is a finite region of the phase diagram that is known to contain a domain wall fluid phase [32, 39], see Figs. 1.6 and 1.7. In this phase the monolayer is still locally in the commensurate phase. A hexagonal network of domain walls permeates the monolayer. As the coverage (density) of the N_2 monolayer increases it compresses through the formation of domain walls between the three equivalent domains of the CS phase. The domain walls contain the extra atoms adsorbed to the surface. Within the domain walls the adsorbed atoms are not in registry with the high binding sites of the graphite surface, thus the formation of the domain walls is energetically unfavorable. A schematic of the structure of the domain wall phase is shown in Fig. 1.7. The phase is called a domain wall fluid as the domain walls can freely translate across the graphite surface, converting the areas of one domain into a different one without energy penalty [20].

The phase transition from the CS phase to the domain wall fluid phase is described by the helical 3-state Potts model universality class [11, 59]. At high enough monolayer density the domain wall fluid phase undergoes a phase transition into the rotated ICS phase. This phase transition is expected to occur through a Kosterlitz-Thouless phase transition driven by dislocations of the ICS phase [44, 59].

The actual widths of the domain walls are not experimentally known [59]. For Kr, from computer simulations they are expected to be on the order of 5 to 10 CS lattice vectors wide [1, 36, 71]. As discussed in the previous section the formation of a defect free $\sqrt{3}\times\sqrt{3}$ CS phase on graphene is expected to create a bandgap in the electronic spectrum, and thus is expected to reduce conductance. The presence of domain walls within the monolayer complicates the situation. It is unclear if a network of domain walls would modify the con-

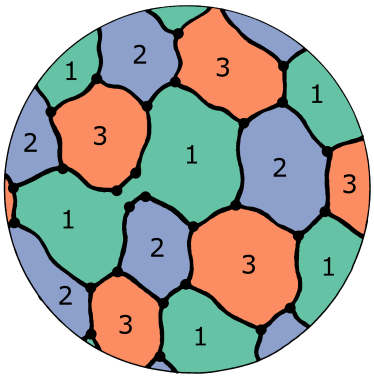

Figure 1.7: A schematic of a hexagonal domain wall phase. The monolayer is comprised of patches of the three CS domains. A network of domain walls separate the patches. The figure is adapted from [59].

ductance of the device. The effect of domain walls on conductance has not been theoretically investigated.

1.3.2 2D ideal gas, Henry's law behavior

At low pressures the atoms adsorbed on the surface are far enough apart that the interatomic interactions can be neglected. Thus the atoms within the adsorbed monolayer act as a 2D ideal gas. In this adsorption regime the 3D pressure P is linearly related with the areal density of the monolayer $n = N_a/A$, where N_a is the number of adsorbed molecules and A is the total area of the sample. This relationship is called Henry's law. The equation of state relating P and n can be derived by equating the chemical potentials of the 3D ideal gas μ_{3D} and the chemical potential of the 2D ideal gas monolayer, μ_{2D}. Henry's law is important for our determination of single particle binding energies ϵ_b of gases to the surface of nanotubes, see section 3.3. The derivation of Henry's law according to references [23, 46] is provided below.

For a 3D ideal gas the energy per atom is given by

$$\epsilon(\boldsymbol{p}) = \frac{p_x^2 + p_y^2 + p_z^2}{2m} \ . \tag{1.3}$$

The free energy is given by

$$F = -NT \ln \left[\frac{e}{N} \int e^{-\epsilon(\boldsymbol{p})/T} d\tau \right] \ , \tag{1.4}$$
$$d\tau = \frac{d\boldsymbol{p} d\boldsymbol{q}}{(2\pi\hbar)^r} \ ,$$

where $r = 3$ is the number of degrees of freedom, N is the total number of atoms in the gas, and $k_{\mathrm{B}} = 1$. For a 3D ideal gas the free energy is thus:

$$F_{3D} = -NT \ln \left[\frac{e}{N} \frac{1}{(2\pi\hbar)^3} \int_V \iiint_{-\infty}^{\infty} e^{-\frac{p_x^2 + p_y^2 + p_z^2}{2mT}} dp_x dp_y dp_z dV \right] \tag{1.5}$$
$$= -NT \ln \left[\frac{eV}{N} \left(\frac{mT}{2\pi\hbar^2} \right)^{3/2} \right] \ . \tag{1.6}$$

The chemical potential is obtained from Eq. (1.6):

$$\mu_{3D} = \left(\frac{\partial F_{3D}}{\partial N} \right)_{T,V} = -T \ln \left[\frac{V}{N} \left(\frac{mT}{2\pi\hbar^2} \right)^{3/2} \right] = -T \ln \left[\frac{T}{P} \left(\frac{mT}{2\pi\hbar^2} \right)^{3/2} \right] \ . \tag{1.7}$$

The energy per atom of a 2D ideal gas adsorbed on a surface with a uniform single particle binding energy ϵ_b is

$$\epsilon(\boldsymbol{p}) = \frac{p_x^2 + p_y^2}{2m} - \epsilon_b \ . \tag{1.8}$$

Going through the same calculation as above gives

$$F_{2D} = -N_a \left(\epsilon_b + T \ln \left[\frac{eA}{N_a} \left(\frac{mT}{2\pi\hbar^2} \right) \right] \right) \ . \tag{1.9}$$

The chemical potential of the 2D ideal gas is obtained from Eq. (1.9)

$$\mu_{2D} = \left(\frac{\partial F_{2D}}{\partial N_a} \right)_{T,A} = -\epsilon_b + T \ln \left(\frac{N_a}{A} \frac{2\pi\hbar^2}{mT} \right) \tag{1.10}$$

In equilibrium $\mu_{2D} = \mu_{3D}$, so equating Eq. (1.10) and Eq. (1.7) we get

$$P = \frac{N_a}{A} \sqrt{\frac{m}{2\pi\hbar^2}} T^{3/2} \exp\left(-\frac{\epsilon_b}{T} \right) \ . \tag{1.11}$$

Our definition of monolayer coverage on carbon nanotubes is $\phi = N_a/N_c$, where N_c is the total number of carbon atoms on the surface, see section 3.1. The area is thus $A = a_0^2 N_c$, where a_0^2 is the effective area per carbon atom. Rewriting Eq. (1.11) in this form results in the Henry's law equation

$$\frac{P}{\phi} = \frac{1}{a_0^2}\left(\frac{m}{2\pi\hbar^2}\right)^{1/2} T^{3/2} \exp\left(-\frac{\epsilon_b}{T}\right) \quad . \tag{1.12}$$

We use this equation to extract the single particle binding energy ϵ_b to the surface of carbon nanotubes, see section 3.3.

Chapter 2
EXPERIMENTAL METHODS

This chapter covers the experimental aspects of this dissertation. The first part of the chapter describes the suspended nanotube and graphene device fabrication procedure. The second part covers the measurement setup.

2.1 Device fabrication

2.1.1 Suspended nanotube device fabrication

We grow suspended carbon nanotubes by chemical vapor deposition (CVD) on top of pre-patterned trench structures. Thin film electrodes made out of platinum with a titanium adhesion layer extend to the edges of the trench. The schematic of the device cross section is shown in Fig 2.3. In our nanotube devices the trench between the source and drain electrodes is 1.0 µm wide. The CVD growth is performed as the last step of the device fabrication process. Suspended nanotube devices fabricated in this manner do not come in contact with any processing chemicals, and are only exposed to air during probing and transfer into the cryostat cell. The in situ CVD growth method of suspended nanotubes was first developed in the Hongjie Dai group in 2005 [13]. This is now a standard and widely employed technique for suspended nanotube field effect transistor fabrication.

We follow the growth procedure with parameters practically identical to those used for nanotube growth in the Bockrath group [7]. Catalyst consisting of $Fe(NO_3) \cdot 9H_2O$ (CAS Number 7782-61-8) and $MoO_2(acac)_2$ (CAS Number 17524-05-9) supported by aluminum oxide nanowire powder [43] is used for the nanotube growth. The catalyst is suspended in deionized water through a sonication procedure and deposited on top of a chip with prefabricated electrodes and trench structures. The surface of the chip is coated with

photoresist with exposed windows in the vicinity of the trench structures. Liftoff is performed by dissolving the photoresist in acetone. This leaves rectangular islands of catalyst on top of the platinum contacts in the vicinity of the trenches. An optical microscope image of such a catalyst pad is shown in Fig. 2.1b. During the CVD growth nanotubes extend out of the pad in all directions. The size and distance of the catalyst pad to the trench needs to be optimized in order to produce devices with individual nanotubes bridging the trench. The probability of nanotubes reaching the trench is expected to follow a Poisson distribution. The placement of the catalyst is tuned in such a way that most of the trenches end up with no nanotubes across them. The average yield from our typical CVD growth was one device out of approximately one hundred starting trench structures (one device per every two to four chips, with fourty to fifty trench structures per chip).

The CVD growth was performed in a one inch diameter tube furnace at $T = 800\,^{\circ}\mathrm{C}$ and at atmospheric pressure. The gas used for the growth was a mixture of H_2 and CH_4. The growth phase of the CVD process lasts approximately 5 min. During the temperature ramp an Ar/H_2 mixture was used as a purge gas. The temperature during the growth needs to be high, preferably $T > 800\,^{\circ}\mathrm{C}$, as amorphous carbon is known to deposit on the surface of the nanotubes at lower temperatures [41]. The $800\,^{\circ}\mathrm{C}$ growth is problematic as the platinum thin films become damaged at high temperatures [77], partially through surface roughening and partially through the diffusion of the metal adhesion layer. Properly fabricated Pt thin films with high quality adhesion layers can survive exposures of up to $900\,^{\circ}\mathrm{C}$, but with significant surface roughening. Shuttle growth, where the chip is held outside of the active zone of the furnace during heating and only exposed to high temperatures for the duration of the growth phase is used by some groups to partially mitigate these problems [72]. The above described issues make the nanotube growth result in an inconsistent yield.

2.1.2 Trench structure fabrication

The chips on which the carbon nanotubes are grown were fabricated at the UCSB nanofabrication facility. Two different versions of the trench structures were used for the work in

this thesis. In both cases the chips were fabricated on highly p-doped 10 cm diameter silicon wafers, which were subsequently diced into 5 mm $\times$ 5 mm chips. The chips consisted of a common drain electrode running down the center of the chip. The common drain electrode branched out and converged with multiple source electrodes. Trenches were etched in the chips at the converged locations. An image of one trench structure is shown in Fig. 2.1b.

The two versions of the wafers were fabricated in a slightly different manner. In the first version of the devices the starting point was a silicon wafer with a 300 nm layer of thermally grown SiO_2. A layer of silicon nitride Si_3N_4 was further deposited on top of the SiO_2. During the fabrication process the following steps were performed:

1. Photolithography using an "i-line" stepper was performed to define the trench pattern.
2. The Si_3N_4 was etched away using a reactive ion etching (RIE) process.
3. The SiO_2 was etched using a wet etch process, which created a slight undercut in the sidewalls of the trench below the Si_3N_4.
4. A second step of photolithography was performed to create exposed windows over the region of the trench.
5. Metal was deposited into the trench and the resist was lifted off. This step created the local gate electrode at the bottom of the trench.
6. A third step of photolithography was performed to define the source and drain electrode windows outside the trench structure.
7. A final step of metallization and liftoff was performed, which created the source and drain electrodes.

The above described fabrication technique is prone to errors. Fine alignment tolerances of the lithographic process to the edge of the etched trench is required in steps 4 and 6 in order to prevent the deposition of metal onto the vertical edges of the trench. If this were to

occur the gate electrode would short to either the source or drain electrode during the high temperature CVD growth procedure.

A different fabrication method was performed on the second set of wafers in order to minimize the above described issues. This time, a buried gate structure was fabricated with the trench made using a self aligned etch to the edge of the source and drain contacts. The process started with a highly p-doped Si wafer with 90 nm of thermally grown SiO_2. The following fabrication steps were used:

1. Photolithography using an "i-line" stepper was performed to define the location for the gate electrodes.
2. Metallization and lift off was performed, which created the gate electrodes.
3. 500 nm of SiO_2 was deposited on top of the wafer using a plasma-enhanced chemical vapor deposition (PECVD) process. This step buried the gate electrode underneath the deposited layer of SiO_2.
4. A second step of photolithography was performed to define the locations of the source and drain electrodes. The electrodes slightly overlapped the buried gate. This overlap reduced the alignment tolerances.
5. Metallization and lift off was performed which created the source and drain electrodes.
6. A third step of photolithography was performed to open widows over the gap between the source and drain electrodes.
7. The trench was etched using RIE. The etch does not affect the Pt thin film, so the trench ends up self alligned to the edge of the source and drain contacts.

The wafers fabricated at the UCSB nanofabrication facility turned out to be problematic. In all of the fabricated wafers the platinum thin film would suffer various levels of degradation and blistering at much lower temperatures than expected. The last set of wafers fabricated by method two described above was the most severely affected, see Fig. 2.2a. On these

wafers the source and drain electrodes metallized in step 5 of the fabrication process could not withstand temperatures above 500 °C without severe blistering. The gate electrodes metallized in step 2 of the fabrication process on the other hand, were able to survive temperatures of 800 °C without significant degradation. The exact cause of the different behavior of the two metallizations was unclear. The blistering pattern seen on some bond pads (Fig. 2.2b) implies that uncontrolled contamination from the photolithographic process was likely left behind underneath the metal layer and produced the delamination of the Pt film from the SiO_2 surface. Nanotube growth on chips with such severe blistering was not possible. These chips were instead used to fabricate suspended graphene devices, which does not require high temperature exposure.

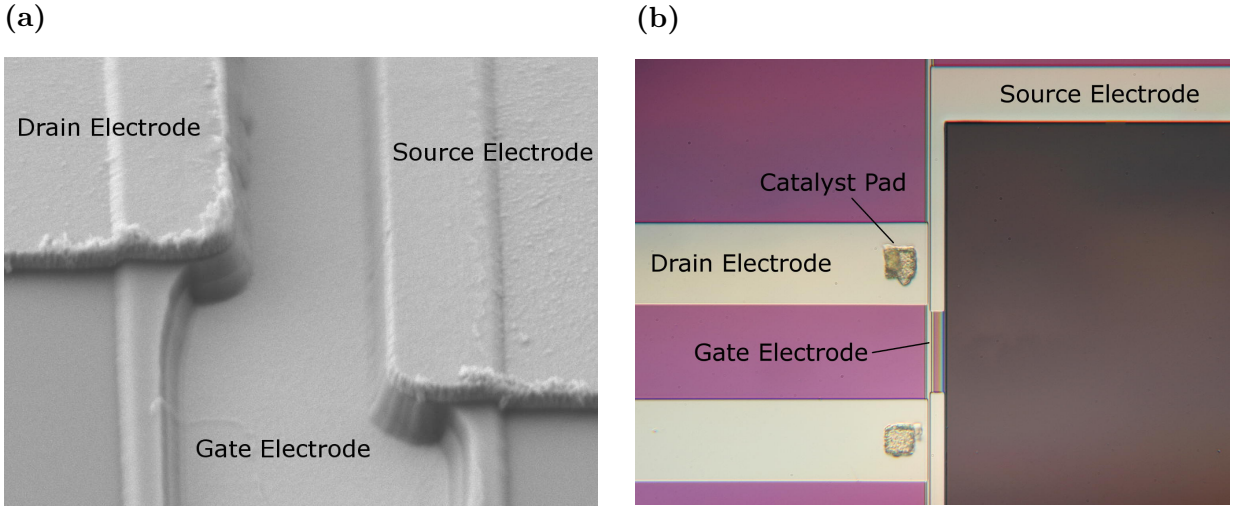

Figure 2.1: (a) An SEM image of the electrodes and trench structure used for fabricating the suspended nanotube devices. The partially buried gate electrode is visible on the bottom of the image. (b) An optical microscope image of the the structure showing the deposited catalyst pads. The size of the catalyst pads is 10 µm × 10 µm. The liftoff of the catalyst was not perfect, as it is protruding past the expected edge of the pad.

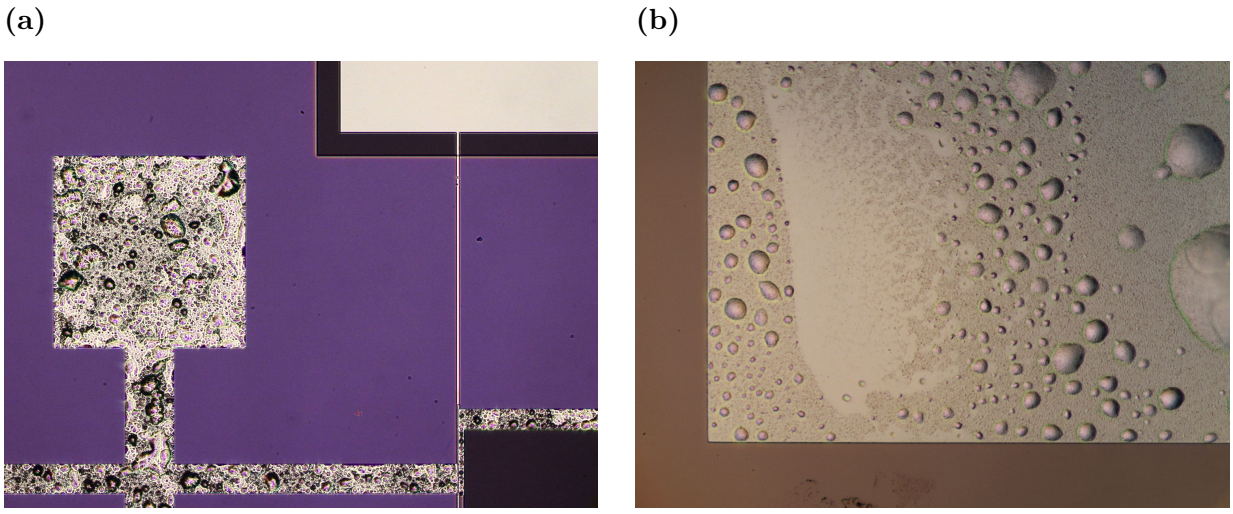

Figure 2.2: (a) An optical microscope image of the platinum electrodes after a high temperature exposure at $T = 800\,^{\circ}\mathrm{C}$. The two metallization layers are affected differently. The gate electrode in the top right corner of the image appears mostly unaffected, while the source and drain electrodes have delaminated and are covered in bubbles. (b) A zoom in on the Pt bond pads showing a distribution of undamaged regions. Such behavior implies that contamination distributed underneath the evaporated thin film is the cause of the high-T film damage.

2.1.3 Suspended graphene fabrication

Suspended graphene devices were fabricated on trench structures similar to the ones used for suspended carbon nanotubes. The chips with 1 µm trench structures were the same ones used for carbon nanotube growth (fabricated at the UCSB nanofabrication facility). These chips included a local Pt gate at the bottom of the trench. Structures with trench widths of 1.75 µm and 2.25 µm were fabricated at the University of Washington, Seattle, and did not include a local gate electrode; the p-doped Si wafer was used as the gate instead. The fabrication of these chips was much simpler as only one step of metallization followed by a self aligned etch of the trench was performed. The cross section of the trench structures is

shown in Fig. 2.3, to scale.

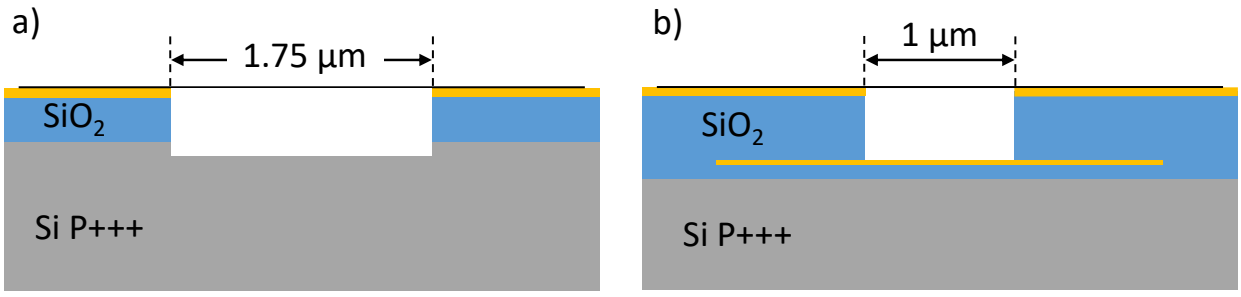

Figure 2.3: A schematic cross section of the trench structures used for making suspended devices. The schematic is to scale. Structure (a) was fabricated at the University of Washington and was used for making suspended graphene devices. The p-doped silicon was used as a global gate. Structure (b) contains a buried Pt local gate and was fabricated at the UCSB nanofabrication facility.

Mechanically exfoliated graphene was transfered over the trench structures using the now standard and widely used polycarbonate (PC)/polydimethylsiloxane (PDMS) stamp dry transfer technique [90]. In this technique a thin cylindrical piece of PDMS with a thickness of $\approx 2\,\mathrm{mm}$ and a diameter of $\approx 4\,\mathrm{mm}$ is placed on the surface of a glass microscope slide. A thin film of PC with a thickness of several micrometer is picked up using a piece of Scotch tape with a cut out window and stretched over the PDMS. The stamp is mounted to a micromanipulator. The PC/PDMS stamp is transparent so it can be aligned over and pressed into a piece of graphene. The procedure is performed in an optical microscope with long working distance objectives. At temperatures $T \approx 90\,^{\circ}\mathrm{C}$ the graphene flake has a higher adhesion to the PC film than to the SiO_2 surface, so can be picked up by the stamp as it retracts from the SiO_2 surface.

The flake is aligned over a prefabricated trench structure and gradually pressed down.

The chip is heated to soften the PC film and tear it from the PDMS stamp. PC polymer is known to undergo a glass transition at $T \approx 147\,^{\circ}\mathrm{C}$ and start to flow at $T > 155\,^{\circ}\mathrm{C}$. As the chip with the trench structure is heated to this temperature range, the stamp is gently raised away from the surface. The PC film remains attached to the chip surface. It first detaches from the PDMS portion of the stamp and eventually tears at the periphery as the stamp is completely retracted.

The $T = 90\,^{\circ}\mathrm{C}$ pickup process can be repeated multiple times with flakes of different materials in order to create a heterostructure. We utilize this process to create suspended monolayer graphene devices backed with few nanometer thick hexagonal boron nitride (hBN). On these devices adsorption is restricted to only one side of the graphene sheet. To build such devices, a suitably sized boron nitride flake is picked up first and then is used to in turn pick up a piece of monolayer graphene. The alignment and melt down procedure is the same as for freestanding graphene. Optical images taken at several steps during the fabrication process are shown in Fig. 2.5.

Across the majority of the hBN backed graphene heterostructures, the graphene and hBN are in atomic contact. During the pickup process hydrocarbon contaminants are pushed away from the graphene-hBN interface. Bubbles (pockets) of these contaminants get trapped between the two surfaces [61, 45]. The bubbles are usually connected by sharp ridges or folds, with heights on the order of a few nanometers. The bubbles themselves can be tens of nm tall and are typically several hundred nm in diameter, see Fig. 2.4. The amount of such bubbles trapped within the heterostructure is dependent on the rate at which the graphene and hBN surfaces were brought together. It is unclear how the presence of such features in the graphene-hBN heterostructures might affect gas adsorption. It is possible that the binding energy ϵ_b of adsorbates to the graphene stretched over the bubbles is different than ϵ_b to the graphene in contact with the hBN.

After pickup of the graphene + hBN heterostructures we scan their surfaces with an atomic force microscope (AFM) to determine the presence and location of the contaminant bubbles, see Fig 2.4. Subsequently, during the alignment and meltdown process care is

taken to minimize the amount of bubbles present in the suspended portion of the final device. This process is complicated as monolayer graphene is often invisible in the optical microscope underneath the hBN flake. Oftentimes the distribution of the bubbles on the hetorostructure surface makes it impossible to completely avoid their placement within the trench.

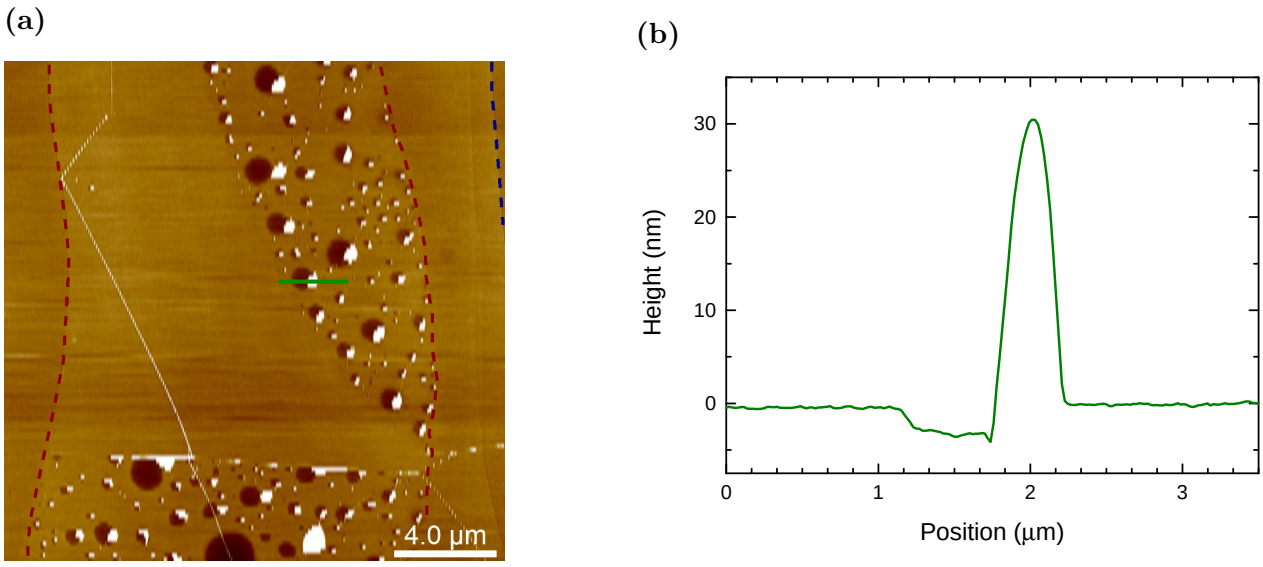

Figure 2.4: (a) An AFM topography scan of a monolayer graphene flake backed by few nm thick hBN. The heterostructure is attached to the surface of a PC/PDMS stamp. The stamp is turned over and positioned in the AFM for scanning. After the fabrication process the scanned graphene surface ends up facing the trench. Gas adsorption in the device occurs on this bottom surface. The edges of the graphene sheet are outlined with dashed red lines. The edge of the few nm thick hBN flake is outlined by the blue dashed line. A large fraction of the heterostructure surface is devoid of contaminant bubbles. The bubbles are several tens of nm tall. The dips in the surface of the heterostructure next to the bubbles is interpreted to arise due to a slight compression of the PC polymer underneath the heterostructure during pickup. Panel (b) shows an AFM line trace taken over the location of one of the contaminant bubbles.

(a) hBN flake pickup

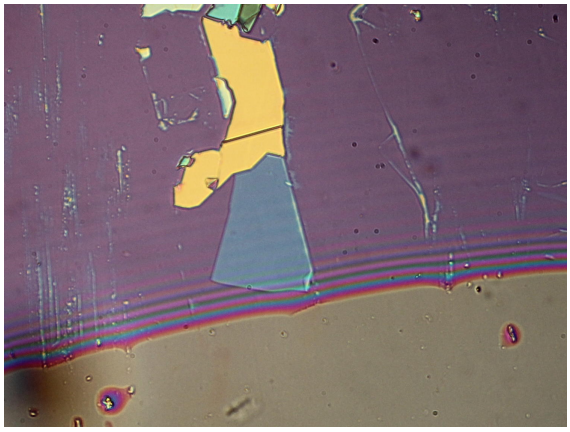

(b) picked up hBN flake on stamp

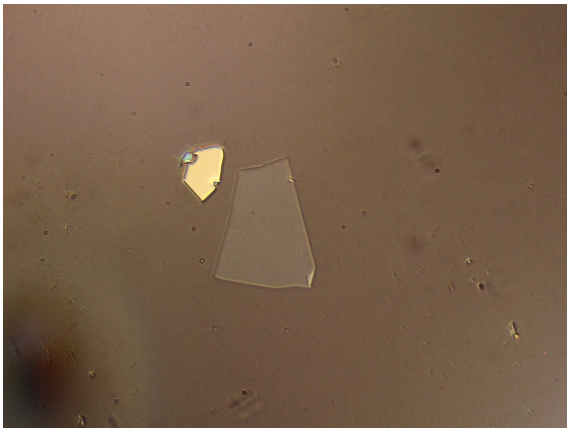

(c) graphene pickup

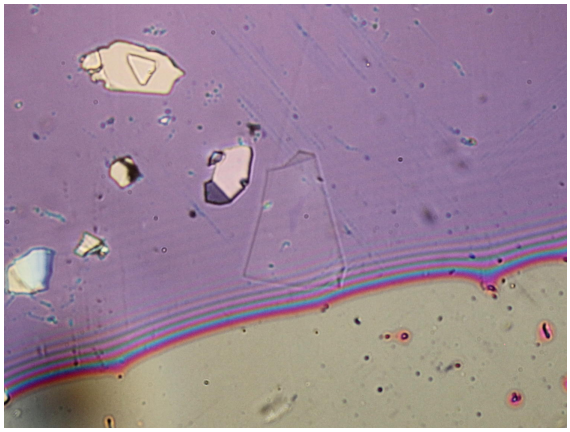

(d) deposition of the graphene + hBN stack

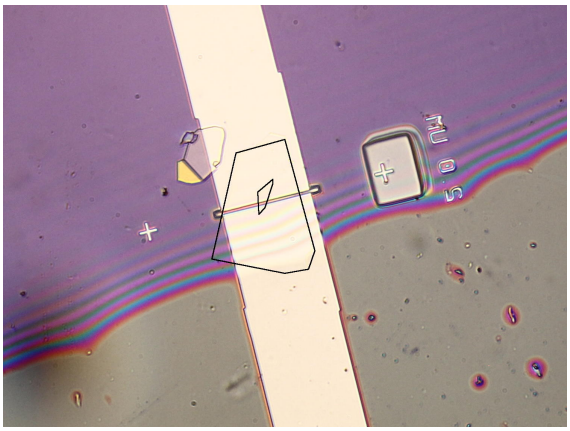

(e) melting of the PC film

(f) final removal of the stamp

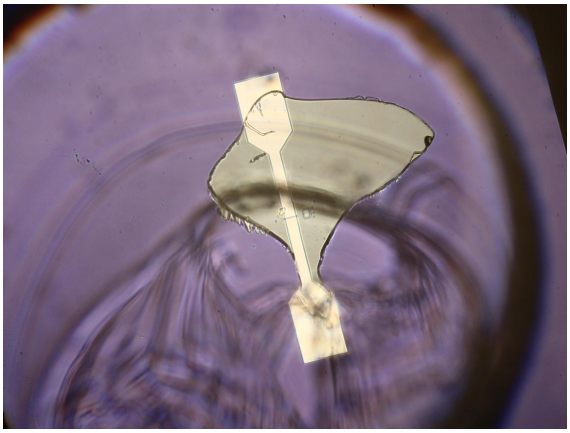

Figure 2.5: The fabrication process of a graphene + hBN device. See the main text for description. Newtons rings form as the stamp comes in contact with the substrate.

After a successful meltdown, a fairly large area ($\approx 1\,\text{mm} \times 1\,\text{mm}$) of the PC polymer film is left on the chip surface, see Fig. 2.5f. The film remains in contact with the graphene flake and completely covers the trench structure. The entire chip is submerged in chloroform to dissolve the PC film. The dissolution process takes approximately 30 min. During the removal of the suspended devices from solvent the liquid interface can tear the graphene sheets due to the applied force of the surface tension. Nevertheless we are able to fabricate suspended devices without employing a critical point dryer. The devices are first transferred into hexane and then into perfluorohexane, a low surface tension fluid. The suspended graphene devices are removed from the liquid and blow dried with nitrogen. The low surface tension of the liquids increases the yield of the suspended graphene devices [78]. The yield of this step of the fabrication process is fairly low. It is dependent on the graphene flake thickness, the flake width, and the size of the trench. For freestanding monolayer graphene over a 1.75 µm trench approximately one out of every ten fabricated devices survived without tearing.

2.1.3.1 Furnace annealing

After removal from chloroform the suspended graphene devices are still coated with PC polymer residue. We can scan the surface of the suspended graphene devices with an AFM using the Peak Force Tapping mode without damaging the sheets. This allows us to directly image the polymer residue distribution across the device surface. This residue forms patches several nm thick with what appear to be clean regions in between. An AFM scan of this residue on a trilayer graphene device is shown in Fig. 2.6. Furnace annealing of the suspended devices at $T = 400\,^{\circ}\text{C}$ in an Ar/H_2 atmosphere effectively removes the PC residue, exposing a smooth graphene surface, see Fig 2.6e. Furnace annealing alone is not enough to produce a clean graphene surface for gas adsorption. Electric current annealing at cryogenic temperatures has to be carried out on the graphene devices to remove further contaminants from the device surface, see discussion in section 4.1.

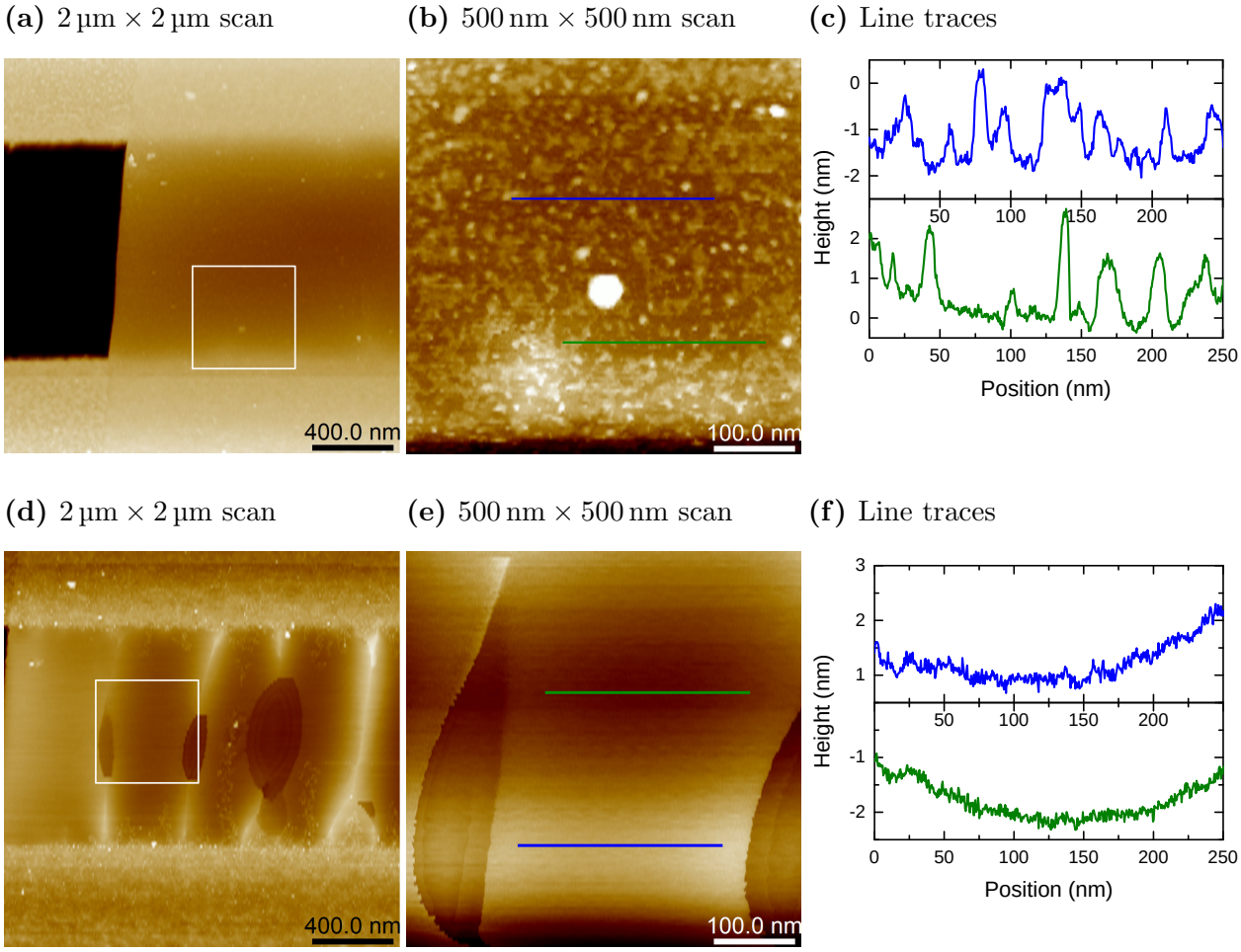

Figure 2.6: A set of AFM scans of a suspended trilayer graphene device fabricated over a 1 µm width trench. Panel (a) shows the edge of the device after it has been removed from chloroform. Panel (b) is a zoom-in on the suspended region. Patches of PC polymer residue coat the graphene surface. (c) Line profiles showing the typical height of the residue patches. Panel (d) shows the same region of the device after a furnace anneal. The majority of the device surface is residue free. Ridges form on the suspended graphene after thermal cycling. The low thermal expansion of graphene compared to the substrate structure causes a reduction in tension of the suspended sheet [4]. Panel (e) shows a zoom-in on a clean region of the suspended sheet. (d) Line traces in this region show height variations much less than a nanometer indicating that the surface of the device is indeed uniform. Because of this the surface might seem to be clean, however, this is probably not the case, see section 4.1.2 for details.

2.2 Measurement apparatus

2.2.1 Cryostat and gas cell

The gas adsorption measurements on the suspended nanotube and graphene devices were performed in a Janis closed cycle cryocooler. The cryocooler was equipped with an SHI RDK-305D two stage GM cycle cold head with a cooling power of 0.4 W at $T = 4$ K. The cryostat can operate in a temperature range from 4.2 K to 300 K. A custom built gas cell, fabricated at the University of Washington Physics Department Instrument Shop, was attached to the top plate of the cold head. The cell was machined entirely out of brass. Apiezon N cryogenic grease was used to improve thermal conductivity at the mating interface. A picture of the setup is shown in Fig 2.7.

The top part of the gas cell (the can) is removable for sample insertion. It is sealed to the bottom portion of the gas cell using an indium wire compression seal. The vacuum cell was connected to the gas system with a 1/4 inch gas feed tube. The tube was made out of 304 Stainless steel with a wall thickness of 0.01 inch in order to minimize thermal conductivity and reduce the thermal load on the cold head. The gas feed tube was hard soldered to the vacuum cell.

The vacuum cell was build with twelve hermetic low temperature electrical feedthroughs, fabricated by Corning Gilbert, part number Y007-L42-02. The feedthroughs were made out of Kovar (Iron-Nickel-Cobalt alloy) mated to borosilicate glass. The thermal expansion coefficients of the two materials are well matched, which allows the hermetic feedthroughs to be repeatedly thermal cycled down to temperatures of $T = 4$ K without compromising the vacuum seal. The mini feedthroughs had a diameter of 0.1 inch, which allowed us to easily fit them in a 4 cm diameter ring around the bottom of the cell, see Fig. 2.7a. The feedthroughs were soft soldered to the cell with a low melting temperature eutectic solder. The soldering procedure was performed by gradually heating up the entire cell to the solder melting temperature and carefully inserting the feedthroughs into machined pockets.

Four of the electrical connections to the cell were made with low temperature miniature

coaxial cable manufactured by Lake Shore Cryotronics. The coaxial cables were used for the high frequency signal in the nanotube mechanical resonance measurements. The rest of the electrical connections were made with 32 gauge enamel coated copper magnet wire. The wires were thermal lagged to the $T = 40\,\mathrm{K}$ first cooling stage of the cold head.

(a)

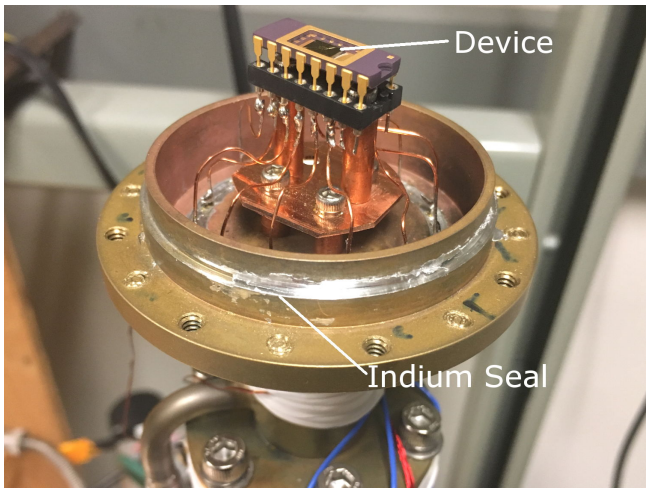

(b)

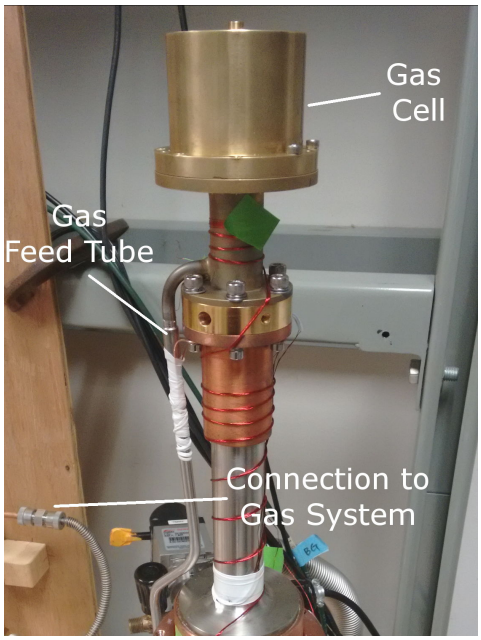

Figure 2.7: Panel (a) shows the internal layout of the gas cell. The device is inserted into a sixteen pin DIP socket. The location of the indium seal is shown. When the cell is closed only the space inboard of the seal is exposed to gas. The main chamber of the cryocooler remains under vacuum. Panel (b) shows the cell mounted in the cryocooler. The gas feed tube and the connection to the gas system is visible.

2.2.2 Gas system

The schematic of the gas system used for adsorption measurements is shown in Fig. 2.8. The gas system was made with 1/4 inch copper tubing with Swagelok compression fittings. Three

capacitive pressure gauges with different full range scales were used: 0.25, 10, and 1000 Torr. These gauges measure the true pressure of a gas through the force that it applies to a membrane. Thus calibration factors for different gases are not needed. The gauges output a voltage that is linearly related to the measured pressure. Full scale corresponds to an output of 10 V. The lowest measurable pressure in our gas system was thus $\approx 2.5 \times 10^{-5}$ Torr with the 0.25 Torr gauge.

The gas system is connected to a turbo pump for gas pumpout. Since the gas system was not used for volumetric measurements, the absolute volumes were not calibrated. The volume of the gas system was approximately 3.5 times smaller than the volume of the gas cell.

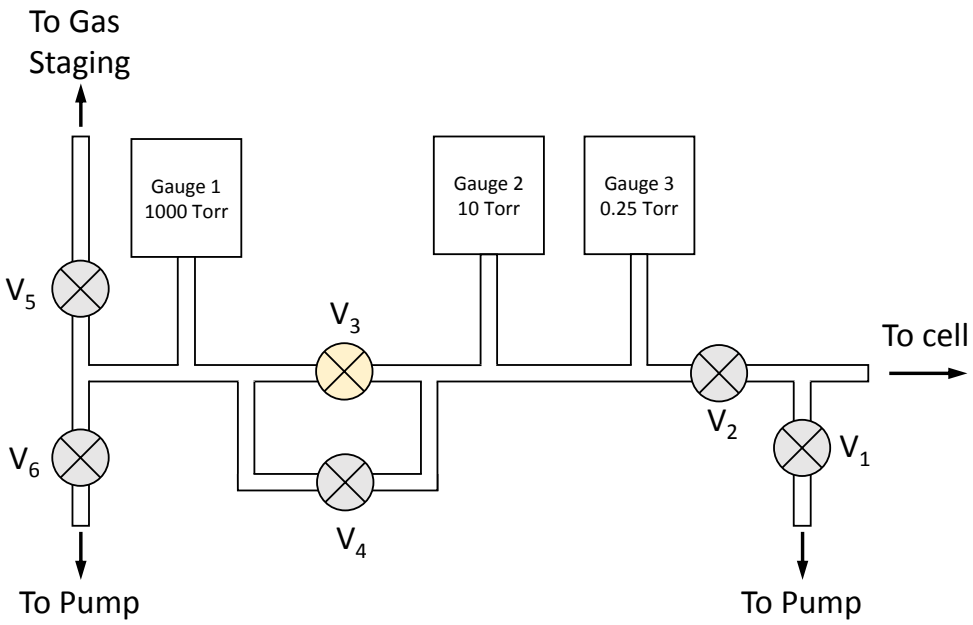

Figure 2.8: Schematic of the gas system. The gas system was made using 0.25 inch copper tubing with Swagelok compression fittings. Three capacitive pressure gauges were installed allowing for pressure measurements in the range from 1×10^{-4} Torr to 1000 Torr. Valve V_3 is a needle valve. The other valves are bellows-sealed valves. The gas system was connected to the cell using a 0.25 inch stainless steel gas feed tube.

2.2.2.1 Continuous isotherm measurements

During gas adsorption measurements we perform what we call continuous conductance isotherms: we record conductance of the device as a function of pressure as gas is either continuously added (continuous adsorption isotherms) or pumped out of the system (continuous desorption isotherms).

During continuous adsorption isotherms we start by first pressurizing the part of the gas system closed off by valves V_3 through V_6 while monitoring the pressure by the 1000 Torr pressure gauge #1, see Fig 2.8. We stop the cell pumpout by closing valve V_1, and slowly bleed gas into the system through needle valve V_3. In this way we can measure a continuous isotherm starting from vacuum until a pressure of 10 Torr. If an isotherm to pressures above 10 Torr needs to be carried out, then valve V_4 is opened, and gas is slowly bled into the system through valve V_5, from the gas staging area. A continuous desorption isotherm is performed by opening valve V_1 by a fixed amount while pumping on the system with a turbo pump.

During a continuous isotherm a pressure gradient is set up between the gas system (where the pressure is measured) and the gas cell (where adsorption occurs) due to a finite flow rate along the gas feed tube: $P_{\mathrm{g}} = P_{\mathrm{cell}} - \Delta P$. During an adsorption isotherm $P_{\mathrm{g}} > P_{\mathrm{cell}}$, while during a desorption isotherm $P_{\mathrm{g}} < P_{\mathrm{cell}}$. Because the pressures during an isotherm can change by more than five orders of magnitude, the pressure gradient ΔP between the cell and the gas system is difficult to control, especially at low pressures during an adsorption isotherm. A pressure gradient on the order of $\Delta P \approx 0.5$ mTorr is created as soon as the needle valve V_3 is opened. As the pressure in gas system increases, the rate of gas inflow has to be also proportionally increased. Every time the flow rate through the needle valve is adjusted, the pressure offset between the cell and the gas system changes. This effect produces distortions in the adsorption isotherm measurements as a function of pressure. The distortions are most pronounced in the adsorption isotherms below a pressure of $P_g < 10$ mTorr. Any phase transitions occurring in this pressure range are artificially shifted towards a higher measured

gauge pressure.

The pressure gradient during a desorption isotherm is significantly better controlled. The pressure on the pump side of valve V_1 is negligible, which results in the flow rate during a pumpout isotherm to be proportional to P_g. As P_g decreases the flow rate automatically slows down. In the Knudsen flow regime the pressure in the system is expected to exponentially decrease as a function of time. This indeed appears to be the case in our gas system up to pressures $P_g > 20\,\text{mTorr}$, see Fig. 2.9. In this case the ratios of pressure P_{cell} and P_g are expected to be constant: $P_{cell}/P_g = \text{const}$. This produces a shift of the entire isotherms towards lower pressures on a $\log P$ plot with minimal distortion in the shapre of the isotherm as a function of $\log P$. For this reason the majority of isotherms presented in this thesis are desorption isotherms. At pressures $P_g < 20\,\text{mTorr}$ there is a crossover to the molecular flow regime. It is unclear if the above relation should still hold in this pressure limit.

2.2.2.2 Thermomolecular pressure correction

During adsorption measurements the room temperature gas in the gas system is in dynamic equilibrium with the low temperature gas in the cell. Due to the temperature difference a pressure gradient is set up along the gas feed tube. The pressure inside the cell is lower that the pressure measured by the room temperature pressure gauges. This is called the thermomolecular effect or thermal transpiration [75]. The thermomolecular pressure correction has to be applied to the measured gauge pressure P_g to obtain the cell pressure P_{cell}. At high pressures the effect is negligible and the two pressures are almost identical $P_g \approx P_{cell}$, see Fig. 2.9. In the low pressure limit the following equation holds: $P_{cell} = (T_{cell}/T_{room})^{1/2} \times P_g$. In the intermediate pressure range the correction is done according to an widely employed empirical relation derived by Takaishi and Sensui [75]. The correction is different for every gas and is dependent on the diameter of the gas feed tube.

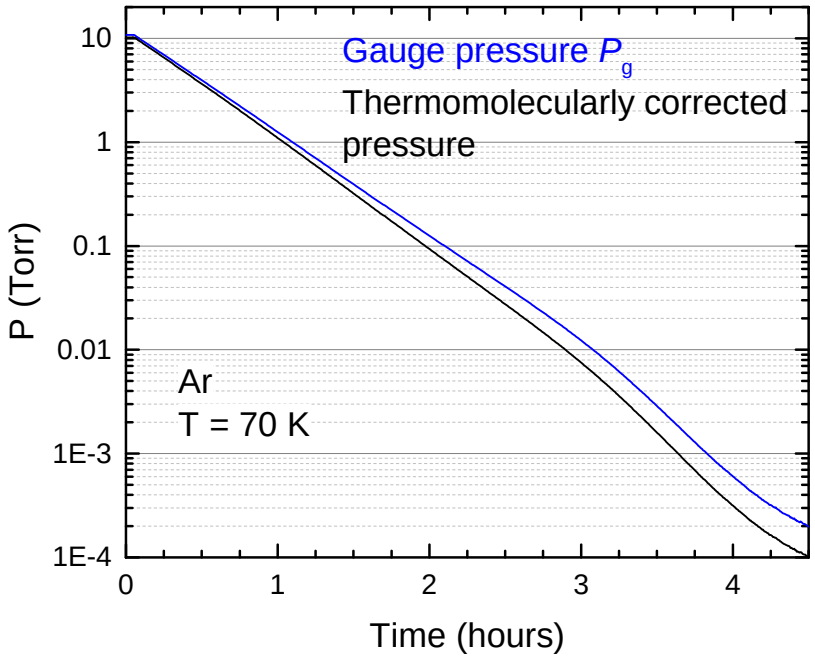

Figure 2.9: Pressure as a function of time during a continuous pumpout isotherm. The blue curve is the measured gas pressure P_g. The black curve is the pressure after the application of thermomolecular pressure correction. The pressure decreases exponentially vs. time as is expected for flow through a fixed opening. Deviation from this behavior starts at pressures $P_g \approx 20\,\mathrm{mTorr}$, when a crossover to molecular flow occurs.

2.2.3 Electrical measurement setup

The electrical setup used for measuring suspended nanotubes is shown in Fig. 2.10. To measure the mechanical resonance of the nanotube we used an amplitude modulated one-source mixing technique [70]. An RF voltage at a frequency f with amplitude modulated at a frequency $f_{\mathrm{AM}} = 1\,\mathrm{kHz}$ was applied to the source of the device:

$$V(t) = V_0\,[1 + \cos(2\pi f_{\mathrm{AM}} t)]\cos(2\pi f t)\ . \tag{2.1}$$

The RF signal was generated using an HP 8657A signal generator and brought up to the cell with a low temperature miniature coaxial cable. The frequency f was swept in the range

of 20 to 300 MHz. When the frequency f matched the resonance frequency of the nanotube a low frequency current I_{mix} at f_{AM} was produced due to nonlinearities of the conductance of the nanotube. At the same time DC biasing and AC conductance measurements of the device could be performed.

The circuit shown in Fig. 2.10 could be improved by adding a 50 Ω resistor with an appropriate blocking capacitor to ground for impedance matching to the signal generator.

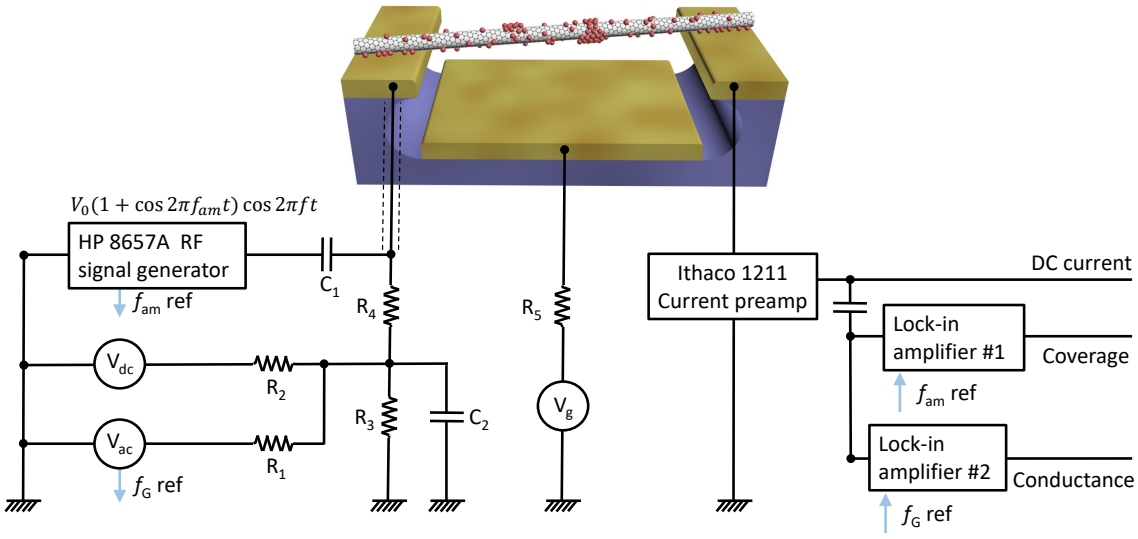

Figure 2.10: Electric measurement setup used for combining vibrational and conductance measurements on suspended carbon nanotube devices [29]. The resistors $R_1, R_2 = 100\,\mathrm{k\Omega}$ and $R_3 = 10\,\mathrm{k\Omega}$ form a voltage divider for the DC and AC conductance measurements. The capacitor $C_1 = 500\,\mathrm{pF}$ blocked the low frequency voltages from reaching the signal generator. The combination of $R_4 = 10\,\mathrm{k\Omega}$ and $C_2 = 500\,\mathrm{pF}$ blocked the high frequency RF signal from reaching the DAC card and the lock in amplifier. The figure is adapted from the publication of our group [29].

Chapter 3

ADSORPTION ON INDIVIDUAL SUSPENDED NANOTUBES

This work builds on the expertise accumulated in the Cobden group [48, 84] regarding gas adsorption on suspended nanotubes. We continue our goal of studying the interaction of adsorbed atoms and molecules with the electron subsystem of individual suspended carbon nanotubes.

The coverage of the monolayer adsorbed on the surface of a carbon nanotube can be determined with high accuracy from the mechanical resonance frequency shift of the suspended nanotube [85]. At the same time the adsorbed atoms change the conductance of the carbon nanotube field effect transistors, in part through charge transfer from the adsorbates to the nanotube. By tracking the shifts of conductance as a function of gate voltage, $G = G(V_g)$, and comparing these shifts with the periodicity of the coulomb blockade CB oscillations we can quantify the charge transfer to the nanotubes with high accuracy. It turns out that for all studied gases (He, Ar, Kr, Xe, N_2, CO, and O_2) the charge transfer has a similar magnitude and is rather small, on the order of 10^{-5} to 10^{-3} electrons per atom. Furthermore, on some devices the charge transfer is nonmonotonic as a function of coverage, with the adsorbed atoms donating electrons at low coverage and accepting them from the nanotube at high coverage [29].

Our studied nanotube devices fall into two distinct classes: on some devices the adsorbed monolayers undergo phase transitions analogous to those that occur in adsorbed monolayers on bulk graphite, albeit at higher pressures due to lower binding energy; we refer to these nanotube devices as Class I. On most fabricated and studied devices, however, first order phase transitions are absent: adsorption happens gradually and at pressures several orders of magnitude higher than expected; we call such devices Class II. The latter devices attain

a maximum coverage at pressures near 3D saturation that is significantly lower compared to devices which exhibit first order phase transitions [49].

This raises the possibility that the difference in adsorption behaviors between the two classes of nanotube devices is due to adsorbed contaminants coating the surfaces of some devices. However, in the low coverage region of isotherms we observe Henry's law behavior: coverage ϕ is proportional to pressure P. This is direct evidence that the surface of the suspended nanotubes is highly homogeneous and is difficult to reconcile with contamination. Measurements of Henry's law allows us to extract the single particle binding energy ϵ_b of adsorbates to the surface of the nanotubes with high precision.

3.1 Coverage isotherms

Coverage measurements on suspended nanotube resonators were pioneered in the Cobden group by Z. Wang [85, 84]. As atoms/molecules adsorb on the surface of the nanotube they increase its total mass, M. This causes the resonant frequency of the device $f_{\rm res}$ to decrease, as $f_{\rm res} \propto M^{-1/2}$. Coverage ϕ of the adsorbed monolayer, which we define as the number of adsorbed atoms $N_{\rm ads}$ in the monolayer divided by the number of carbon atoms in the nanotube $N_{\rm C}$, is obtained from the mechanical resonance frequency shifts,

$$\phi = N_{\rm ads}/N_{\rm C} = (m_{\rm C}/m_{\rm ads}) \left[(f_0/f_{\rm res})^2 - 1\right] \quad , \tag{3.1}$$

where $m_{\rm C}$ and $m_{\rm ads}$ are the masses of the carbon atom and the adsorbed molecule, respectively; f_0 is the vibrational resonance frequency of the bare nanotube in vacuum, while $f_{\rm res}$ is the resonance frequency of the nanotube in the presence of the adsorbed molecules. The total mass of the nanotube is

$$M = m_{\rm C} N_{\rm C} + m_{\rm ads} N_{\rm ads} \quad . \tag{3.2}$$

A set of representative resonance measurements on a nanotube device YB30 in the presence of Ar is shown in Fig. 3.1.

For Eq. (3.1) to hold, several assumptions have to be satisfied. First, the resonances of the nanotube have to be fairly linear. Second, the adsorbed atoms have to be uniformly

distributed along the nanotube surface. The final assumption is that in vacuum the nanotube surface is completely bare, without any contaminants. The first two assumptions can be verified by checking that the extracted coverage values measured using different vibrational modes of the nanotube are consistent with each other. Furthermore, coverage ϕ extracted from the shift of a particular resonance mode should remain constant as the tension in the nanotube changes. The tension can be modified by the electrostatic force between the nanotube and the gate electrode due to the applied gate voltage V_g [70]. In our nanotube resonator devices the first two assumption have been verified, see the discussion in the thesis of Z. Wang [84].

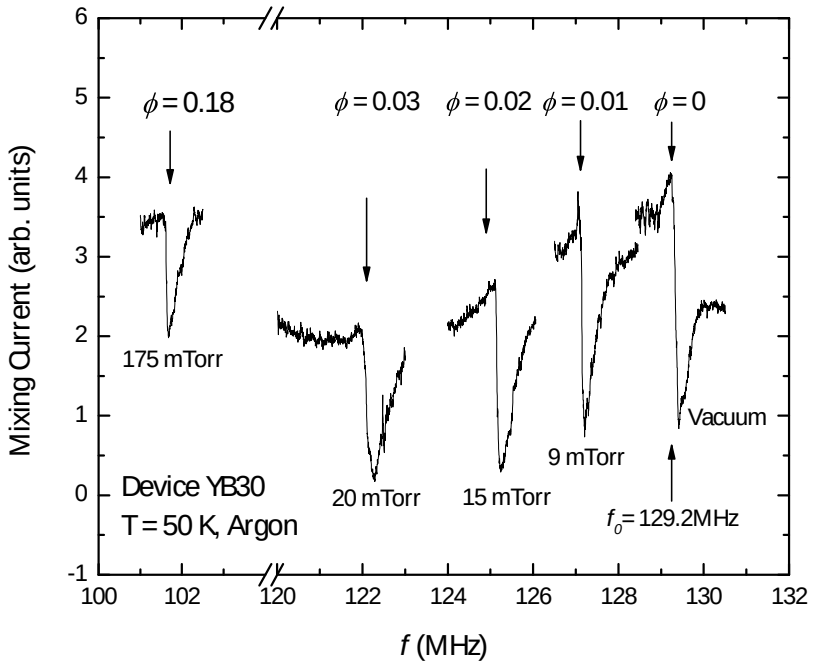

Figure 3.1: The shift of the mechanical resonance frequency f of nanotube device YB30 as Ar adsorbs on its surface at $T = 50\,\mathrm{K}$. The coverage values are extracted from the frequency shifts according to Eq. (3.1). The figure is adapted from the publication of our group [29].

Since the nanotube resonances are inherently nonlinear [30, 65], the smallest RF voltages

have to be used while driving the nanotube resonances in order to measure reliable coverage isotherms $\phi(P, T = \text{const})$. The applied RF amplitude has to be below $V_0 < 1\,\text{mV}$. Higher driving voltages cause the coverage isotherms to be shifted to higher pressures. The mechanism responsible for the shifts of the coverage isotherms towards higher pressure is unclear. This is because the power dissipated by the nanotube due to the applied RF voltage is expected to be small, due to impedance mismatch between the nanotube and the RF signal generator, see section 2.2.3. Thus the temperature increase of the nanotube due to Joule heating is expected to be minimal, not enough to explain the shifts of the isotherms. Only a limited subset of fabricated devices exhibited detectable resonances at low driving voltages.

3.2 Two classes of adsorption behavior

Isotherms of argon measured on two nanotube devices, device YB14 (Class I adsorption behavior) and device YB18 (Class II adsorption behavior) are shown in Fig. 3.2. The two devices exhibit rather different adsorption behaviors, and at the same time rather different responses of conductance G due to the formation of an adsorbed monolayer. The behaviors of the two devices due to adsorption are representative of the behaviors of all devices that correspond to their respective device class. These differences are discussed below.

The isotherms measured on device YB14, shown in Fig. 3.2a, are continuous conductance isotherms: the conductance of the device at a fixed gate voltage is measured continuously as pressure is increased in the system, $G = G(P, V_g = \text{const})$. On this particular device we were unable to detect mechanical resonances, so coverage isotherm measurements were not possible. Device YB14 shows phase transitions that are analogous to those that occur in the argon monolayer on the surface of bulk graphite, and thus belongs to Class I according to our classification. At temperatures above the 2D critical temperature of argon $T > T_c \approx 55.5\,\text{K}$ the conductance G increases gradually as a function of pressure. This increase is due to the condensation of a supercritical Ar fluid on the surface of the nanotube. As T approaches T_c the slopes of the main riser in the isotherms become steeper and finally diverge at T_c. In this device the divergence of the slopes of Ar isotherms, $dG/d(\ln P)$, as $T \to T_c$ followed the

critical scaling of the 2D Ising model universality class: $(T/T_c - 1)^{-\gamma}$, with $\gamma = 7/4$ [29]. Below T_c the main vertical step in the conductance isotherms corresponds to the 2D Ar first order liquid-vapor (L-V) transition. Conductance isotherms measured on the device also exhibited a second smaller step which corresponded to the 2D Ar melting transition. This step, which is marked with green arrows and shown in the inset in Fig 3.2a, merges with the main L-V step at the 2D triple point, $T_{\rm tr} = 48\,\mathrm{K}$.

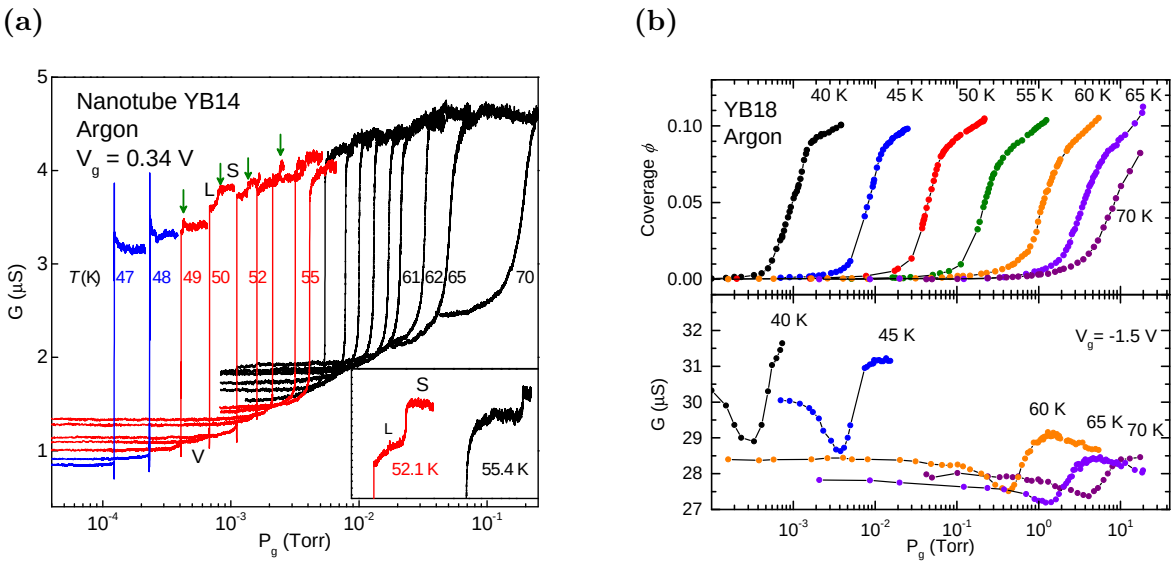

Figure 3.2: (a) Continuous conductance isotherms of Ar on nanotube device YB14. $P_{\rm g}$ is the measured gas pressure, see section 2.2.2.1. The isotherms show representative adsorption behavior of Class I devices. First order phase transitions within the monolayer are present. The response of the conductance G due to increasing monolayer coverage is monotonic except for spikes in the vicinity of first order phase transitions, see main text for details. The inset shows the blow-up of the isotherms in the vicinity of the solid to liquid (L-S) transition (2D melting). (b) Coverage and conductance isotherms of Ar on nanotube device YB18. The adsorption behavior of Ar and the changes in the device conductance G are representative of the adsorption behavior of Class II devices. First order phase transitions in the monolayer are absent. The conductance G changes non-monotonically with monolayer coverage.

The adsorption behavior of Ar on device YB18, shown in Fig 3.2b, is quite different. Coverage isotherms on this device lack any signs of first order phase transitions within the monolayer. The coverage isotherms appear qualitatively similar to the supercritical fluid isotherms of Ar on device YB14 at $T > T_c$. For a given temperature, the midpoint of the main riser in the isotherms on device YB18 occurs at pressures approximately two orders of magnitude higher than on device YB14. As an example, at T =70 K it occurs at a gauge pressure of $P_g \approx 8$ Torr compared to $P_g \approx 0.2$ Torr for device YB14. The slopes of the isotherm risers on device YB18 do not become steeper at lower temperatures. No first order phase transitions occur on this device down to the lowest accessible temperatures and pressures in our apparatus (pressure can be reliably measured down to 1×10^{-4} Torr, which corresponds to the lowest measurable Ar isotherm temperature of $T \approx 37$ K, see section 2.2.2). This behavior is practically identical for all adsorbed gases studied on nanotube devices belonging to Class II.

As gas adsorbed on their surfaces, the change in conductance of Class I nanotube devices was mostly monotonic with increasing coverage ϕ. This holds true for device YB14 during Ar adsorption, apart form nonmonotonic spikes which are present in the vicinity of first order 2D L-V phase transitions above $T_{\rm tr}$ and V-S phase transition below $T_{\rm tr}$. If measured at high bandwidth the spikes show temporal fluctuations [29]. Away from the first order phase transitions, as the density of the 2D phases within the monolayer adsorbed on the device surface gradually increased, conductance G changed monotonically with coverage. The monotonic change of G with coverage appears to be a universal response of nanotube devices belonging to Class I due to the adsorption of the studied gases.

Nanotube devices belonging to Class II, on the other hand, exhibit nonmonotonic changes in conductance during gas adsorption, see bottom panel of Fig. 3.2b. This nonmonotonic response of G to gas adsorption is similar for all gases studied on all nanotube devices belonging to Class II and is due to a nonmonotonic shift of the $G(V_g)$ along the V_g axis, see section 3.4.

Out of approximately twenty suspended nanotube devices on which adsorption has been

measured in the Cobden lab only three belonged to Class I (adsorbed monolayers host first order phase transitions). All the other devices ended up belonging to Class II (absence of first order phase transitions). The positions of phase boundaries of Ar on nanotube devices belonging to the two classes is shown in Fig 3.3a. For nanotubes belonging to Class II the positions of the midpoints of the gradual risers in the coverage isotherms are plotted. There is a slight spread in pressures of the risers in different Class II devices. The origin of the difference in behavior between the two classes of devices is not quite clear (see a related discussion involving a possible role of contaminants in section 3.3 and for graphene device in section 4.1).

Coverage isotherms of Ar on several devices belonging to the two classes are shown in Fig. 3.3b. The maximum coverage of the Ar monolayer on Class I nanotube devices is slightly higher than on bulk graphite (the latter is shown by a dashed line in Fig. 3.3b). This is due to the cylindrical curvature of the nanotubes providing an effectively larger surface area for adsorption compared to a planar surface. The increase in coverage compared to graphite is expected to be of the order $(R+d)/R$, where R is the radius of the nanotube and d is the distance of the adsorbate from the nanotube surface. With typical values of $R = 1\,\text{nm}$ and $d = 0.35\,\text{nm}$ the estimate for the increase is $\approx 35\,\%$.

At pressures near 3D saturation, the Ar coverage on devices exhibiting Class II adsorption behavior is significantly lower compared to Class I devices. The same holds true for all other gases studied on these devices; similar results for Kr are presented in the publication of our group [49]. This raises the question of whether the difference in adsorption behavior can be explained by contaminants coating the surface of Class II devices, somehow disrupting first order phase transitions while at the same time reducing the maximum monolayer coverage. When we apply Eq. (3.1) to extract coverage ϕ from the shifts of the resonant frequency we make an assumption that in vacuum the nanotubes are completely bare, without any extra contaminants attached to their surfaces. If above assumption is not valid and in vacuum the nanotube device is coated with contaminants with a total mass M_{cont}, the coverage extracted

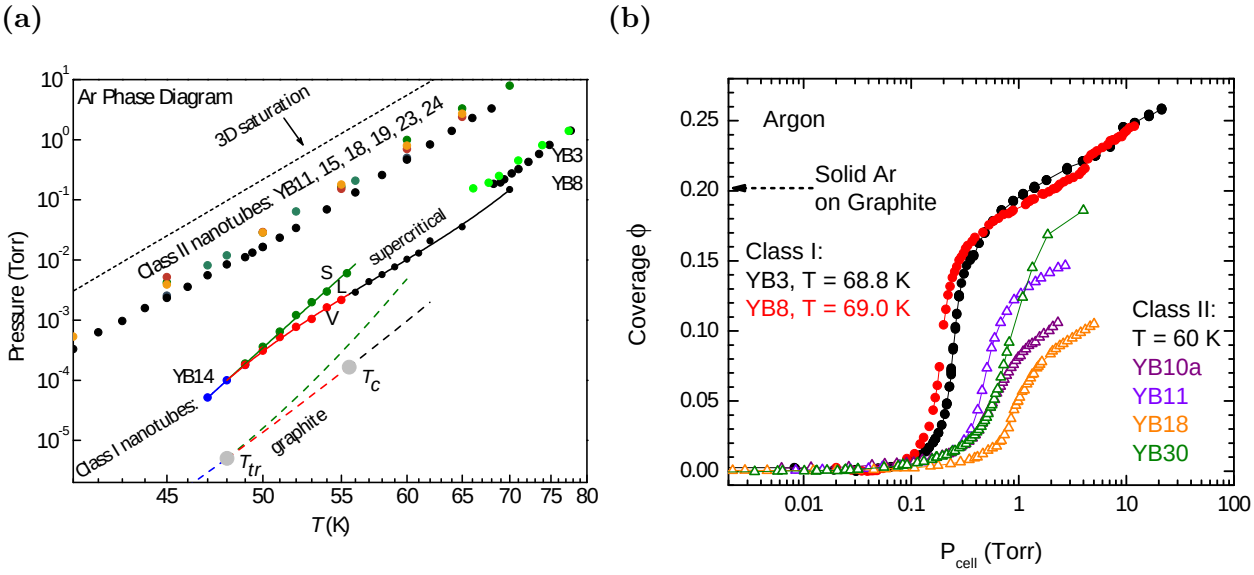

Figure 3.3: (a) Phase diagram of Ar adsorbed on nanotubes. The pressure has been thermomolecularly corrected, see section 2.2.2.2. For Class I devices the positions of the phase boundaries between the 2D vapor (V), liquid (L) and solid (S) phases are plotted. For Class II devices the points show the midpoints of the gradual risers in the isotherms. The dashed lines show the 2D phase boundaries of Ar on bulk graphite. (b) Coverage isotherms of Ar on nanotubes. Devices YB3 and YB8 exhibit Class I adsorption behavior. Devices YB10a, YB11, YB18, and YB30 exhibit Class II adsorption behavior. The maximum monolayer coverage of Class II devices at pressures near 3D saturation is significantly lower compared to Class I devices. See main text for discussion.

using Eq. (3.1) will instead be:

$$\phi = \frac{M}{M + M_{\text{cont}}} \phi' \ , \tag{3.3}$$

where ϕ is the measured coverage using the clean nanotube assumption, M is the total mass of the bare nanotube Eq. (3.2), and $\phi' = N_{\text{ads}}/N_{\text{C}}$ is the actual coverage. The highest attained ϕ on a particular device would then depend on M_{cont} and the effective total area

for adsorption.

If we follow the above arguments, the variability of the highest attained coverages of Type II devices implies that the devices have a variable amount of contamination deposited on their surfaces. Such contaminants would then be naturally expected to form patches on the surface of the devices. In this case we would expect adsorption to first occur to higher binding sites, most likely at the edges of the patches. Instead, from low coverage regions of isotherms where we observe Henrys law behavior, we have direct evidence that in actuality the surfaces of Class II nanotubes are highly homogeneous.

3.3 Henry's law and measurements of single particle binding energy

Coverage isotherms of Ar and Kr on nanotube device YB30 at several temperatures are shown in Fig. 3.4. When the isotherms are plotted on a log–log plot, Henry's law behavior is easily discernible at low coverages $\phi < 0.01$. In our experiments Henry's law behavior on the device holds down to the lowest measurable coverages of $\phi \approx 5 \times 10^{-4}$. Lower coverages can not be reproducibly measured due to slight drifts of the vacuum resonance frequency of the device f_0. If we assume that in vacuum the device YB30 is a bare nanotube with radius $R = 1\,\mathrm{nm}$ and is suspended perpendicularly across the $1\,\mu\mathrm{m}$ trench, then the coverage range in which Henry's law holds corresponds to between approximately 100 to 2500 atoms adsorbed on the surface of the nanotube. A solid Ar monolayer is expected to contain approximately 60000 atoms.

The slopes of the isotherms in the low coverage region where Henry's law holds in the Boltzmann approximation [23] are given by:

$$P/\phi = C_0 T^{3/2} \exp\left(-\epsilon_b/T\right) \quad , \tag{3.4}$$
$$C_0 = \frac{1}{a_0^2}\sqrt{\frac{m_{\mathrm{ads}}}{2\pi\hbar^2}} \quad ,$$

where a_0^2 is the effective area of one carbon atom, and ϵ_b is the single particle binding energy of the adsorbate to the surface. In the above equation the binding energy ϵ_b is measured in units of temperature T (Kelvin), thus Boltzmann's constants are absent in Eq. (3.4).

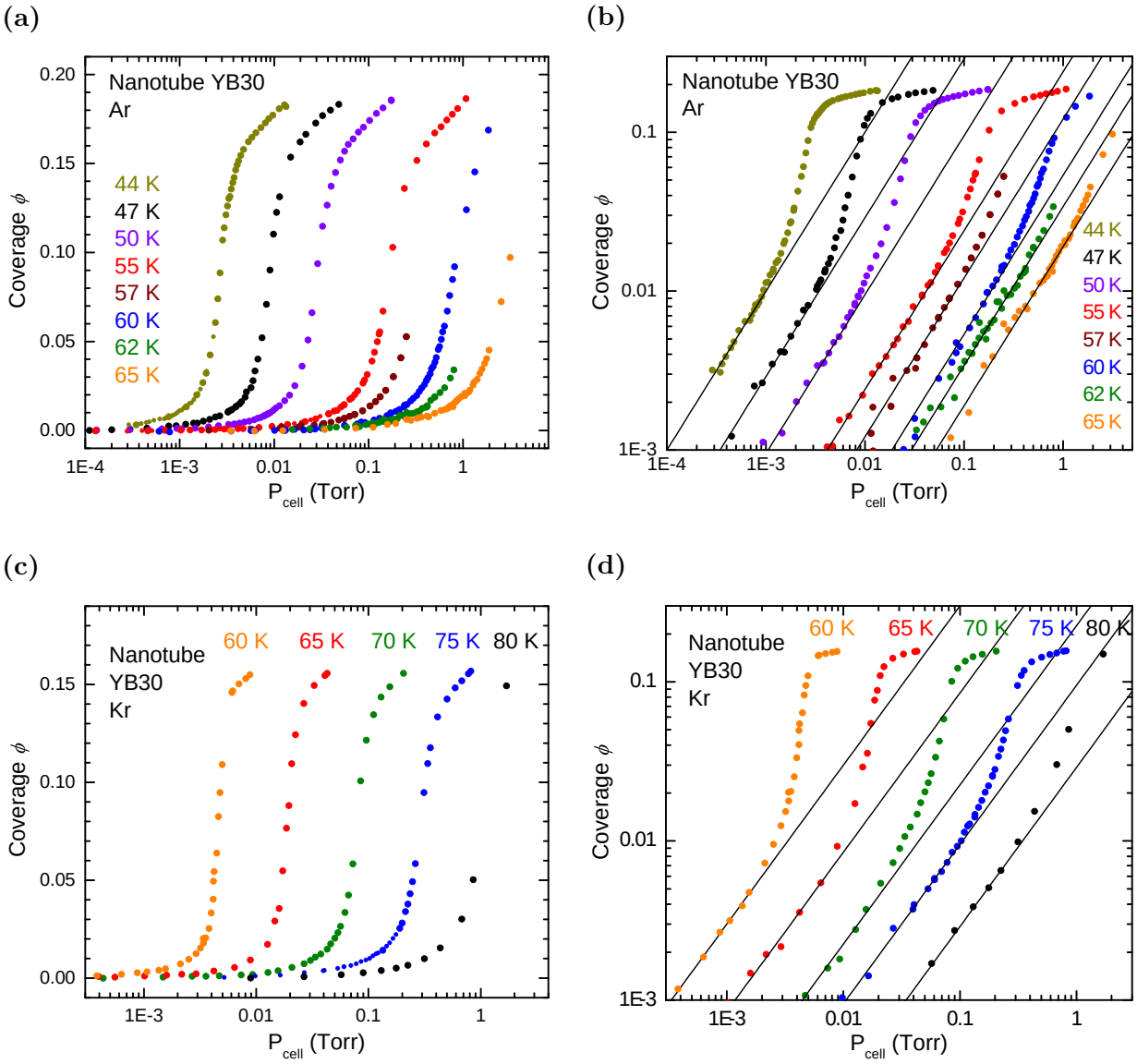

Figure 3.4: Coverage isotherms of (a) Ar and (c) Kr measured on device YB30. Panels (b) and (d) show the same isotherms plotted on a log–log plot. Henry's law behavior ($\phi \propto P$) occurs in the isotherms at coverage $\phi < 0.01$.

From the slopes of the Henry's law regions of isotherms we can determine the binding

energy ϵ_b. To this end we first rewrite Eq. (3.4) in dimensionless form

$$\exp\left(\epsilon_b/T\right) = C_0 T^{3/2} \frac{\phi}{P} \tag{3.5}$$

and take the natural log of both sides. We introduce dimensionless variable

$$Y = \ln(\phi/P) + \frac{3}{2}\ln(T) = \epsilon_b/T + C \ , \tag{3.6}$$

where $C = \ln(C_0)$. Plotting Y versus inverse temperature $1/T$ we obtain a linear dependence with the slope giving the binding energy ϵ_b. The linear fits are shown in Fig. 3.5. The determined single particle binding energies on device YB30 are $\epsilon_b = (776 \pm 10)\,\mathrm{K}$ and $\epsilon_b = (997 \pm 37)\,\mathrm{K}$ for Ar and Kr, respectively. These binding energies are approximately 70 % of the single particle binging energies of Ar and Kr to the surface of bulk graphite. On graphite $\epsilon_b = (1150 \pm 40)\,\mathrm{K}$ for Ar and $\epsilon_b = (1450 \pm 60)\,\mathrm{K}$ for Kr [81]. The reduction of ϵ_b compared to bulk graphite is due to the presence of only one layer of carbon atoms in the nanotube and, also due to curvature.

It is important to note that the fit we use to determine the single particle binding energy is not sensitive to extra mass present on the nanotube, e.g., due to contaminants. If the assumption that the nanotube is bare does not hold, the coverage extracted from the mechanical resonance shift will be rescaled according to Eq. (3.3). The rescaling of coverage will lead to a modification of the the constant C in Eq. (3.6), unaffecting the extracted binding energy ϵ_b.

This analysis in fact shows that in the limit of low adsorbate coverage we measure an accurate single particle binding energy to a highly homogeneous surface of the device. Indeed the observation of Henry's law implies that the surface of the device is highly uniform. If high binding sites were present on the surface, for example next to edges of patches of contamination, adsorption would occur at those sites preferentially. The linear relationship between P and ϕ would not hold in this case.

If the Class II adsorption behavior is due to contaminants present on the surface of the suspended nanotube devices, they must completely coat the nanotube surface and in turn

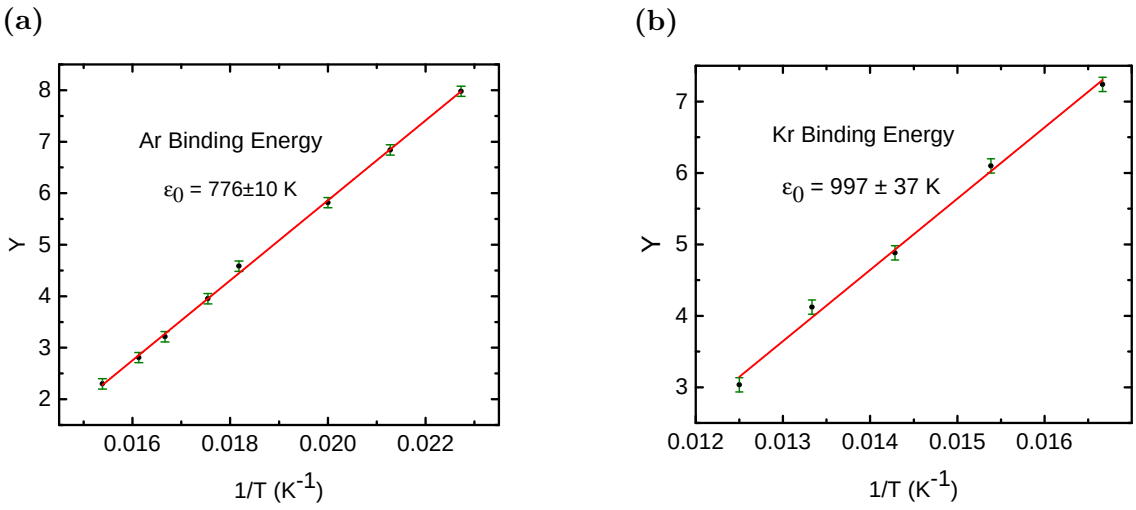

Figure 3.5: The linear fits used to extract the single particle binding energy from the slopes of Henry's law isotherms of Ar and Kr on nanotube device YB30. The dimensionless variable Y is given by Eq. (3.6). According to Henry's law, Eq. (3.4), the slope of the linear fit gives the binding energy ϵ_b. See text for more details.

form and expose a highly uniform surface to adsorption. The exposed surface must have a well defined almost constant single particle binding energy in different locations over the entire surface. This is difficult to reconcile with the variable maximum coverages ϕ attained by different Class II nanotubes, as it implies (if the contaminant scenario is to hold true) that the amount of contaminants are widely variable between devices. These contaminants would have to deposit on the nanotube devices either during exposure to air or during cooldown in the cryostat, as the nanotubes do not come in contact with any processing chemicals during device fabrication, see section 2.1.1.

None of the nanotube devices studied in the Cobden lab have been aggressively current annealed at cryogenic temperatures. It is important to note (as we later found) that upon exposure to air the studied suspended graphene devices become contaminated with some unknown contaminant that disrupts the expected graphite like adsorption behavior of ad-

sorbed monolayers. The suspended graphene devices require very aggressive current anneals at cryogenic temperatures to expose a clean surface for adsorption, which becomes recontaminated upon exposure to air, see section 4.1. The presence of the same contaminant can not be ruled out on Type II nanotube devices. On the other hand it is possible that we are measuring adsorption on clean nanotube surfaces and the two classes of adsorption behavior on nanotube devices arise through some different mechanism.

3.4 Charge transfer from adsorbates to carbon nanotubes

During gas adsorption the conductance as a function of gate voltage $G(V_g)$ of suspended carbon nanotubes is modified by the presence of the adsorbates. The main effect on $G(V_g)$ that is consistently present across all nanotube devices is the shift of the $G(V_g)$ curve along the gate voltage axis by ΔV_g. This shift can be unambiguously determined at low temperatures in the presence of Coulomb Blockade (CB) oscillations by tracking the positions of the CB peaks (see e.g. Fig. 3.7b), the procedure is discussed in reference [29]. At high temperatures, in addition to the shifts, there is also a modification of the shape of the $G(V_g)$ curve at V_g away from the gap [29]. The representative changes of $G(V_g)$ of several nanotube devices due to the presence of a dense monolayer of various gases are presented in appendix A.

Specifically, at high temperatures, ΔV_g can be determined by tracking the shift of the p-channel threshold of the nanotube, see Fig 3.7a. The charge transferred to the nanotube from the adsorbates can be extracted by comparing ΔV_g to the periodicity of the CB oscillations ΔV_{CB}. The charge transfer in units of electrons is determined by [29]

$$\Delta Q = e\frac{\Delta V_g}{\Delta V_{\mathrm{CB}}} \quad . \tag{3.7}$$

For nanotube devices the total charge transfer due to the formation of a full monolayer of adsorbates is small, $\Delta Q < 1e$. This corresponds to a charge transfer of $\approx 1 \times 10^{-5}$ electrons per adsorbed atom within the monolayer. The charge transfer is quite variable among different gases and devices. A table of measured charge transfers on several different devices in the presence of a dense monolayer of various gases is presented in appendix A.

On Class I nanotube devices ΔV_g and thus, according to Eq. (3.7) the charge transfer appear to be monotonic as a function of coverage ϕ, see Fig 3.7e. On the other hand, on devices exhibiting Class II adsorption behavior the charge transfer is nonmonotonic as a function of coverage, see Fig. 3.7c and Fig. 3.6. On the latter devices the amount of charge transfer at low ϕ is highly temperature dependent.

Let us discuss the features present in Fig. 3.6. On device YB30 we measured G and ϕ at fixed equilibrium pressures. The conductance G was measured at the p-channel threshold. The changes in G are due to the nonmonotonic shift of the p-channel threshold by ΔV_g. The charge transfer can be determined from G by

$$\Delta Q = e\Delta G \frac{dV_g}{dG} \frac{1}{\Delta V_{\mathrm{CB}}} \quad . \tag{3.8}$$

At low coverage the linear dependence $G \propto \phi$ indicates that the effect on conductance due to the adsorption of each individual atom is constant. This shows the absence of inter-atomic interactions within the adsorbed monolayer in the low coverage limit. At a higher coverage $\phi \approx 0.01$ we observe a very sharp turnaround point in the $\Delta Q(\phi)$ dependence at coverages where Henry's law ceases to work indicating the onset of the inter-atomic interactions within the monolayer. We interpret this as indications to the relevance of collective effects within the monolayer affecting charge transfer.

In conclusion, this Chapter 3 summarizes our experimental studies of the effects of various gas adsorbates on the surface of carbon nanotubes. One of the main results is the presence of two qualitatively different behaviors we called Classes I and II of nanotubes. We present evidence that the physical difference between the two classes is in that Class I devices are clean, while Class II are likely uniformly covered by an unknown type of contaminant. The related discussion of graphene behavior is present in Chapter 4.

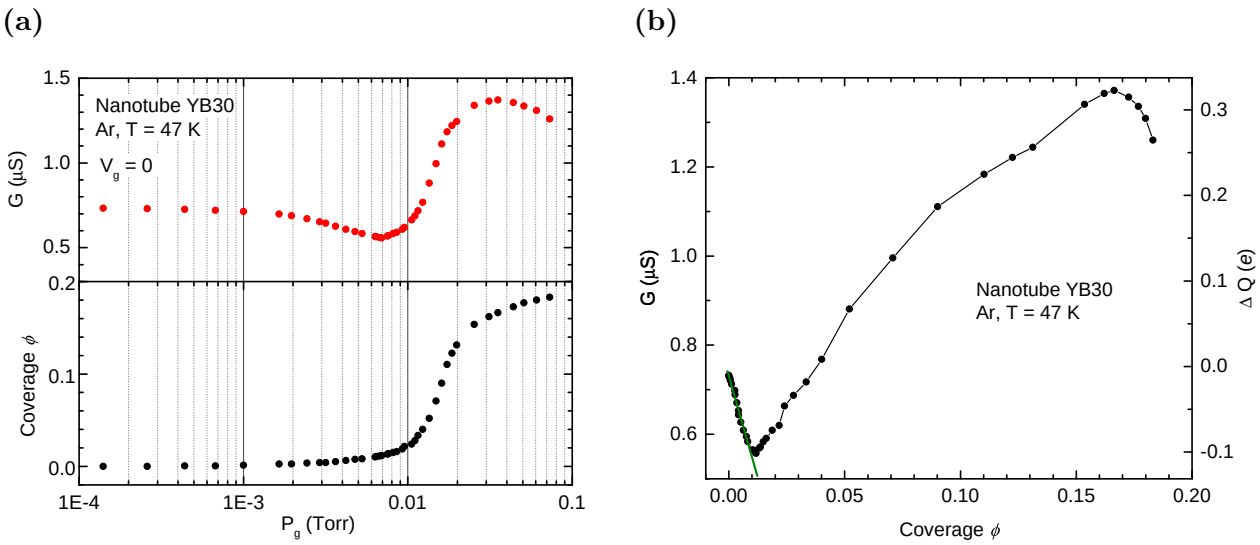

Figure 3.6: (a) A conductance and coverage isotherm of Ar on nanotube device YB30 (Class II) at $T = 47\,\mathrm{K}$. The conductance G is measured at $V_g = 0\,\mathrm{V}$ near the p-channel threshold. (b) Conductance G and charge transfer ΔQ vs. coverage ϕ. See text for discussion.

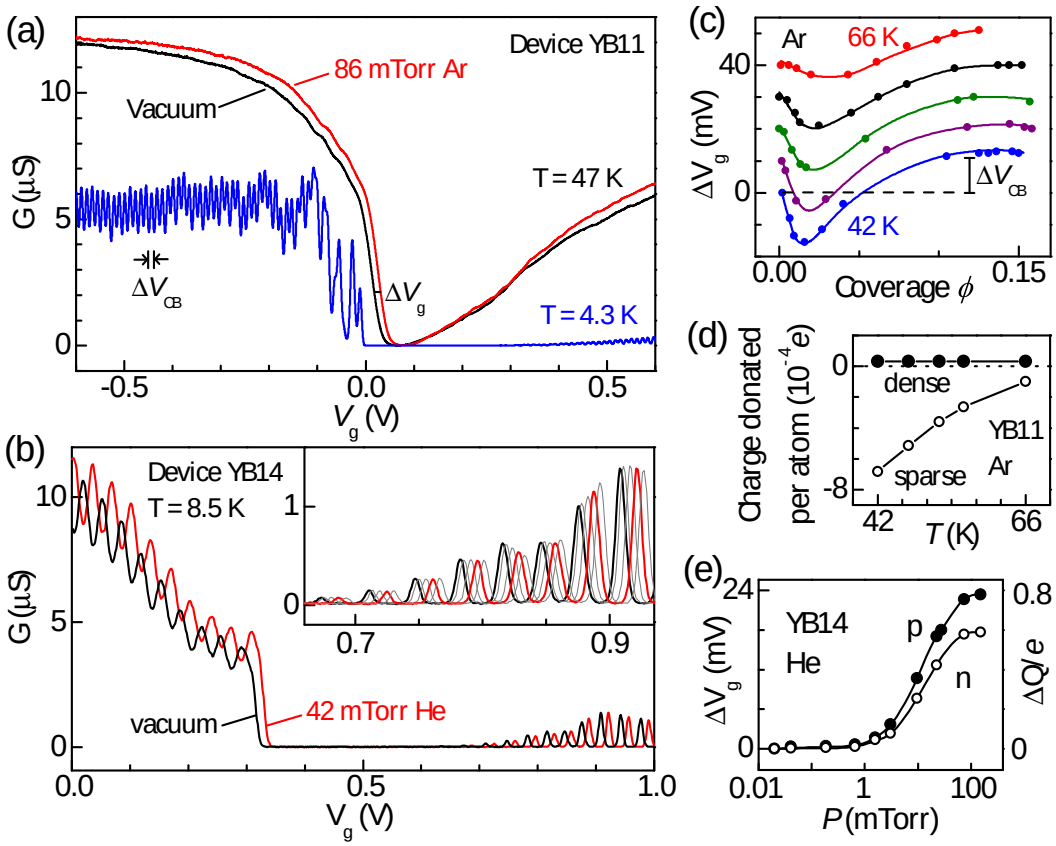

Figure 3.7: (a) The conductance as a function of gate voltage $G(V_g)$ of nanotube device YB11 (Class II) at $T = 47\,\mathrm{K}$ in vacuum and with a monolayer of Ar. The formation of a dense monolayer produces a shift of the p-channel threshold by $\Delta V_g \approx 10\,\mathrm{mV}$. The $G(V_g)$ of the device at $T = 4.3\,\mathrm{K}$ shows the Coulomb Blockade (CB) oscillations with periodicity $\Delta V_{\mathrm{CB}} = 11\,\mathrm{mV}$. (b) The shifts of $G(V_g)$ of nanotube device YB14 (Class I) due to the adsorption of helium. (c) The shifts of the p-channel threshold of device YB11 as a function of monolayer coverage at temperatures $T = 42, 47, 52, 56,$ and 66 K. The shifts are nonmonotonic as a function of coverage. (d) Charge transfer to the nanotube YB11 from the adsorbed Ar atoms. The charge transfer at low coverage is highly temperature dependent and is of opposite sign compared to high coverage. (e) Shifts of the CB oscillations of device YB14 in p-channel and n-channel due to the adsorption of He. The shifts are monotonic as He adsorbs on the device. The figure is adapted from the publication of our group [29].

Chapter 4

ADSORPTION ON GRAPHENE

This chapter will cover the outcome of our study of the effects of gas adsorption on the conductance of suspended graphene devices. It will cover our investigations of the behaviors and structures of the adsorbed monolayers obtained through their effects on the conductance of the suspended devices. A comprehensive study of gas adsorption of noble gases (Ar, Kr, Xe, Ne) and diatomic molecules (N_2, CO, O_2) was performed on graphene devices with thicknesses ranging from trilayer down to monolayer. The phase diagrams of the adsorbed monolayers on clean graphene were determined from features present in the conductance isotherms. Adsorbed monolayers on clean graphene devices uncovered by current annealing exhibit phases analogous to those seen in adsorbed monolayers on the surface of bulk graphite. Phase transitions of adsorbed gases on bilayer, trilayer and hBN backed devices occur at pressures comparable to that on bulk graphite, while on monolayer graphene devices they occur at slightly elevated pressures due to a very small reduction of binding energy compared to that of bulk graphite and the studied thicker devices.

The measured bilayer and trilayer devices were all freestanding with adsorption occurring on both sides of the device. Monolayer devices were fabricated both freestanding and capped with multilayer hexagonal boron nitride (hBN). In the hBN capped devices adsorption was restricted to only one side of the graphene sheet. Comparison of the adsorption behaviors of hBN capped vs. freestanding monolayer graphene devices allowed us to study the effects of the interactions of physisorbed monolayers across the graphene sheet. This is a new phenomenon which does not occur in monolayers adsorbed on the surface of bulk graphite crystals.

Because each fabricated graphene device can contain a variable level of contamination

and disorder which is difficult to control, it is important to separate features present in adsorption measurements which result from the interaction of the adsorbates with this foreign contamination versus those effects the occur due to the adsorption on the clean regions of graphene. Those features resulting from adsorption on clean graphene should be universal across all measured low disorder devices. The clean regions of the suspended graphene devices are uncovered by aggressive current annealing. To this end I will present adsorption data which has been obtained on 18 separate devices: 1 trilayer graphene device, 3 bilayer devices, 10 freestanding monolayer devices, and 4 monolayer devices capped with hBN.

In contrast to carbon nanotube devices, where coverage of the monolayer can be directly obtained from the mechanical resonance frequency shifts (see section 3.1), only conductance isotherms can be performed on the graphene devices. Coverage cannot be measured due to the fact that our graphene devices do not support mechanical resonances with high enough Q-factor. The fabrication process produces graphene devices with low tension, corrugations, and polymer residue which significantly broaden the mechanical resonances.

I start the chapter by discussing pre-annealed adsorption behavior that is present in all of the measured devices upon initial cooldown, which hints at the presence of a ubiquitous high binding contaminant that coats the surface of all of the devices upon exposure to air or during the cooldown in our cryostat. Subsequently I will discuss the adsorption that occurs on clean regions of the graphene devices that are cleared of any contaminants following aggressive current annealing.

4.1 Pre-annealed adsorption behavior on graphene devices

4.1.1 Isotherms before current annealing the suspended graphene

The ultimate goal of the project was to measure gas adsorption behavior on a pristine, contamination free graphene surface. We performed adsorption measurements on as fabricated devices and devices that have been furnace annealed. Upon initial cooldown these devices do not show the adsorption behavior that is expected to occur on bulk graphite. In order

to recover the conventional bulk graphite–like adsorption behavior the suspended graphene devices need to be aggressively current annealed. All of the fabricated devices showed surprisingly similar adsorption behavior prior to current annealing and would recover this behavior if warmed up to room temperature and exposed to air after a current anneal has been carried out at cryogenic temperature. In the rest of this section I will refer to this adsorption behavior before a current anneal procedure has been carried out as "pre-annealed" adsorption behavior.

As described in section 2.1.3, after a successful fabrication process, upon the removal of a suspended device from solvent, it will contain a variable amount of polycarbonate polymer residue which can be several nanometers thick and coats the device surface. An AFM topography scan of this residue on an as fabricated suspended device is shown in figure 2.6b. The residue forms patches with what appear to be small clean regions of graphene exposed in-between. The typical size of the clean regions separating the patches is on the order of 20 nm in the typical fabricated devices. The inhomogeneously deposited polymer residue causes a severe reduction in the mobility (μ) of graphene. This results in the suspended devices having a minimal dependence of conductance on gate voltage $G(V_g)$ in the range of several volts that can be safely applied to the suspended devices. To achieve the goal of measuring adsorption on clean graphene we developed a reproducible procedure of current annealing the devices following similar procedure as reported in the literature [40, 57]. During the development of the current annealing procedure we discovered strong evidence that there is another type of contamination that disrupts monolayer formation on the graphene devices. This contamination either deposits on the device during cooldown inside the cryocooler gas cell or during an exposure to air at room temperature. The contaminant has relatively strong binding to graphene.

On polymer residue coated devices gas adsorption should still occur onto the exposed regions of the graphene with an unmodified binding energy. Due to the short range nature of the Van der Waals interaction the adsorbates should not be sensitive to any contaminants more than about a nanometer away from the adsorption site. The edges of the polymer

residue patches on the other hand should present higher binding sites to the gas adsorbates than the clean graphene regions, due to the added attraction of both the graphene surface and the contaminants. One might reasonably expect that adsorption on such devices to occur at lower pressures than on pristine graphene, with the monolayer growth expanding out from the edges of the polymer contaminated patches, out from the higher binding sites. The phase transitions in the clean patches should become smeared out due to the finite size effects of their small areas. At higher pressures the exposed graphene patches should still become covered by a dense, close packed monolayer for all of the adsorbates. The adsorption behavior of such contaminated devices would be expected to be greatly dependent on the amount and distribution of the polymer residue contamination and thus be highly device dependent.

As discussed in section 2.1.3 the polycarbonate residue contamination can be greatly reduced by furnace annealing the devices in an inert Ar/H_2 atmosphere at temperatures of several hundred °C. Due to large exposed clean surface areas (see Fig. 2.6e), such devices would be expected to have adsorption behavior analogous to bulk graphite, qualitatively different from the non furnace annealed devices.

Surprisingly following an initial cooldown, none of the studied devices showed any adsorption isotherm features related to phase transitions seen on bulk graphite. The adsorption isotherms for both the furnace annealed and as fabricated devices are extremely similar. For all of the measured gases the conductance isotherms show one main broad step which occurs at a pressure of approximately two orders of magnitude higher than the expected initial condensation into a dense 2D monolayer on bulk graphite. For all of the devices studied this initial step occurs at almost the same pressure for a given temperature. Argon adsorption isotherms measured at $T = 60\,\mathrm{K}$ on eight separate devices are presented in figure 4.1. The total change in conductance ΔG due to the argon adsorption has been normalized for easier comparison: $\Delta G_{\mathrm{normalized}}(P_g) = (G(P_g) - G(0))/(G(P_{\mathrm{sat}}) - G(0))$.

When the rescaled pre-annealed adsorption isotherms are plotted together they fall on top of each other. This indicates that the pre-annealed adsorption behavior occurs regardless

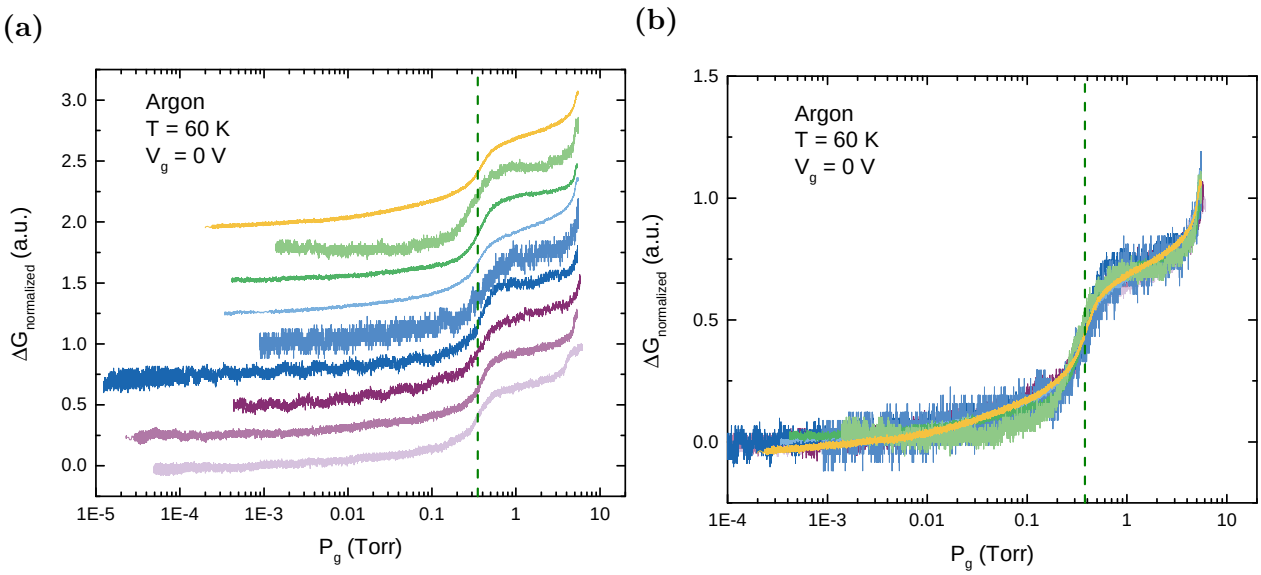

Figure 4.1: Pre-annealed conductance isotherms of argon at $T = 60\,\mathrm{K}$ on various suspended devices. Conductance has been normalized for easier comparison. P_g is the measured gas pressure, see section 2.2.2.1. (a) Bottom to top: Device #2 – bilayer graphene, furnace annealed; Device #3 – trilayer graphene, furnace annealed; Device #4 – bilayer graphene, not furnace annealed; Device #4 after current annealing and subsequent exposure to air; Device #9 – bilayer, not furnace annealed; Device #13 – bilayer, not furnace annealed; Device #14 – monolayer, not furnace annealed; Device #18 – bilayer, not furnace annealed; Device #28 – bilayer, not furnace annealed.

of the amount and distribution of polycarbonate residue on the surface of the devices. The significantly less contaminated furnace annealed devices exhibit the same adsorption behavior as non furnace annealed devices. The magnitude of the change in conductance ΔG vacuum to saturation during a pre-annealed isotherm is small and similar for all gases on a particular device. For argon, ΔG varies between about 2% to 0.3% among all the devices measured.

In all of the studied devices there is minimal change in conductance at low pressures where the initial monolayer condensation on pristine graphene in expected to occur. For

some gases such as Kr and O_2, the conductance on pre-annealed devices sharply increases as the cell pressure approaches the saturated vapor pressure of the gas, see Fig. B.2c. This is indicative of multilayer condensation occurring on the surface device (wetting). Such multilayer condensation behavior can be truncated by small temperature gradients in the measurement apparatus near saturated vapor pressure [63, 6]. A complete set of pre-annealed adsorption isotherms for all measured gases is presented in appendix B.1. Some gases such as neon, O_2 and N_2 exhibit a second smaller step at higher pressures in the pre-anneled conductance isotherms, see Fig B.2. The attribution of this step to specific adsorption processes on the surface of the device is unclear. There is a possibility that the step might be might be due to second layer condensation on the device.

4.1.2 Current annealing to recover conventional adsorption behavior

An aggressive current anneal at cryogenic temperatures is required in order to recover the bulk–graphite like adsorption behavior. Current annealing is a standard procedure widely used to remove contamination and improve the mobility of suspended devices [57, 52, 40, 83]. During a current anneal a high bias voltage is applied across the device, which causes its temperature to increase due to Joule heating. Effective current annealing of suspended graphene devices is possible because thermal conductivity of the graphene sheet decreases at elevated temperatures, which causes a hotspot to develop at the center of the suspended device. The temperature of this central region can exceed 2500 K before device breakdown occurs [42]. As the device heats up, any contamination adhered to its surface either migrates away from the hot region or desorbs from the surface. A large temperature gradient occurs across the device away from the central region towards the contacts which act as heat sinks that are effectively thermally anchored to the temperature of the cryocooler cell[42]. There is always a region of remnant contamination located near the contacts which is impossible to remove by current annealing the device[40].

An incremental current annealing procedure was performed on our devices. The source–drain bias voltage was gradually ramped up to a predefined value, at which point the ramp

was reversed and the voltage was swept back down to zero. A typical anneal ramp was performed in vacuum, at a pressure lower than 1×10^{-5} Torr and at a ramp rate of 0.5 V/min. After each anneal cycle the gate dependence $G(V_g)$ of the device was measured and an adsorption isotherm was performed. The current anneal procedure was typically done at a temperature of $T = 60$ K so that an adsorption isotherm of either argon or nitrogen could be performed immediately after each anneal cycle. The source–drain bias V_{sd} was increased for each subsequent current anneal, typically in increments of 0.1 V to 0.2 V until the device started to show the expected graphite-like adsorption behavior.

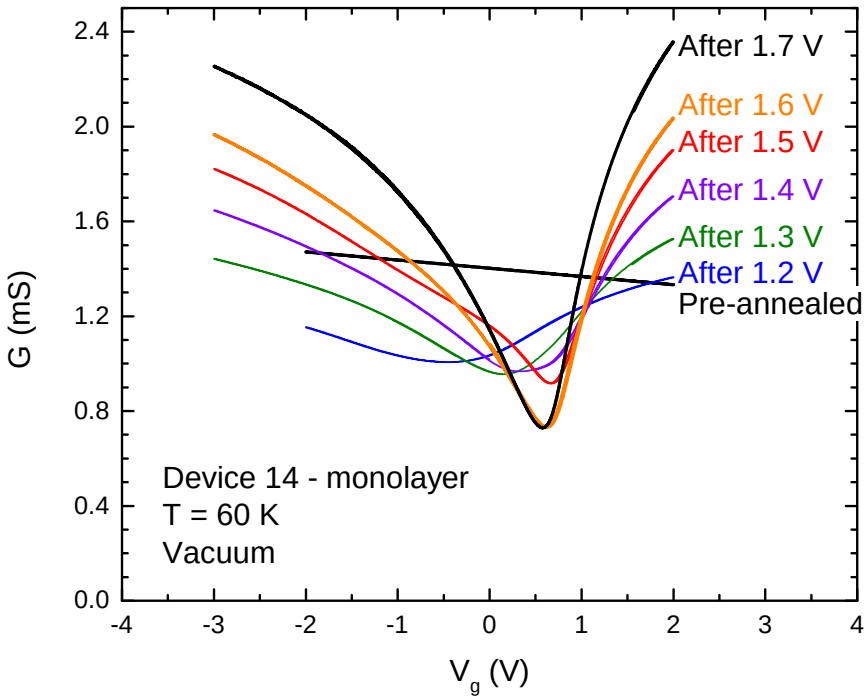

Figure 4.2: Conductance as a function of gate voltage $G(V_g)$ of monolayer graphene device #14 at $T = 60$ K after various levels of current anneal. The device is suspended over a 1.75 µm trench. Graphite-like adsorption behavior was completely absent on the device until the 1.3 V anneal. The device burned out during the 1.8 V anneal. The estimated field effect mobility of the device after the 1.7 V anneal was $\mu_{FE} \approx 5 \times 10^5$ cm^2/Vs at $T = 4.2$ K.

A decision has to be made when to terminate the current annealing procedure and stop going to higher source–drain biases. This turns out to be quite difficult as the cleanest devices result after current anneals with applied V_{sd} very close to the device breakdown. This typically occurs at significantly higher applied voltages than the current anneal threshold required to recover the graphite–like adsorption behavior. For example on monolayer device #14 the first traces of the graphite-like adsorption behavior in the isotherms appeared after the $V_{sd} = 1.3\,\mathrm{V}$ anneal. The device mobility along with the magnitude of the effect of adsorption on conductance kept increasing until the highest anneal level that the device was able to tolerate before burnout of $V_{sd} = 1.7\,\mathrm{V}$. Conductance as a function of gate voltage $G(V_g)$ of the device after various levels of current anneal are shown in Fig. 4.2. After the $1.7\,\mathrm{V}$ anneal the estimated field effect mobility μ_{FE} of the device approached $5 \times 10^5\,\mathrm{cm}^2/\mathrm{Vs}$ at $T = 4.2\,\mathrm{K}$ before the device finally burned out during the subsequent $1.8\,\mathrm{V}$ anneal.

As the bias is ramped up during successive current anneal, a central region of the device becomes contamination free, and this region expands after each successively higher applied source–drain bias level. This can be seen in AFM scans performed on a suspended bilayer graphene device after different stages of current anneal, Fig. 4.4.

By performing isotherms on devices after progressive levels of current anneal we can study the evolution of the adsorption behavior as the contamination is gradually removed from the surface of the device. A set of adsorption isotherms of argon after increasing levels of current anneal on trilayer graphene device #3 suspended over a $1\,\mu\mathrm{m}$ trench are shown in Fig. 4.3. On this device current anneals at voltages below $V_{sd} < 1.5\,\mathrm{V}$ resulted in little change in the adsorption behavior from the pre-annealed case. This indicates that the central region of the device did not reach a high enough temperature to desorb the contamination giving rise to the pre-annealed adsorption behavior. After the $1.5\,\mathrm{V}$ anneal the pre-annealed adsorption step became broader, but there was still no sign of any feature in the isotherm related to the argon supercritical liquid–vapor (L–V) phase transition which is expected to occur on a graphite surface at $T = 60\,\mathrm{K}$. Finally after a $2.0\,\mathrm{V}$ anneal a step related to the supercritical L–V phase transition appeared in the conductance isotherm. The Ar L–V step is

in coexistence with the broadened pre-annealed adsorption feature. A change in conductance is also present at low pressures in the isotherm, indicating that there are higher binding sites on the surface of the device. After the $V_{sd} = 2.3\,\mathrm{V}$ anneal, both the pre-annealed and the higher binding adsorption behavior completely disappeared from the isotherm. At the same time the change of conductance of the supercritical L-V transition increased in magnitude.

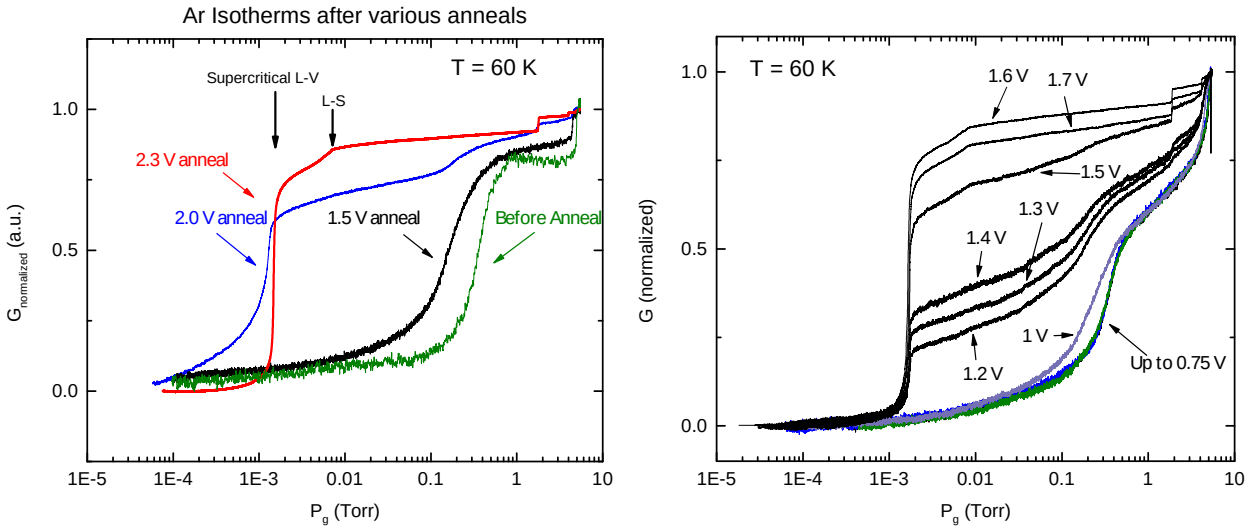

Figure 4.3: Argon isotherms on trilayer graphene device at T = 60 K after various levels of current annealing. The conductance for each isotherm has been normalized so that $G_{Vac} = 0$ and $G_{sat} = 1$.

The coexistence of both the pre-annealed and the post annealed, graphite-like adsorption behavior on the devices indicates that the two adsorption behaviors occur on different parts of the device surface which are spatially separated. The post-annealed graphite like adsorption behavior has to occur in the cleaned out central region of the device which attains the highest temperature during the current anneal, while the pre-annealed adsorption behavior has to occur at the periphery of the device, in regions that fail to attain a high enough temperature during the current anneal to remove the contamination giving rise to the pre-annealed adsorption behavior. Similar behavior can be seen in the set of isotherms

performed on a bilayer device shown in Fig. 4.4a. As the source–drain bias is increased during subsequent current anneals the clean area of the graphene sheet giving rise to the graphite-like adsorption behavior grows in size, resulting in an increase of ΔG due to the adsorption on clean region. We can acquire AFM images of the exposed clean central region of the suspended devices after various levels of current anneal once the device is removed from the cryocooler, figure 4.4c. The clean region of the graphene device is easily seen using the adhesion data obtained with PeakForce Tapping imaging mode of our AFM.

4.1.3 Device recontamination by atmospheric adsorbate

If a current annealed device showing the graphite–like adsorption behavior is warmed up, exposed to air and subsequently re–cooled, it reverts back to the pre-annealed adsorption behavior. This reversion to the pre-annealed adsorption behavior is universally seen on all of our devices which have been removed and reinserted into the cryocooler. The adsorption isotherms on such devices look identical to the pre-annealed adsorption isotherms before any current annealing has been performed. This is quite surprising because current annealed devices at cryogenic temperatures initially contain a completely contaminant free surface in the center of the suspended region. If imaged with the AFM upon device removal such a region appears to have a surface roughness of less than $< 0.1\,\mathrm{nm}$. Clearly something must be adsorbing into this clean region and disrupting the graphite–like adsorption behavior either during exposure to air or upon a subsequent cooldown in the cryocooler.

A set of argon isotherms during an original current anneal run on a bilayer graphene device are shown in Fig. 4.4a. Argon isotherms following a recontamination of the same bilayer device are shown in figure 4.4b. Upon the initial cooldown, during the first round of current anneals the argon L-V phase transition became observable after the 2.4 V anneal. Upon the subsequent cooldown the device had to be current annealed to 1.75 V to recover the argon L-V adsorption behavior. There was no change in the adsorption isotherms at milder anneals below the $V_{sd} = 1.75\,\mathrm{V}$. The power dissipated by the device during the quite aggressive anneal was about 16 mW.

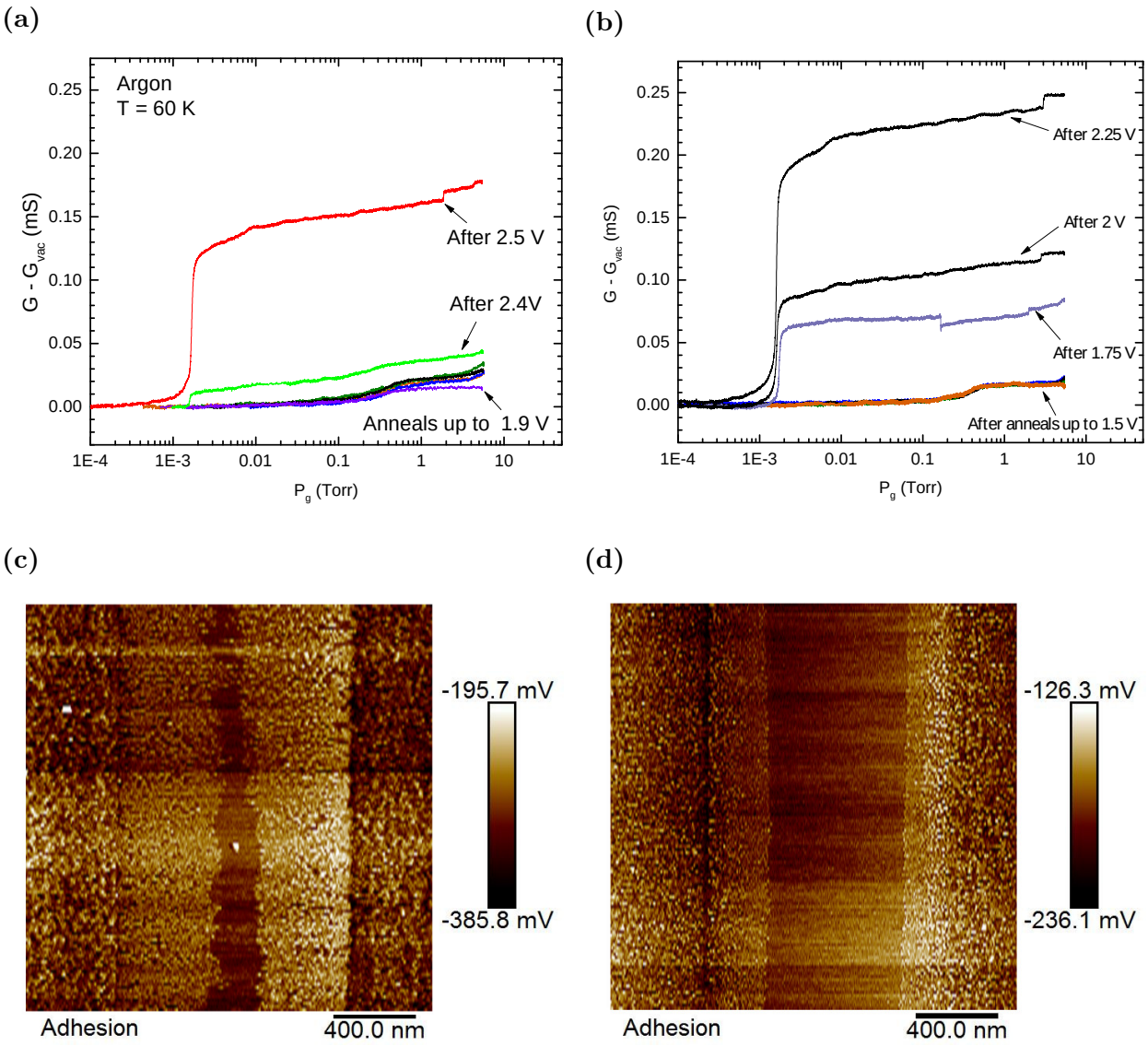

Figure 4.4: (a) Adsorption isotherms of argon on a bilayer device suspended over a 1 µm trench after various levels of anneal. There is minimal change in the adsorption behavior below an anneal of 1.9 V. (b) Another set of adsorption isotherms after the device has been exposed to air. The device had to be reannealed to 1.75 V to recover the argon L–V transition. (c) An AFM scan of the device after the first 2.5 V anneal. The residue free central region is clearly visible. (c) An AFM scan of the same device device after a 3.0 V anneal. The clean region is significantly larger, with polycarbonate residue still remaining near the contacts.

Whatever the nature of this foreign adsorbate, it disrupts the graphite–like adsorption behavior of the device. The above discussion implies that the contaminant has a relatively high binding energy to the graphene device surface. The disruption of adsorption due to the contaminant occurs in an identical manner on all studied devices giving rise to very similar pre-annealed adsorption behavior. To explain the similarity in the pre-annealed adsorption isotherms we propose that the contaminating adsorbate must be covering the entirety of the graphene device surface across all of our devices. The coverage of the contaminant adsorbate must be close to a full monolayer, otherwise we would expect to see high binding sites at the edges of the contaminant molecules, which we don't observe on any of the more than thirty studied pre-current annealed samples. This contaminant must have high binding to graphene in order to remain on the surface with little perturbation during relatively aggressive current anneals, indicating that it has to be made up of rather large molecules. The vapor pressures of these contaminants is low enough below at least $T < 200\,\mathrm{K}$ for them to not redeposit on the device surface after a current anneal. If the contaminants deposit on the device from air, it is natural to assume that they would be some mixture of chemical species with various chemical groups exposed on their surface. For the adsorption behaviors to be virtually the same across all of the studied graphene devices the composition of the contaminant species must be very similar across all of the studied devices. If the contaminants coat the surface of the device at room temperature, they are not seen in our AFM topography images performed using typical tapping mode tips with typical diameters of $\approx 10\,\mathrm{nm}$.

The contamination of exposed surfaces upon an exposure to air by hydrocarbons is a well known phenomenon. It is widely seen in the XPS community and is referred to as "adventitious carbon" [47]. Groups performing XPS studies observe contamination which gives rise C–C and C–O peaks in the emission spectrum. This contamination is seen to deposit on exposed surfaces from air and even inside UHV chambers at low pressures. The distributions of the contaminant species across samples and measurement runs is reported to be somewhat variable [47]. The hydrocarbon contamination of freshly cleaved graphite surfaces after exposure to air has also been reported by groups performing wettability contact

angle studies [2]. The water contact angles are seen to undergo large changes from 30° to over 90° over the course of hours and can serve as a reliable indicator of surface hydrocarbon contamination.

It has been reported by several groups performing high resolution AFM studies of graphene surfaces [19, 34, 86] that all exfoliated graphene and BN sheets fabricated in the lab become coated by an adsorbed layer of linear chain like molecules which give rise to subtle stripe like features observable in surface topography. The reported features have a periodicity of about 4 nm and can only be imaged using high aspect ratio tips with diameters of less than 1 nm. The adsorbed molecules are proposed to self assemble into periodic lamella like monolayers. The orientation of the stripes is claimed to be aligned with the armchair axis of the graphene lattice [34] which is consistent with the behaviors of adsorbed alkanes at densities near monolayer completion. These linear alkane like hydrocarbons are proposed to be originating from various sources in the laboratory environment such as outgassing plastics or vacuum pump oil, and might be ubiquitously permeating the laboratory air in minute concentrations. Alkane like hydrocarbons of various lengths are known to adsorb onto graphene with their zig-zag backbones lying in plane and with the CH_2 subgroups of the molecule locking in registry with the hexagonal cells of the graphene substrate, which are the higher binding sites [26, 33].

The formation of such well ordered periodic monolayers of contaminant hydrocarbons on our graphene devices could explain most of the features seen in the pre-annealed adsorption behavior. The main riser in the conductance isotherms might be due to a second layer of gas adsorption on top of a monolayer of such close packed hydrocarbons on top of the graphene. The surface of the hydrocarbons could be inhomogeneous enough to cause the broadening of the adsorption step. The explanation for the shift of the adsorption behavior to higher pressures is not readily apparent.

According to [34], the adsorbed monolayer of contamination would not be observed in conventional contact or tapping mode AFM topography measurements as the tips with moderate diameters would not penetrate the adsorbed layer. This is a possible explanation for

the height discrepancy observed in AFM measurement of the first layer of graphene and hBN flakes as reported by various groups. The anomalous thickness of about 1 nm of the first layer of graphene could be the result of the measurement of the extra thickness of the adsorbed contaminant layer. A monolayer step within the same flake would produce the expected monolayer graphene height since the surface on either side of the step would be coated with the same layer of adsorbate. There is a high likelihood that all fabricated graphene and BN flakes studied in the laboratory are actually coated in a uniform film of hydrocarbon residues.

4.1.4 Similarity to Class II nanotube adsorption behavior

The pre-annealed conductance isotherms on graphene are reminiscent of the adsorption behavior seen on Class II carbon nanotube devices, discussed in section 3.2. In both cases the expected graphite–like adsorption behavior is completely absent. The main step in the isotherms is broadened and occurs at elevated pressures, approximately two orders of magnitude higher than expected for the adsorption on a pristine graphene surface. The locations of the phase boundaries of argon on nanotubes and on an hBN backed graphene device are shown in Fig. 4.5. For this device the midpoint of the main step in the pre-annealed conductance isotherms is plotted as large black circles. The position of the step is representative of the positions on all pre-annealed graphene devices. The step occur at pressures approximately two times lower than the adsorption on Class II carbon nanotubes. Once the hBN backed monolayer device is current annealed the phase boundaries for argon adsorption match well with those occurring on bulk graphite.

This raises the question of whether the adsorption behavior on Class II carbon nanotube devices has the same origin as the pre-annealed adsorption behavior on graphene, possibly related to the same adsorbed contaminants. It has to be stated that none of the Class II carbon nanotube devices studied have been aggressively current annealed, which seems to support the argument of contaminants covering their surface.

On the other hand several observations of adsorption behavior on Class II carbon nan-

otubes are difficult to reconcile with contamination. We observe Henry's law in the low coverage ($\phi < 0.01$) regions of the isotherms, see section 3.3. Such behavior can only occur on surfaces with a very high degree of homogeneity. This implies that if contaminants are indeed present on the surface of the nanotubes they must be highly homogeneous. At the same time they have to coat the entire surface of the nanotube. On Class II nanotube devices the maximum monolayer coverages obtained at saturation was variable among devices, which is difficult to reconcile with the above stated behavior. A dense layer of hydrocarbons on a nanotube surface is expected to increase its mass by $\approx 50\,\%$, and would significantly reduce the maximum attained adsorbate coverages, see discussion in section 3.2.

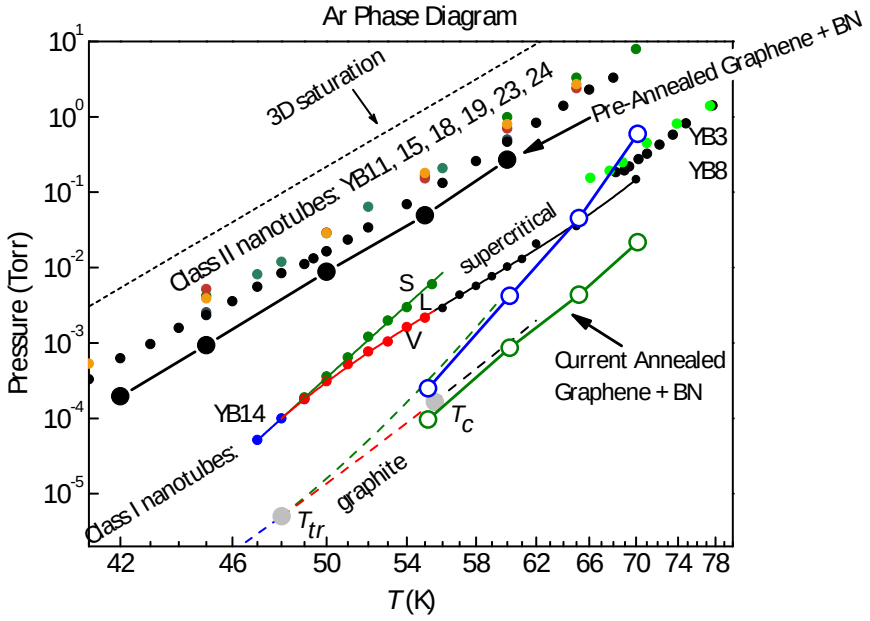

Figure 4.5: Pressure-Temperature phase diagram of argon on hBN backed graphene. Thermomolecular correction has been applied to the gauge pressure following [75]. The open green circles indicate the midpoints of the phase boundary of the supercritical fluid transition. Open blue circles indicate the phase boundary of the transition to 2D solid. The solid black circles show the midpoint of the pre-annealed adsorption step from Fig. B.1.

4.2 Post annealed adsorption behavior

4.2.1 Adsorption on Trilayer Graphene

I will begin the description of adsorption on clean graphene with adsorption on a Bernal–stacked (ABA) trilayer device. Adsorption on only one such device has been measured. The binding energies of adatoms to trilayer graphene are expected to be virtually identical to that of bulk graphite [66]. Also, the condensed monolayers formed on the top and bottom sides of the freestanding trilayer graphene are far enough apart so that no significant interaction of the monolayers occurs [9]. Thus, the two monolayers are expected to be almost completely decoupled. That is, the coupling is much smaller than the thermal energy kT at typical adsorption temperatures. We expect the structures of the adsorbed monolayers on the trilayer graphene device to completely reproduce the structures of monolayers that occur on bulk graphite. Accordingly, the phase boundaries between various monolayer phases should occur at identical pressures. Our measurements corroborate this picture. The novel effects of the formation of these adsorbed monolayers on the conductance of the device G are discussed below.

4.2.1.1 Effects on conductance

A conductance isotherm of argon Ar on the trilayer graphene device at $T = 60\,\mathrm{K}$ is shown in Fig. 4.7. To our knowledge, this is the first measurement of the effect of adsorption on the conductance G of disorder-free few-layer graphene device under equilibrium thermodynamic conditions. The shape of the conductance isotherm appears surprisingly similar to volumetric adsorption isotherms of argon performed on bulk graphite at the same temperature [55]. Features present in the conductance isotherm can be directly identified with phase transitions that are known to occur on bulk graphite and take place at identical pressures within experimental uncertainty. The same holds true for the adsorption of other noble gases measured on the trilayer device. The features corresponding to the phase transitions of argon are labeled in Fig. 4.7. Apart from remnants of the pre-annealed adsorption behavior

around $P_g = 0.1\,\mathrm{Torr}$ in the $T = 60\,\mathrm{K}$ isotherm, no new features in the isotherms are found. A complete set of isotherms for Ar, Kr, Xe, and Ne on the suspended trilayer device are presented in Appendix B, Fig. B.5.

The above described behavior implies that the effect of the adsorption of noble gas atoms into a monolayer with a particular structure on the conductance of the suspended trilayer device G does not depend on the actual structure of the adsorbed monolayer, but only on the coverage. For example the solid close-packed argon monolayer is known to undergo the Novaco-McTague [60] epitaxial rotation with respect to the graphite substrate lattice as the monolayer density increases. In our experiment the conductance on the trilayer device appears to be insensitive to this rotation. For krypton, the conductance is insensitive to the commensurability of the adsorbed monolayer, as there is no qualitative difference in the effects on conductance upon the formation of the $\sqrt{3}\times\sqrt{3}$ commensurate solid Kr phase; the isotherms are presented in Appendix Fig. B.5b. Other gases that form the $\sqrt{3}\times\sqrt{3}$ commensurate solid have not been studied on the trilayer device. It is important to note here that in the case of adsorption on bilayer graphene the effect of the formation of the $\sqrt{3}\times\sqrt{3}$ commensurate solid of N_2 resulted in qualitatively different behavior from krypton. The effect of adsorption of noble gases was quite similar for both bilayer and trilayer graphene, see Section 4.2.2.3.

To describe quantitatively our experimental findings let us introduce the following relevant physical quantities. The conductance of the device in vacuum (without any adsorbates present on its surface) will be denoted as G_0. In the trilayer graphene device at the temperatures at which adsorption isotherms of Ar, Kr, and Xe were performed, G_0 has minimal dependence on gate voltage: $G_0(V_g) \approx \mathrm{const}$ in the range of gate voltages V_g experimentally accessible in our suspended devices. This is due to the conductance being dominated by thermally excited carriers present as a result of the parabolic band structure of ABA stacked trilayer graphene [3].

In order to facilitate the comparison of the effects of adsorption across devices with varying levels of surface inhomogeneity and contamination, it is useful to track the change in

conductance of the device ΔG while the adsorbed monolayer is in an easily reproducible and identifiable state. An obvious choice is the initial point of the formation of a solid monolayer of the adsorbate on the surface of the device. For argon the formation of the solid monolayer occurs at the fluid to solid (2D solidification) phase transition. The conductance at this point in the isotherm will be denoted as G_1. The isotherms exhibit an easily identifiable kink at this phase boundary, see Fig. 4.7. The structure of the solid argon monolayer on bulk graphite near this phase transition is a triangular close packed lattice with a nearest neighbor spacing of $L_{nn} = 3.97\,\text{Å}$ [21]. The change in conductance of the device upon the formation of the close packed first layer will be defined as $\Delta G_1 = G_1 - G_0$; the relative change is denoted as $\delta G_1 = \Delta G_1 / G_0$.

As the ambient vapor pressure is increased past the fluid to solid transition, the incommensurate monolayer density increases due to the reduction of nearest neighbor atom spacing. The monolayer reaches maximum density before condensation into the second layer occurs. We will denote the conductance of the device at the monolayer completion, right before the condensation of the second layer as G_{1C}. The change in conductance $\Delta G_{1C} = G_{1C} - G_1$ contains contributions from two sources. As the adsorbed monolayer on the clean region of the device increases in density and affects the conductance, simultaneously adsorption on the contaminated regions of the device occur, see section 4.1. The magnitude of the effect on conductance of the contaminated region varies with surface contamination and changes upon different levels of current annealing.

At higher ambient vapor pressures the adsorbed film undergoes layer by layer growth. At low temperatures this occurs through first order layering transitions [25]. At each subsequent layering transition the N layer condenses on top of the previous $N-1$ layers through a first order transition from a dilute 2D gas to a close packed solid. Surprisingly, the conductance of the studied trilayer graphene device is sensitive to the formation of these extra layers. Steps up to the fifth layer of argon were detected before onset of saturated vapor pressure. We will denote the change in conductance upon the formation of layer N by ΔG_N. Since each subsequent layer forms on top of the same surface area as occupied by the previous layers,

one might expect that the ratio of $\Delta G_N/\Delta G_1$ to be universal on pristine, contamination free graphene. It is unclear if this relation should hold in the two terminal conductance of our suspended devices.

The argon isotherm presented in Fig. 4.7 was measured after an intermediate level of anneal of 2.0 V. The formation of a close packed monolayer of argon resulted in a change of conductance of the device of $\delta G_1 \approx 7\,\%$. After the most aggressive current anneal performed on the device of 2.3 V, the change in conductance δG_1 increased approximately three times, $\delta G_1 \approx 22\,\%$. At the same time the ratio of the effect of the formation of the second layer compared to the first $\Delta G_2/\Delta G_1$ remained constant, consistent with the above discussion. On the other hand, the ratio of the effect of the formation of the third layer $\Delta G_3/\Delta G_1$ decreased by approximately 25 %; the data are present in table 4.1. The comparison of the argon isotherms at 60 K after two levels of anneal are shown in Fig. 4.6. The change in conductance due to the pre-annealed adsorption behavior, which was present in the isotherm after the 2.0 V anneal, is completely absent from the isotherm performed after the aggressive 2.3 V anneal.

After the 2.3 V anneal, the effect on conductance of the trilayer device due to the adsorption of neon was larger than the effect of the other noble gases studied, with $\delta G_1 \approx 40\,\%$ at the charge neutrality point. The isotherms of neon on the trilayer device are shown in Appendix Fig. B.5d. Such large increases in conductance due to the adsorption of the noble gases is quite surprising. The mechanisms responsible for such large enhancements of conductance upon the adsorption of noble gas atoms on the trilayer device is unclear. The details of the mechanism responsible for the conductance enhancement can hopefully be revealed by studying the adsorption effects at different gate voltages V_g. This can be achieved by measuring $G(V_g)$ at fixed pressures P_g while the monolayer is in different states of adsorption with respect to coverage.

Due to its relatively smaller binding energy ϵ_b, adsorption of neon Ne was studied at lower temperatures than other noble gases, around 17 to 25 K. At these lower temperatures the trilayer device had a larger gate dependence of $G(V_g)$ than at the higher temperatures for the

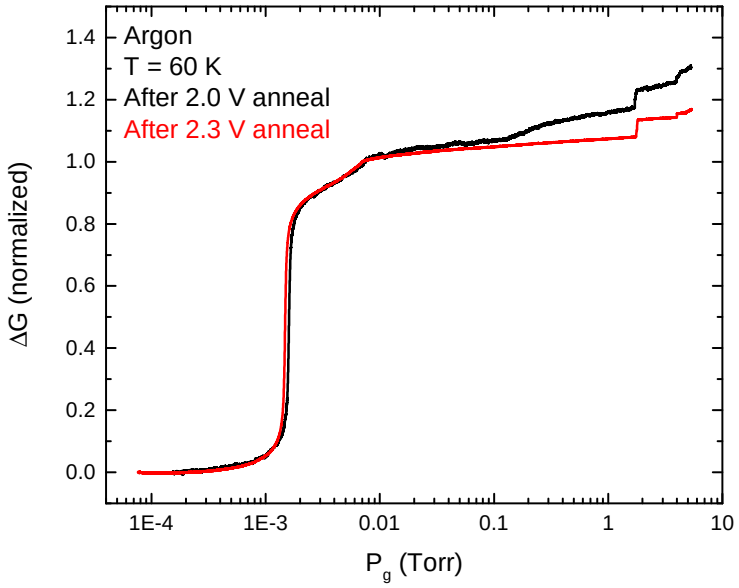

Figure 4.6: Argon isotherms on the trilayer graphene device #3. The relative conductance has been normalized by ΔG_1 for easier comparison. The isotherm after the 2.0 V anneal (black curve) shows the remnants of the pre-annealed adsorption behavior around $P_g = 0.1$ Torr. This pre-annealed adsorption behavior is undetectable in the isotherm after the 2.3 V anneal (red curve).

other gases studied. For other noble gases studied the temperature ranges were significantly higher: 50 to 70 K for for argon and 80 to 120 K for krypton. At these temperatures the $G(V_g)$ of the device was almost flat.

The main effect on conductance G due to the adsorption of all noble gases studied was a gate voltage V_g insensitive conductance increase, $G(V_g) \approx$ const. The main difference between the effects of the different noble gases was the magnitude of this conductance enhancement. For neon along with the V_g insensitive conductance enhancement there was also a small shift of the charge neutrality point by $\Delta V_g = 0.23$ V. The shift of the neutrality point did not significantly contribute to the change in conductance of the device. Such a shift of the neutrality point suggests that there is a charge transfer from the adsorbed neon mono-

layer to the trilayer graphene. Taking into account the gate capacitance of the device, the charge transfer is $\Delta n \approx 3 \times 10^9\,\mathrm{cm}^{-2}$. For the other noble gases studied on the suspended trilayer such minimal shifts of the neutrality point are not detectable due to $G(V_g) \approx$ const.

The adsorption of noble gases onto bilayer graphene devices resulted in a very similar V_g insensitive conductance enhancement, discussed in section 4.2.2.4. The behavior is quite different from what is observed on monolayer graphene devices, where there is an almost complete absence of any V_g insensitive conductance increase. On monolayer graphene adsorption of gases into phases not in commensuration with the graphene lattice resulted in changes of conductance mostly due to a shift of the charge neutrality point ΔV_g, see section 4.2.3.1.

It is important to note that during the adsorption of all of the noble gas species studied on the trilayer device the adsorption resulted in a monotonic increase of conductance with coverage, $\Delta G > 0$. This rules out scattering by the adatoms as a mechanism responsible for the change in conductance ΔG.

The explanation for the above described effects along with the long range influence on the conductance upon the condensation of multilayers of noble gas atoms is physically interesting and needs theoretical input. From the experimental point of view, with the two terminal measurements of the trilayer device we cannot differentiate whether the effect on conductance upon adsorption is uniform across the device surface or if there are any differences between the effect of adsorption on the central region of the device compared to the contact dominated regions near the device source and drain. Using the four terminal geometry is experimentally advantageous but technically very difficult to realize on suspended samples [52].

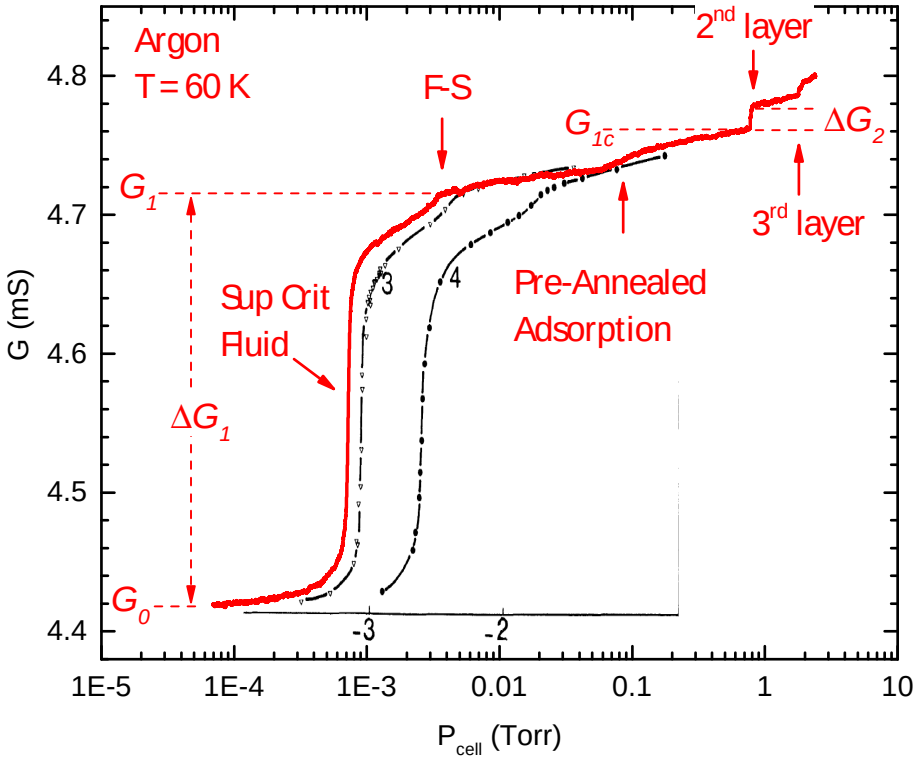

Figure 4.7: Argon conductance isotherm (red) performed on the trilayer device at $T = 60\,\mathrm{K}$. The pressure has been thermomolecularly corrected. The superimposed isotherms labeled 3 and 4 are volumetric isotherms of argon on Grafoil taken at $T = 59.5\,\mathrm{K}$ and $62.4\,\mathrm{K}$ from reference [55]. The y-axis has been stretched to match our conductance isotherm. Brief description of the features: the temperature is above the argon liquid–vapor (L-V) critical point ($T_\mathrm{c} = 55\,\mathrm{K}$). The main riser in the conductance isotherm at $P = 7.5 \times 10^{-4}\,\mathrm{Torr}$ is due to the condensation of argon into a supercritical fluid phase. The inflection point in the isotherm at $P = 3.8 \times 10^{-3}\,\mathrm{Torr}$ is the solidification transition between the dense fluid phase and an incommensurate close packed solid. The sharp step at $P = 0.8\,\mathrm{Torr}$ is the condensation of argon into the second layer. The small broad step in the middle of the solid region around $P = 8.5 \times 10^{-2}\,\mathrm{Torr}$ is the remnant of the pre-annealed adsorption behavior, which we suggest to take place on a separate region of the device. The phase transitions of the conductance isotherm are shifted to slightly lower pressures as a result of a pressure lag in our apparatus, see Section 2.2.2.1.

4.2.1.2 Surface homogeneity measurements

As we perform gas adsorption measurements we do not have a direct experimental probe of the actual condition of the device surface. Thus we do not know what fraction of the suspended device is actually participating in gas adsorption and what fraction of it is still covered by fabrication residue and adventitious carbon. Surface inhomogeneity might play an important role in the effect of the monolayer formation on the conductance of the device. As the monolayer undergoes first order phase transitions below a critical point, it is very sensitive to binding energy inhomogeneities across the surface of the device [24]. Some handle on the surface inhomogeneity of the trilayer device can be obtained from features present in the conductance isotherms as the device undergoes the liquid-vapor transition of Ar.

Below the argon 2D critical point ($T_c \approx 55\,\mathrm{K}$, $P_{\mathrm{cell}} \approx 1 \times 10^{-4}\,\mathrm{Torr}$) the step in the conductance isotherms corresponding to the 2D liquid-vapor (L-V) phase transition does not become vertical as a function of pressure as one would expect for a first order phase transition on an ideal infinite substrate. This broadening of the transition can be a result of binding energy inhomogeneity across the device surface causing the phase transition to occur at slightly different pressures across the device. Conductance measurements through the L-V phase transition in the vicinity of the argon critical point are shown in Fig. 4.9. The conductance G of the device was measured as a function of time as the pressure was pumped out of the system at a constant rate, with pressure $P(t) = P_0 - \dot{P}t$, through a valve opened to have a fixed leak rate. The pump-out rate $\dot{P}$ was determined by tracking the pressure over several minutes of measurement. The Ar pressures at and below the L-V transition ($P_g < 1 \times 10^{-4}\,\mathrm{Torr}$) are near the lower sensitivity limit of our capacitance pressure gauges. The pressure gradient along the gas feed tube from the gas dosing part of the setup to the gas cell at cryogenic temperature arising due to pumpout is unknown. The pump out was performed slowly enough that the argon L-V phase transition took place over several tens of seconds as the gas was slowly evacuated out of the system.

At a temperature of $T = 56\,\mathrm{K}$ (i.e., slightly above T_c) there are several steep step-like

features present in the conductance G as the argon monolayer goes through the supercritical L-V transition. The four steepest features are labeled by arrows in Fig. 4.9a. The same four features persist in the conductance measurements at lower temperatures. As the temperature was reduced below T_c ($T < 54.4\,\mathrm{K}$), these steep features became discontinuous on the bandwidth of our measurements, even at the highest sample rates of 500 samples/s. If the pumpout measurements through the L-V phase transition are repeated the exact distribution of the vertical features is slightly variable, but the same main steps are reproducible, see Fig. 4.8. As is shown in the inset of Figure 4.9d, one of the steps never becomes truly vertical and remains as several separate finite width sub steps down to $T = 51\,\mathrm{K}$. The high bandwidth and continuous nature of our conductance isotherm measurements allow us to detect these changes in conductance separated by minute differences in pressure which would be impossible to detect using low bandwidth techniques such as volumetric isotherms.

If we assume, as discussed above, that the conductance of the trilayer device only depends on the monolayer coverage, this implies that there are separate regions of the device surface on which the argon monolayer undergoes the L-V phase transition at slightly different ambient vapor pressures. The largest of the steps results in a change in conductance of approximately 3 % of the total ΔG_1 of the L-V transition, implying that the regions can be large relative to the total active device area. The binding energy inhomogeneity between the different regions can be obtained from the difference in the vapor pressures at which the phase transitions occur. In equilibrium the chemical potential μ_g of the 3D gas in contact with the adsorbed monolayer has to be equal to the chemical potential of the monolayer: $\mu_g = \mu_m - \epsilon_b$, where ϵ_b is the adsorbate binding energy to the substrate and μ_m is the chemical potential of the 2D monolayer responsible for the phase transition [24]. Regardless of the distributions of binding energies across the device, at the moment when the patches undergo the L-V phase transition, their chemical potential μ_m has to be equal. If the only difference giving rise to a shift in pressure at the phase transition between the patches is the binding energy ϵ_b, then

$\Delta\mu_g = -\Delta\epsilon_b$. For an ideal gas

$$\Delta\mu_g = k_{\mathrm{B}}T\Delta(\ln P) \approx k_{\mathrm{B}}T\Delta P/P = -\Delta\epsilon_b \tag{4.1}$$

The pressure separation $\Delta P/P$ between the four quasi vertical steps in the $T = 55\,\mathrm{K}$ isotherm is between 0.01, 0.02, and 0.04 respectively. This corresponds to a binding energy difference $\Delta\epsilon_b$ between the patches of between 0.6 K and 2.3 K, $\Delta\epsilon_b/\epsilon_b \approx 0.05$ and 0.2 %. The sharpness of each step implies a very high level of binding energy heterogeneity within each patch. It is difficult do come up with a mechanism responsible for such an effect.

The above argument assumes that the monolayer undergoing the phase transition is in equilibrium with the 3D gas. At a pressure of $P \approx 1 \times 10^{-4}\,\mathrm{Torr}$ the monolayer arrival time is on the order of $\tau \approx 10\,\mathrm{ms}$, (from gas kinetics the flux of molecules through an area is $F = P/\sqrt{2\pi m k_{\mathrm{B}}T}$, the monolayer arrival time is $\tau = \rho/F$, were $\rho \approx 6\,\mathrm{nm}^{-2}$ is the density of the monolayer). The observed vertical steps are separated by several seconds during the pumpout measurement. This time separation is several orders of magnitude longer than the monolayer arrival time, implying that the adsorbed monolayer has enough time to equilibrate with the 3D gas.

Surprisingly the observed individual steps in conductance G occur on timescales faster than the monolayer arrival rate. We can put a limit on the width of the vertical steps in conductance G to be $\Delta t < 2\,\mathrm{ms}$ below T_c ($\tau > 10\,\mathrm{ms}$). This implies that for each sudden jump we are observing a kinetic process that occur within a particular region of the argon monolayer, while the monolayer doesn't have time to equilibrate with the 3D gas. Thus, our interpretation is that the jumps in conductance G do not occur as a result of a sudden desorption of liquid Ar puddles into the 3D gas, but instead occur as a result of the liquid Ar puddles suddenly converting into a dilute 2D Ar gas and diffusing away to other parts of the surface of the device. This is a plausible explanation since the kinetics within the monolayer is expected to occur on much faster timescales than the exchange of the atoms from the monolayer to the 3D gas, due to low translational energy barriers on the surface [79, 80]. The gas molecule exchange between the monolayer and the 3D gas should occur on timescales

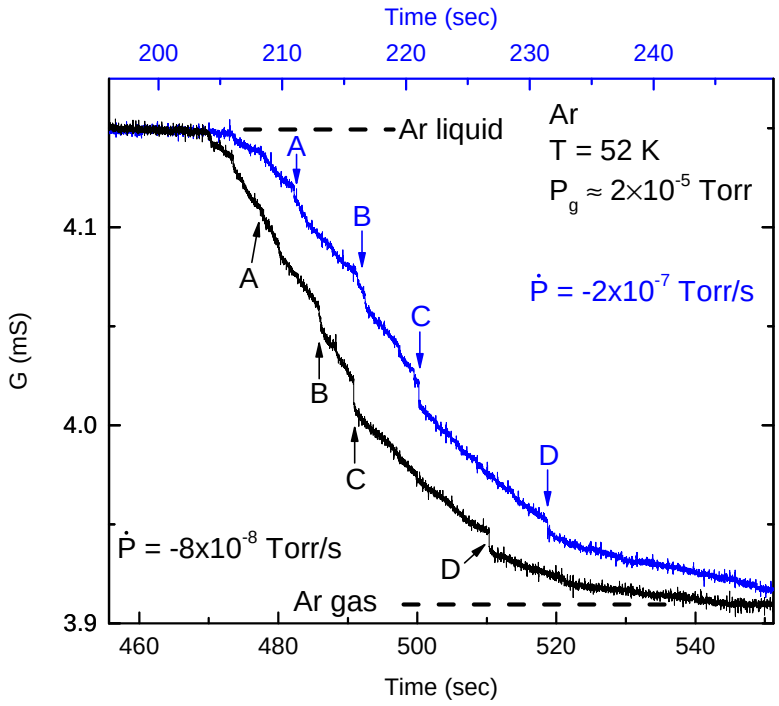

Figure 4.8: Two pumpout runs through the argon L-V phase transition on monolayer device #3. $T = 52\,\mathrm{K}$ (below T_c). The two pumpouts are performed at different rates. Similar steps in the two runs are labled with the same letters.

comparable to the monolayer arrival time τ due to the detailed balance of the adsorption and desorption rates of the monolayer in a steady state at equilibrium with the 3D gas [79].

The puddles of Ar liquid could arise due to pinning on remnant contamination, such as adventitious carbon. The sudden conversion of a 2D liquid Ar puddle to 2D gas could be due to critical nucleation. We expect the actual desorption of the atoms from the surface of the monolayer to occur on longer timescales than the widths of the steps in G.

Such kinetics within a monolayer during a phase transition could not be studied before in bulk systems, although the kinetics of adsorption of a monolayer have been measured on bulk graphite by ellipsometry techniques after the monolayer has been desorbed by a laser pulse [50, 5].

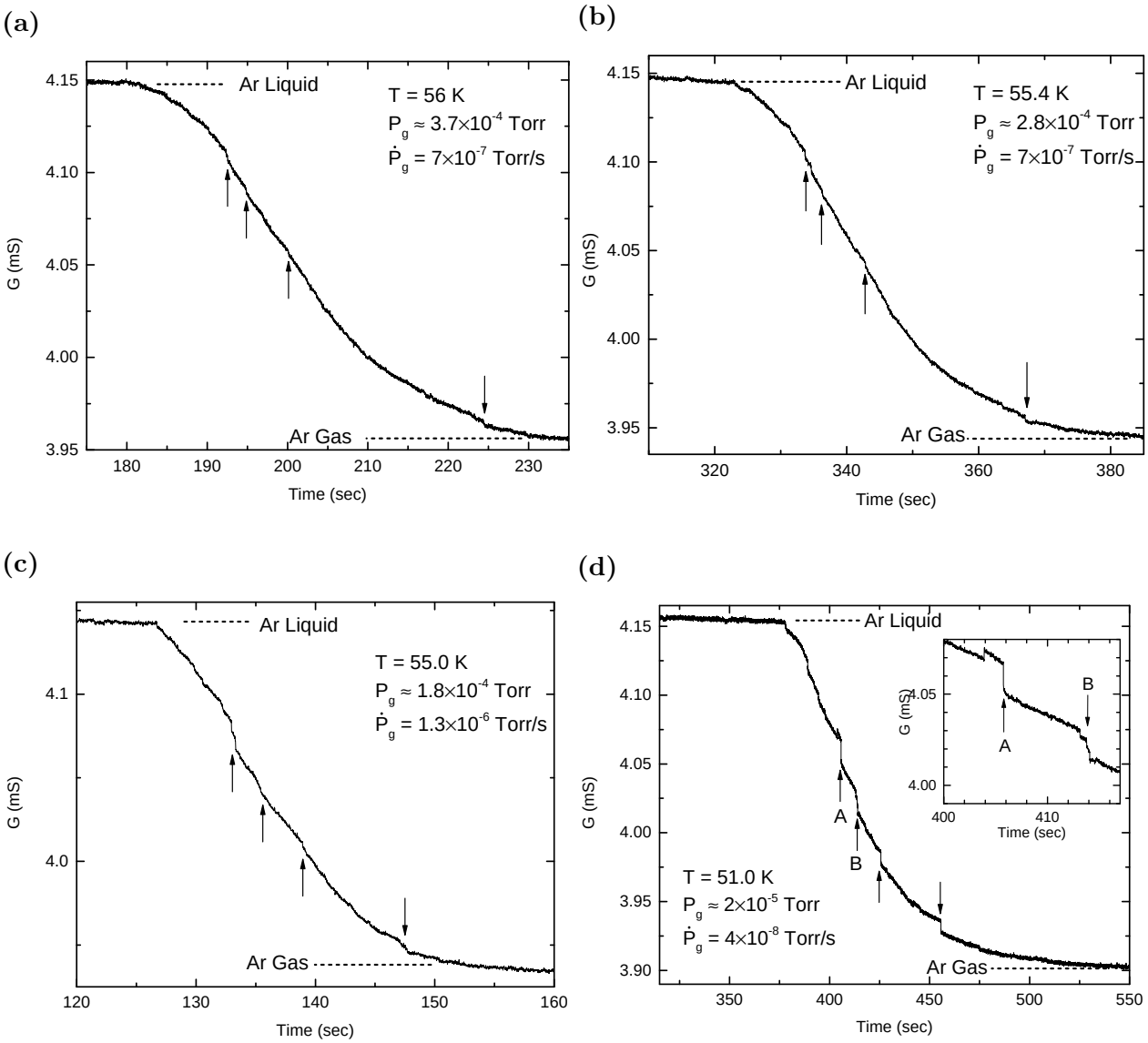

Figure 4.9: The conductance G of the trilayer device #3 as a function of time as argon was slowly pumped out of the gas cell. As the pressure is reduced, the adsorbed monolayer undergoes the argon liquid-vapor (L-V) phase transition. The critical point for the L-V transition is located at $T_c \approx 54.5\,\mathrm{K}$, $P_{cell} \approx 1 \times 10^{-4}\,\mathrm{Torr}$. (a) $T = 56\,\mathrm{K}$, $P_g \approx 3.7 \times 10^{-4}\,\mathrm{Torr}$, pumpout rate $\dot{P}_g = 6.9 \times 10^{-7}\,\mathrm{Torr/s}$. (b) $T = 55.4\,\mathrm{K}$, $P_g \approx 2.8 \times 10^{-4}\,\mathrm{Torr}$, $\dot{P}_g = 7.1 \times 10^{-7}\,\mathrm{Torr/s}$, (c) $T = 55.0\,\mathrm{K}$, $P_g \approx 1.8 \times 10^{-4}\,\mathrm{Torr}$, $\dot{P}_g = 1.3 \times 10^{-6}\,\mathrm{Torr/s}$, (d) $T = 51\,\mathrm{K}$, $P_g \approx 2 \times 10^{-5}\,\mathrm{Torr}$, $\dot{P}_g = 4 \times 10^{-8}\,\mathrm{Torr/s}$. Inset to (d) is a blow up of the sharp features.

4.2.2 Adsorption on Bilayer Graphene

The arguments regarding the similarity of the binding energies of adsorbates between trilayer graphene and graphite described in section 4.2.1 should also apply to bilayer graphene. Likewise, just as in the case of adsorption to trilayer graphene no detectable interaction of the adsorbed monolayers across the bilayer graphene sheet are expected to take place. Thus the structures of monolayers adsorbed on bilayer graphene are expected to be identical to those formed on trilayer graphene and graphite. The positions of the phase boundaries of the adsorbed monolayers should be experimentally indistinguishable between the bilayer and trilayer devices. This is indeed the case, as discussed below.

Adsorption measurements on three separate bilayer devices have been performed (device #13, device #18, device #28). The devices were suspended over trenches with widths of $L = 1.75\,\mu\text{m}$, $1\,\mu\text{m}$, and $2.2\,\mu\text{m}$ respectively. The effect of adsorbed monolayer formation of noble gases on the conductance of all three bilayer graphene devices studied was very similar to the effect on the trilayer device. A comparison of argon isotherms taken at $T = 60\,\text{K}$ on the trilayer and two of the bilayer devices are shown in Fig. 4.10. The relative change in conductance of the isotherms has been normalized by ΔG_1 (defined in section 4.2.1.1). The conductance isotherms on the bilayer and trilayer devices share all of the same features corresponding to phase transitions in the adsorbed monolayer at identical pressures. There are no new features in the conductance isotherms on bilayer graphene compared to trilayer graphene for the noble gases studied on both types of devices (Ar, Kr, and Ne). In fact, the isotherms between the bilayer and trilayer devices are similar enough that one would not be able to distinguish on which type of device the isotherms were measured. A set of adsorption isotherms of various gases measured on the bilayer devices are presented in Appendix B.2.2.

4.2.2.1 Comparison of effects on conductance between Bilayer Devices

Even though adsorption isotherms on all bilayer devices contain identical features related to monolayer phase transitions identified with those occurring on bulk graphite, there are

significant differences in the magnitudes of the features between the three studied bilayer devices. The magnitude of the features on each studied device was also strongly dependent on the current anneal level after which the isotherm was measured. The differences in magnitude of the effect of adsorption on conductance $G(V_g)$ must arise as result of varying distributions of surface contaminants on the devices. No systematic relation between the magnitude of the effect of adsorption on conductance and the length of the suspended region of the devices L has been observed.

The fractional change in conductance, δG_1, upon the formation of a solid argon monolayer on the three bilayer devices was smaller than on the trilayer device for all three devices measured, and was highly variable among the three devices. After the highest levels of current anneal performed on the devices, δG_1 for argon was $\delta G_1 = 9.5\,\%$, $2.5\,\%$, and $1\,\%$, for devices #13, #18, and #28, respectively. The results are summarized in Table 4.1. One might reasonably expect that the cleanest devices would have the highest sensitivities of conductance $G(V_g)$ to adsorption. On the contrary, the bilayer device with the smallest effect of adsorption on conductance (device #28) had the highest field effect mobility $\mu > 5 \times 10^4\,\mathrm{cm}^2/(\mathrm{V\,s})$ at $4\,\mathrm{K}$ out of the three devices studied and had the longest suspended region. On bilayer device #13, δG_1 had a nonmonotonic dependence on the level of current annealing, with the highest magnitude of the effect of adsorption on conductance occurring after the $1.6\,\mathrm{V}$ anneal. Note that the magnitude of δG_1 decreased upon the subsequent $1.7\,\mathrm{V}$ current anneal, see Table 4.1.

Even though the bilayer device #18 had similar two terminal conductance in vacuum G_0 compared to bilayer device #13, it required the application of a significantly higher source drain bias during the current anneal process in order to recover the graphite-like adsorption behavior. This might occur if device #18 had a significantly larger contact resistance contributing to the total two terminal conductance of the device. Four terminal conductance measurements are required for proper clarification of the effect of adsorption on conductance of graphene. However, it was not possible to fabricate suspended devices with a four terminal contact geometry using our fabrication methods.

4.2.2.2 Multilayer adsorption

Adsorbed multilayer formation on the surface of bilayer graphene devices had a significant effect on conductance G just like in the case of adsorption on trilayer graphene. The mechanism through which the formation of multilayers affected the conductance of the devices is unclear. Since each subsequent layer formed on the device is farther away from the graphene surface, one would expect that the magnitude of the effect on conductance upon the formation of each subsequent adsorbed monolayer should be substantially reduced compared to the magnitude of the effect of the formation of the previous layer. This is indeed the case for adsorption on the trilayer device and bilayer device #13. On both of these devices the ratio of effect on conductance of the formation of the second layer of argon compared to the first was $\Delta G_2/\Delta G_1 \approx 5\,\%$. The effect on conductance of the formation of each subsequent layer $\Delta G_{n+1}/\Delta G_n$ was reduced by approximately a factor of three to four, see Table 4.1.

The conductance of bilayer device #18 behaved quantitatively differently in the multilayer adsorption regime compared to the other bilayer and trilayer devices. As can be seen from Fig. 4.10, the magnitude of the effect of multilayer formation on the conductance of device #18 was significantly larger: $\Delta G_2/\Delta G_1$ is approximately a factor of two larger than for the other devices.

The effect of subsequent layer formation on conductance did not decrease in magnitude up to the formation of the fifth layer. The effect on conductance of up to the eight individual layer was resolved before the onset of saturated vapor pressure. This is quite a surprising result and raises the question of whether the steps observed in the conductance isotherms really correspond to multilayer formation. To prove this claim we compared the positions of the steps as a function of pressure with multilayer condensation pressures measured on bulk graphite using the ellipsometric isotherm technique [88]. A conductance isotherms of argon on bilayer device #18 as a function of reduced pressure was plotted along with an ellipsometic isotherms taken on HOPG graphite, Fig. 4.11. The pressures of the steps in our conductance isotherms are in good agreement with the pressures of the multilayer condensation transitions

on bulk graphite. This definitively proves that the changes in conductance originate from the multilayer condensation on top of the suspended graphene. The mechanism of the long range effect on conductance upon multilayer condensation is unclear and, in our opinion, deserves theoretical considerations.

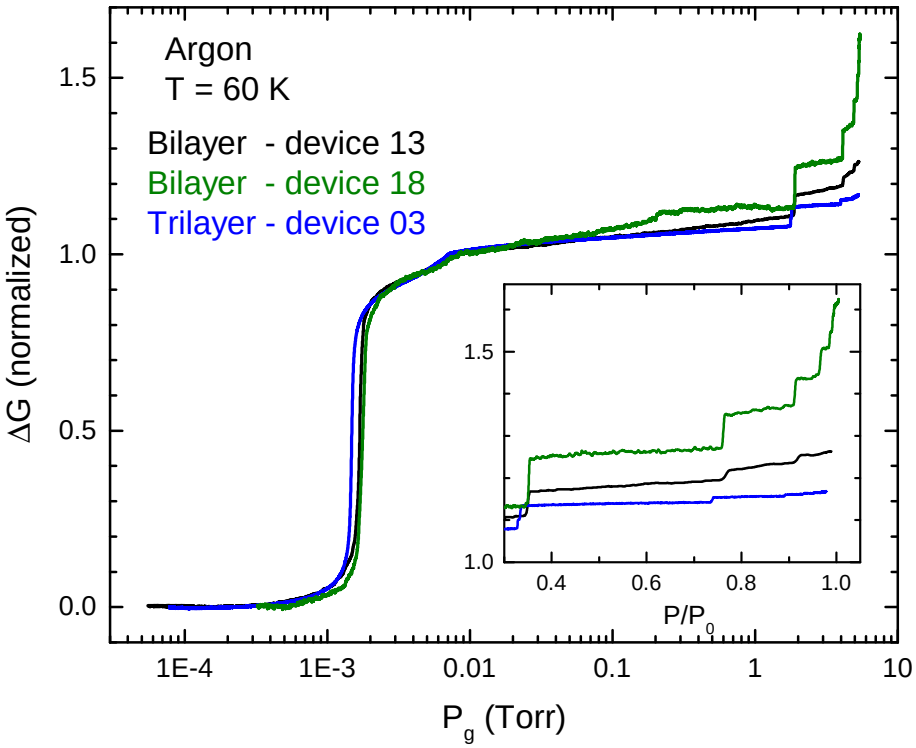

Figure 4.10: Comparison of argon isotherms on two bilayer and a trilayer device at $T = 60\,\mathrm{K}$. The conductance is normalized so that the change in conductance ΔG from vacuum to the top of the melting transition is set to 1.

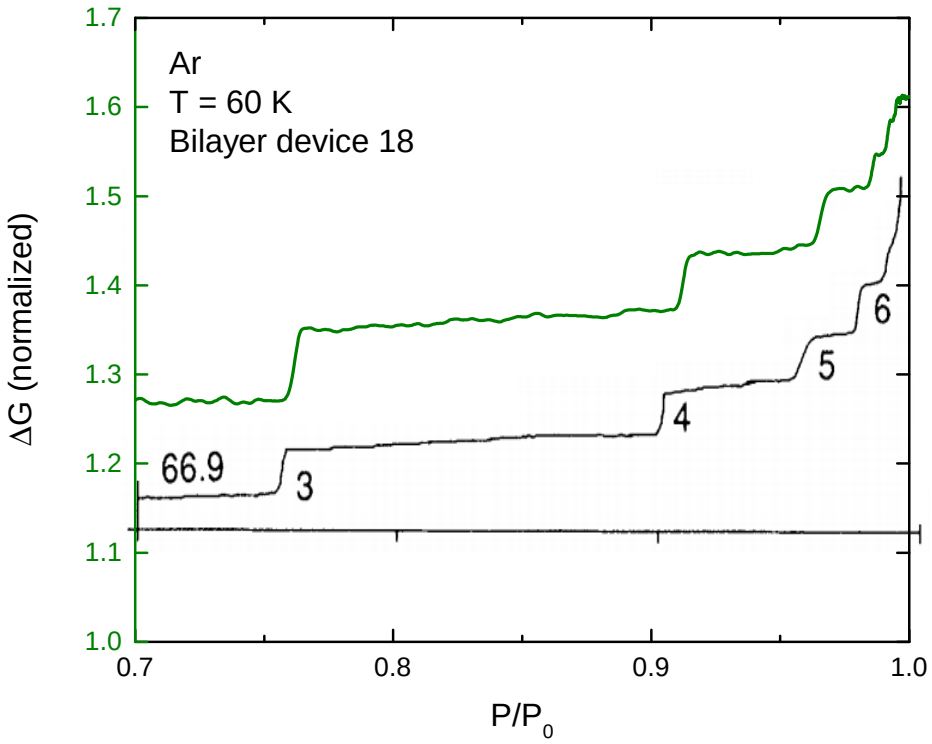

Figure 4.11: The multilayer region of the conductance isotherms on bilayer device #18 (green curve) compared to ellipsometric data on single crystal graphite from [88] (black). The isotherms are plotted as a function of reduced pressure P/P_0, where the saturated vapor pressure P_0 at $T = 60\,\mathrm{K}$ is $P_0 = 5.4\,\mathrm{Torr}$. The steps in the ellipsometic isotherm correspond to N-th layer formation and are numbered.

Anneal Level (V)	G_0 (mS)	δG_1 (%)	δG_2 (%)	δG_3 (%)	δG_4 (%)	$\Delta G_2/\Delta G_1$ (%)	$\Delta G_3/\Delta G_1$ (%)	$\Delta G_4/\Delta G_1$ (%)
Trilayer, Device 03								
2.0	3.6	6.8	0.36	0.11	—	5.4	1.6	—
2.3	4.4	22.3	1.2	0.26	0.08	5.5	1.2	0.34
Bilayer, Device 13								
1.3	4.6	1.0	—	—	—	—	—	—
1.4	3.9	1.2	—	—	—	—	—	—
1.5	3.7	4.3	0.23	0.1	—	5.4	2.4	—
1.6	3.4	15.0	0.66	0.24	0.09	4.4	1.6	0.59
1.7	3.8	9.5	0.55	0.22	0.17	5.8	2.4	1.8
Bilayer, Device 18								
3.75	4.5	0.1	—	—	—	—	—	—
4.0	4.2	0.5	0.04	—	—	8.4	—	—
4.4	4.1	0.9	0.06	0.06	0.06	7.2	7.1	6.6
4.6	4.2	2.5	0.28	0.20	0.16	11.1	7.9	6.3
Bilayer, Device 28								
2.0	2.4	1.1	—	—	—	—	—	—

Table 4.1: The effect of the adsorption of argon on the conductance of trilayer and bilayer devices at various annealing levels.

4.2.2.3 N_2 on Bilayer Graphene

From numerous diffraction studies performed on bulk graphite it is known that adsorbed monolayers of N_2 and Kr form phases with identical structures on the surface of graphite, see, e.g., review [51] and references therein. Due to the interaction with the graphite substrate, the monolayers of both gases undergo a transition from a dense fluid into a commensurate $\sqrt{3}\times\sqrt{3}$ solid phase, see section 1.3.1. In our work, we measured the effect on conductance of the formation of the $\sqrt{3}\times\sqrt{3}$ commensurate solid (CS) phase of both nitrogen N_2 and krypton Kr on bilayer graphene devices. The formation of the CS resulted in different effects on conductance G for nitrogen and krypton: a reduction of the conductance of the devices $\Delta G < 0$ for N_2, and an increase in conductance $\Delta G > 0$ for Kr. The details are presented below.

The adsorption of nitrogen was measured on two separate bilayer devices, device #18 and device #28. The effect of nitrogen adsorption was similar between the two devices. The conductance isotherms on the two devices had identical features resulting from phase transition within the adsorbed monolayer. An isotherm of nitrogen on bilayer device #18 at $T = 60\,\mathrm{K}$ is shown in Fig. 4.12a. It is instructive to compare the conductance isotherms of nitrogen and argon. This is because the two adsorbates have similar binding energies [81], but argon does not form a commensurate solid phase. Both isotherms in Fig. 4.12a were performed close together in time after an agressive $V_{sd} = 4.4\,\mathrm{V}$ anneal, to insure that the device surface would have very similar distributions of contaminants at the time that the two isotherm were measured.

At pressures below the fluid-CS transition, as nitrogen was condensing into the fluid phase the conductance of the device increased monotonically with coverage. The change in conductance due to the formation of the fluid nitrogen phase ΔG was similar in magnitude to the change in conductance upon the formation of the supercritical fluid argon phase. The formation of the $\sqrt{3}\times\sqrt{3}$ CS phase of nitrogen resulted in a decrease in conductance, $\Delta G < 0$. The magnitude of the decrease compared to the conductance increase from the

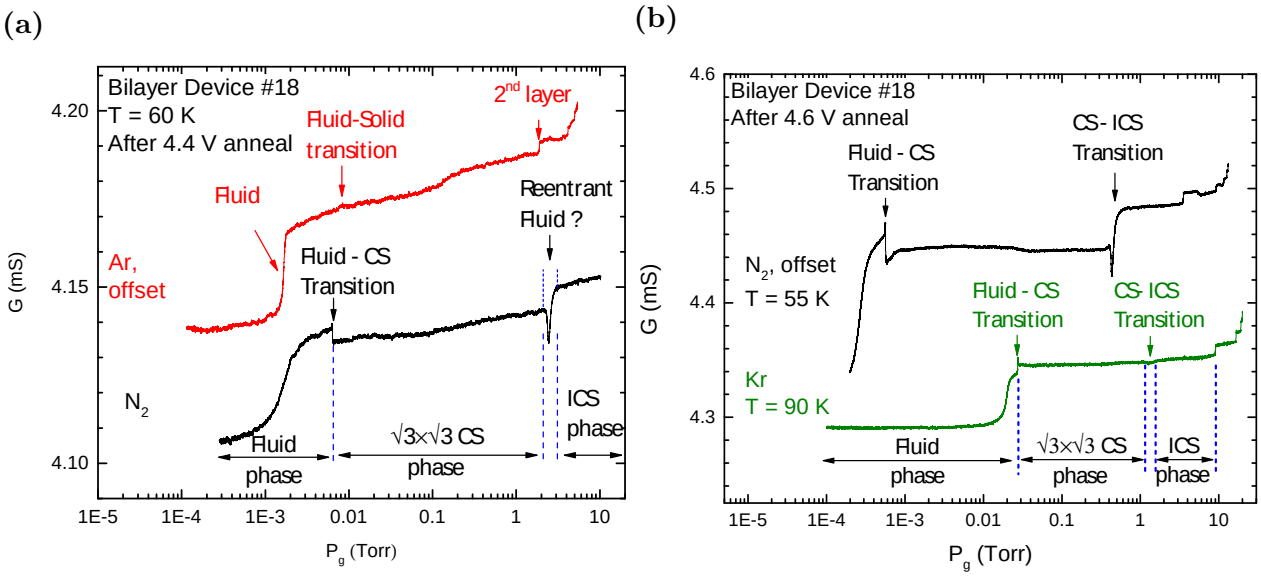

Figure 4.12: (a)Comparison between argon and nitrogen conductance isotherms on bilayer device #18 at $T = 60\,\mathrm{K}$. For the purpose of visual representation the absolute value for conductance of argon was offset. See text for discussion of the features. (b) Comparison between N_2 and Kr isotherms on the same device. The current anneal level is different between isotherms in panel (a) and (b).

fluid formation was rather different between the two studied bilayer devices, see Fig. 4.13a. Bilayer device #28 had a significantly larger relative decrease in conductance compared to device #18.

A sharp, continuous dip in conductance is present in the isotherms of nitrogen on both bilayer devices near the vicinity of the commensurate to incommensurate solid transition (CS-ICS), $P_g \approx 2\,\mathrm{Torr}$ at $T = 60\,\mathrm{K}$, see Figs. 4.12a and 4.13a. In bulk graphite near the CS-ICS transition there is a narrow region of the phase diagram in which the monolayer is in a reentrant domain wall fluid phase [51]. We attribute the dip in conductance to the formation of this domain wall fluid phase. A similar dip of conductance near the CS-ICS transition of nitrogen occurs on all studied hBN backed monolayer graphene devices and

approximately half of the studied freestanding monolayer graphene devices. On freestanding monolayer graphene, an interesting hysteresis in conductance occurs with the onset near the CS-ICS phase transition possibly due to commensurability effects of adsorbed monolayers on opposite sides of the graphene sheet. This is discussed in detail in section 4.2.3.6. No observable hysteresis in conductance of the two studied bilayer graphene devices is present.

A comparison of a nitrogen and krypton isotherm on device #18 is shown in Fig. 4.12b. Both isotherms were performed after a $V_{sd} = 4.6\,\mathrm{V}$ anneal of the device. In contrast with the decrease of the conductance due to the formation of $\sqrt{3}\times\sqrt{3}$ CS phase of nitrogen, the formation of the $\sqrt{3}\times\sqrt{3}$ CS phase of krypton resulted in an increase in conductance, $\Delta G > 0$. On device #18 a very slight, barely observable decrease in conductance is present near the CS-ICS phase transition of krypton. A similar feature is observed on the trilayer graphene device. This feature is absent on the bilayer device #13 where the CS-ICS transition resulted in a change in slope of the conductance isotherm, with no detectable decrease in conductance at the phase transition, see Fig 4.13b. In all three devices there is very little change in conductance at the CS-ICS phase transition of krypton. It is unclear what causes the differences in the effects of conductance between nitrogen and krypton on bilayer devices.

Let us discuss the gate dependence of the effect on conductance due to the adsorption of nitrogen. Three isotherms taken at $T = 60\,\mathrm{K}$ at different gate voltages V_g on bilayer device #28 are presented in Fig. 4.14a. Qualitatively, in all three isotherms the same features corresponding to the phase transitions of the nitrogen monolayer are present at identical pressures regardless of the applied gate voltage V_g. Quantitatively, the relative magnitudes of the changes in conductance ΔG due to the formation of the various monolayer phases of nitrogen vary with V_g. The largest difference between the isotherms is the magnitude of the dip near the CS-ICS transition. The dip is approximately three times smaller in the isotherm taken at $V_g = -3.5\,\mathrm{V}$ than in the isotherm at $V_g = 5\,\mathrm{V}$.

More information about the effects of nitrogen adsorption on the device can be obtained by measuring the conductance as a function of gate voltage $G = G(V_g)$ at different pressures P_g, while the adsorbed nitrogen monolayer is in different phases. Measurements of $G(V_g)$ of

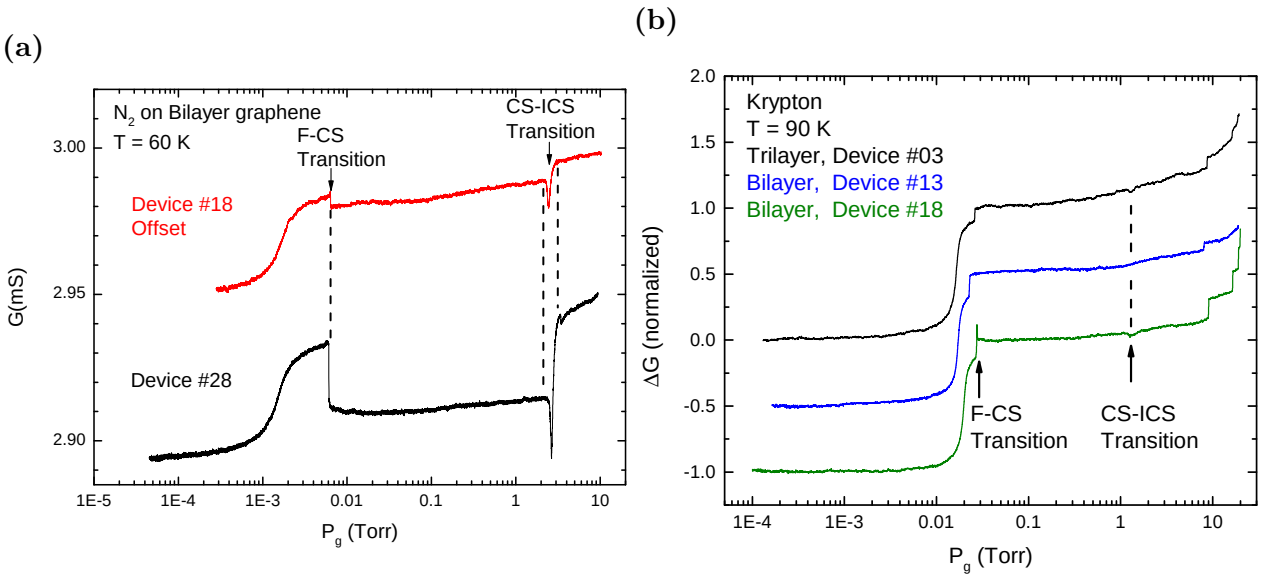

Figure 4.13: Comparison of (a) N_2 and (b) Kr isotherms on bilayer and trilayer devices. N_2 adsorption was not measured on the trilayer device.

device #28 at several different pressures are shown in Fig. 4.14b. The applied gate voltage range was conservatively restricted to $|V_g| \leq 5\,\mathrm{V}$ to prevent electrostatic force damage to the device due to the potential difference between the gate electrode and the suspended bilayer graphene. In vacuum, the charge neutrality point on the device was located at $V_g \approx -4\,\mathrm{V}$.

The changes in conductance due to the formation of the various phases of nitrogen on the device can be decomposed into several different effects. The formation of the fluid phase results in an overall increase in conductance, $\Delta G > 0$, as can be seen by tracking the conductance at the charge neutrality point. Along with the overall increase in conductance, there is a slight reduction in the slope dG/dV_g of the $G(V_g)$ dependence away from the charge neutrality point upon the formation of the fluid nitrogen phase. The reduction of the slope of $G = G(V_g)$ can be attributed to a slight reduction of the field effect mobility. The formation of the $\sqrt{3}\times\sqrt{3}$ CS phase resulted in an overall reduction in conductance compared to the fluid phase, independent of V_g: $\Delta G(V_g) \approx \mathrm{const} < 0$. The conductance in the ICS phase was

similar to the conductance in the fluid phase across the entire gate voltage range V_g. There does not appear to be any significant shift of the charge neutrality point of the device upon the formation of these three phases of nitrogen. The nitrogen monolayer at the bottom of the "dip" near the CS-ICS transition produced a qualitatively different effect on $G(V_g)$ from the other phases. When the conductance is measured with the pressure fixed to the bottom of the "dip" there is a shift of the neutrality point by $\Delta V_g \approx +1\,\mathrm{V}$ compared to other phases of nitrogen.

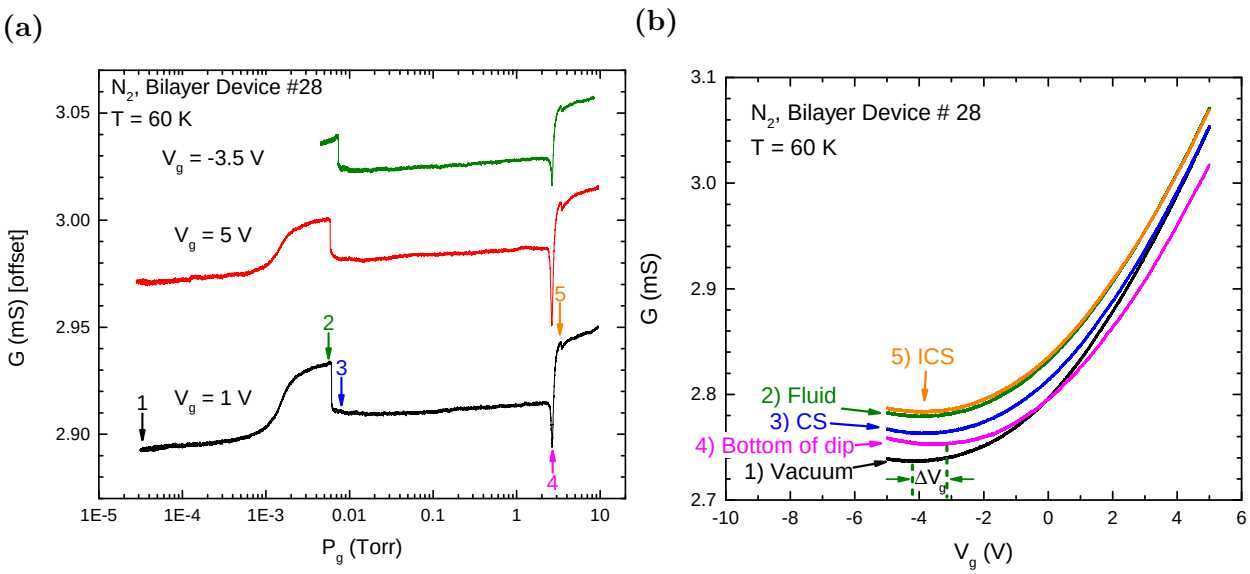

Figure 4.14: Effect of N_2 adsorption on device #28: (a) Adsorption isotherms at three different gate voltages V_g and (b) Conductance as a function of gate voltage $G(V_g)$ of the device in the vacuum while the adsorbed monolayer is in several different phases. The positions along the isotherm where the $G(V_g)$ traces were measured are labeled by arrows in (a)

4.2.2.4 Neon on Bilayer Graphene

The adsorption of neon onto bilayer graphene resulted in a much larger change in conductance compared to all other studied gases. This is similar to the behavior observed on the trilayer graphene device, Fig 4.15. In both the bilayer and trilayer devices the change in conductance due to the adsorption of neon was dominated by an overall V_g insensitive conductance increase, $\Delta G(V_g) \approx \text{const} > 0$. Apart from the much larger magnitude of the increase, the response of $G(V_g)$ is similar for neon and other noble gases studied. The mechanism responsible for this effect is not understood. Similar to trilayer graphene, there is a small shift of neutrality point in the bilayer graphene due to the adsorption of neon. The shift on the bilayer device #13 has the opposite sings to trilayer device, see Fig 4.15.

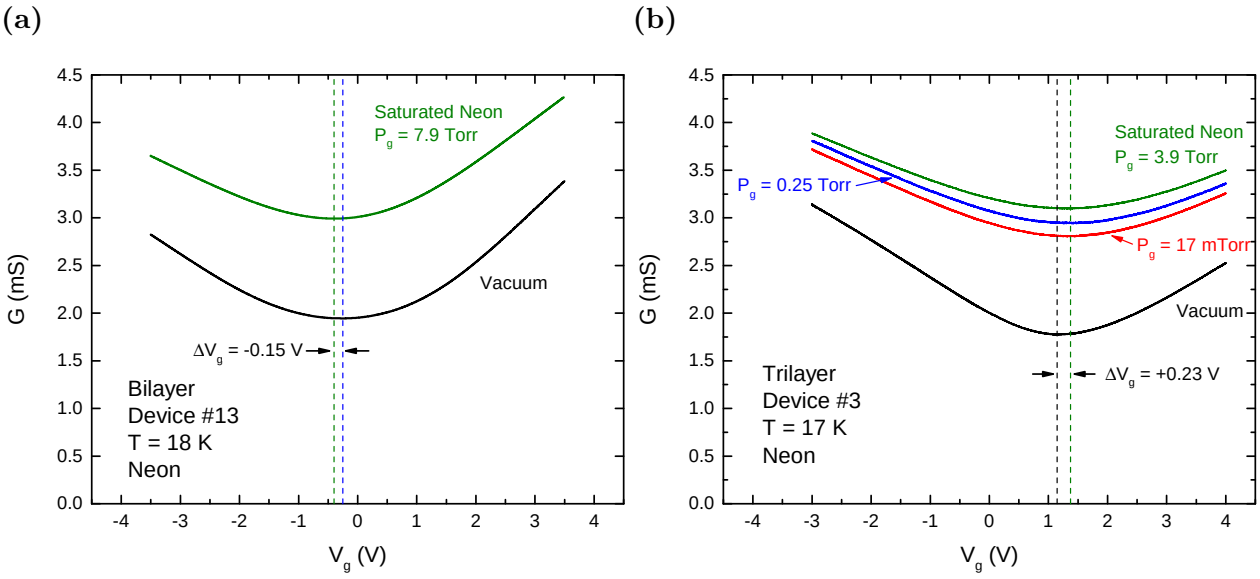

Figure 4.15: Comparison of the effect of neon adsorption on conductance as a function of gate voltage $G(V_g)$ of (a) bilayer and (b) trilayer devices.

4.2.3 Adsorption on Monolayer Graphene

We have performed adsorption measurements on two types of suspended monolayer graphene devices, freestanding monolayer graphene and monolayer graphene backed with several nm thick hBN, see section 2.1.3 for the fabrication procedure. It is known that bulk hBN has binding energies quite similar to bulk graphite [53]. In our hBN backed monolayer graphene devices (for short, monolayer + hBN devices) the lattice vectors of hBN are arbitrarily aligned with respect to those of graphene, as the orientational alignment of the hBN flakes with respect to the graphene lattice is not controlled. Nevertheless, the monolayer hBN devices are expected to have adsorbate binding energies ϵ_b virtually identical to that of bulk graphite: The hBN would produce the same attractive potential as subsequent layers of bulk graphite. The spatial variation of the binding energy across the device surface ("corrugation" of the potential) is also expected to be similar to bulk graphite, as it is mainly determined by the top layer of the carbon atoms [66]. For these devices the formed monolayer phases are therefore expected to be identical to those known to form on bulk graphite and the few layer graphene devices studied by us. We can directly compare the positions of the phase boundaries obtained from the conductance isotherm measurements with those on bilayer and trilayer devices measured in our gas adsorption setup. This removes systematic uncertainties in the pressure measurements between different adsorption apparatuses which arise when comparing our results to those of other groups.

Freestanding monolayer graphene on the other hand is expected to have a binding energy reduced by $\Delta\epsilon_b/\epsilon_b \approx 10\,\%$ [66] compared to bulk graphite. This is due to the fact that in the case of adsorption on bulk graphite the interaction is dominated by the Van der Waals force of the top layer of carbon atoms, with the subsequent layers only weakly contributing to the so called attractive C_3 tail [66] of the interaction. The formation of two adsorbed monolayers on opposite surfaces of the graphene layer are expected to produce an attractive interaction, which leads to approximately a 5 % increase of the total binding energy ϵ_b [9]. This interaction is expected to favor AA stacking of solid monolayers on opposite sides of

the graphene sheet.

From the results of our measurements we found that the positions of the phase boundaries on hBN backed monolayer graphene are indeed very similar to bilayer and trilayer graphene devices, although some new features are present in the conductance isotherms that are not observable on the bilayer and trilayer devices, see appendix B.2.4. We find that the reduction of the binding energy on freestanding monolayer graphene does not significantly affect the phases of the adsorbed monolayers.

Most features present in the conductance isotherms on freestanding monolayer graphene can be directly identified with the phase transitions known to occur on bulk graphite. The main effect of the reduced binding energy ϵ_b is a shift of the pressures of the phase boundaries towards slightly higher pressures. By comparing the adsorption behavior on freestanding monolayer graphene devices versus monolayer graphene capped with hBN, we observed effects of interactions of two adsorbed monolayers on opposite sides of freestanding graphene sheets only for monolayers that form the $\sqrt{3}\times\sqrt{3}$ commensurate phase. Interaction effects on freestanding graphene are not observable when the adsorbed monolayers are in phases not commensurate with the graphene lattice. Even though the phases of adsorbed monolayers formed on monolayer graphene devices were found to be quite similar to monolayer phases formed on bilayer and trilayer devices, the effects on conductance G of the device were quite different, see below.

4.2.3.1 Effects on conductance, non commensurate phases

As discussed in sections 4.2.1.1 and 4.2.2.1, the studied bilayer and trilayer graphene devices had surprisingly large responses of conductance G to the adsorption of all studied noble gases. For the four studied devices the main contribution to the change in two terminal conductance ΔG upon the adsorption of noble gas monolayers was a practically gate voltage V_g independent increase in the total conductance of the device: $\Delta G(V_g) \approx \text{const} > 0$. This effect manifested itself as if only the effective contact resistance of the devices was modified by the formation of the monolayer. The effect was quite large, up to $\delta G \approx 40\,\%$ for neon.

The mechanisms responsible for this effect are currently unclear to us.

In contrast, for monolayer graphene devices the adsorption of gases into monolayers — when the formed phases were not commensurate with respect to the graphene lattice — resulted in relatively small changes in conductance δG. The main effect of the formation of such adsorbed monolayer phases was a shift of the charge neutrality point (CNP). In contrast with bilayer and trilayer devices, the V_g independent conductance increase is almost completely absent on monolayer graphene devices.

The shift of the CNP is variable among the different studied gases and devices, but several common trends were observed. On all monolayer devices, the adsorption of neon resulted in the largest shift of the CNP. All other gases studied, which adsorb at higher temperatures (all phases of Ar, O_2, fluid and incommensurate solid N_2, fluid and incommensurate Kr), produced smaller shifts. The larger shift of the CNP for neon in conjunction with the fact that monolayer graphene devices exhibited larger differential transconductance dG/dV_g at the neon adsorption temperatures ($T \approx 20\,\mathrm{K}$) resulted in neon producing the largest changes in conductance ΔG in adsorption isotherms out of all adsorbed gases that did not form commensurate phases.

4.2.3.2 Neon on Monolayer Graphene

Neon isotherms have been measured on four monolayer graphene devices. An isotherm of neon on freestanding monolayer device #14 compared with one taken on bilayer device #13 at the same temperature of $T = 18\,\mathrm{K}$ are shown in Fig. 4.16. At this temperature on bulk graphite, as the pressure is increased starting from vacuum, neon is known to first condense into a supercritical 2D fluid phase. The monolayer then undergoes a transition into a 2D incommensurate solid. As the pressure is further increased, the 2D incommensurate solid compresses slightly. The incommensurate monolayer is known to be rotated by 17° with respect to the $\sqrt{3}\times\sqrt{3}$ lattice [12]. At higher pressures extra layers of neon condense on the device. For temperatures below the critical point temperature of the second layer $T < T_c \approx 19\,\mathrm{K}$, the second layer condensation occurs through sharp first order phase transition.

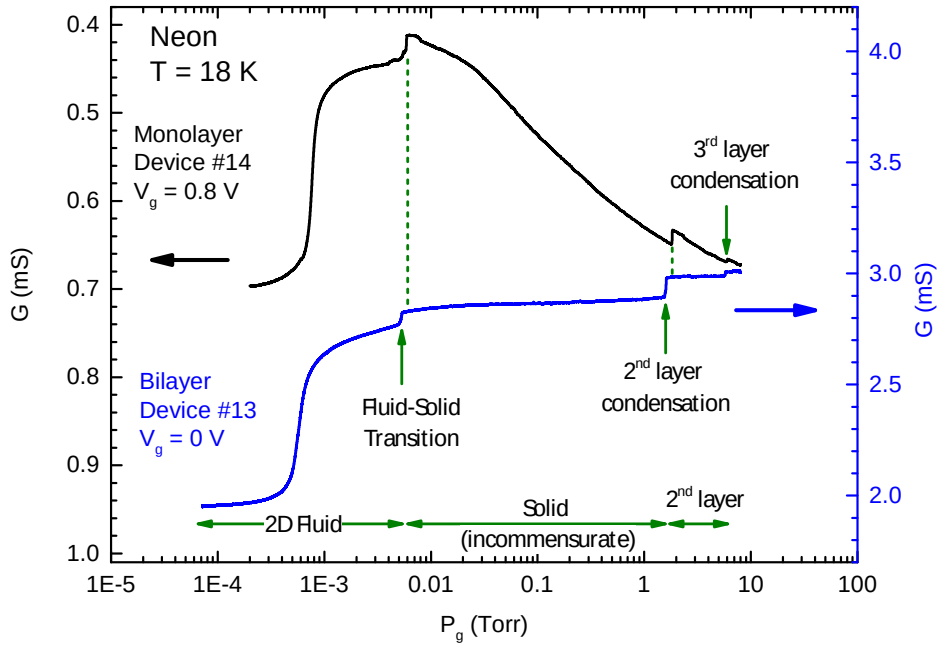

Figure 4.16: Neon adsorption isotherms on monolayer graphene device #14 compared to bilayer graphene device #13. The conductance axis for the monolayer graphene isotherm is increasing down the page. The isotherm is measured on the electron (n-doped) side of the CNP. For the effect of neon adsorption on $G(V_g)$ of monolayer device #14 see Fig. 4.17.

The conductance isotherms on both the monolayer and bilayer devices show similar features that correspond to these transitions. As is expected, the pressures of the phase boundaries on the monolayer graphene device are located at slightly higher pressures than on the bilayer device due to the small reduction of binding energy, ϵ_b. The major difference between the conductance isotherms on monolayer graphene compared to the isotherms on bilayer and trilayer graphene is the gradual change in conductance which starts while the adsorbed neon monolayer is in the incommensurate solid phase. The gradual change in conductance on monolayer graphene devices persists up to the saturated vapor pressure. This feature is present for all studied monolayer graphene devices while it is completely absent in the isotherm for all studied bilayer and trilayer devices. Neon conductance isotherms are very

similar across all measured monolayer graphene devices, see the figures in Appendix B.2.3.

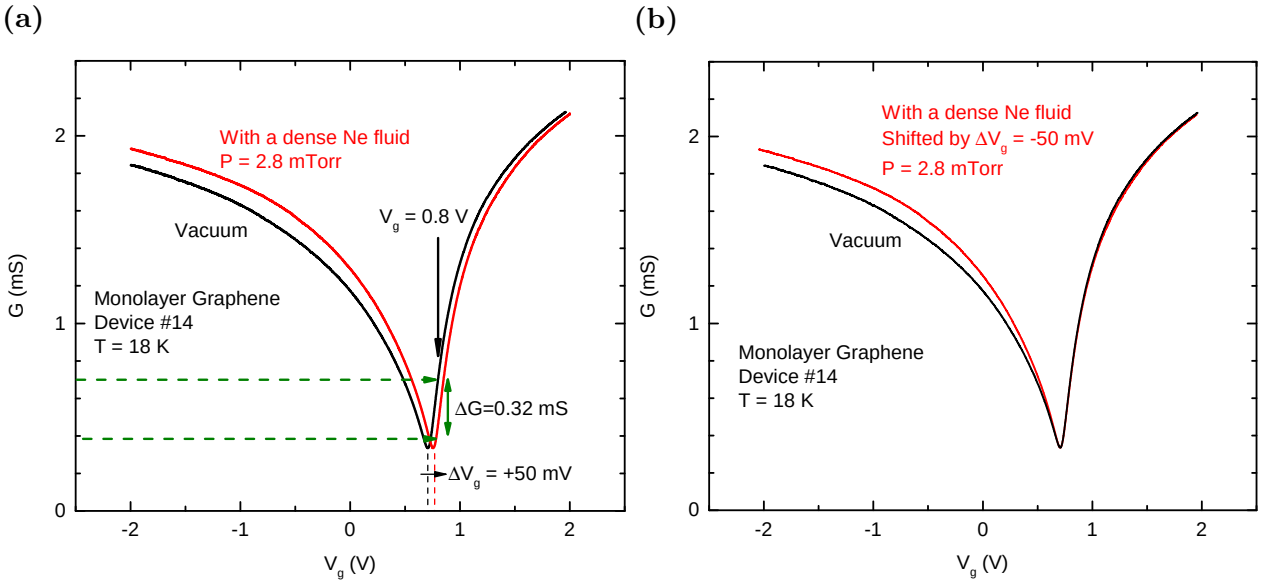

Figure 4.17: The effect of a Neon fluid condensation on the $G(V_g)$ of monolayer device #14. (a) $G(V_g)$ in vacuum and at $P_g = 2.8\,\text{mTorr}$. At $P_g = 2.8\,\text{mTorr}$ the neon monolayer should be in a dense supercritical fluid phase. The result of the fluid formation is a shift of the neutrality point by $\Delta V_g = +50\,\text{mV}$. Conductance measured at $V_g = 0.8\,\text{V}$ decreases by $\Delta G = 0.32\,\text{mS}$. For the isotherm see Fig. 4.16. (b) The same $G(V_g)$ curves as in (a), but with the shift of the neutrality point of the $P_g = 2.8\,\text{mTorr}$ curve subtracted: $G(V_g - \Delta V_g)$. The adsorption of the neon fluid leaves n-doped branch is unaffected, while causing an increase in conductance at the p-doped branch. The minimum of conductance at the charge neutrality point is unaffected.

Even though the conductance isotherms of neon $G(P, V_g{=}\text{const})$ on monolayer graphene appear similar to those on the bilayer and trilayer devices, the effect of adsorption on $G(V_g)$ is quite different. The $G(V_g)$ of monolayer graphene device #14 measured in vacuum and at a pressure of $P_g = 2.8\,\text{mTorr}$, when the device is covered with a dense supercritical neon fluid is shown in Fig. 4.17a. The formation of the neon fluid on the surface of the device

produced a shift of the charge neutrality point by $\Delta V_g = +50\,\mathrm{mV}$. Apart from the shift of the CNP, the condensation of the neon fluid caused an increase in conductance G on the hole (p-doped) side of the CNP, with the effect more pronounced at higher hole doping. The conductance of the device at the CNP and on the electron (n-doped) side remained largely unchanged, see Fig 4.17b. The change of $G(V_g)$ due to adsorption of Ne on bilayer and trilayer graphene devices is quite different as discussed in Sect. 4.2.2.4. For the change of $G(V_g)$ of bilayer and trilayer devices due to neon adsorption, see Fig. 4.15.

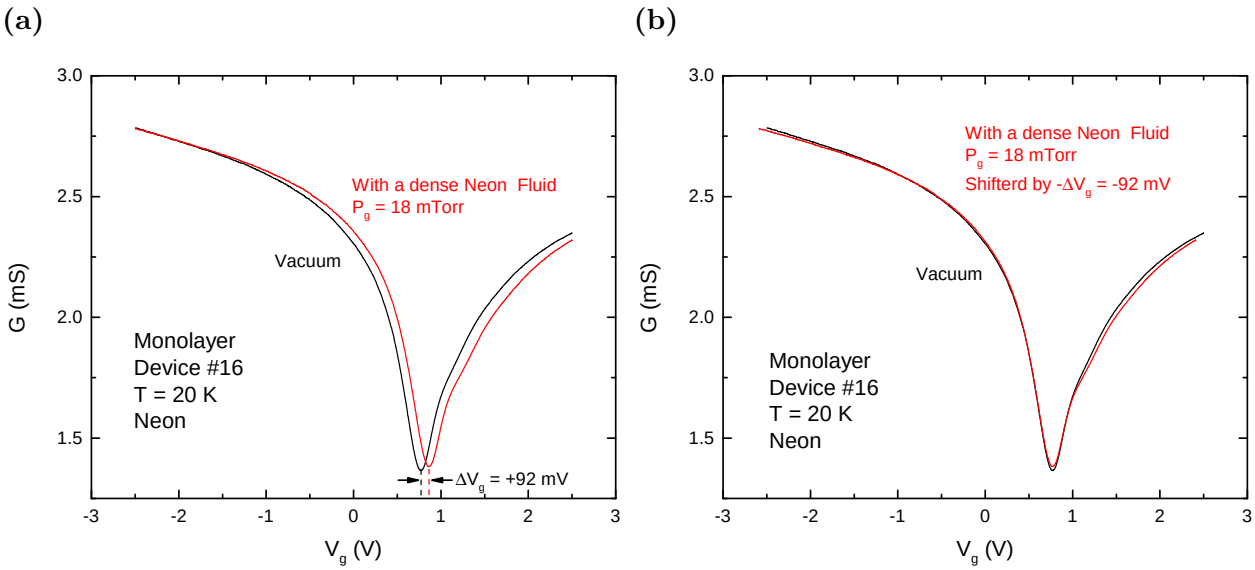

Figure 4.18: (a) $G(V_g)$ of monolayer device #16 in vacuum and at $P_g = 18\,\mathrm{mTorr}$ with a dense fluid neon. The condensation of the neon fluid resulted in a shift of the CNP by $\Delta V_g = +92\,\mathrm{mV}$. (b) The same $G(V_g)$ curves as in (a) with the shift of the CNP removed.

Apart from the shift of the CNP due to the adsorption of neon, the other changes in conductance away from the CNP are not universal across different monolayer graphene devices. The effect of fluid neon condensation on monolayer device #16 produced a shift of the CNP by $\Delta V_g = +92\,\mathrm{mV}$, Fig. 4.18. Almost all other changes in conductance apart from the shift of the CNP in this device are absent, although a slight decrease in conductance away from

the CNP does occur. Monolayer device #16 was fabricated over an identical trench structure as device #14. Clearly the changes of $G(V_g)$ upon neon adsorption must be affected by the device surface homogeneity, as this is the main difference expected to be present between the devices.

Monolayer device #14 was the highest mobility device studied by us. It was suspended over an $L = 1.75\,\mu\text{m}$ trench and had a width $W \approx 8.5\,\mu\text{m}$. After the 1.7 V anneal the device attained a field effect mobility of $\mu_{FE} \approx 5 \times 10^5\,\text{cm}^2\,\text{V}^{-1}\,\text{s}^{-1}$ at $T = 4.2\,\text{K}$. The field effect mobility was extracted using the equation

$$\mu_{FE} = \frac{L}{W}\frac{1}{C_g}\frac{dG}{dV_g} \quad , \tag{4.2}$$

where dG/dV_g is taken at the steepest part of the $G(V_g)$ curve, C_g is the gate capacitance per unit area. This estimate of μ_{FE} ignores contact resistance and is thus a crude estimate. The residual charge inhomogeneity on the device was estimated from the width of the dip of in conductance $G = G(V_g)$ near the CNP to be $\delta n < 1 \times 10^9\,\text{cm}^{-2}$. Device #16 had a field effect mobility $\mu_{FE} \approx 1.4 \times 10^5\,\text{cm}^2\,\text{V}^{-1}\,\text{s}^{-1}$, i.e., four times lower than device #14. It is important to note that both of the devices had a similar remnant doping of $\Delta n \approx 1.3 \times 10^{10}\,\text{cm}^{-2}$ corresponding to $V_{CNP} \approx 0.7\,\text{V}$. This can be attributed to charge transfer from the graphene sheet to the platinum contacts due to a difference in work function [52, 35]. In this spirit, the shift of the CNP due to the adsorption of neon can be attributed to charge transfer from the adsorbed monolayer to the graphene sheet. Understanding the variability in the effect on conductance of the monolayer graphene devices away from the CNP upon neon adsorption requires theoretical considerations. It is important to note that even though the two devices described were fabricated on identical trench structures, they had opposite e-h conductance asymmetries.

The shift of the $G(V_g)$ dependence during neon adsorption on the monolayer graphene devices was nonmonotonic. For all studied monolayer devices the CNP shifted toward positive gate voltage $\Delta V_g > 0$ upon the formation of the neon fluid, see Table 4.2. The gradual change of conductance with increasing pressure that started when the neon monolayer is

	Dimensions (µm)	Trench depth (nm)	ΔV_g shift (mV)	Δn (cm^{-2})
Device #14	8.5×1.75	450	+50	6×10^8
Device #15	13×1.75	450	+190	2.3×10^9
Device #16	15.5×1.75	450	+90	1.1×10^9
Device #27	15×1	475	+60	7×10^8

Table 4.2: Shift of the charge neutrality point CNP by ΔV_g of monolayer graphene devices due to the formation of a dense Ne fluid.

expected to be in the incommensurate solid phase was a result of a shift of the CNP in the opposite direction, towards negative gate voltage $\Delta V_g < 0$. This gradual shift persisted as the neon film experienced multilayer condensation transitions. The multilayer condensation transitions produced a positive shift of the CNP, $\Delta V_g > 0$. The $G = G(V_g)$ curves taken at several pressures along with a neon isotherm on monolayer graphene device #15 are shown in Fig. 4.19. Near saturated vapor pressure the location of V_{CNP} returned to almost the same position as in vacuum. It is unclear if the nonmonotonic shift of V_{CNP} is related to pre-annealed adsorption behavior. The latter is observed in isotherms of the heavier gases on all studied monolayer graphene devices, see next section.

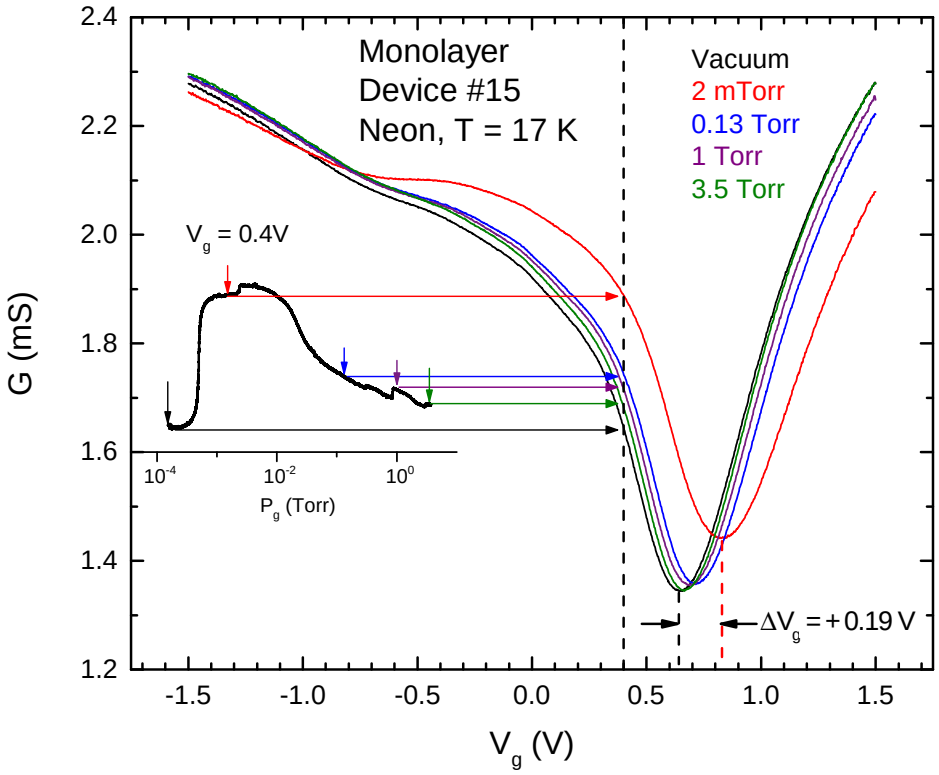

Figure 4.19: Conductance as a function of gate voltage $G(V_g)$ of monolayer graphene device #15 at $T = 17\,\mathrm{K}$ measured at several different neon pressures P_g. The inset shows a conductance isotherm measured at $V_g = 0.4\,\mathrm{V}$; the vertical axis for the inset is the same as for the main plot.

4.2.3.3 Heavier gases, incommensurate phases

We have performed adsorption measurements of heavier gases on monolayer graphene. For all monolayer phases in which the structures do not form a commensurate phase, the main effect on conductance was also a shift of the CNP by ΔV_g, similar to the case of Ne. Because of their higher binding ϵ_b energy than Ne, the temperature at which the adsorption of heavier gases is measured is significantly higher. The adsorption isotherms of Ar, O_2, and N_2 are measured in our gas system at temperatures $T \geq 55\,\mathrm{K}$, for Kr $T \geq 80\,\mathrm{K}$. At these higher temperatures

the suspended monolayer graphene hosts thermal excitations. Due to the interaction with the flexural phonons the mobility μ decreases rapidly with temperature [14]. This leads to a rapid reduction of dG/dV_g with temperature in our devices and causes a reduction of sensitivity to the shift of the CNP in the conductance isotherm measurements.

Due to the lower sensitivity of our measurements, the experimental results for the quantitative shifts of the CNP are not very accurate. Qualitatively, the adsorption of all the heavier gases into non commensurate phases produced a shift of the CNP of the opposite sign compared to Ne, $\Delta G < 0$. The magnitudes of the shifts for O_2, fluid N_2 and fluid Kr were approximately a factor of two to three smaller than for Ne. The effect of the lower sensitivity precluded us from measuring high quality isotherms for Ar and O_2.

Surprisingly, the shifts of the CNP due to the adsorption of Ar were much smaller than for Ne on all studied monolayer graphene devices. On monolayer device #14 (the highest mobility device, $\mu_{FE} \approx 5 \times 10^5\,\mathrm{cm^2\,V^{-1}\,s^{-1}}$ at $T \approx 4\,\mathrm{K}$ after a $V_{sd} = 1.7\,\mathrm{V}$ current anneal) the condensation of a dense argon fluid at the supercritical L-V transition produced a shift of only $\Delta V_g \approx -5\,\mathrm{mV}$. At the argon adsorption temperature $T \approx 60\,\mathrm{K}$, the differential transconductance was $dG/dV_g \approx 2\,\mathrm{mS/V}$, two times smaller than at the adsorption temperature of of neon ($4.5\,\mathrm{mS/V}$ at $T \approx 20\,\mathrm{K}$). This resulted in the argon fluid formation producing a ΔG of twenty times less compared to neon. This small effect on conductance G for monolayer graphene devices contrasts sharply with the large effects on conductance of Ar on the bilayer and trilayer devices. On the bilayer and trilayer graphene device ΔG for Ar was approximately half compared to Ne, see section 4.2.2.

On monolayer graphene devices the pre-annealed adsorption behavior was still present in the isotherms of the heavier gases even after the most aggressive current anneals. For the heavier gases with incommensurate phases the pre-annealed adsorption behavior produced a larger effect on conductance ΔG than the condensation onto the clean region of the device. Isotherms of argon on monolayer device #14 after several levels of current anneal are shown in Fig. 4.20. After the $V_{sd} = 0.75\,\mathrm{V}$ anneal the change in conductance due to the Ar L-V transition was completely absent. The only changes in conductance ΔG of the device

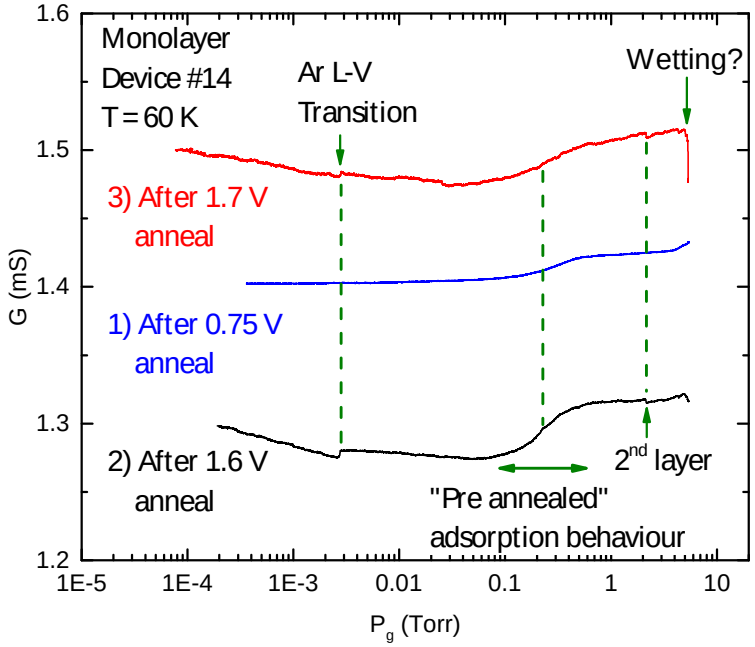

Figure 4.20: Ar isotherms on monolayer device #14 after various levels of current anneal. Only the "pre-annealed" adsorption behavior is present in the isotherm after the $V_{sd} = 0.75\,\mathrm{V}$ anneal. A step corresponding to the argon L-V phase transition appears in the isotherm after the 1.6 V anneal. The "pre-annealed" adsorption behavior persists after the 1.7 V anneal. The sharp decrease in conductance near saturation might be due to multilayer adsorption. After the 1.7 V anneal the device had a high field effect mobility of $\mu_{FE} \approx 5 \times 10^5\,\mathrm{cm^2\,V^{-1}\,s^{-1}}$ at $T = 4.2\,\mathrm{K}$, implying that a large fraction of the device surface should be contamination free. For the $G(V_g)$ of the device after various levels of anneal see Fig. 4.2.

are due to the pre-annealed adsorption behavior, $P_g \approx 0.2\,\mathrm{Torr}$ at $T = 60\,\mathrm{K}$. After the most aggressive current anneal of the $V_{sd} = 1.7\,\mathrm{V}$ the pre-annealed adsorption behavior is still present on the device, in coexistence with the small step due to the Ar L-V transition. After this level of current anneal the device attained $\mu_{FE} \approx 5 \times 10^5\,\mathrm{cm^2\,V^{-1}\,s^{-1}}$ at $T = 4\,\mathrm{K}$ indicating that the device surface is very clean. The pre-annealed adsorption must

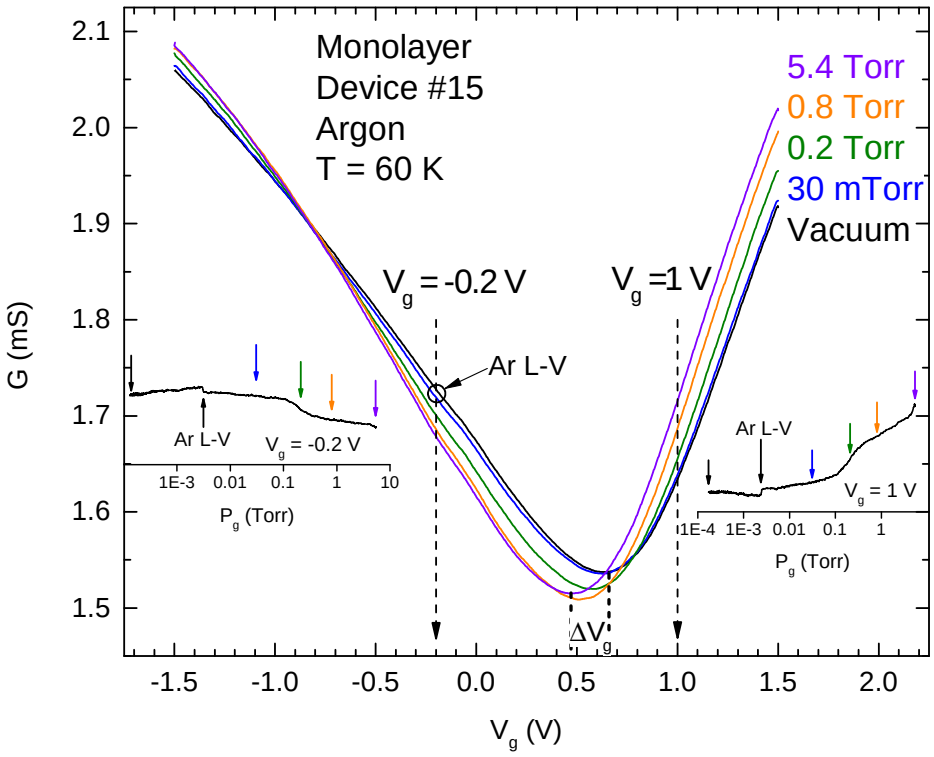

Figure 4.21: The conductance as a function of gate voltage $G(V_g)$ of monolayer device #15 in the presence of various phases of Ar monolayer. The insets show two isotherms taken at $V_g = -0.2\,\mathrm{V}$ on the hole doped side and at $V_g = 1\,\mathrm{V}$ on the electron doped side of the CNP. The insets use the same conductance axes as the main figure.

be occurring near the device contacts due to residual contamination. This pre-annealed adsorption behavior is present in all isotherms of heavier gases on all monolayer graphene devices even after the most aggressive current anneals. The pre-annealed adsorption behavior produces a further shift of the CNP toward negative gate voltage $\Delta V_g < 0$ for all studied heavy gases, both noble and diatomic. This shift is typically either comparable or several times larger than the shift due to the adsorption onto the clean part of the device. The effects on $G(V_g)$ due to adsorption of Ar on monolayer device #15 is shown in Fig. 4.21. The adsorption on the contaminated region of the device produces the dominant effect on

conductance compared to the adsorption on the clean region even after the most aggressive current anneals.

4.2.3.4 Commensurate $\sqrt{3}\times\sqrt{3}$: N_2

The $\sqrt{3}\times\sqrt{3}$ commensurate solid (CS) structure is formed by several adsorbates in a wide range of easily experimentally accessible temperatures and pressures: N_2, CO, Kr, see section 1.3 for the discussion of their phase diagrams on bulk graphite. H_2 also forms the $\sqrt{3}\times\sqrt{3}$ CS phase but at pressures too low to controllably access in our gas system.

In the CS $\sqrt{3}\times\sqrt{3}$ structure the adatoms sit on top of the centers of every third graphene hexagon. As discussed in section 1.2.0.1, the reciprocal lattice vectors of the $\sqrt{3}\times\sqrt{3}$ superlattice on graphene couple the K and K' points. Thus, the formation of such a superlattice produces inter-valley scattering. Zone folding due to the formation of the superlattice maps the K and the K' points onto the Γ point of the new reciprocal lattice. In an ideal, disorder free system it is expected that the formation of a $\sqrt{3}\times\sqrt{3}$ CS super-lattice will open up a gap in the graphene spectrum and give rise to a single particle mass [67, 31]. There are no estimates in the literature for the magnitude of the gap for the gases studied by us. In disordered samples at finite temperature, the effects on conductance of a small gap might be expected to be obscured by disorder.

In our experiment, the formation of the $\sqrt{3}\times\sqrt{3}$ CS structure in the adsorbed monolayer of N_2 leads to a dramatic reduction of the conductance G of our suspended graphene devices. The conductance as a function of gate voltage $G(V_g)$ of monolayer device #16 at $T = 55\,\mathrm{K}$ is shown in Fig. 4.22a. At this temperature the CS phase of N_2 exists over a pressure range of $P_g \approx 1\times10^{-3}\,\mathrm{Torr}$ to $0.5\,\mathrm{Torr}$. The $G(V_g)$ measurements are taken at three different pressures, when the device is in vacuum, in the presence of an adsorbed CS monolayer of N_2, and at higher pressure when the monolayer is in the incommensurate solid state. The formation of the CS phase results in a reduction of conductance by as much as a factor of three compared to the conductance of the device in vacuum. The reduction in conductance only occurs when the adsorbed monolayer of N_2 is in the CS phase. This effect is in sharp

contrast with the effects on conductance of all the other phases of N_2, which mainly produce a shift of the CNP. At higher pressures when the monolayer is in the incommensurate solid phase the conductance G recovers close to the vacuum conductivity level, with the main effect being a shift of the CNP. The shift of the CNP is similar to the effect of other gases on the device that do not form the CS phase, see 4.2.3.3.

A conductance isotherm of N_2 on the same monolayer device #16 at $T = 55\,\mathrm{K}$ is shown in Fig. 4.22b. The isotherm was taken at $V_g = 0\,\mathrm{V}$. During the isotherm the pressure in the cell was slowly increased starting from vacuum. The main feature present in the isotherm is the decrease of conductance due to the formation of the CS N_2 phase. Several other features are also present in the isotherm.

At $T = 55\,\mathrm{K}$, N_2 first condenses into a 2D fluid phase. From the accepted temperature-coverage phase diagram of N_2 [16, 74] it is known that above $T > 45\,\mathrm{K}$ the fluid can reach a relatively high maximum density before the transition into the CS phase. At $T = 55\,\mathrm{K}$ the maximum fluid density at the fluid-CS melting transition is $\approx 80\,\%$ of the CS density ($6.37\,\mathrm{nm}^{-2}$). The fluid-CS melting transition of N_2 is known to be first order on graphite [51] up to temperatures $T_{tr} \approx 85\,\mathrm{K}$. In the isotherm in Fig. 4.22b the decrease in conductance is indeed quasi-vertical on the pressure conductance measurement timescales.

At pressures around $P_g \approx 1 \times 10^{-3}\,\mathrm{Torr}$ there is a slight, gradual decrease in conductance G present in the isotherm. We interpret that this decrease in G is due to the condensation of the N_2 fluid. The decrease in conductance $\Delta G < 0$ is a result of a shift of the CNP by $\Delta V_g < 0$. If the isotherm was measured on the electron (n-doped) side of the CNP instead of the hole (p-doped) side, the conductance would have undergone a slight increase ($\Delta G > 0$).

The conductance of the device while the N_2 monolayer is in the CS phase does not remain constant. There is a further decrease in G around $P_g \approx 0.1\,\mathrm{Torr}$. We interpret this feature to be the remnant of the pre-annealed adsorption behavior arising from adsorption near the device source and drain contacts. This pre-annealed adsorption behavior produces a further shift of the CNP of the device toward negative gate voltage $\Delta V_g < 0$. A similar effect is

present in other gases adsorbed at this temperature such as Ar and O_2, see section 4.2.3.3.

At a pressures around $P_g \approx 0.5\,\text{Torr}$ there is a gradual increase in conductance corresponding to a phase transition from the CS phase to the ICS phase. On bulk graphite a domain wall reentrant fluid phase is present in the vicinity of the CS-ICS transition [51]. On approximately half of the suspended graphene devices there is an extra spike in conductance present near this transition, see section 4.2.3.8. In the ICS phase at $V_g = 0\,\text{V}$ the conductance is slightly lower than in vacuum. This is due to a shift of the CNP toward negative gate voltage which arises from two contributions: the shift due to condensation of nitrogen monolayer onto the clean region of the device and due to the remnant pre-annealed adsorption behavior. Finally at a pressure of $P_g \approx 4\,\text{Torr}$ there is a further reduction in conductance due to the condensation of the second layer of N_2. The reduction of conductance G arises due to a slight further shift of the CNP.

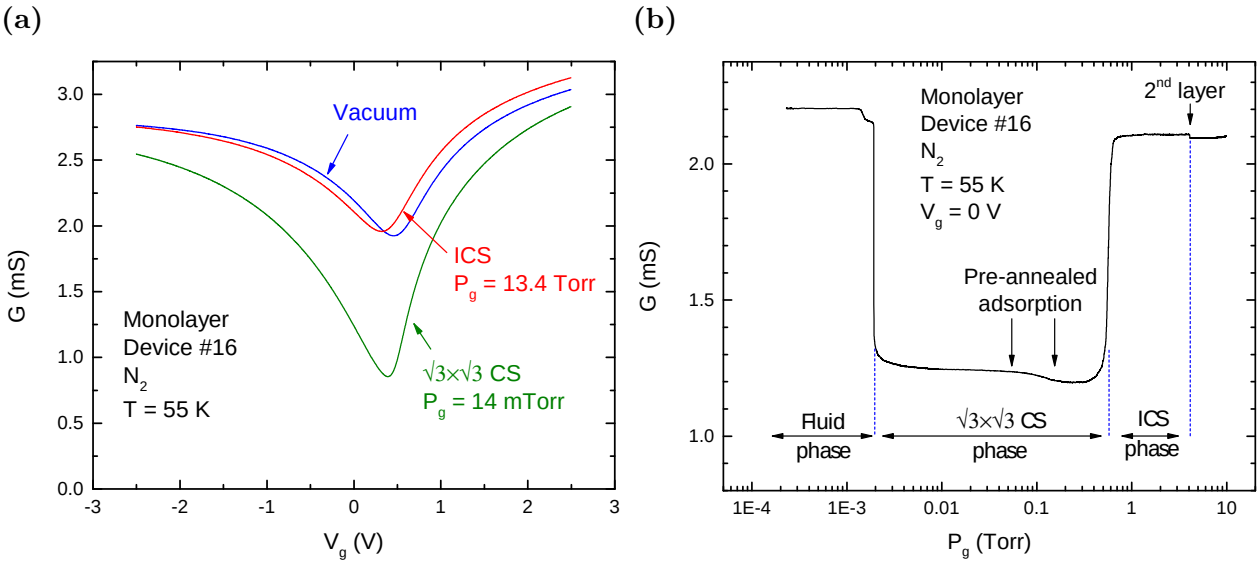

Figure 4.22: N_2 on freestanding monolayer device #16. (a) $G(V_g)$ measurements while the device is bare and with an adsorbed monolayer of N_2 in the CS and ICS phase. (b) N_2 conductance isotherm taken at $V_g = 0\,\text{V}$.

4.2.3.5 Effect of the $\sqrt{3}\times\sqrt{3}$ N_2 phase at low temperature

The reduction of the conductance of graphene due to the $\sqrt{3}\times\sqrt{3}$ CS phase of N_2 occurs at high temperatures, up to the critical point of the CS phase, $T_c \approx 87\,\mathrm{K}$, See Fig. 4.34 for the high temperature isotherms in the vicinity of the critical point. If the mechanism responsible for the reduction of conductance is the opening of a band gap, the large magnitude of the effect at high temperature implies that the created gap has to be fairly large. The mechanism responsible for the reduction of conductance is unclear. To further elucidate the mechanism through which the $\sqrt{3}\times\sqrt{3}$ CS phase reduces the conductance on graphene devices it is important to be able to measure the temperature dependence of the conductance of monolayer graphene devices covered by a CS phase to low temperatures. Since the CS phase forms in equilibrium with the 3D vapor, it was initially unclear if it is in principle possible to cool the graphene devices down to the base temperature of our cryostat while preserving the CS structure of the monolayer. Eventually a reproducible procedure was developed to achieve this goal.

In literature bulk graphite samples cooled to low temperatures in the presence of adsorbed monolayers of a particular gas are referred to as "plated graphite" [10]. When the samples are cooled to low enough temperatures the 3D vapor pressure decreases to negligible values. The adsorbed monolayers eventually come out of equilibrium with the vapor. Nevertheless if there are no external perturbations of the graphite sample the monolayer can remain in a phase with constant coverage. It is fairly easy to control the coverage of the monolayer on exfoliated graphite samples during the cooldown process due to their large surface areas. In a cryostat cell with a high surface area bulk graphite sample the system comprised of the adsorbed monolayer in equilibrium with the 3D gas can be prepared in such a way that it is dominated by the adsorbed monolayer on the surface of the bulk graphite. The 3D gas will contain only a relatively small fraction of the gas molecules in the total system. If during the sample cooling process the molecules from the gas phase adsorb onto the graphite the coverage of the monolayer does not get significantly perturbed.

In the case of our suspended graphene devices, the system is dominated by the molecules present in the 3D vapor. To cool the device to low temperatures while preserving the CS monolayer structure we can start at some arbitrarily chosen high temperature and pressure at which the monolayer of N_2 is in the CS phase and slowly cool the cryostat to base temperature. As the cryostat cell cools, the 3D pressure inside the cell is going to be determined by the equation of state of the gas, the relative volumes of the cold part of the cell inside the cryostat compared to the volume of the external gas handling system which is at room temperature, and by temperature gradients within the cell. While the 3D ambient pressure inside the cell is high enough for the monolayer to be in equilibrium with the gas, the monolayer coverage is going to be determined by the relative 3D vapor pressure in the vicinity of the sample.

Upon cooldown several outcomes can happen. Either the device cools while preserving the CS phase, with the monolayer eventually coming out of equilibrium with the 3D vapor. Or, if the relative 3D vapor pressure in the vicinity of the device increases past the CS-ICS phase boundary the monolayer will end up with a higher coverage in the ICS phase. If upon cooldown the 3D vapor pressure decreases and crosses the CS-F phase boundary the CS phase will desorb from the device. This latter case typically occurs if there is a large temperature gradient in the cell.

We can track the state of the adsorbed monolayer by measuring the conductance G of the device at fixed V_g while we perform the cooldown. Any sudden increase in G would indicate that the adsorbed monolayer underwent a phase transition from the CS phase into either the F or the ICS phase. Since the CS-F phase transition is first order while the CS-ICS transition is continuous we can use the sharpness of the change in G to tell which one of the two transition occurred.

After some trial and error we determined that the monolayer of N_2 can be preserved down to the base temperature of our cryostat $T = 4.2\,\mathrm{K}$ in the CS phase if we start the cooldown process at $T = 55\,\mathrm{K}$ and $P_g \approx 1 \times 10^{-3}\,\mathrm{Torr}$. The monolayer starts in the CS phase, close to the F-CS phase boundary. To preserve the CS phase on the device the cooldown rate has

to be slow, $\dot{T} \approx 0.2\,\mathrm{K/min}$, as faster cooldown rates lead to the desorption of the CS phase. As the cell reaches a temperature of $T < 25\,\mathrm{K}$ we can start pumping on the gas system as the pressure of N_2 is negligible at this temperature. At this point we can also increase the temperature ramp rate of the cryostat to maximum as the monolayer is out of equilibrium with the 3D gas, so temperature gradients in the cell should not affect the CS monolayer.

The monolayer of N_2 is known to undergo a phase transition at $T \approx 28\,\mathrm{K}$ from an orientationally disordered $\sqrt{3}\times\sqrt{3}$ CS phase at $T > 28\,\mathrm{K}$ temperatures to an orientationally ordered $\sqrt{3}\times\sqrt{3}$ CS phase at $T < 28\,\mathrm{K}$. In the orientationally ordered CS phase the backbones of the N_2 molecules form a herringbone structure with a doubled unit cell in one direction [51]. We do not see any discontinuous features in conductance G in our devices as we cool the monolayer through this temperature range.

At some temperature below $T < 30\,\mathrm{K}$ as the 3D N_2 pressure becomes negligible, the adsorbed CS monolayer should come out of equilibrium with the 3D vapor due to ever longer monolayer arrival times ($\tau > 1\,\mathrm{min}$ at $P < 1 \times 10^{-8}\,\mathrm{Torr}$). If any atoms desorb from the CS monolayer on the surface of the device, they would never get replaced by the incoming atoms from the 3D gas on the timescales of our measurement. This implies that over time if significant desorption is occurring the monolayer will start to accumulate defects.

We check the stability of the adsorbed CS monolayer to structural changes by monitoring the conductance of the device over multi hour time spans while holding it at low temperature. As can be seen in Fig. 4.23 there are some slight changes in conductance $G(V_g)$ over a $10\,\mathrm{h}$ time span at $T = 20\,\mathrm{K}$. Some slow changes must be occurring in the CS N_2 at this temperature over this timescale. At $T = 20\,\mathrm{K}$ we expect the main residual gas present in the cell to be H_2 due to the low compression of light gases by the turbo pump. H_2 does not adsorb onto graphite at the low residual gas pressures at this temperature, thus our interpretation is that the change in conductance is most likely due to a gradual desorption process occurring from the N_2 monolayer or possibly some rearrangement of domains within the monolayer.

Since at low temperature the monolayer is out of equilibrium with the gas another way

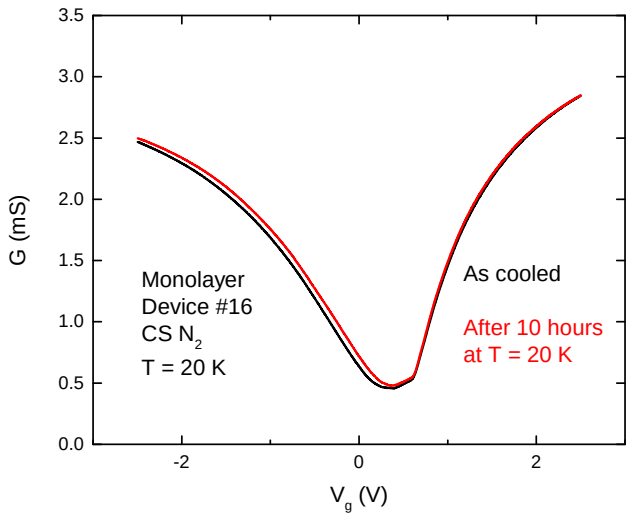

Figure 4.23: The stability of the N_2 monolayer at $T = 20\,\mathrm{K}$ over a 10 h timespan.

to verify that it is in a CS phase is to test the reproducibility of the conductance of the device over multiple cooldown attempts starting form high temperatures. If the cooldown is performed properly according to the procedure described above the $G(V_g)$ of the device at a given T down to $T = 4.2\,\mathrm{K}$ is indeed reproducible between different cooldown runs.

The temperature dependence of the conductance as a function of gate voltage $G(V_g)$ of monolayer device #16 with a CS N_2 phase adsorbed is shown in Fig. 4.24. A flat plateau appears in the $G(V_g)$ of the device around the location of the CNP. This plateau first becomes apparent at $T = 30\,\mathrm{K}$ and gradually widens at lower temperature. There is minimal temperature dependence of $G(V_g)$ of the device below $T < 20\,\mathrm{K}$. The minimum conductance at $T = 4.2\,\mathrm{K}$ is reduced from 1.6 mS for bare graphene to 0.4 mS for CS N_2 coated graphene. The effect on conductance of the device of the adsorbed CS N_2 monolayer does not seem to be consistent with a simple interpretation of a band-gap opening as the only mechanism responsible for the reduction of conductance (section 4.2.3.4). A more complicated effect must be at work here.

It is important to note that we do not know what the actual structure of the $\sqrt{3}\times\sqrt{3}$ CS

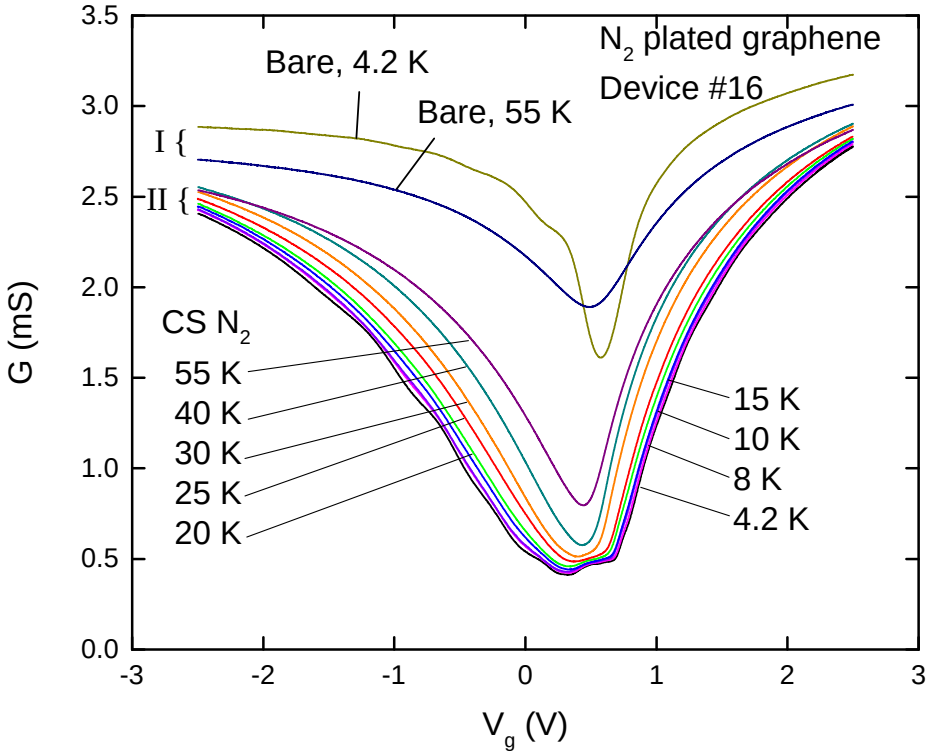

Figure 4.24: Conductance as a function of gate voltage $G(V_g)$ of monolayer device #16 in the presence of an adsorbed CS N_2 monolayer. The set of curves labeled I show the $G(V_g)$ of the bare device. The set of curves labeled II show the $G(V_g)$ of the device in the presence of the adsorbed CS N_2 monolayer. The device was adsorbed with a CS N_2 at $T = 55\,\mathrm{K}$ and cooled down to $T = 4.2\,\mathrm{K}$. The $G(V_g)$ of the bare device at $T = 4.2\,\mathrm{K}$ was obtained by desorbing the N_2 monolayer through ohmic heating.

N_2 monolayer is at this temperature. In equilibrium, a network of domain walls is expected to be permeating the monolayer, separating regions of the device surface which contain different equivalent domains of the CS phase [51]. It is unclear what effect on conductance such a network of domain walls will have. The network of domain walls is expected to be highly sensitive to residual contaminants present on the surface of the device [59], and may be pinned down.

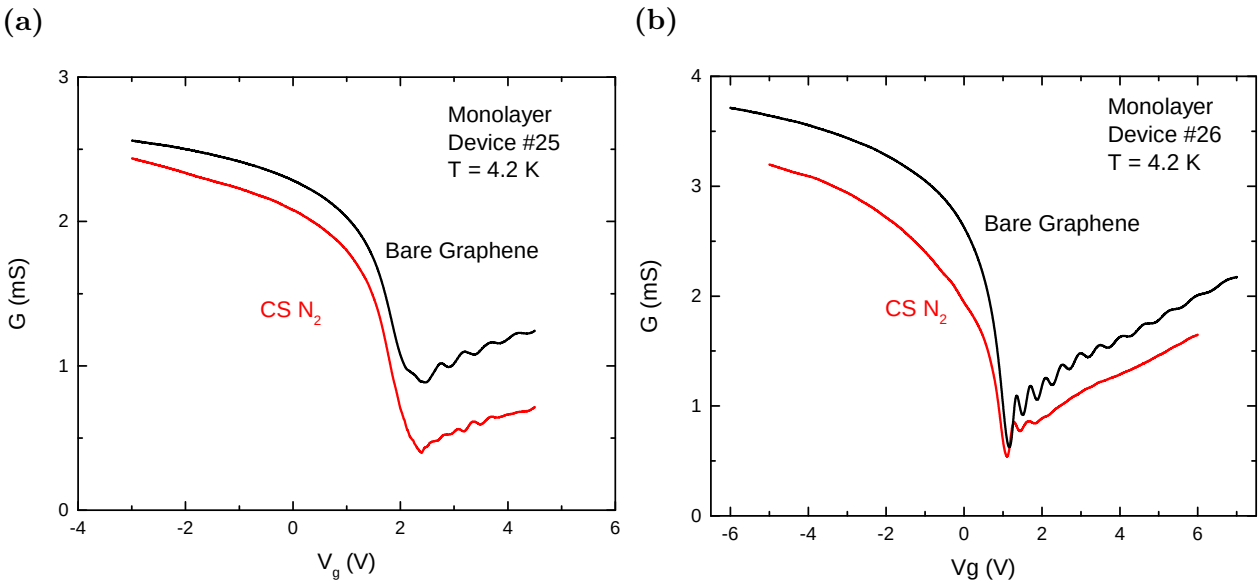

Figure 4.25: Conductance as a function of gate voltage $G(V_g)$ of (a) monolayer graphene device #25 and (b) monolayer device #26 at $T = 4.2\,\mathrm{K}$. Both devices are suspended over a 1 µm trench. Red curves are in the presence of a CS N_2 monolayer. Black curves are the $G(V_g)$ of the bare devices with no adsorbates present. The CS N_2 monolayer was desorbed through mild ohmic heating.

The conductance as a function of gate voltage $G(V_g)$ of two other monolayer devices plated with a CS N_2 monolayer are shown in Fig. 4.25. Both devices are suspended over a 1 µm trench and show Fabry-Pérot (FP) oscillations in $G(V_g)$ on the electron (n-doped) side of the CNP at low T. The effect on $G(V_g)$ of the CS N_2 monolayer is quite different from that on device #16. The V_g insensitive plateau is absent on these devices. On monolayer device #26 the reduction of conductance at the charge neutrality point $G_{\mathrm{min}} = G(V_{\mathrm{CNP}})$ is quite small, from 0.63 mS in vacuum to 0.54 mS in the presence of the CS N_2 phase.

On these two devices the CS N_2 monolayer strongly affects the FP oscillations. The presence of a CS N_2 monolayer strongly suppresses the FP oscillations at higher doping away from the CNP. On monolayer device #25 (Fig. 4.25a) the periodicity of the FP oscillations is

modified by as much as 40 %. In graphene the spacing of the FP oscillations depend on the sample dimensions and the renormalized Fermi velocity v_F [62, 37]. It is important to note that the spacing of the FP oscillations on our suspended graphene devices does not show the expected periodicity in gate voltage V_g as expected for modes in a simple rectangular cavity.

4.2.3.6 Hysteresis in N_2 isotherms

During typical conductance isotherms the adsorbed monolayers on the surface of our graphene devices are in equilibrium with the ambient 3D gas present in the cell of our cryostat. At a fixed pressure P_g the monolayer is continuously exchanging molecules with the 3D gas on timescales set by the monolayer arrival time, which at higher pressure, $P_g > 1 \times 10^{-3}$ Torr is fast ($\tau < 1$ ms) compared to our conductance measurement times. Thus it is expected that the structure of the monolayer only depends on T and P_g. When we measure a conductance isotherm, the conductance of the device $G(P_g, T = \text{const})$ is expected be identical regardless if we start from vacuum and slowly add gas into the system or if we start near saturation and perform a pumpout. For gases that do not form the CS phase this indeed appears to be the case: the conductance isotherms are completely reproducible upon gas adsorption and desorption. Since it is significantly easier to control the pressure in our system during a continuous pumpout (see section 2.2.2.1) most of the continuous conductance isotherms presented in this thesis are "pumpout" isotherms.

The isotherms of N_2 and CO on monolayer graphene devices on the other hand show dramatic hysteresis behavior in $G(P_g)$ when the adsorbed monolayer is in the CS phase. The hysteresis behavior has an onset as the adsorbed monolayer undergoes the CS-ICS transition, and occurs only on monolayer graphene devices where adsorption occurs on both sides of the graphene sheet. Fig. 4.26a shows two isotherms of N_2 on monolayer graphene device #16 at $T = 55$ K. The isotherm in black color was performed starting from vacuum and ending at a high pressure, $P_g \approx 14$ Torr. At this point two layers of N_2 were adsorbed on each side of the device, with the first layer being in the ICS phase. The features present in this isotherm are described in detail in section 4.2.3.4. As the adsorption isotherm is performed the N_2

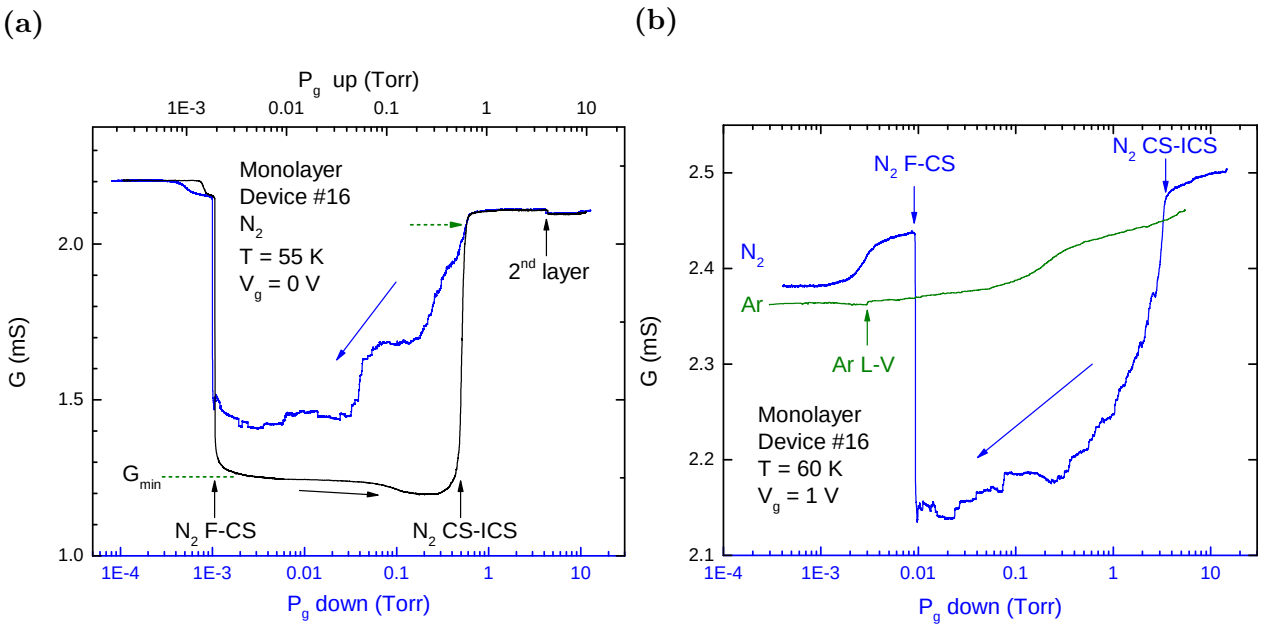

Figure 4.26: (a) Hysteresis in N_2 isotherms on monolayer device #16 at $T = 55\,\mathrm{K}$. The black isotherm is measured with increasing pressure. The blue isotherm is a "pumpout" isotherm measured with decreasing pressure. The pressure axes have been shifted to remove an offset between the two isotherms due to pressure lag in our gas system, see section 2.2.2.1. (b) A pumpout isotherm of N_2 at $T = 60\,\mathrm{K}$ at a different gate voltage $V_g = 1\,\mathrm{V}$. For the $G(V_g)$ of the device see Fig. 4.22a. A pumpout isotherm of Ar is included to show the effect on conductance of an adsorbed monolayer in the absence of the CS phase.

monolayer first undergoes the F-CS transition, then the CS-ICS transition and finally the 2nd layer condensation transition. The other isotherm in blue is a "pumpout" (desorption) isotherm, started from the high pressure ($P_g \approx 14\,\mathrm{Torr}$) and ran until vacuum. During the desorption isotherms the monolayer first undergoes a transition from the ICS phase into the CS phase and then into the F phase. The conductance G of the device while the monolayer is in the CS phase is rather different in the two isotherms, and shows the hysteretic behavior. The difference in $G(P_g)$ between the adsorption and desorption isotherms below the F-CS

transition ($P_g < 1 \times 10^{-3}$ Torr) is an artifact of the pressure lag in our gas system.

As the pressure is lowered through the CS-ICS transition, the conductance $G(P_g)$ of the device first follows the same conductance level as during pressure increase (adsorption), but quickly begins to deviate from the conductance values of the adsorption isotherm. The point of deviation is labeled by a dotted arrow in Fig. 4.26a. This point of deviation is reproducible upon repeated isotherm measurements. At pressures P_g below this point the conductance $G(P_g)$ is higher than in the adsorption isotherm at the same pressure and slowly tends towards the original conductance in the CS phase through a series of quasi-vertical steps. These steps in conductance $G(P_g)$ are non monotonic. Furthermore, the distribution of the steps is variable upon repeated runs of the isotherm, see appendix B.2.3, Figs. B.10b, B.9c, and B.14a. In most desorption isotherms the conductance G never reaches the original minimum value in the CS phase (labeled $G_{\min}$ in Fig. 4.26a) before the CS-F transition. To recover the original conductance $G_{\min}$ of the CS phase attained in the adsorption isotherm, the N_2 monolayer has to be cycled through the F-CS transition, into fluid phase and back into the CS phase.

To investigate whether the hysteretic behavior in the CS phase is due to some long lived metastable state of the N_2 monolayer we measured the conductance of the device at a fixed pressure P_g after the adsorbed monolayer has been cycled through the CS-ICS transition. No gradual relaxation of the conductance of the device $G(P_g = \text{conts})$ towards the original CS phase conductance $G_{\min}$ (reached upon adsorption into CS phase) was observed, Fig. 4.27a. Instead the conductance of the device stayed relatively constant over multi hour timespans. Some nonmonotonic steps in G ware observed over this time period. This behavior implies that monolayer is in a very stable state with any relaxation processes occurring on very long timescales.

To investigate the onset of the hysteresis we measured how close we have to approach the ICS phase at the CS-ICS transition to first see the hysteretic behavior. Since the CS-ICS transition is fairly broad (P_g =0.49 to 0.65 Torr at $T = 55$ K) we could stop the gas adsorption while the device was in the middle to the CS-ICS transition and start a gas pumpout. The

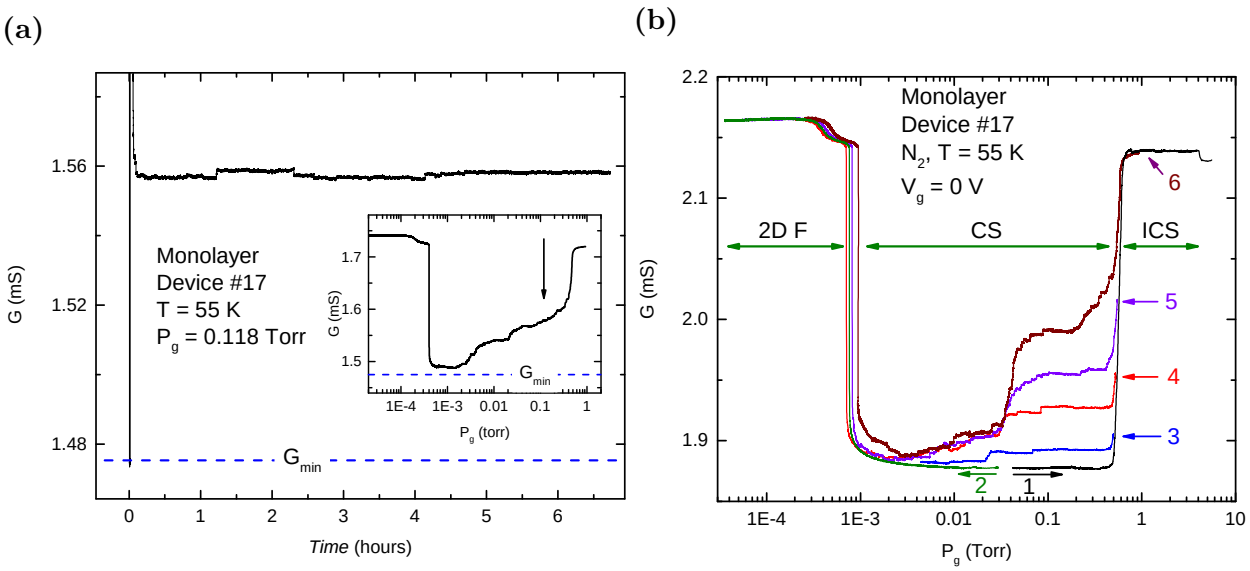

Figure 4.27: (a) Conductance G of monolayer device #17 over time at fixed pressure $P_g = 0.118$ Torr. The device is covered with a CS N_2 monolayer after it has been cycled through the CS-ICS transition. The original conductance attained in the CS phase right after the F-CS transition is labeled by $G_{\min}$. (b) Several pumpout isotherms of N_2 showing hysteresis behavior. The starting points for the pumpout isotherms are at different locations through the CS-ICS transition and are labeled with arrows. The spread in pressure of the F-CS transition is due to pressure lag in our gas system at varying pumpout rates.

hysteresis becomes observable as soon as the conductance of the device at the turnaround point starts to increase from the CS level at the CS-ICS transition, see Fig. 4.27b. The turnaround points where pumpout was started for the different isotherm runs are labeled with arrows. It is interesting to note that in all of the pumpout isotherm runs there is a small region of continuous conductance decrease before the onset of the hysteresis behavior.

4.2.3.7 Interpretation of hysteresis behavior

The hysteretic behavior described in the previous section is only observed on freestanding monolayer graphene devices. It is absent on monolayer graphene devices backed with hBN or thicker graphene devices such as bilayer devices. On the devices on which hysteresis is not observed, the interaction of the two adsorbed monolayers is expected to be absent either because only one monolayer adsorbs on the device (in the case of graphene + hBN devices) or because the two adsorbed monolayers are far apart (in the case of bilayer and thicker graphene devices). This strongly suggests that the hysteretic behavior is a result of the interactions of two CS monolayers across the graphene sheet. The $\sqrt{3}\times\sqrt{3}$ CS monolayer on graphite and on a single side of the graphene sheet can form three equivalent domains. In the case of adsorption on freestanding graphene the CS monolayers can form in either the AA or the AB stacking configuration, see Fig. 4.28. This increases the possible number of domain configurations to six. In the case of AB stacked CS monolayers the structure is still a $\sqrt{3}\times\sqrt{3}$ lattice, but with a different unit cell compared to the AA stacked case. It is unclear if AA versus AB stacked CS monolayers should have a different effect on the conductance of the graphene sheet. If this were to be the case, the conductance of the device would be

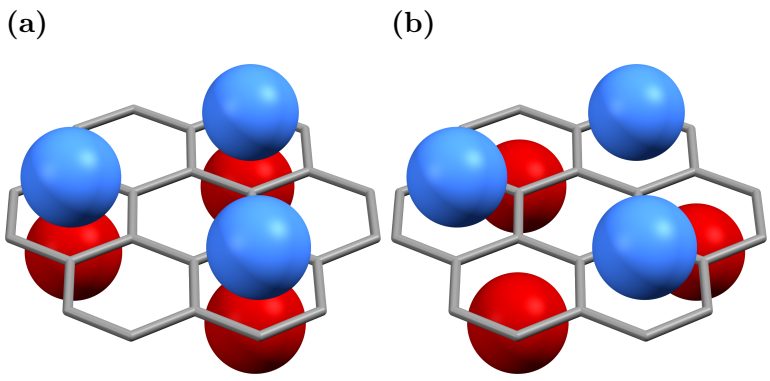

Figure 4.28: (a) AA stacked $\sqrt{3}\times\sqrt{3}$ CS monolayers. (b) AB stacked $\sqrt{3}\times\sqrt{3}$ CS monolayers.

sensitive to the distribution of AA versus AB stacked domains.

The adsorbed monolayers on opposite surfaces of the graphene sheet are expected to have a weak attractive interaction of $\approx 5\,\%$ of the total binding energy ϵ_b to the graphene surface [9]. This attractive energy favors the AA stacking of solid monolayers across the graphene sheets. Also, the extra energy of a domain is proportional to its area, therefore the energy barrier for conversion of an AA into an AB stacked domain can be large. As the adsorbed monolayers of N_2 undergo the first order F-CS transition, the lower density mobile 2D fluid is in coexistence with patches of higher density CS phase. The patches of the CS solid are expected to undergo edge grow out of their nucleation sites. It can be reasonably expected that upon the completion of the F-CS phase transition the two adsorbed nitrogen monolayers end up mostly in the more favorable lower energy AA stacked configuration.

At high pressures and large density, it is unclear whether the epitaxially rotated ICS N_2 monolayers on opposite surfaces of the graphene device should still have a stacking that is locked with respect to each other. During the phase transition from the ICS phase into the CS phase the adsorbed monolayers might attain a different configuration of AA and AB stacking domains. The relaxation processes at the coexistence of the ICS and CS phases (which are both high density phases) should be significantly reduced compared to the processes at the coexistence of the CS and 2D fluid phase [59]. In this scenario different effects on conductance of AA versus AB stacked CS N_2 domains might explain the difference in conductance of the graphene device G as a function of pressure upon adsorption and desorption. In such a scenario the observed jumps in conductance G during the desorption isotherms would correspond to a conversion of a part of the graphene device surface from an AB to an AA stacked N_2 monolayer domain.

4.2.3.8 Spike in conductance at the CS-ICS transition

Nitrogen adsorption has been measured on a total of ten freestanding monolayer graphene devices. On half of the studied devices the N_2 conductance isotherms exhibit an extra spike near the CS-ICS transition. This spike in the N_2 isotherm on monolayer graphene device #25

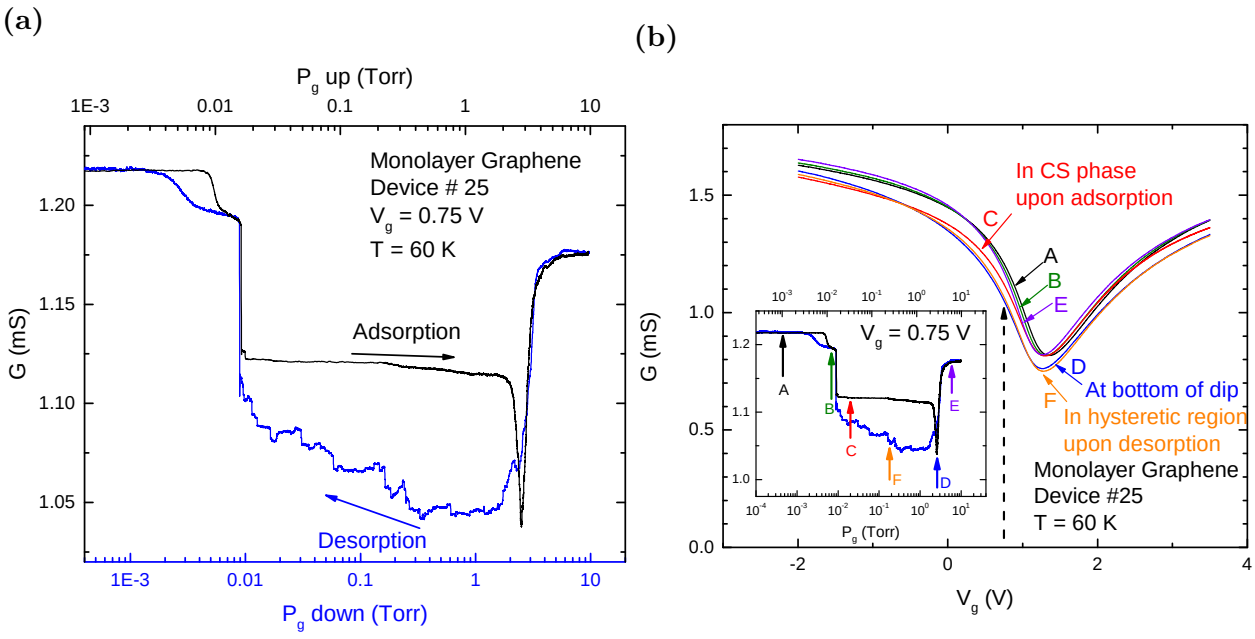

Figure 4.29: (a) Conductance isotherms of N_2 on monolayer graphene device #25 at $T = 60\,\mathrm{K}$. The isotherm contains the extra spike feature near the CS-ICS transition. The adsorption isotherm pressure scale (top axis) has been shifted left to remove the effect of pressure lag in the gas system. (b) $G(V_g)$ measurements on the same device while the N_2 monolayer is in different phases. The arrows in the inset show the locations along the isotherm where the $G(V_g)$ traces were measured. The $G(V_g)$ labeled A, B, E are taken in vacuum (bare device), in the fluid phase, and in the ICS phase. The main difference between them is a shift of the CNP which is difficult to discern in the scale of the figure. $G(V_g)$ trace labeled D is measured at bottom of the spike. $G(V_g)$ trace F is measured after desorption into the hysteretic region of the isotherm.

at $T = 60\,\mathrm{K}$ is shown in Fig. 4.29a. It occurs in the region of the N_2 phase diagram on bulk graphite that is known to contain the reentrant hexagonal domain wall fluid phase [59, 10].

The adsorption isotherms of N_2 exhibiting the spike on monolayer graphene devices appear quite similar to isotherms on bilayer graphene devices, see Fig. 4.13a, and to isotherms

on the graphene + hBN devices, see Fig. 4.31. Since on both of those types of devices interactions of adsorbed monolayers across the graphene sheet is absent, the spike in conductance has to result from the formation of some phase or structure within one N_2 monolayer on one side of the devices only. It is unclear why only half of the freestanding monolayer devices devices show this feature.

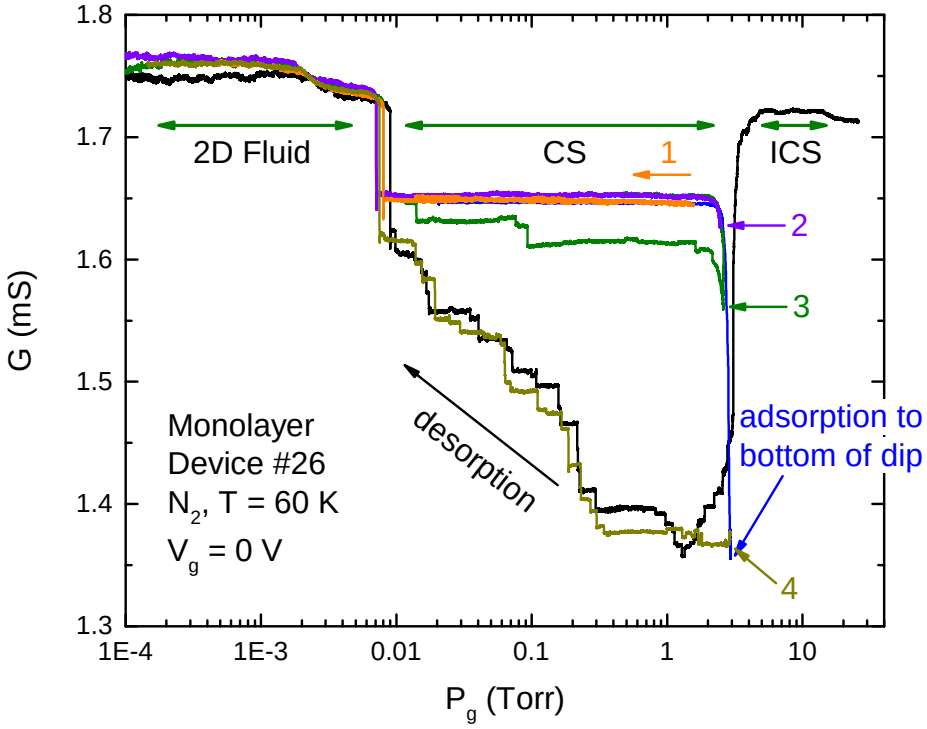

Figure 4.30: Isotherms of N_2 on monolayer graphene device #26 at $T = 60\,\mathrm{K}$ showing the onset of the hysteretic behavior near the CS-ICS transition. The blue trace is an adsorption isotherm which is performed down to the bottom of the conductance spike. The black trace is a pumpout isotherm starting from the ICS phase at $P_g \approx 20\,\mathrm{Torr}$. The traces labeled 1 through 4 are pumpout isotherms started without going past the transition into the ICS phase. The starting pressures are 1.47 Torr, 2.45 Torr, 2.59 Torr, and 2.92 Torr, respectively. The bottom of the spike occurs at $P_g \approx 2.92\,\mathrm{Torr}$. While the isotherm labeled 2 does not show hysteretic behavior, isotherm 3 does.

On freestanding monolayer graphene devices with the spike in the N_2 isotherms, the hysteretic behavior is slightly different than on devices that do not display the spike. The conductance during the desorption isotherms in the hysteretic region is lower than the original conductance attained during adsorption after the F-CS transition. The hysteretic behavior has an onset at pressures where the conductance begins to decrease into the spike, see Fig. 4.30. Just like in the case of desorption on devices without the spike, the conductance $G(P_g)$ tends towards the original conductance level attained right after the F-CS transition upon adsorption but does not fully reach that level before the F-CS transition. The two types of hysteretic behavior can be compared, see Fig. 4.30 and Fig. 4.27b.

4.2.3.9 N_2 on hBN backed Monolayer Graphene

We have studied N_2 adsorption on a total of three monolayer graphene devices backed with few nanometer thick hexagonal boron nitride. For these devices the adsorption occurs only on the bottom surface of the graphene sheet that is facing the trench, see section 2.1.3 for the discussion of the device geometry and fabrication. The positions of the phase boundaries on graphene + hBN devices are shifted to lower pressure compared to freestanding monolayer graphene due to higher binding energy ϵ_b, see Fig. 4.35 for the N_2 temperature-pressure phase diagram on both types of devices.

Apart from the difference in binding energy, the isotherms on monolayer + hBN devices appear similar to adsorption isotherms on freestanding monolayer graphene. The hysteretic behavior in the CS phase is absent on all monolayer + hBN devices. On all three monolayer + hBN devices there was a spike in conductance in the vicinity of the CS-ICS transition. A set of desorption isotherms on monolayer + hBN device #20 is shown in Fig. 4.31a.

Around the spike in the conductance at the CS-ICS transition the isotherms on all three devices exhibited nonmonotonic features. Several adsorption and desorption isotherms measured through this spike on monolayer + hBN device #20 are shown in Fig. 4.31b. On this device the fine features around the spike were reproducible upon adsorption and desorption. On device #19, on the other hand, the minimum in conductance attained at the

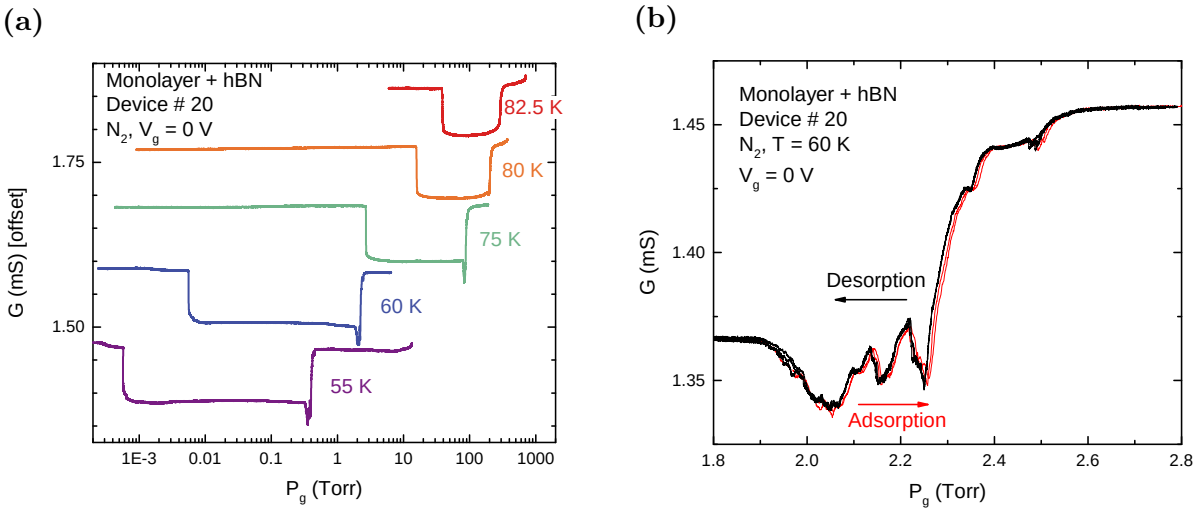

Figure 4.31: (a) A set of desorption isotherms on an hBN backed monolayer graphene device #20. The device exhibits a spike in conductance at the CS-ICS transition. The hysteretic behavior in the CS phase is absent. (b) several adsorption and desorption isotherms through the spike at the CS-ICS transition. The nonmonotonic changes in conductance through the spike appear to be reproducible. The slight shift of the adsorption isotherms to higher pressure is due to a pressure lag in our gas system.

bottom of the spike varied between adsorption and desorption isotherms, see Fig. 4.32. The fine features in the isotherms through the spike varied between adsorption and desorption isotherms, but were reproducible between different runs of the adsorption isotherm, see the red curves in Fig 4.32b.

Our suggested interpretation is that the above described behavior in the vicinity of the CS-ICS transition is likely due to the pinning of domain walls on inhomogeneities present on the graphene + hBN devices. During the fabrication process pockets of contamination are known to form between the monolayer graphene sheet and the hBN. Along with these pockets sharp folds or ridges form between these pockets, see section 2.1.3. Note that, at pressures away from the domain wall region of the phase diagram, the conductance of the device $G(P_g)$

is single valued upon both adsorption and desorption implying that the structure of the N_2 monolayer is rather similar during both adsorption and desorption; this corroborates the model of the relevance and presence of domain wall pinning.

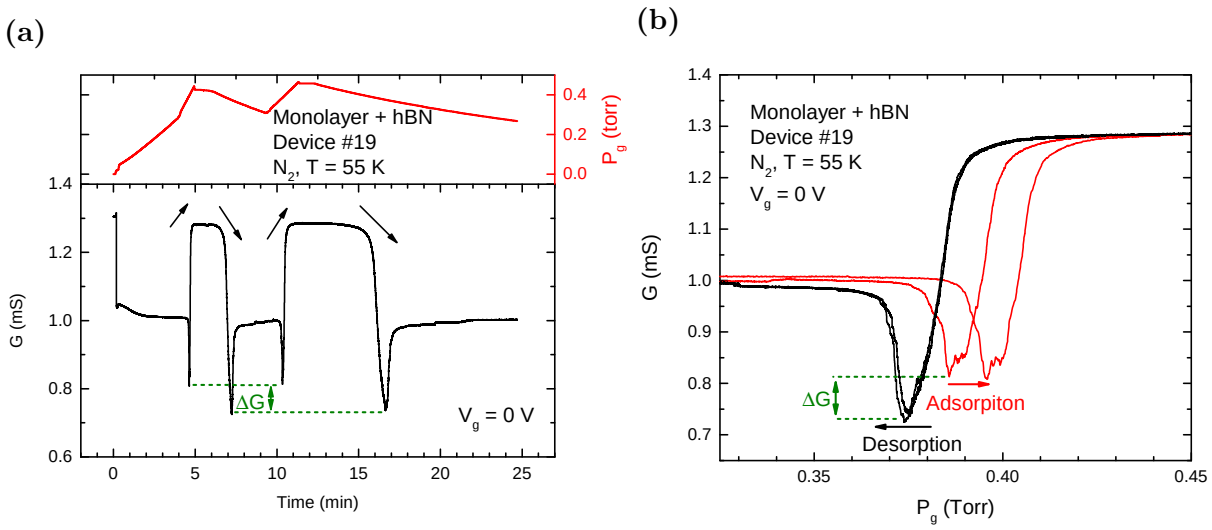

Figure 4.32: Two adsorption and desorption isotherms of N_2 though the CS-ICS transition on monolayer + hBN device #19 plotted (a) as a function of time and (b) as a function of pressure. The shift of the adsorption isotherms to higher pressure is due to gas lag in our system. The minimum in conductance at the CS-ICS transition is different between the adsorption and desorption isotherms.

4.2.3.10 High temperature N_2 adsorption behavior

Our gas system allows us to measure adsorption isotherms up to pressures of $P_g = 1000\,\text{Torr}$ without damaging the suspended graphene devices. This allows us to perform isotherms of N_2 above the critical point of the $\sqrt{3}\times\sqrt{3}$ CS phase ($T_c \approx 87\,\text{K}$, $P_c \approx 300\,\text{Torr}$). At temperatures $T > T_c$ the CS phase does not exist. At these temperatures, as the pressure is increased, the 2D fluid is expected to continuously evolve into the ICS phase. In this section

I will describe the high temperature behavior of the CS N_2 phase on our suspended graphene devices as observed in conductance isotherm measurements at $T > 80\,\mathrm{K}$ and approaching T_c.

On freestanding monolayer graphene devices both the hysteretic behavior in the CS phase and the spike at the CS-ICS transition gradually disappear as the temperature is increased above $T \approx 80\,\mathrm{K}$. The hysteresis in the isotherms disappears at a lower temperature than the conductance spike. The magnitude of the hysteretic steps in the pumpout isotherms is gradually reduced as the temperature is increased.

The temperature at which the hysteresis disappears is slightly variable among devices. On monolayer graphene device #17 the hysteresis is still present at $T = 80\,\mathrm{K}$ but is absent at $T = 82.5\,\mathrm{K}$, see appendix Fig. B.12. A set of high temperature N_2 conductance isotherms on two other freestanding monolayer graphene devices, device #21 and device #26, are shown in Fig. 4.33. These devices exhibit both the spike at the CS-ICS transition and the hysteretic behavior in the CS phase. The hysteretic behavior is clearly present in the $T = 82.5\,\mathrm{K}$ pumpout isotherm on device #21. At $T = 85\,\mathrm{K}$ the hysteretic behavior is absent on both devices. The spike in conductance at the CS-ICS transition persisted at $T = 85\,\mathrm{K}$ on both devices, with a greatly reduced magnitude compared to lower temperatures.

On the studied hBN backed monolayer graphene devices the spike in conductance at the CS-ICS phase transition disappeared at somewhat lower temperatures. On device #19 it is already absent in the $T = 80\,\mathrm{K}$ isotherm, see Fig. 4.32a. On the other hand a very slight trace of the conductance spike is still present in the isotherm on device #20 at this temperature, but is absent in the $T = 82.5\,\mathrm{K}$ isotherm, see Fig. 4.31a.

We performed a set of conductance isotherms on the monolayer + hBN device #19 in the vicinity of T_c, see Fig. 4.34b. The large decrease in conductance due to the formation of the $\sqrt{3}\times\sqrt{3}$ CS N_2 phase is present all the way up to a temperature of $T = 86.62\,\mathrm{K}$ above which it begins to rapidly reduce in magnitude. At this temperature the jumps in conductance G at the F-CS and the CS-ICS phase transitions begin to round out as a function of pressure. A very slight trace of the reduction of G is still observable at $T = 86.89\,\mathrm{K}$. Above this temperature the decrease in G is absent.

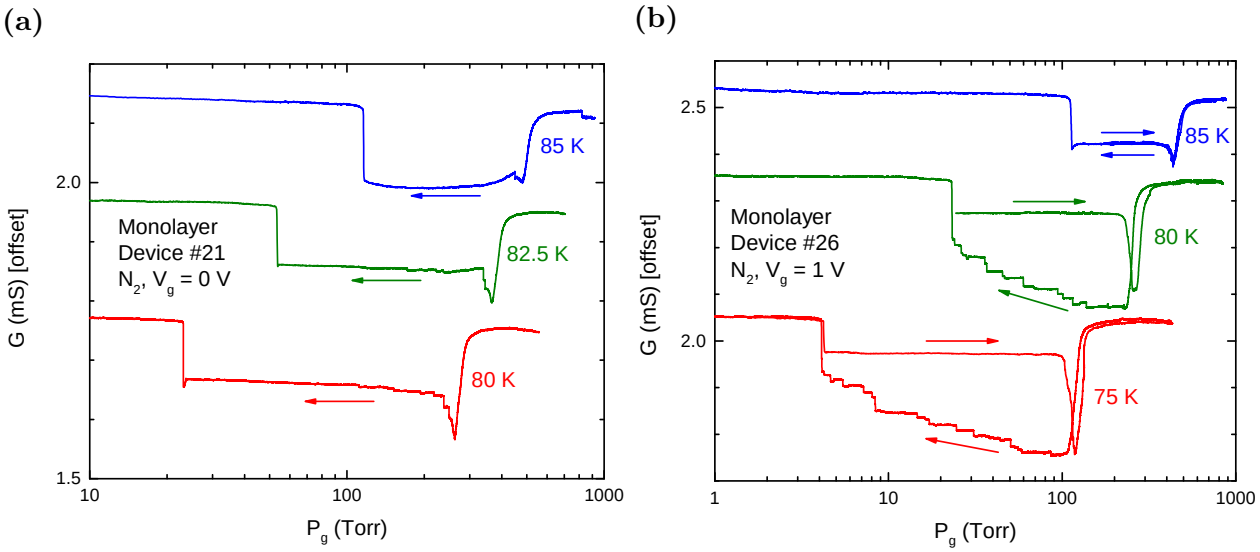

Figure 4.33: High temperature N_2 isotherms on (a) device #21 and (b) device #26. Both devices exhibit a spike in conductance $G(P_g)$ at the CS-ICS transition. Panel (a) shows only desorption isotherms, while panel (b) shows both adsorption and desorption isotherms. The hysteretic behavior in the isotherms disappears at lower T than the spike at the CS-ICS transition.

According to the accepted phase diagram of N_2 on bulk graphite [16, 51, 56], at high temperature the F-CS phase transition stops being first order at a tricritical point $T_{trc} \approx 85\,\mathrm{K}$. As the temperature of the tricritical point is approached, the density of the fluid and the densities of the CS phase, which are in coexistence at the phase boundary, becomes equal and the phase transition becomes second order. According to the accepted N_2 phase diagram, above T_{trc} the density of the CS phase at the F-CS transition is significantly higher (up to 15 %) than the density of a defect-free CS phase. The increase in density is proposed to occur through the formation of heavy domain wall defects or promotion of extra molecules into the second layer. The true average density and structure of the CS N_2 monolayer in this high T region of the phase diagram was difficult to determine experimentally on bulk

graphite due to large uncertainties in the coverage scales; this is discussed in detail in the review [51].

In our measurements at these high temperatures the conductance isotherm is still highly sensitive to the formation of the $\sqrt{3}\times\sqrt{3}$ CS phase. The persistence of the decrease in conductance indicates that the local structure of the N_2 monolayer is still mostly the $\sqrt{3}\times\sqrt{3}$ CS phase: this CS phase has to cover a fairly large fraction of the device surface up to $T = 86.62\,\mathrm{K}$ to produce the decrease in conductance G.

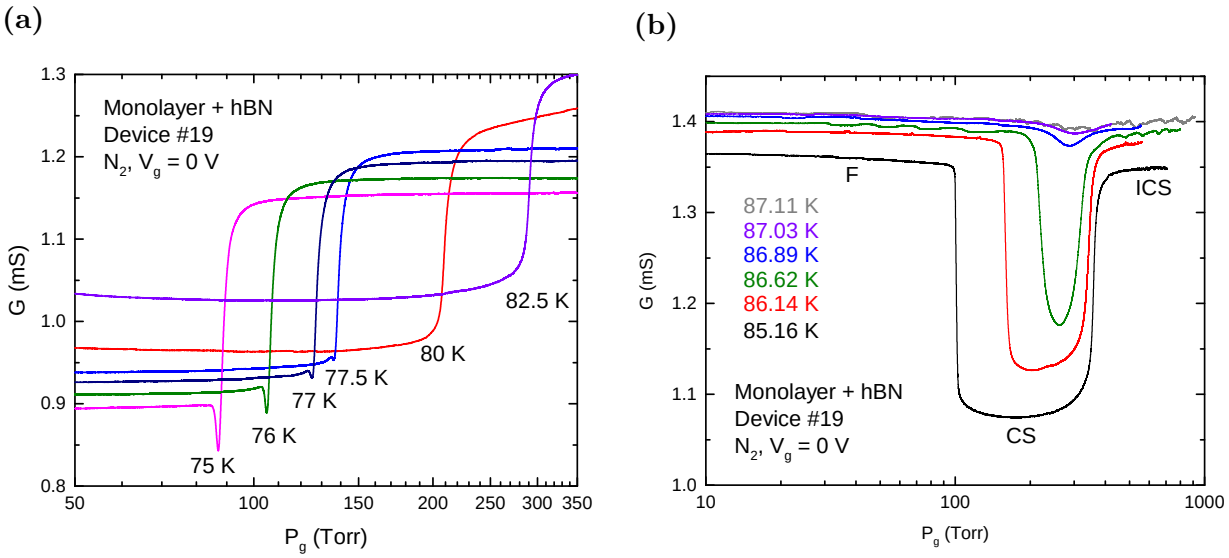

Figure 4.34: High temperature isotherms on an hBN backed monolayer graphene device #19. (a) Desorption isotherm through the CS-ICS phase transition showing the gradual disappearance of the conductance spike. (b) Isotherms in the vicinity of T_c. See text for details.

4.2.3.11 N_2 P-T phase diagram

The temperature-pressure phase diagram of N_2 as measured on our suspended graphene devices is shown in Fig. 4.35a. The pressures have been thermomolecularly corrected according to the empirical formula presented in reference [75]. The phase diagram shows phase

boundaries on both a freestanding and an hBN backed monolayer devices. Apart form the differences in pressures of the phase boundaries the two phase diagrams look quite similar. Our measurements indicate that T_c of the CS N_2 phase on the surface of freestanding monolayer graphene devices might be lower than on the hBN backed monolayer by at most 0.5 K. The decrease of T_c is likely due to a slight difference in binding energy ($\approx 3\,\%$).

The black squares in the 2D fluid region of the phase diagram plotted in Fig. 4.35a indicate the midpoints of the *gradual change* in conductance that occurs in the fluid phase due to the shift of the CNP of the graphene device. The position of this feature on the phase diagram appears to merge with the F-CS phase boundary at lower temperatures $T < 52\,\mathrm{K}$ and pressures too low to access in our adsorption apparatus, $P < 1 \times 10^{-4}\,\mathrm{Torr}$. This behavior is consistent with the feature resulting from the formation of the fluid phase; its midpoint likely corresponding to an intermediate density of the fluid.

A comparison of N_2 isotherms at $T = 60\,\mathrm{K}$ on freestanding monolayer, monolayer + hBN and bilayer graphene devices are presented in Fig. 4.35b. The features corresponding to the phase boundaries plotted on the phase diagram are labeled with their respective symbols.

The differences in binding energies $\Delta\epsilon$ between freestanding and hBN backed graphene devices can be extracted from the shifts of the pressures of the phase boundaries according to Eq. (4.1). At $T = 60\,\mathrm{K}$ the F-CS transitions on freestanding monolayer and monolayer + hBN devices occur at pressures $P = 4.9\,\mathrm{mTorr}$ and $P = 2.8\,\mathrm{mTorr}$, respectively. Both of these pressure readings include a slight and comparable offsets due to a pressure lag in our gas system. The CS-ICS transition on the two classes of devices occurs at pressures of $P = 2.90\,\mathrm{Torr}$ and $P = 1.94\,\mathrm{Torr}$, respectively. The extracted changes in energy are approximately $\Delta\epsilon \approx 30\,\mathrm{K}$. The single particle binding energy of N_2 on bulk graphite is $\epsilon_b = 1160\,\mathrm{K}$ [81]. The difference $\Delta\epsilon/\epsilon_b$ is only $\approx 3\,\%$. The binding energy on graphene + hBN devices is expected to be indistinguishable from bulk graphite.

(a) N_2 phase diagram

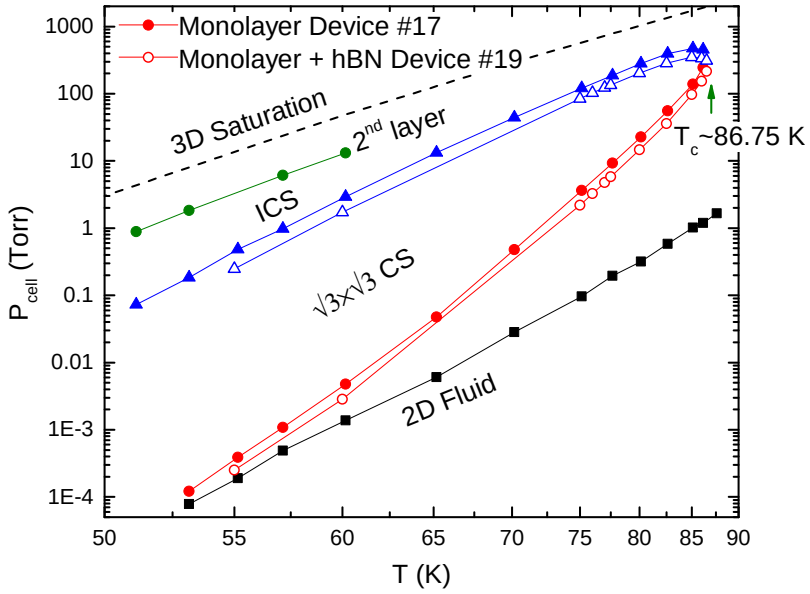

(b) N_2 isotherms at $T = 60\,\mathrm{K}$

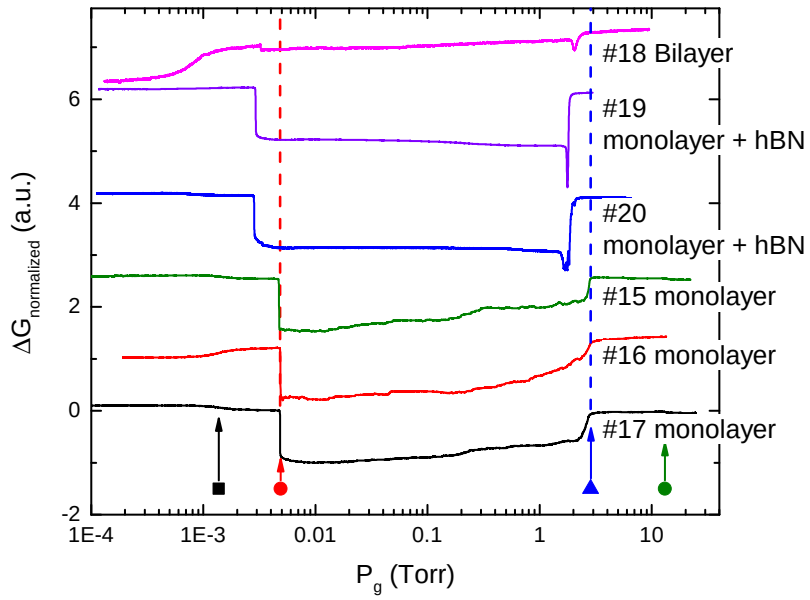

Figure 4.35: (a) Temperature–Pressure phase diagram of N_2 on monolayer graphene. Solid symbols are phase boundaries on freestanding graphene. Open symbols indicate the phase boundaries on an hBN backed monolayer. (b) Desorption isotherms of N_2 at $T = 60\,\mathrm{K}$. The features corresponding to the phase boundaries are labeled with their respective symbols.

The single particle binding energy of monolayer graphene is expected to be reduced by $\Delta\epsilon_b/\epsilon_b \approx 10\,\%$ compared to bulk graphite [66]. The above described difference in energies $\Delta\epsilon$ at the phase boundaries is smaller. This can be explained by the extra attractive interaction of the second monolayer of N_2 on the opposite surface of the freestanding monolayer graphene device. The extra attractive interaction partially compensates the decrease in single particle binding energy. It is expected to be approximately 5 % of the total binding energy [9].

4.2.3.12 Kr on Monolayer Graphene

On bulk graphite Kr, N_2, and CO are all known to have an almost identical phase diagram [10]. As discussed in previous sections, on our suspended monolayer graphene devices the formation of the $\sqrt{3}\times\sqrt{3}$ CS phase of both N_2 and CO produces a large reduction in conductance G. The $\sqrt{3}\times\sqrt{3}$ CS phase of Kr, however, produces a significantly smaller reduction of conductance.

A comparison of several Kr isotherms at $T = 85\,\mathrm{K}$ on suspended graphene devices is shown in Fig. 4.36. On graphene + hBN devices the formation of the Kr CS phase produced a reduction in conductance that appears qualitatively similar to the effect of the N_2 CS phase. There are however some major differences: first, the magnitude of the the reduction of conductance ΔG for Kr is approximately one order of magnitude smaller than for CO and N_2. Furthermore, there is no spike present near the CS-ICS transition on any of the studied graphene + hBN devices. Surprisingly, the conductance of the devices is still highly sensitive to multilayer formation, see appendix Fig. B.17. Up to thirteen extra steps were observable near saturation on monolayer + hBN device #19.

On freestanding monolayer graphene devices the effect on conductance of the CS Kr phase was approximately one order of magnitude smaller than for both CO and N_2 CS phase. There was no observable hysteresis present between the adsorption and desorption isotherms. On freestanding monolayer graphene devices the conductance G did not remain constant in the CS phase, but experienced a gradual increase with pressure, as it was increased towards the CS-ICS transition. Instead of a fairly abrupt (as a function of pressure) increase in

conductance G at the CS-ICS transition, the devices only exhibited an inflection point (kink), see Fig 4.36. Furthermore, none of the studied devices exhibited a spike in the vicinity the CS-ICS transition. It is possible that the gradual increase in conductance while the Kr monolayer is in the CS phase is due to formation of the same proposed domain structures within the adsorbed monolayer which give rise to the hysteretic behavior of N_2 and CO on freestanding devices. In this case these domain structures are proposed to form upon adsorption, while the monolayer is in the CS phase. It is important to note that we do not observe any vertical steps in the isotherms while the Kr monolayer is in the CS phase, possibly due to the smaller effect of Kr on conductance.

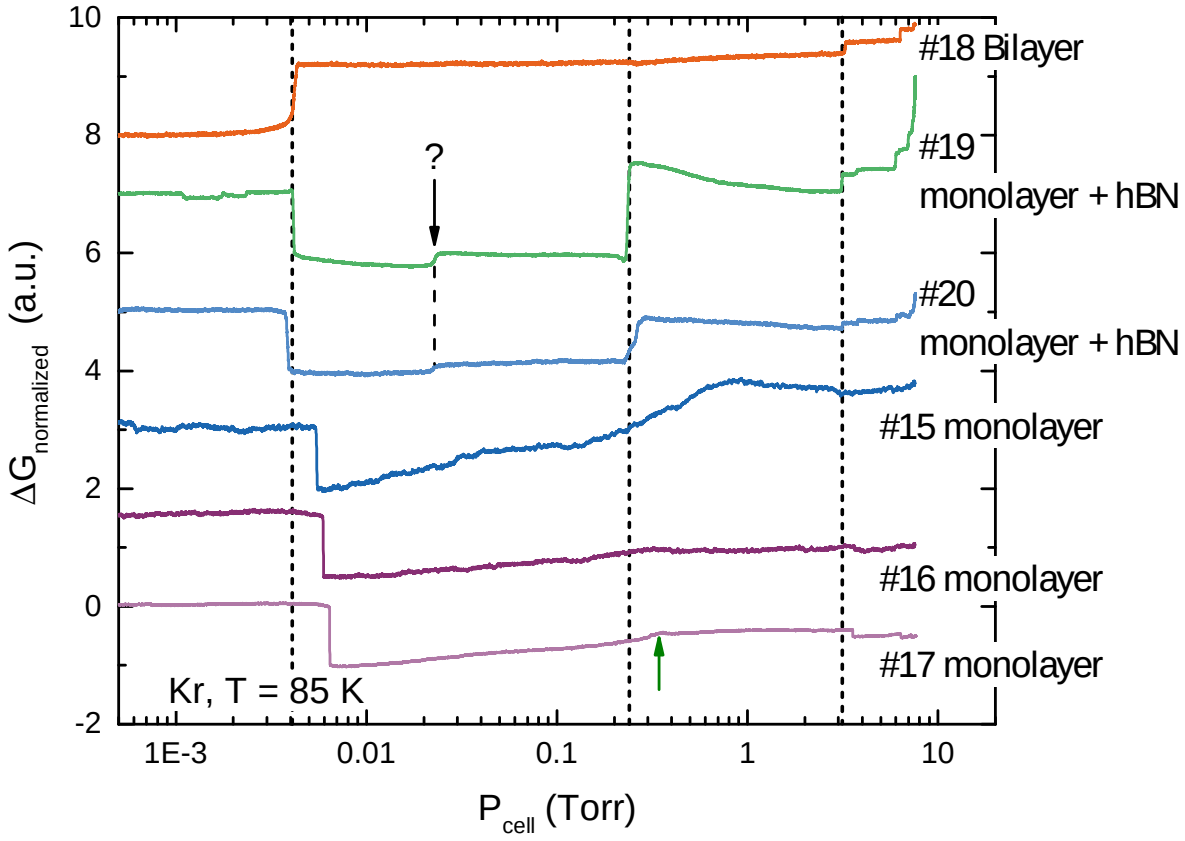

Figure 4.36: Kr isotherms at $T = 85\,\mathrm{K}$ on suspended graphene devices. The pressures have been thermomolecularly corrected. The vertical dotted lines show the F-CS, the CS-ICS and the second layer condensation transitions on monolayer + hBN devices. The phase transitions on freestanding monolayer graphene occur at higher pressures relative to devices with more layers due to a reduced binding energy ϵ_b. The monolayer + hBN devices exhibit an extra step (labeled with question mark) in the isotherms when the monolayer is expected to be in the CS phase. This step does not correspond to any known phase transition of Kr on bulk graphite.

BIBLIOGRAPHY

[1] F. F. Abraham, W. E. Rudge, D. J. Auerbach, and S. W. Koch. Molecular-dynamics simulations of the incommensurate phase of krypton on graphite using more than 100000 atoms. *Physical Review Letters*, 52(6):445–448, 1984.

[2] A. I. Aria, P. R. Kidambi, R. S. Weatherup, L. Xiao, J. A. Williams, and S. Hofmann. Time evolution of the wettability of supported graphene under ambient air exposure. *Journal of Physical Chemistry C*, 120(4):2215–2224, 2016.

[3] W. Bao, L. Jing, J. Velasco, Y. Lee, G. Liu, D. Tran, B. Standley, M. Aykol, S. B. Cronin, D. Smirnov, M. Koshino, E. McCann, M. Bockrath, and C. N. Lau. Stacking-dependent band gap and quantum transport in trilayer graphene. *Nature Physics*, 7(12):948–952, 2011.

[4] W. Z. Bao, F. Miao, Z. Chen, H. Zhang, W. Y. Jang, C. Dames, and C. N. Lau. Controlled ripple texturing of suspended graphene and ultrathin graphite membranes. *Nature Nanotechnology*, 4(9):562–566, 2009.

[5] T. Bar, T. Burns, and K. Knorr. Growth kinetics of ar monolayers physisorbed on graphite (001). *Surface Science*, 383(2-3):362–369, 1997.

[6] M. Bienfait, J. L. Seguin, J. Suzanne, E. Lerner, J. Krim, and J. G. Dash. Complete and incomplete wetting of krypton and oxygen on graphite - reentrant type-2 growth on a scale of substrate strength. *Physical Review B*, 29(2):983–987, 1984.

[7] M. Bockrath and Pan C. Private communication, 2014.

[8] K. I. Bolotin, K. J. Sikes, Z. Jiang, M. Klima, G. Fudenberg, J. Hone, P. Kim, and H. L.

Stormer. Ultrahigh electron mobility in suspended graphene. *Solid State Communications*, 146(9-10):351–355, 2008.

[9] L. W. Bruch, M. W. Cole, and H. Y. Kim. Transitions of gases physisorbed on graphene. *Journal of Physics-Condensed Matter*, 22(30):7, 2010.

[10] L. W. Bruch, Milton W. Cole, and Eugene Zaremba. *Physical adsorption : forces and phenomena*. International series of monographs on chemistry. Clarendon Press ; Oxford University Press, Oxford New York, 1997.

[11] R. G. Caflisch, A. N. Berker, and M. Kardar. Reentrant melting of krypton absorbed on graphite and the helical potts-lattice-gas model. *Physical Review B*, 31(7):4527–4537, 1985.

[12] S. Calisti and J. Suzanne. Orientational epitaxy of an incommensurate neon monolayer adsorbed on graphite. *Surface Science*, 105(1):L255–L259, 1981.

[13] J. Cao, Q. Wang, and H. Dai. Electron transport in very clean, as-grown suspended carbon nanotubes. *Nature Materials*, 4(10):745–749, 2005.

[14] E. V. Castro, H. Ochoa, M. I. Katsnelson, R. V. Gorbachev, D. C. Elias, K. S. Novoselov, A. K. Geim, and F. Guinea. Limits on charge carrier mobility in suspended graphene due to flexural phonons. *Physical Review Letters*, 105(26):4, 2010.

[15] A. H. Castro Neto, F. Guinea, N. M. R. Peres, K. S. Novoselov, and A. K. Geim. The electronic properties of graphene. *Reviews of Modern Physics*, 81(1):109–162, 2009.

[16] M. H. W. Chan, A. D. Migone, K. D. Miner, and Z. R. Li. Thermodynamic study of phase-transitions of monolayer n-2 on graphite. *Physical Review B*, 30(5):2681–2694, 1984.

[17] M. D. Chinn and S. C. Fain. Structural phase-transition in epitaxial solid krypton monolayers on graphite. *Physical Review Letters*, 39(3):146–149, 1977.

[18] B. I. Choi, H. S. Nham, S. Y. Kwon, J. C. Kim, H. S. Youn, and T. K. Lim. Multilayer adsorption of krypton on graphite using an ellipsomeric technique. *Journal of the Korean Physical Society*, 47(5):830–837, 2005.

[19] J. S. Choi, J. S. Kim, I. S. Byun, D. H. Lee, M. J. Lee, B. H. Park, C. Lee, D. Yoon, H. Cheong, K. H. Lee, Y. W. Son, J. Y. Park, and M. Salmeron. Friction anisotropy-driven domain imaging on exfoliated monolayer graphene. *Science*, 333(6042):607–610, 2011.

[20] S. N. Coppersmith, D. S. Fisher, B. I. Halperin, P. A. Lee, and W. F. Brinkman. Dislocations and the commensurate-incommensurate transition in 2 dimensions. *Physical Review B*, 25(1):349–363, 1982.

[21] K. L. Damico, J. Bohr, D. E. Moncton, and D. Gibbs. Melting and orientational epitaxy in argon and xenon monolayers on graphite. *Physical Review B*, 41(7):4368–4376, 1990.

[22] K. L. Damico and D. E. Moncton. X-ray study of orientational epitaxy in rare-gas monolayers on graphite. *Journal of Vacuum Science & Technology A*, 4(3):1455–1458, 1986.

[23] J. G. Dash. *Films on solid surfaces : the physics and chemistry of physical adsorption.* Academic Press, New York, 1975.

[24] J. G. Dash and R. D. Puff. Phase-transitions in heterogeneous films. *Physical Review B*, 24(1):295–309, 1981.

[25] P. Day, M. Lysek, M. Lamadrid, and D. Goodstein. Phase-transitions in argon films. *Physical Review B*, 47(16):10716–10726, 1993.

[26] A. Diama, B. Matthies, K. W. Herwig, F. Y. Hansen, L. Criswell, H. Mo, M. Bai, and H. Taub. Structure and phase transitions of monolayers of intermediate-length n-alkanes on graphite studied by neutron diffraction and molecular dynamics simulation. *Journal of Chemical Physics*, 131(8):10, 2009.

[27] R. D. Diehl and S. C. Fain. Adsorption of nitrogen molecules on graphite for 31 less-than t 52-k - the fluid-to-commensurate-solid transition, multilayer condensation, and the pressure temperature phase-diagram. *Journal of Chemical Physics*, 77(10):5065–5072, 1982.

[28] R. D. Diehl and S. C. Fain. Structure and orientational ordering of nitrogen molecules physisorbed on graphite. *Surface Science*, 125(1):116–152, 1983.

[29] B. Dzyubenko, H. C. Lee, O. E. Vilches, and D. H. Cobden. Surface electron perturbations and the collective behaviour of atoms adsorbed on a cylinder. *Nature Physics*, 11(5):398–402, 2015.

[30] A. Eichler, M. D. Ruiz, J. A. Plaza, and A. Bachtold. Strong coupling between mechanical modes in a nanotube resonator. *Physical Review Letters*, 109(2):5, 2012.

[31] M. Farjam and H. Rafii-Tabar. Energy gap opening in submonolayer lithium on graphene: Local density functional and tight-binding calculations. *Physical Review B*, 79(4):7, 2009.

[32] Y. P. Feng and M. H. W. Chan. Tricritical-point and critical-point melting transitions of commensurate co on graphite. *Physical Review Letters*, 64(18):2148–2151, 1990.

[33] G. M. Florio, T. L. Werblowskyf, B. Ilan, T. Muller, B. J. Berne, and G. W. Flynn. Chain-length effects on the self-assembly of short 1-bromoalkane and n-alkane monolayers on graphite. *Journal of Physical Chemistry C*, 112(46):18067–18075, 2008.

[34] P. Gallagher, M. Lee, F. Amet, P. Maksymovych, J. Wang, S. P. Wang, X. B. Lu, G. Y. Zhang, K. Watanabe, T. Taniguchi, and D. Goldhaber-Gordon. Switchable friction enabled by nanoscale self-assembly on graphene. *Nature Communications*, 7:7, 2016.

[35] R. Golizadeh-Mojarad and S. Datta. Effect of contact induced states on minimum conductivity in graphene. *Physical Review B*, 79(8):5, 2009.

[36] R. J. Gooding, B. Joos, and B. Bergersen. Krypton on graphite - microstructure at zero temperature. *Physical Review B*, 27(12):7669–7675, 1983.

[37] D. Gunlycke and C. T. White. Graphene interferometer. *Applied Physics Letters*, 93(12):3, 2008.

[38] C. Y. Hou, C. Chamon, and C. Mudry. Electron fractionalization in two-dimensional graphenelike structures. *Physical Review Letters*, 98(18):4, 2007.

[39] A. Inaba, T. Shirakami, and H. Chihara. Heat-capacities of physisorbed films on solids .1. nitrogen and carbon-monoxide on graphite. *Journal of Chemical Thermodynamics*, 23(5):461–474, 1991.

[40] W. Jang, W. Bao, L. Jing, C. N. Lau, and C. Dames. Thermal conductivity of suspended few-layer graphene by a modified t-bridge method. *Applied Physics Letters*, 103(13):5, 2013.

[41] A. Jungen, C. Stampfer, L. Durrer, T. Helbling, and C. Hierold. Amorphous carbon contamination monitoring and process optimization for single-walled carbon nanotube integration. *Nanotechnology*, 18(7):6, 2007.

[42] Y. D. Kim, H. Kim, Y. Cho, J. H. Ryoo, C. H. Park, P. Kim, Y. S. Kim, S. Lee, Y. L. Li, S. N. Park, Y. S. Yoo, D. Yoon, V. E. Dorgan, E. Pop, T. F. Heinz, J. Hone, S. H. Chun, H. Cheong, S. W. Lee, M. H. Bae, and Y. D. Park. Bright visible light emission from graphene. *Nature Nanotechnology*, 10(8):676–681, 2015.

[43] J. Kong, A. M. Cassell, and H. J. Dai. Chemical vapor deposition of methane for single-walled carbon nanotubes. *Chemical Physics Letters*, 292(4-6):567–574, 1998.

[44] J. M. Kosterlitz. Kosterlitz-thouless physics: a review of key issues. *Reports on Progress in Physics*, 79(2):59, 2016.

[45] A. V. Kretinin, Y. Cao, J. S. Tu, G. L. Yu, R. Jalil, K. S. Novoselov, S. J. Haigh, A. Gholinia, A. Mishchenko, M. Lozada, T. Georgiou, C. R. Woods, F. Withers, P. Blake, G. Eda, A. Wirsig, C. Hucho, K. Watanabe, T. Taniguchi, A. K. Geim, and R. V. Gorbachev. Electronic properties of graphene encapsulated with different two-dimensional atomic crystals. *Nano Letters*, 14(6):3270–3276, 2014.

[46] L. D. Landau, E. M. Lifshits, and L. P. Pitaevskii. *Statistical physics*. Course of theoretical physics. Pergamon Press, Oxford, New York, 1980.

[47] J. Landoulsi, M. J. Genet, S. Fleith, Y. Toure, I. Liascukiene, C. Methivier, and P. G. Rouxhet. Organic adlayer on inorganic materials: Xps analysis selectivity to cope with adventitious contamination. *Applied Surface Science*, 383:71–83, 2016.

[48] H. C. Lee. *Adsorption of noble gases on individual suspended single-walled carbon nanotubes*. Ph.d. thesis, University of Washington, Seattle, 2013.

[49] H. C. Lee, O. E. Vilches, Z. H. Wang, E. Fredrickson, P. Morse, R. Roy, B. Dzyubenko, and D. H. Cobden. Kr and he-4 adsorption on individual suspended single-walled carbon nanotubes. *Journal of Low Temperature Physics*, 169(5-6):338–349, 2012.

[50] H. Mannebach, U. G. Volkmann, J. Faul, and K. Knorr. Order-parameter kinetics in the liquid-gas coexistence region of ar monolayers physisorbed on graphite. *Physical Review Letters*, 67(12):1566–1569, 1991.

[51] D. Marx and H. Wiechert. Ordering and phase transitions in adsorbed monolayers of diatomic molecules. *Advances in Chemical Physics, Vol 95 - Surface Properties*, 95:213–394, 1996.

[52] A. S. Mayorov, D. C. Elias, I. S. Mukhin, S. V. Morozov, L. A. Ponomarenko, K. S. Novoselov, A. K. Geim, and R. V. Gorbachev. How close can one approach the Dirac Point in graphene experimentally? *Nano Letters*, 12(9):4629–4634, 2012.

[53] A. D. Migone, M. T. Alkhafaji, G. Vidali, and M. Karimi. Thermodynamic study of argon films adsorbed on boron-nitride. *Physical Review B*, 47(11):6685–6696, 1993.

[54] A. D. Migone, Z. R. Li, and M. H. W. Chan. Melting transition of submonolayer Ar adsorbed on graphite. *Physical Review Letters*, 53(8):810–813, 1984.

[55] F. Millot. Adsorption of the 1st layer of argon on graphite. *Journal De Physique Lettres*, 40(1):L9–L10, 1979.

[56] K. D. Miner, M. H. W. Chan, and A. D. Migone. Vapor-pressure-isotherm study of N2 on graphite near the tricritical point. *Physical Review Letters*, 51(16):1465–1468, 1983.

[57] J. Moser, A. Barreiro, and A. Bachtold. Current-induced cleaning of graphene. *Applied Physics Letters*, 91(16):3, 2007.

[58] Angel Mulero and Francisco Cuadros. Rare-gas adsorption. In Jozsef Toth, editor, *Adsorption : theory, modeling, and analysis*, Surfactant science series, book chapter 4, pages 433–507. Marcel Dekker, New York, 2002.

[59] Marcel den Nijs. The domain wall theory of two-dimensional commensurate-incommensurate phase transitions. In Cyril Domb and Joel Lebowitz, editors, *Phase transitions and critical phenomena*, book section 2, pages 220–329. Academic Press, London ; New York, 1988.

[60] A. D. Novaco and J. P. McTague. Orientational epitaxy–orientational ordering of incommensurate structures. *Physical Review Letters*, 38(22):1286–1289, 1977.

[61] K. S. Novoselov, A. Mishchenko, A. Carvalho, and A. H. C. Neto. 2D materials and van der Waals heterostructures. *Science*, 353(6298):7, 2016.

[62] M. Oksanen, A. Uppstu, A. Laitinen, D. J. Cox, M. F. Craciun, S. Russo, A. Harju, and P. Hakonen. Single-mode and multimode Fabry-Perot interference in suspended graphene. *Physical Review B*, 89(12):5, 2014.

[63] R. Pandit, M. Schick, and M. Wortis. Systematics of multilayer adsorption phenomena on attractive substrates. *Physical Review B*, 26(9):5112–5140, 1982.

[64] M. T. Pettes, I. S. Jo, Z. Yao, and L. Shi. Influence of polymeric residue on the thermal conductivity of suspended bilayer graphene. *Nano Letters*, 11(3):1195–1200, 2011.

[65] H. W. C. Postma, I. Kozinsky, A. Husain, and M. L. Roukes. Dynamic range of nanotube- and nanowire-based electromechanical systems. *Applied Physics Letters*, 86(22):3, 2005.

[66] L. Reatto, D. E. Galli, M. Nava, and M. W. Cole. Novel behavior of monolayer quantum gases on graphene, graphane and fluorographene. *Journal of Physics-Condensed Matter*, 25(44):17, 2013.

[67] Y. F. Ren, X. Z. Deng, Z. H. Qiao, C. S. Li, J. Jung, C. G. Zeng, Z. Y. Zhang, and Q. Niu. Single-valley engineering in graphene superlattices. *Physical Review B*, 91(24):8, 2015.

[68] S. Ryu, C. Mudry, C. Y. Hou, and C. Chamon. Masses in graphenelike two-dimensional electronic systems: Topological defects in order parameters and their fractional exchange statistics. *Physical Review B*, 80(20):32, 2009.

[69] M. M. Sadeghi, M. T. Pettes, and L. Shi. Thermal transport in graphene. *Solid State Communications*, 152(15):1321–1330, 2012.

[70] V. Sazonova, Y. Yaish, H. Ustunel, D. Roundy, T. A. Arias, and P. L. McEuen. A tunable carbon nanotube electromechanical oscillator. *Nature*, 431(7006):284–287, 2004.

[71] M. Schobinger and F. F. Abraham. Energetics of the incommensurate phase of krypton on graphite - a computer-simulation study. *Physical Review B*, 31(7):4590–4596, 1985.

[72] T. Sharf, J. W. Kevek, and E. D. Minot. Fabrication of low-noise carbon nanotube

field-effect transistor biosensors. In *2011 11th IEEE International Conference on Nanotechnology*, pages 122–125, 2011.

[73] Jozef Sivekz. Real and reciprocal space unit vectors of graphene lattice, 2015.

[74] W. A. Steele. Monolayers of linear molecules adsorbed on the graphite basal plane: Structures and intermolecular interactions. *Langmuir*, 12(1):145–153, 1996.

[75] T. Takaishi and Y. Sensui. Thermal transpiration effect of hydrogen, rare gases and methane. *Transactions of the Faraday Society*, 59(491):2503–2514, 1963.

[76] G. J. Tatlock. Solid gases. *Ultramicroscopy*, 10(1-2):87–96, 1982.

[77] R. M. Tiggelaar, R. G. R. Sanders, A. W. Groenland, and J. G. E. Gardeniers. Stability of thin platinum films implemented in high-temperature microdevices. *Sensors and Actuators A: Physical*, 152(1):39–47, 2009.

[78] N. Tombros, A. Veligura, J. Junesch, J. J. van den Berg, P. J. Zomer, M. Wojtaszek, I. J. V. Marun, H. T. Jonkman, and B. J. van Wees. Large yield production of high mobility freely suspended graphene electronic devices on a polydimethylglutarimide based organic polymer. *Journal of Applied Physics*, 109(9):5, 2011.

[79] J. A. Venables and M. Bienfait. Reaction order in thermal desorption spectroscopy. *Surface Science*, 61(2):667–672, 1976.

[80] J. A. Venables, G. D. T. Spiller, and M. Hanbucken. Nucleation and growth of thin-films. *Reports on Progress in Physics*, 47(4):399–459, 1984.

[81] G. Vidali, G. Ihm, H. Y. Kim, and M. W. Cole. Potentials of physical adsorption. *Surface Science Reports*, 12(4):133–181, 1991.

[82] P. R. Wallace. The band theory of graphite. *Physical Review*, 71(9):622–634, 1947.

[83] H. D. Wang, X. Zhang, and H. Takamatsu. Ultraclean suspended monolayer graphene achieved by in situ current annealing. *Nanotechnology*, 28(4):7, 2017.

[84] Z. H. Wang. *Phase transitions on the surface of individual nanotubes.* Ph.d. thesis, University of Washington, Seattle, 2010.

[85] Z. H. Wang, J. Wei, P. Morse, J. G. Dash, O. E. Vilches, and D. H. Cobden. Phase transitions of adsorbed atoms on the surface of a carbon nanotube. *Science*, 327(5965):552–555, 2010.

[86] D. S. Wastl, F. Speck, E. Wutscher, M. Ostler, T. Seyller, and F. J. Giessibl. Observation of 4 nm pitch stripe domains formed by exposing graphene to ambient air. *Acs Nano*, 7(11):10032–10037, 2013.

[87] H. Wu and G. B. Hess. Multilayer adsorption of neon on graphite. *Physica B*, 194:965–966, 1994.

[88] H. S. Youn, X. F. Meng, and G. B. Hess. Multilayer adsorption of xenon, krypton, and argon on graphite - an ellipsometric study. *Physical Review B*, 48(19):14556–14576, 1993.

[89] Y. J. Yu, Y. Zhao, S. Ryu, L. E. Brus, K. S. Kim, and P. Kim. Tuning the graphene work function by electric field effect. *Nano Letters*, 9(10):3430–3434, 2009.

[90] P. J. Zomer, M. H. D. Guimaraes, J. C. Brant, N. Tombros, and B. J. van Wees. Fast pick up technique for high quality heterostructures of bilayer graphene and hexagonal boron nitride. *Applied Physics Letters*, 105(1):4, 2014.

Appendix A

EFFECTS OF ADSORBED MONOLAYER FORMATION ON THE CONDUCTANCE OF NANOTUBE DEVICES

This appendix contains the measured charge transfers from adsorbed monolayers of various gases to several nanotube devices. The charge transfer is obtained from Eq. (3.7). For a discussion see section 3.4. The presented data is from a publication of our group [29].

Device	CB spacing (mV)	Shift ΔV_g (mV)	Charge transfer (e)
N_2			
YB14	34	-13	-0.4
YB27	34	-7	-0.2
YB30	120	$+20$	0.2
CO			
YB27	34	-35	-1
YB30	120	$+30$	$+0.25$
O_2			
YB24	54	$+27$	$+0.5$

Table A.1: Charge transfer to nanotube devices due to the formation of a dense monolayer of diatomic molecules N_2, CO, and O_2.

Device	CB spacing (mV)	Shift ΔV_g (mV)	Charge transfer (e)
Ar			
YB11	11	+10	+0.9
YB14	34	+24	+0.7
YB24	54	+38	+0.7
YB27	34	+21	+0.6
YB30	120	+32	+0.25
Kr			
YB11	34	−12	−0.35
YB14	54	+69	+1.3
Xe			
YB14	34	−65	−1.9
He			
YB14	34	+23	+0.7

Table A.2: Charge transfer to nanotube devices due to the formation of a dense monolayer of noble gases.

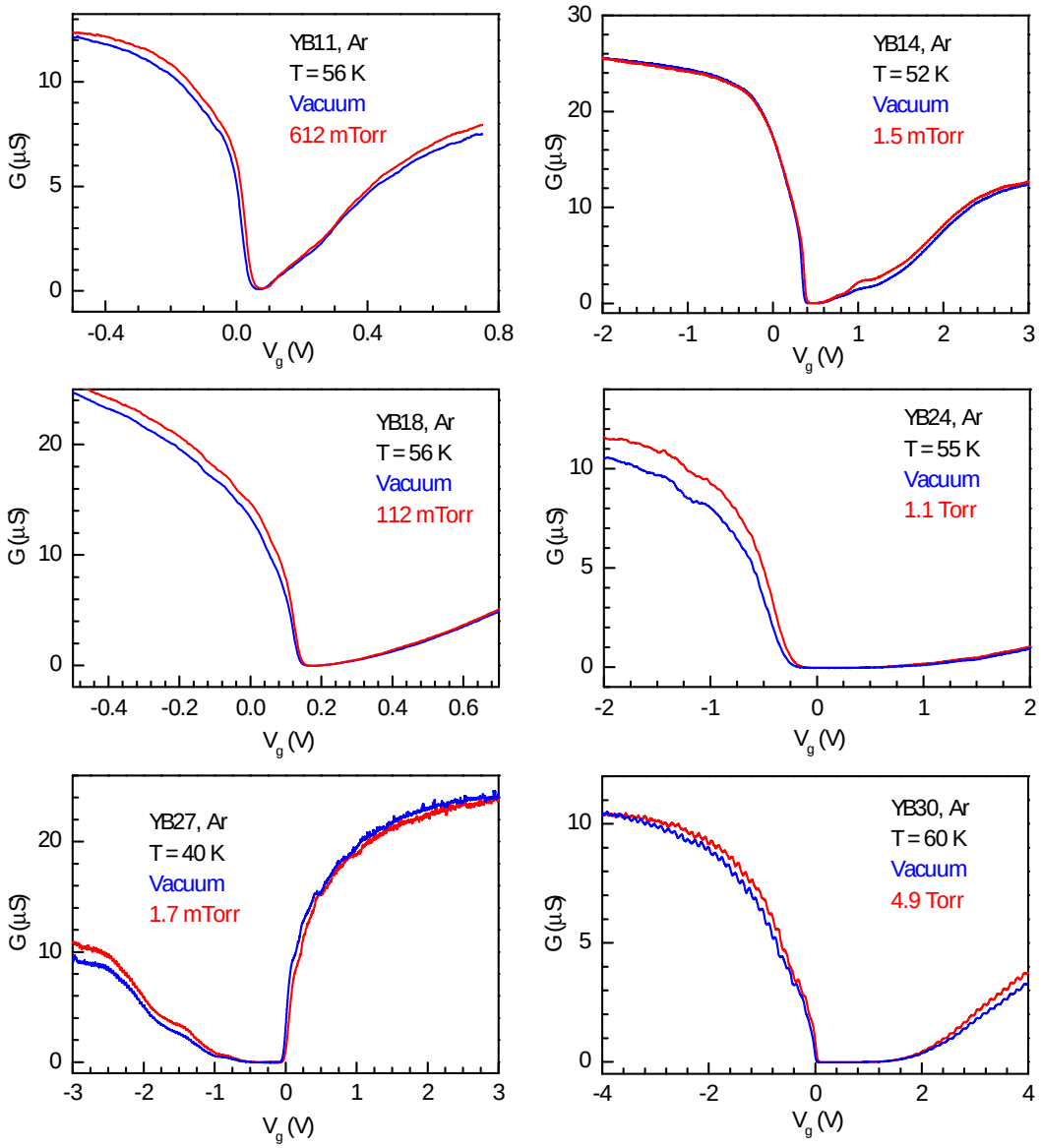

Figure A.1: The effect of a monolayer of Ar on the $G(V_g)$ of suspended nanotube devices.

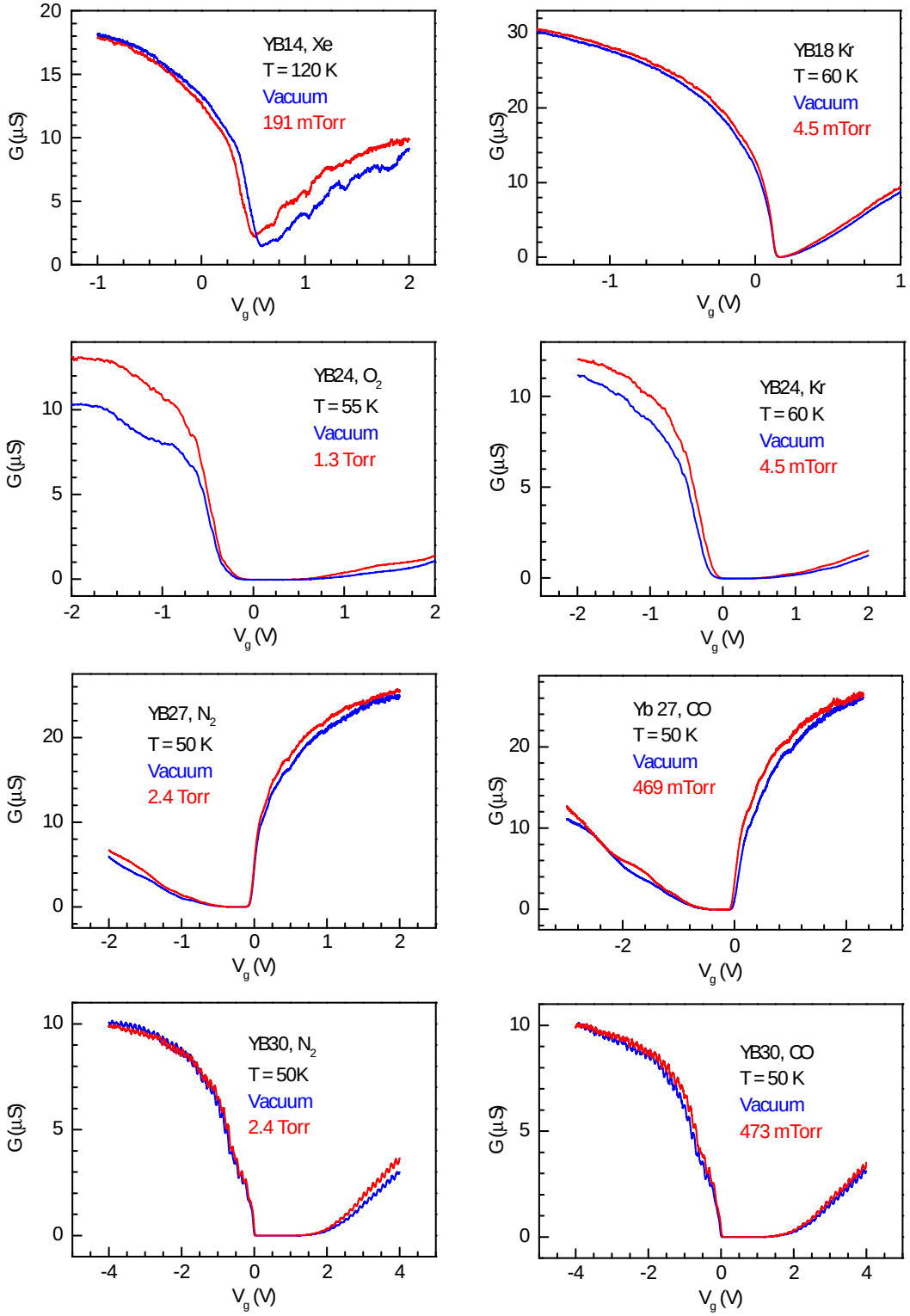

Figure A.2: The effect of a monolayer of Ar on the $G(V_g)$ of suspended nanotube devices.

Appendix B

GRAPHENE ADSORPTION ISOTHERMS

This appendix contains a set of adsorption isotherms measured on the suspended graphene devices.

B.1 Pre-annealed conductance isotherms

Pre-annealed isotherms are measured after devices have been cooled down to cryogenic temperature without current annealing prior to adsorption measurements. We propose that the changes in conductance G are not due to the adsorption onto the surface of graphene, but onto a uniform layer of contaminants. See section 4.1 for discussion.

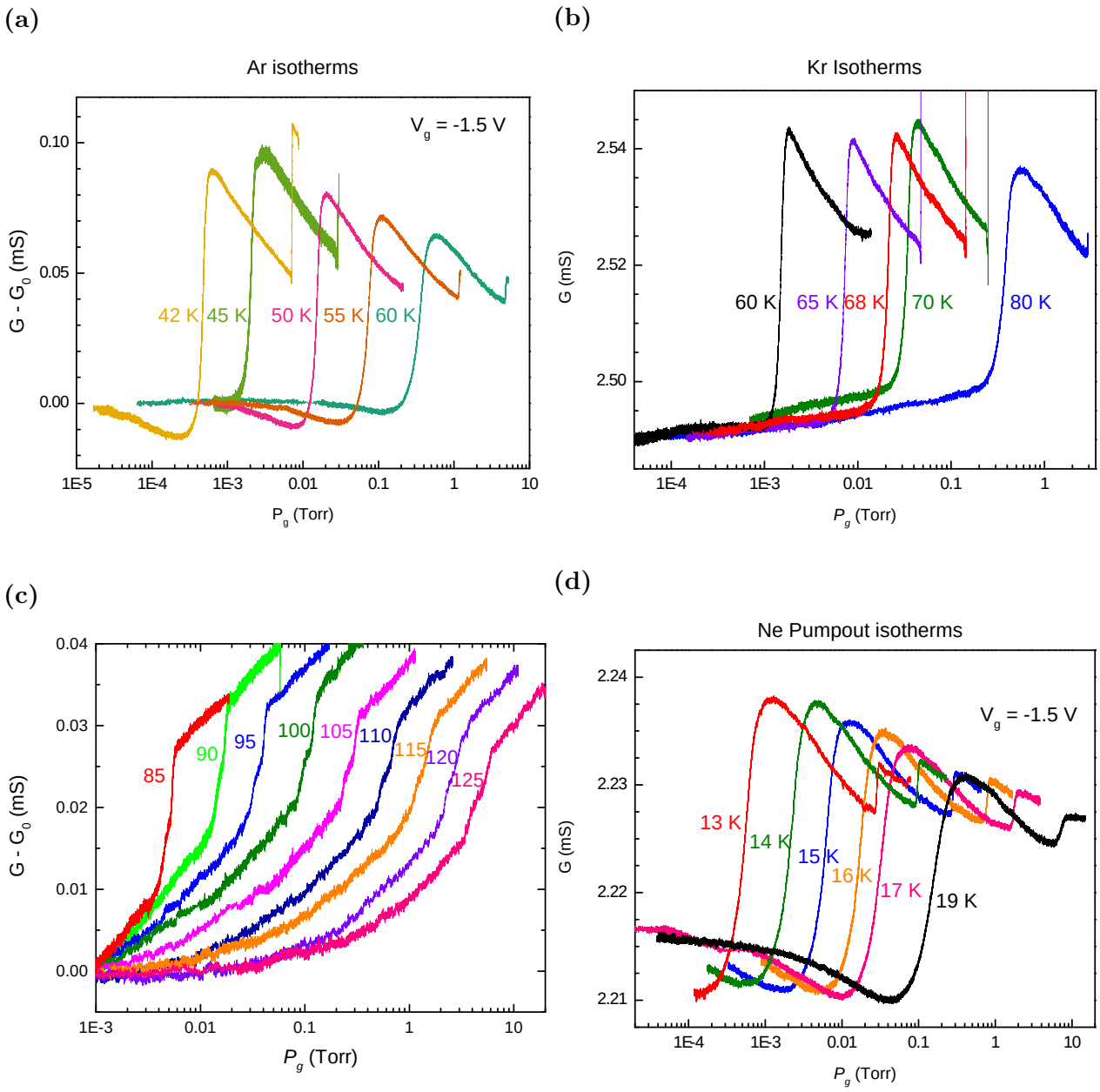

Figure B.1: Pre-annealed conductance isotherms of noble gases on an hBN capped monolayer graphene device #1. The device has been furnace annealed at 450 °C in an Ar/H_2 atmosphere prior to cooldown in order to remove polycarbonate residue from fabrication process. All isotherms show one main broad step feature. The isotherms of Ne exhibit a second step feature at higher pressures. For both Ar and Kr the conductance of the device increased sharply at pressures near 3D saturation. We interpret this behavior to be a result of multilayer condensation on the surface of the device.

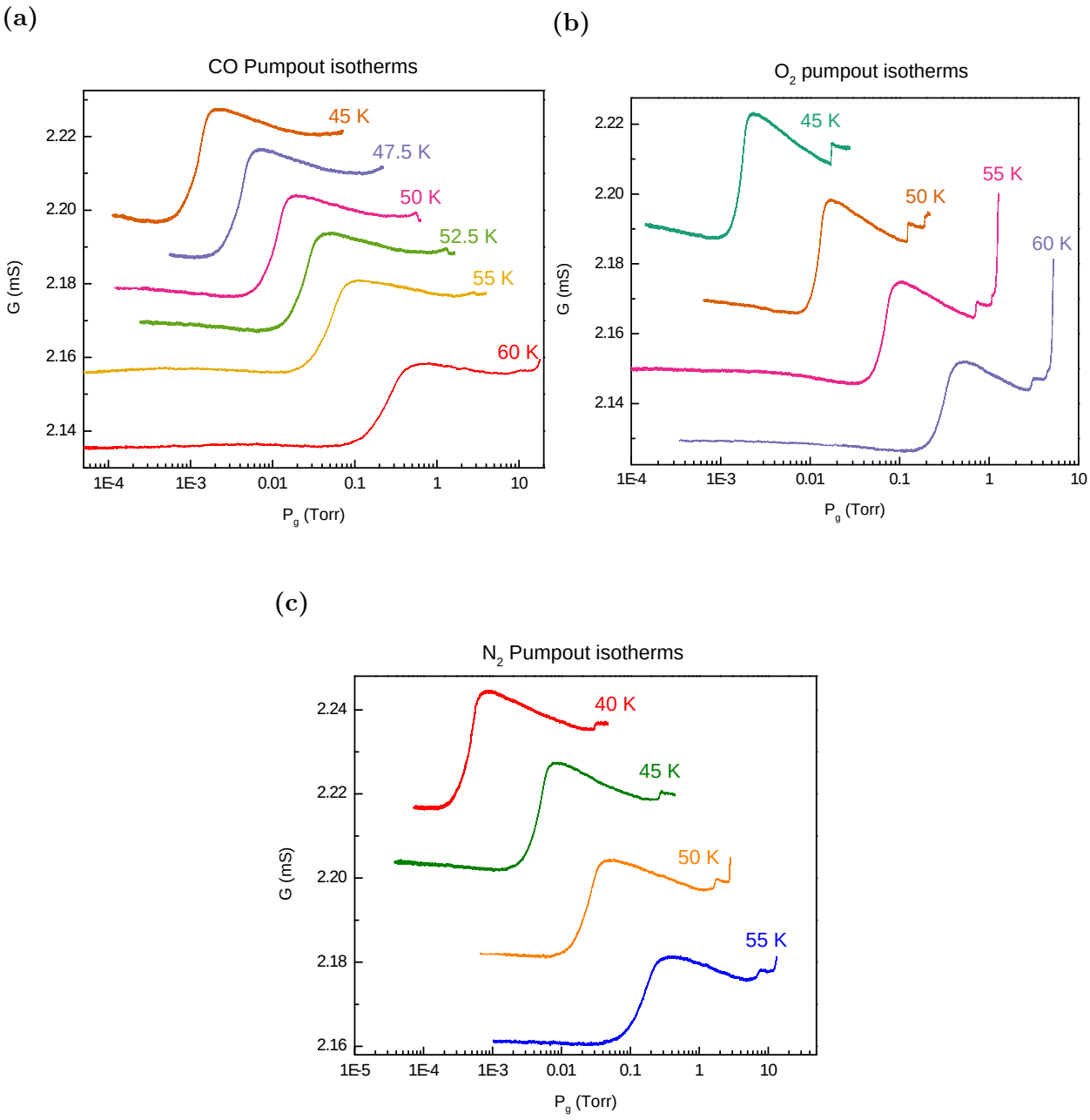

Figure B.2: Pre-annealed conductance isotherms of diatomic gases on an hBN capped monolayer graphene device #1.

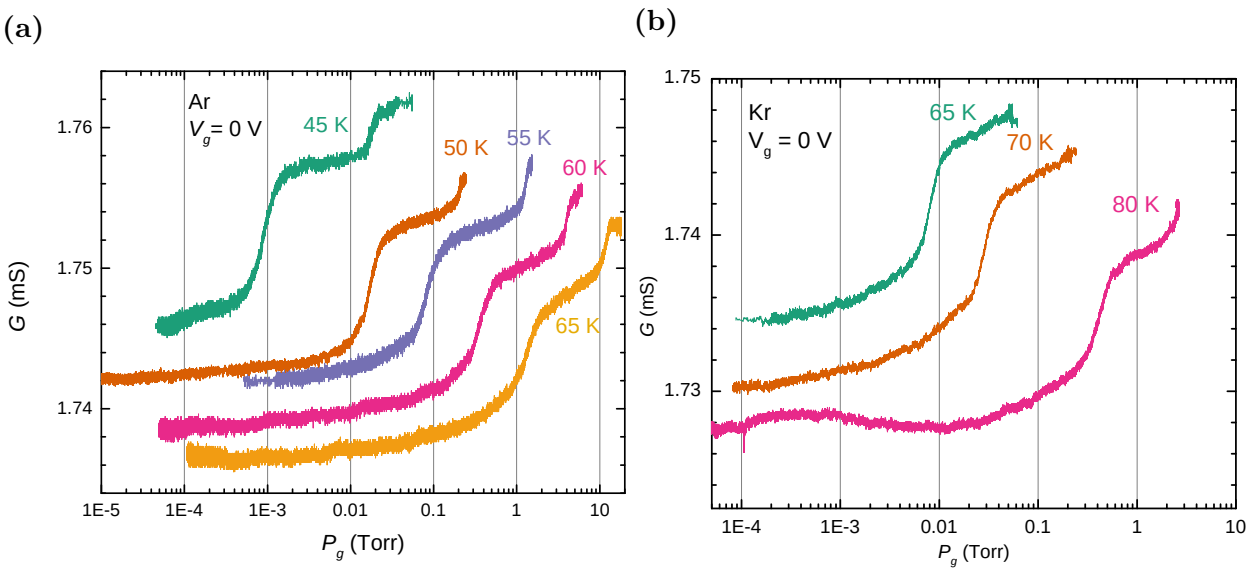

Figure B.3: Pre-annealed adsorption isotherms of Ar and Kr on bilayer graphene device #2.

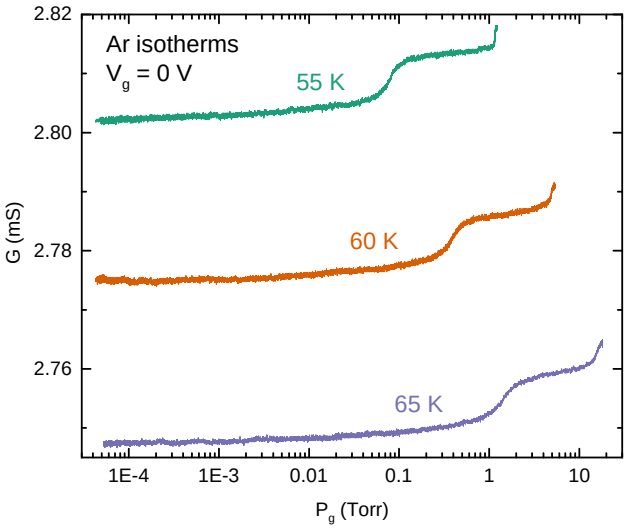

Figure B.4: Pre-annealed conduction isotherms of Ar on trilayer graphene device #3. Two broad steps are visible. The slope of the main step $dG/d(\ln P)$ does not appear to increase at lower temperature. The behavior is reminiscent of Class II nanotubes discussed in section 3.2.

B.2 Post-annealed conductance isotherms

B.2.1 Isotherms on Trilayer Graphene

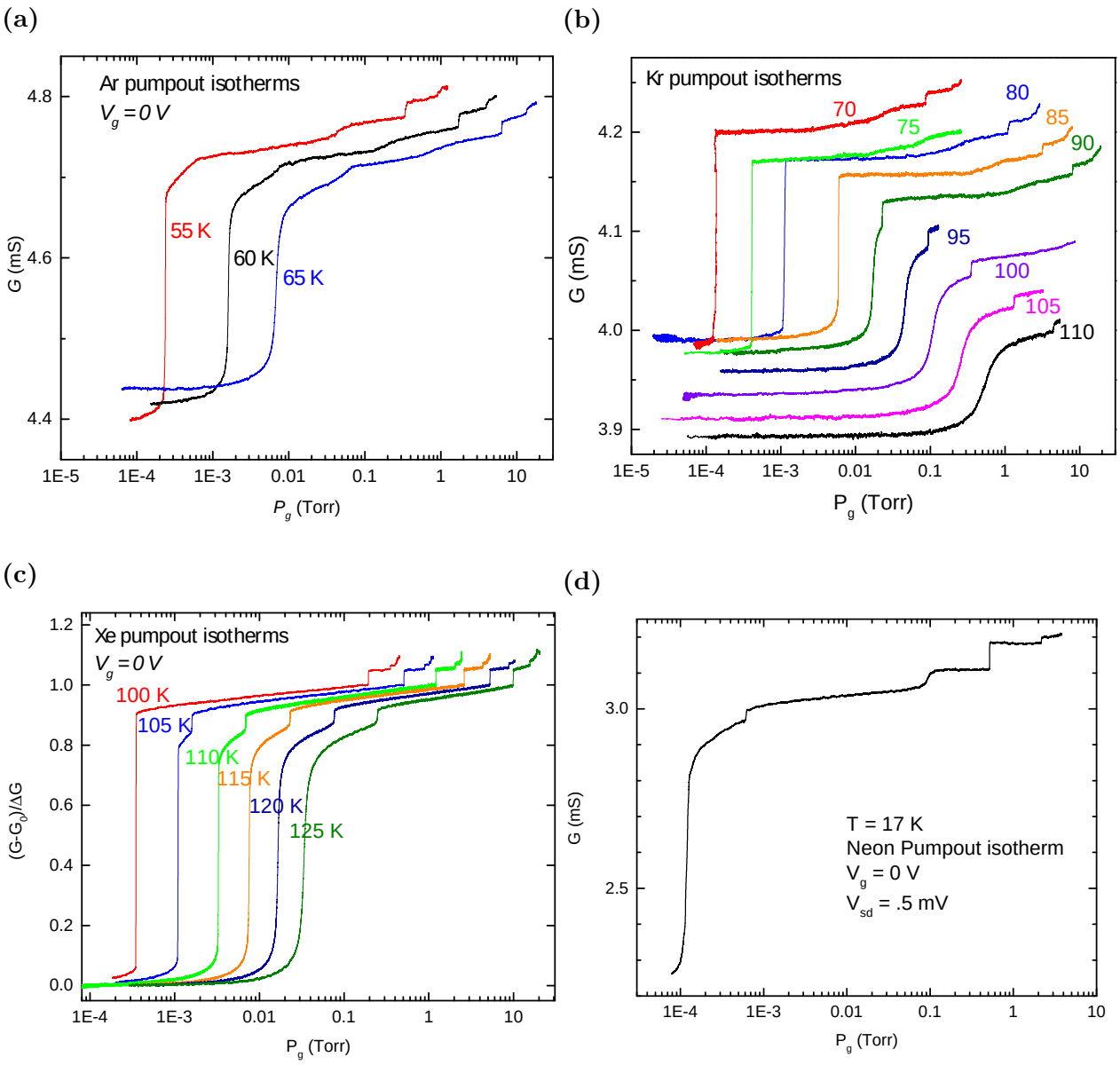

Figure B.5: Isotherms of noble gases Ar, Kr, Xe, and Ne on trilayer graphene device #3.

B.2.2 Isotherms on Bilayer Graphene

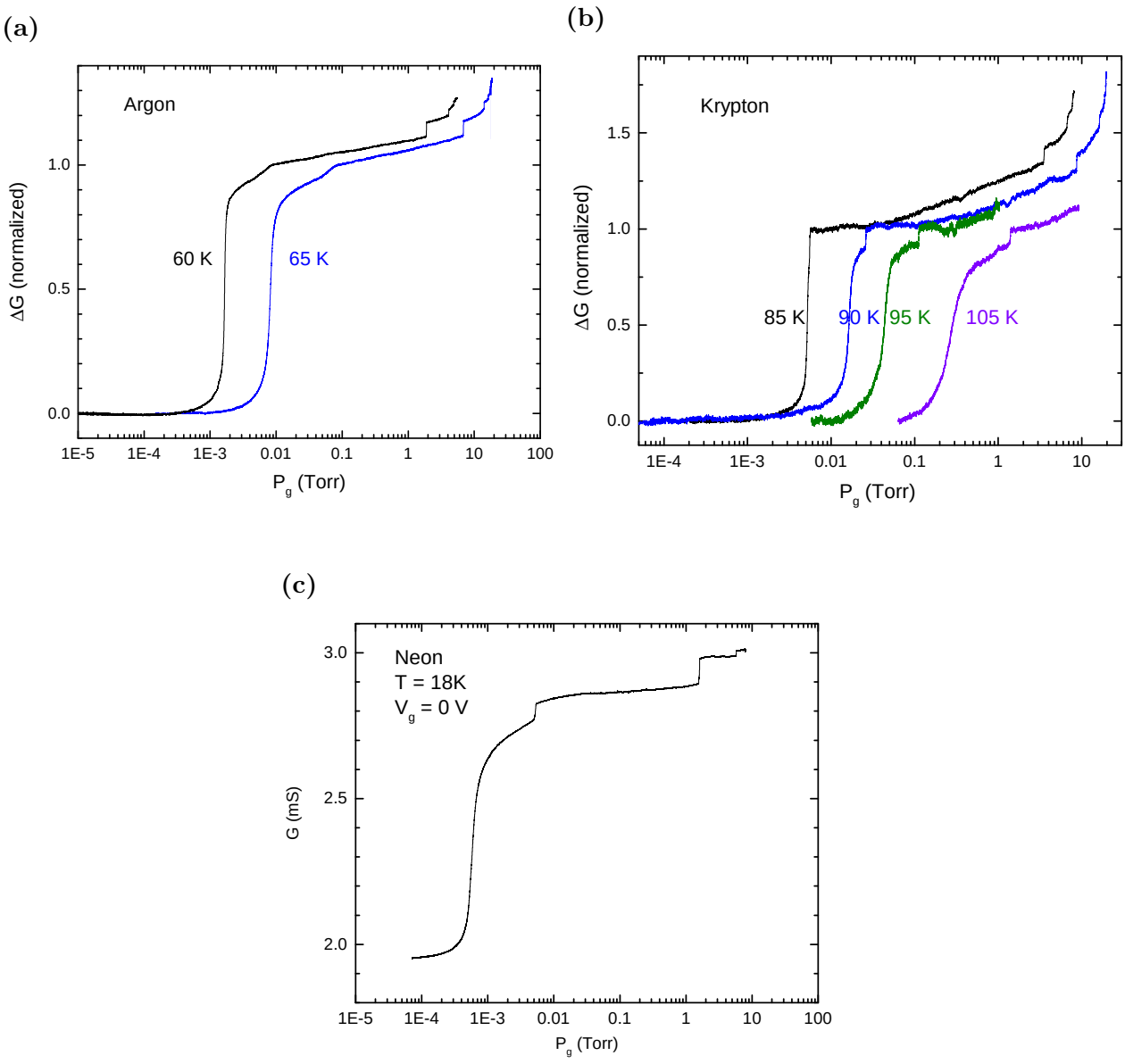

Figure B.6: Conductance isotherms of noble gases Ar, Kr, Ne on bilayer graphene device #13. The isotherms appear similar to those measured on the other bilayer and trilayer devices.

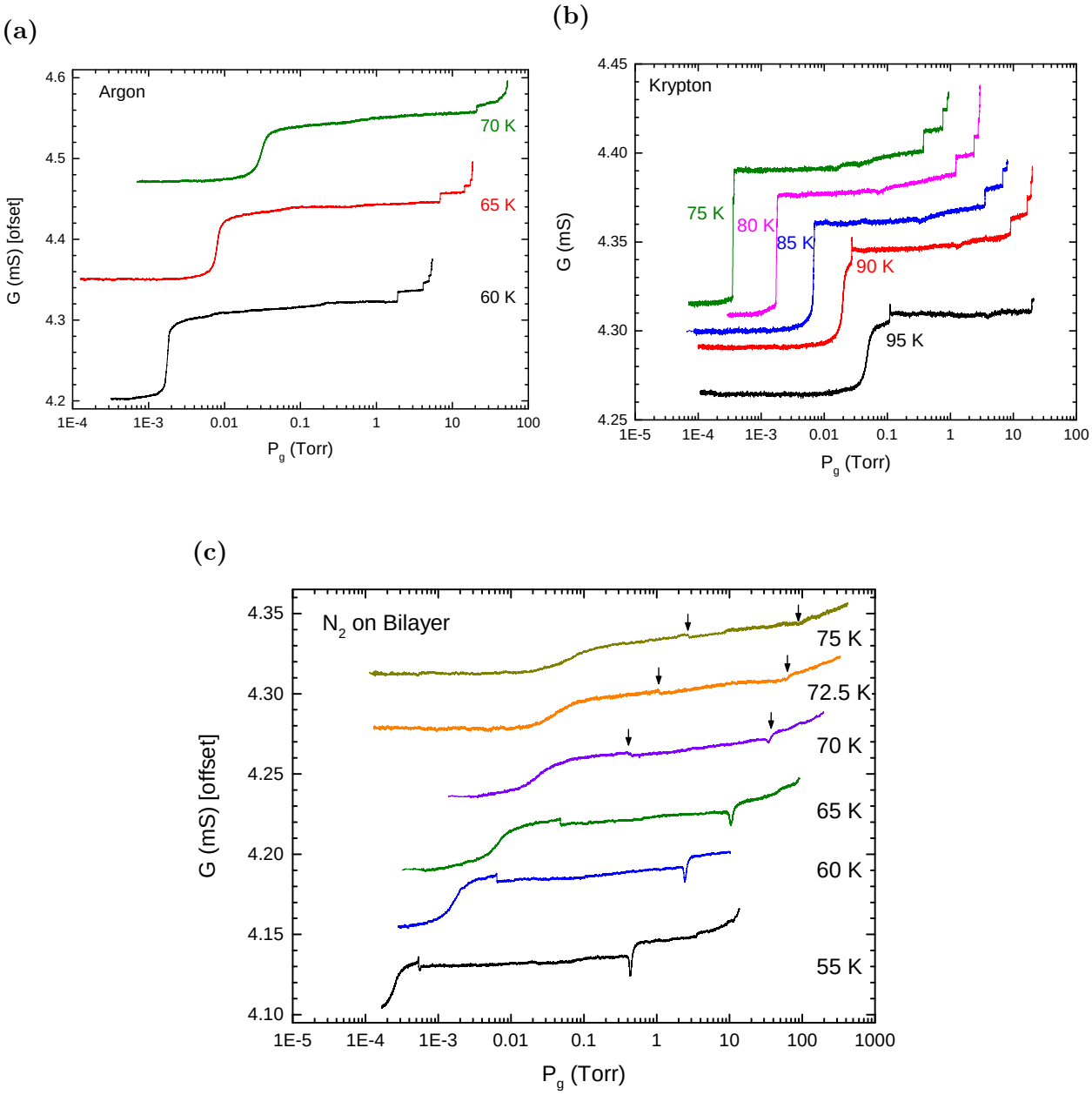

Figure B.7: Isotherms on bilayer graphene device #18. In panel (c) the positions of the F-CS and CS-ICS phase transitions at $T \geq 70\,\mathrm{K}$ are labeled with black arrows.

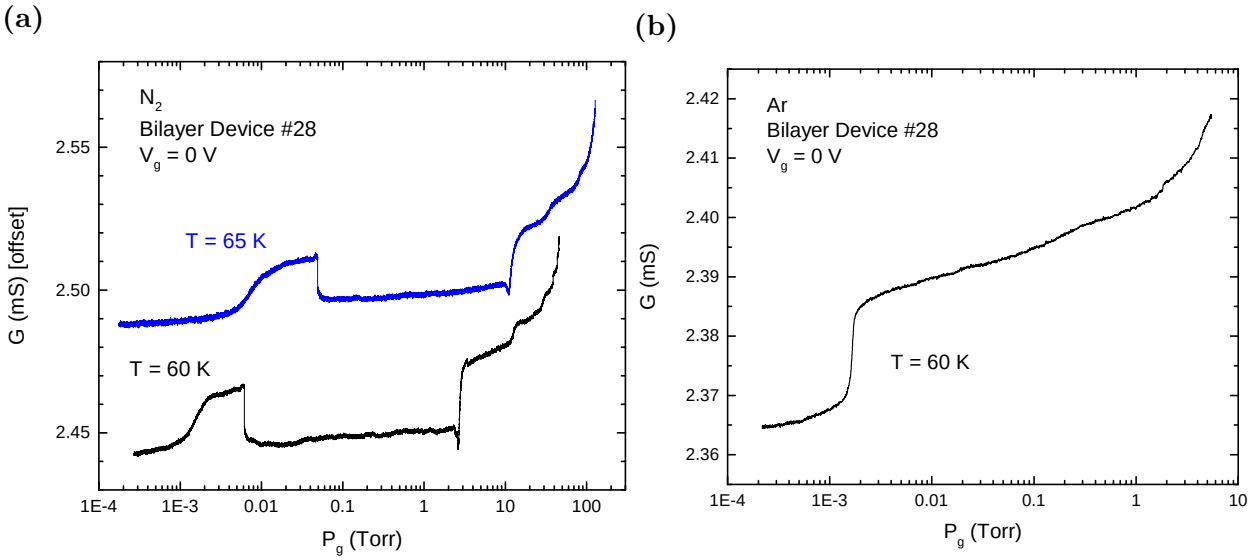

Figure B.8: Isotherms of N_2 and Ar on bilayer graphene device #28.

B.2.3 Isotherms on freestanding Monolayer Graphene

Compared to bilayer and trilayer graphene, the studied monolayer devices exhibited smaller changes in conductance upon the adsorption of gases into 2D phases not in commensuration with the graphene lattice.

All monolayer graphene devices showed a large reduction of conductance G upon the formation of a CS phase of N_2 and CO. In comparison the effect on G due to the formation of a CS phase of Kr was small.

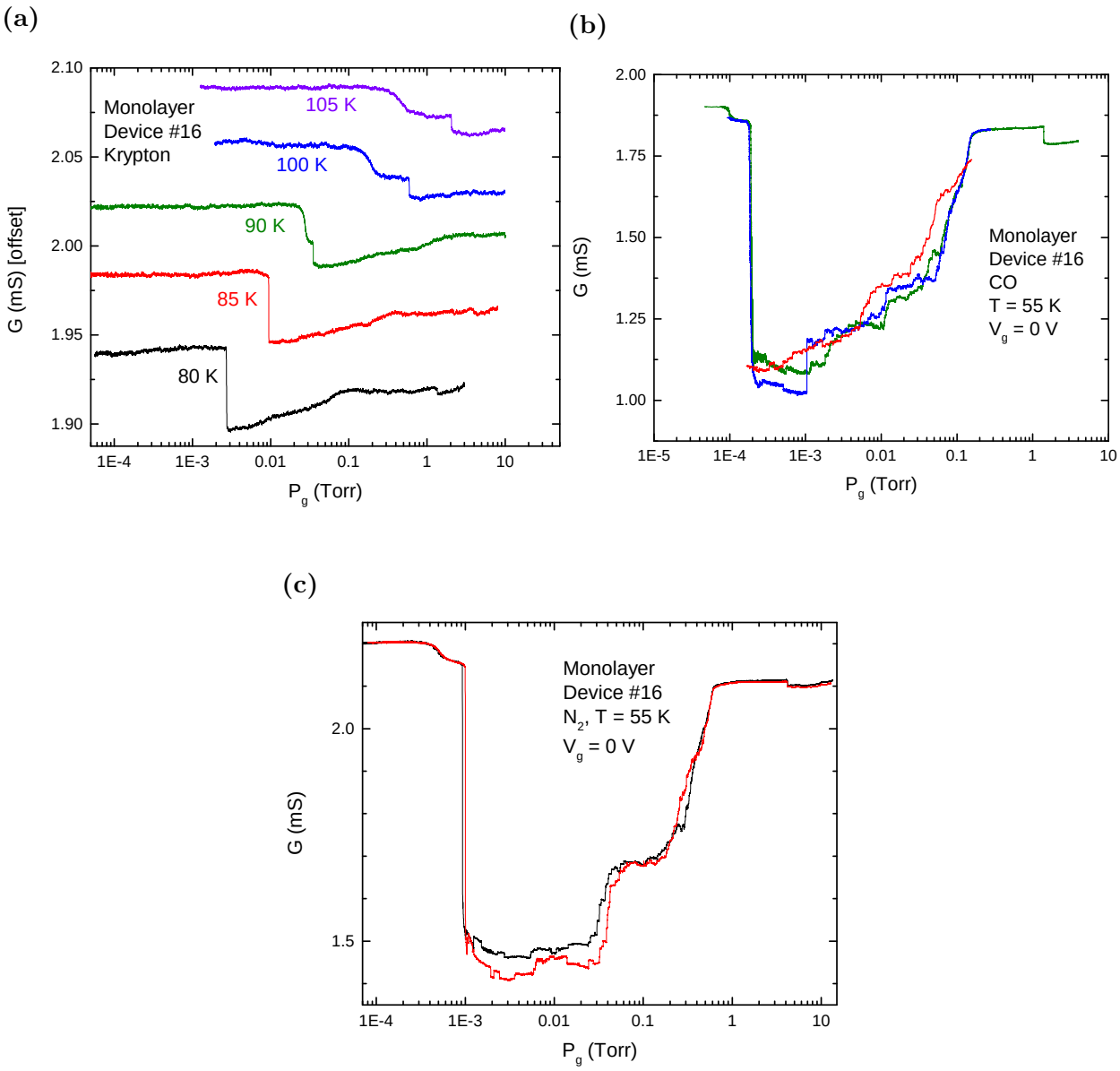

Figure B.9: Isotherms of Kr, CO, and N_2 on monolayer graphene device #16.

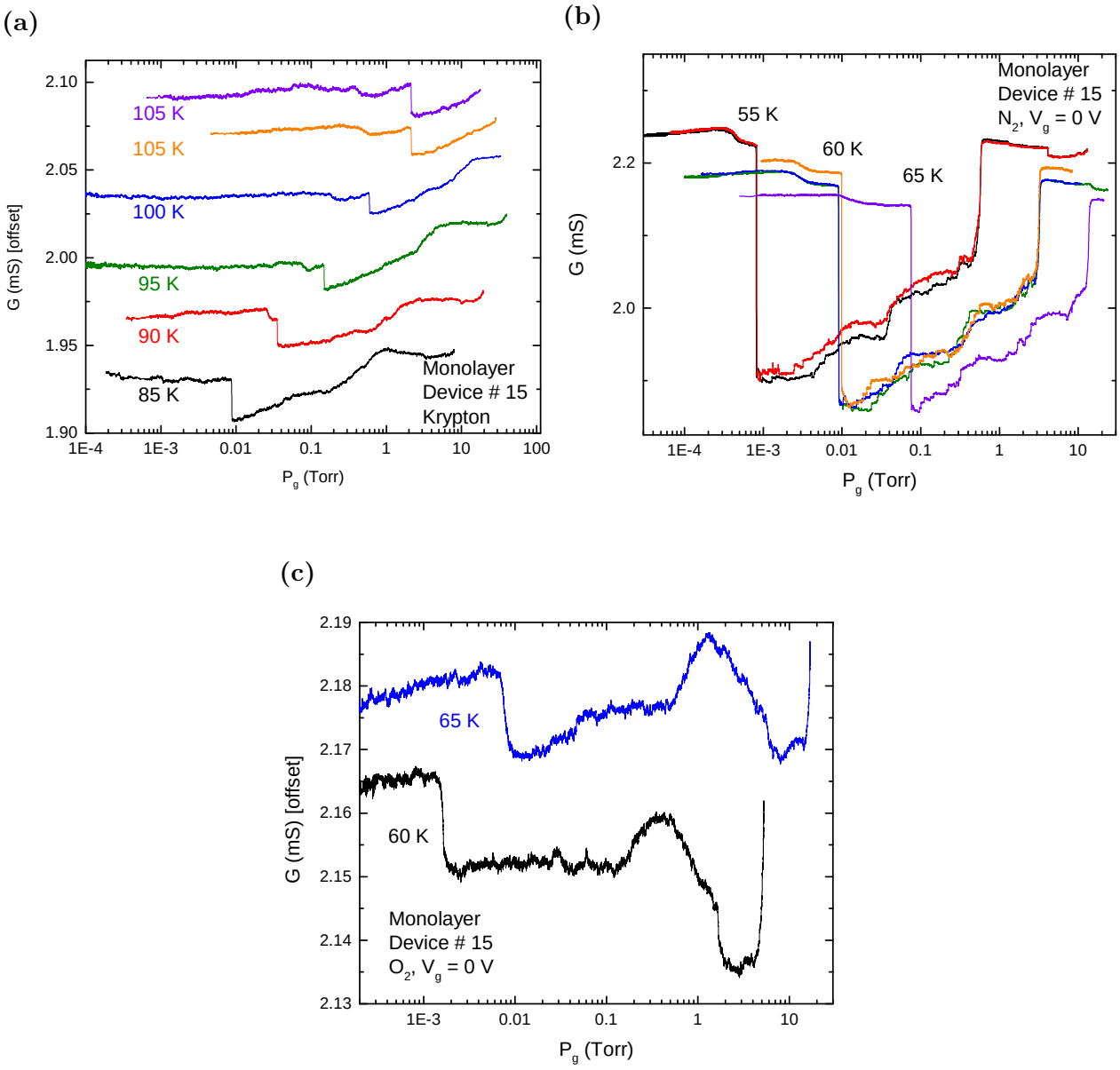

Figure B.10: Isotherms of Kr, N_2 and O_2 on monolayer graphene device #15. The pumpout isotherms of N_2 are repeated several times for a given temperature T. The isotherms at different T show similar distributions of step patterns which might be related to domain pinning on contamination present on the device. The isotherms of N_2 can be compared to those of O_2. The binding energies of the two gases are very similar, but O_2 does not form a CS solid phase and so produces a completely different effect on conductance G than N_2.

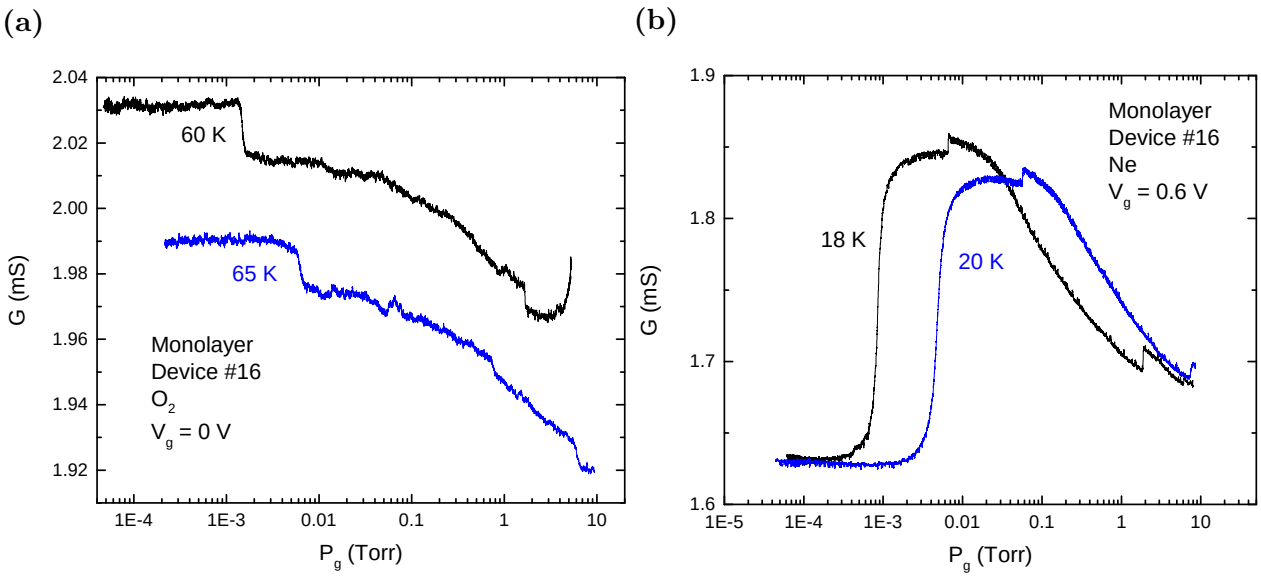

Figure B.11: Isotherms of O_2 and Ne on monolayer graphene device #16.

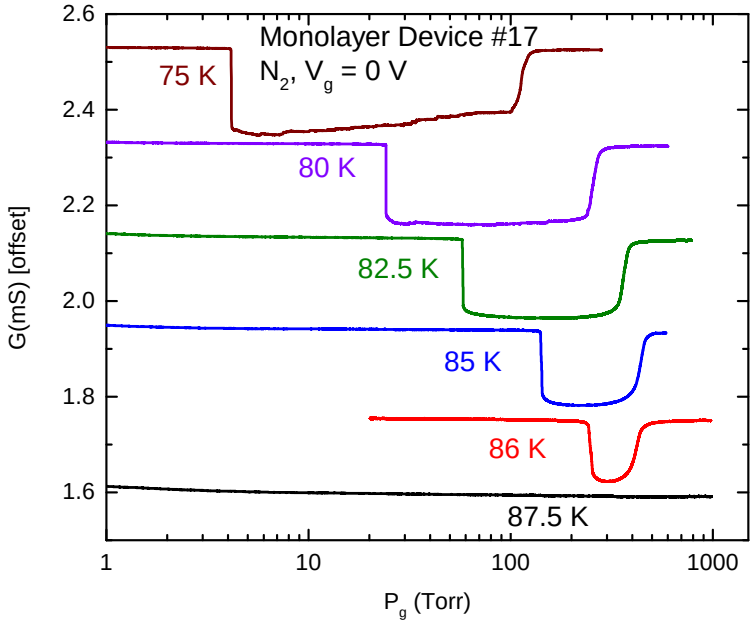

Figure B.12: High temperature isotherms of N_2 on freestanding monolayer graphene device #17. At $T = 87.5\,\mathrm{K}$ the CS phase does not exist, so the drop in G is absent.

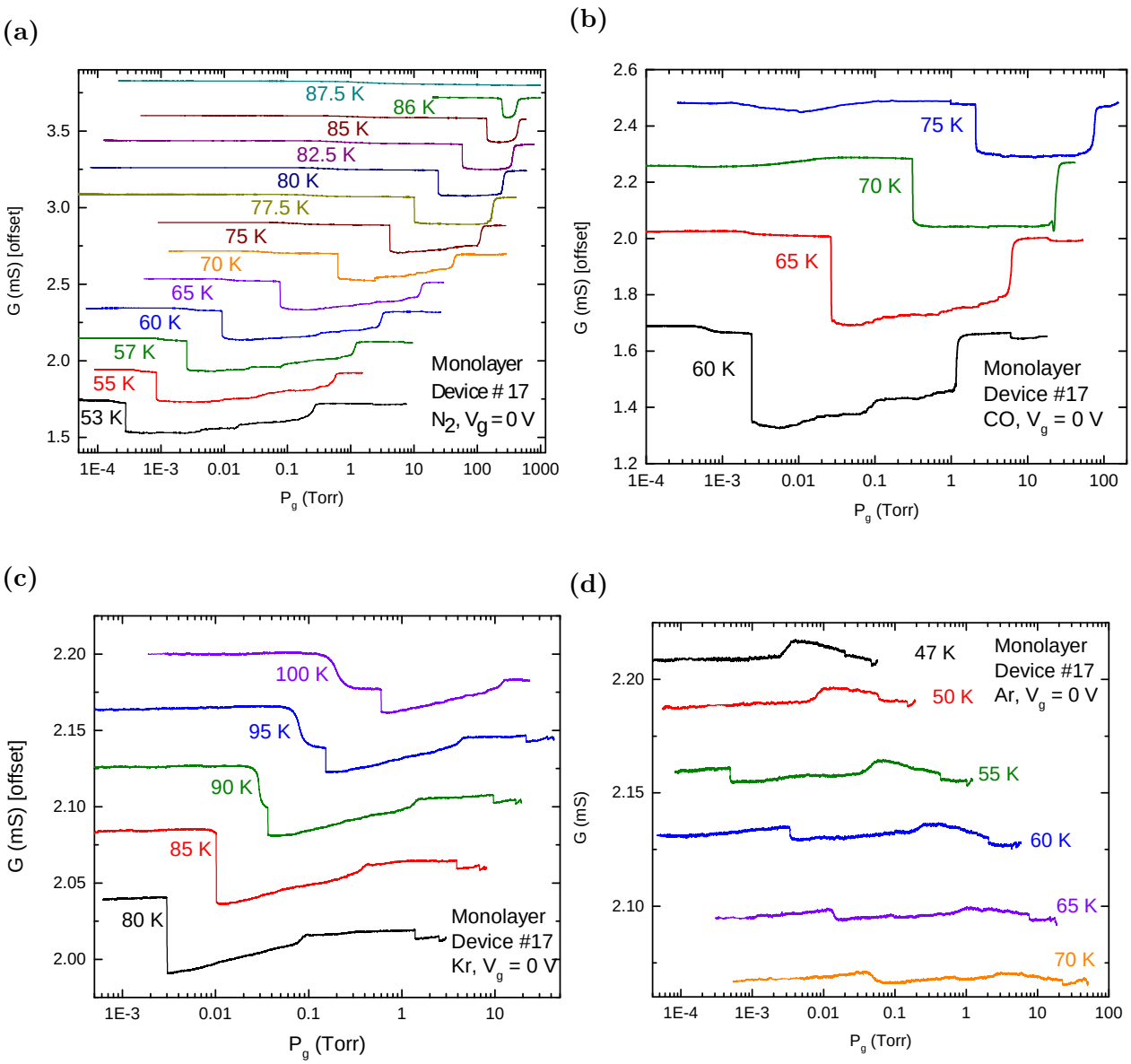

Figure B.13: Isotherms of N_2, CO, Kr, and Ar on monolayer graphene device #17. The isotherms of CO and N_2 appear qualitatively similar, but CO produces a larger reduction of G upon the formation of CS phase.

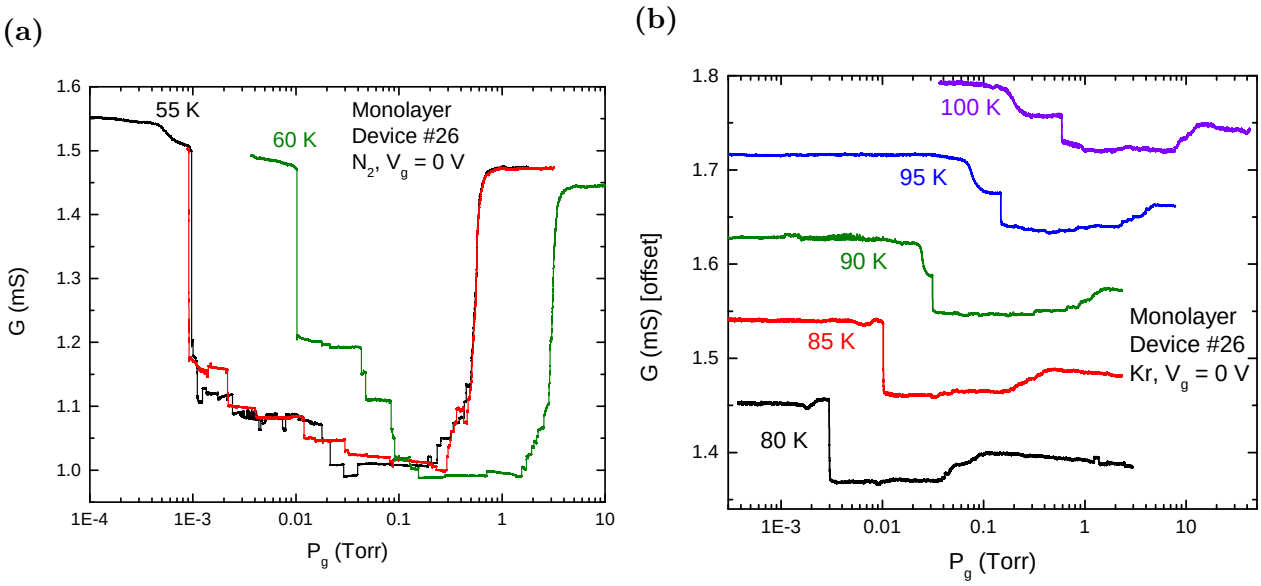

Figure B.14: Isotherms of N_2 and Kr on monolayer graphene device #26.

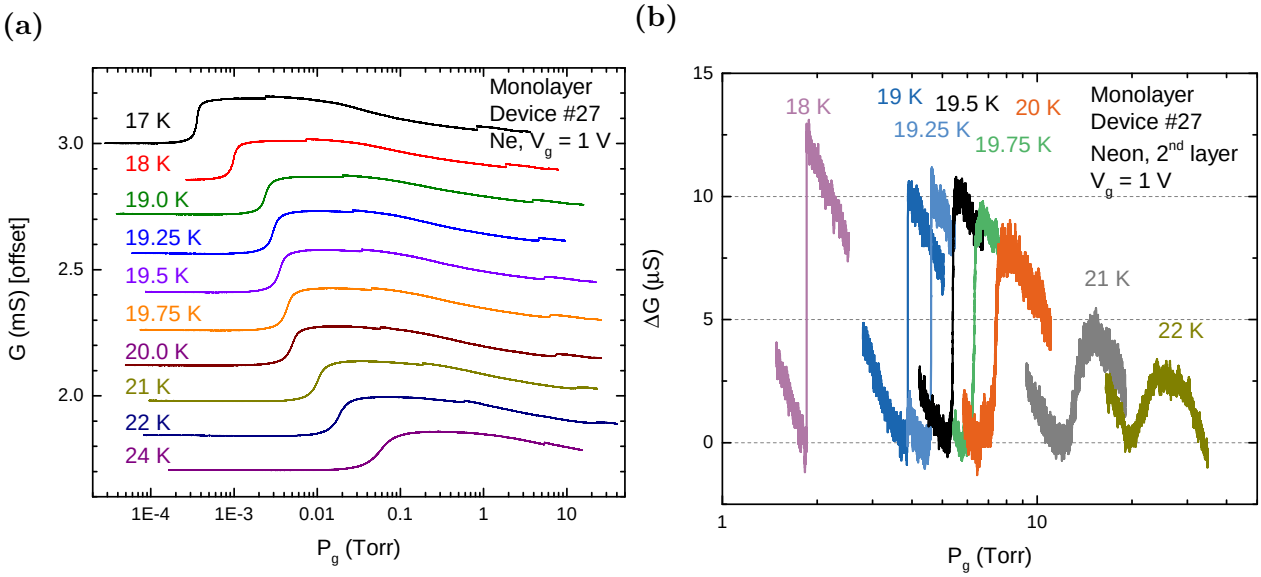

Figure B.15: Isotherms of Ne on monolayer graphene device #27. Panel (b) shows a zoom on the 2nd layer L-V transition, which has a critical point at $T_c = 19.5\,\mathrm{K}$ [87].

B.2.4 Isotherms on hBN backed Monolayer Graphene

Isotherms of N_2 and Kr on two hBN backed monolayer graphene devices, device #19 and device #20, are presented in this section. Gas adsorption on these devices occurs only on one side of the graphene sheet, the side that is facing into the trench, see section 2.1.3 for device fabrication details. The formation of the CS phases of N_2 and Kr produces a sharp decrease of conductance at the phase boundaries.

For Kr, on both devices, there is an extra step feature present in the conductance isotherms while the monolayer is expected to be in the CS phase. The appears to intersect with the F-CS phase boundary around $T \approx 105\,\mathrm{K}$, see Fig B.19b. The feature changes from being discontinuous to continuous (as a function of pressure) at T between 80 and 85 K. It is unclear what phase transition this feature corresponds to as it does not occur in Kr monolayers on graphite.

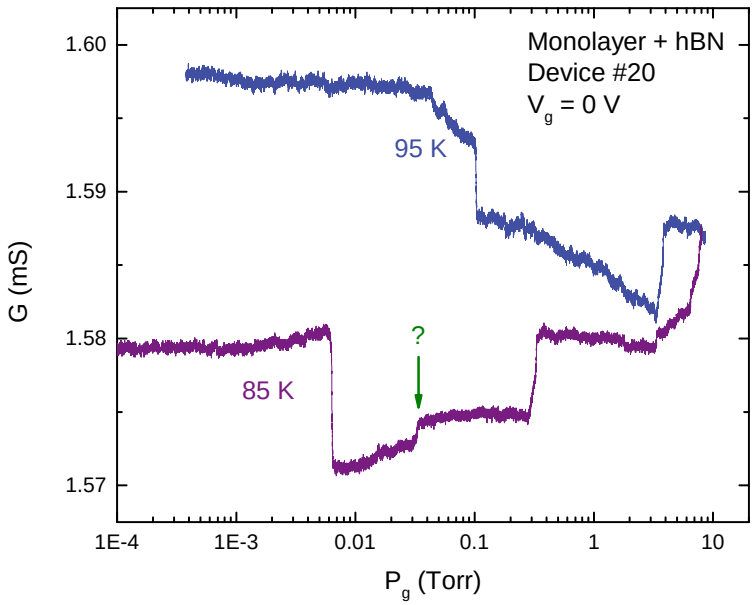

Figure B.16: Isotherms of Kr on monolayer + hBN device #20. A reproducible step in conductance (labeled by green arrow) occurs where on graphite the adsorbed monolayer is known to be in the CS phase.

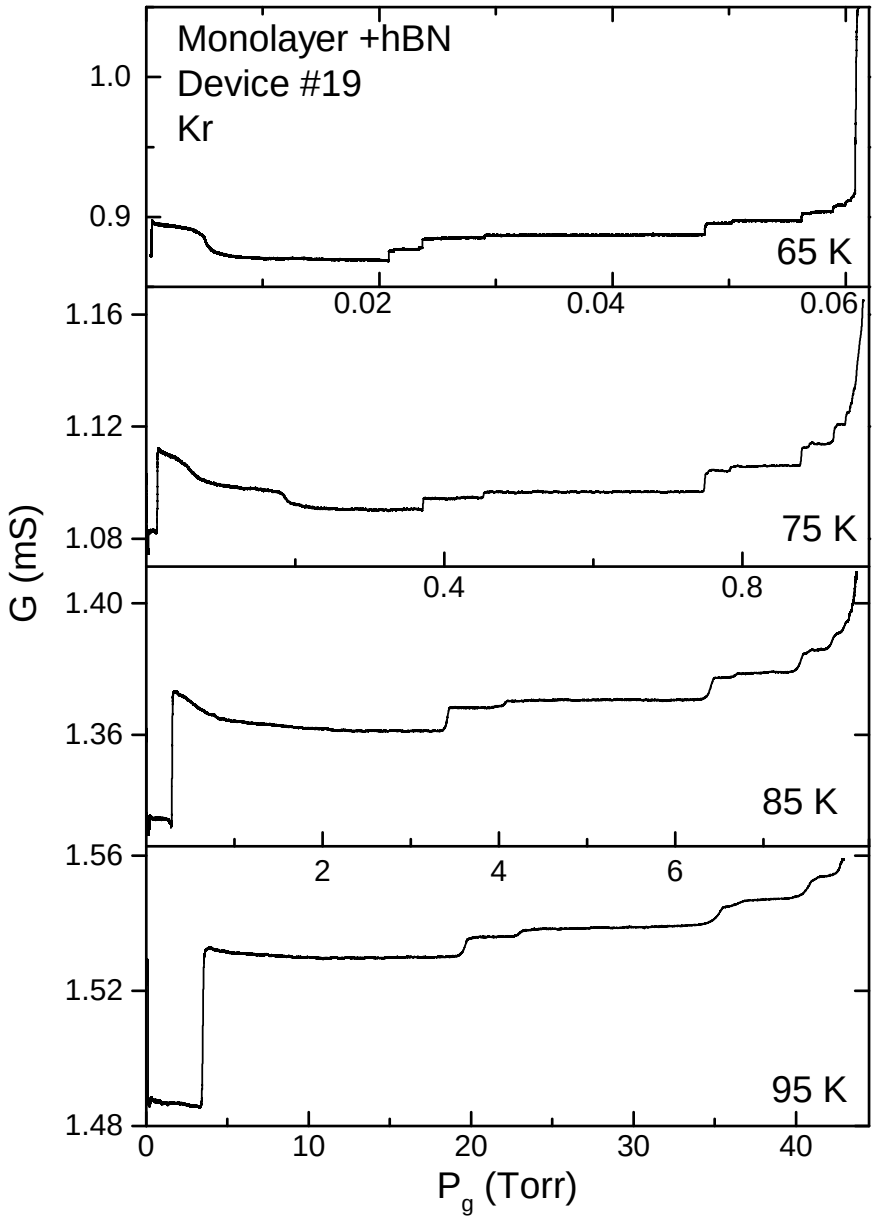

Figure B.17: High coverage regions of Kr isotherms on monolayer + hBN device #19. More than thirteen steps in conductance are discernible. At high T the steps are continuous, while they become vertical at low T. The steps correspond multilayer phase transitions [18].

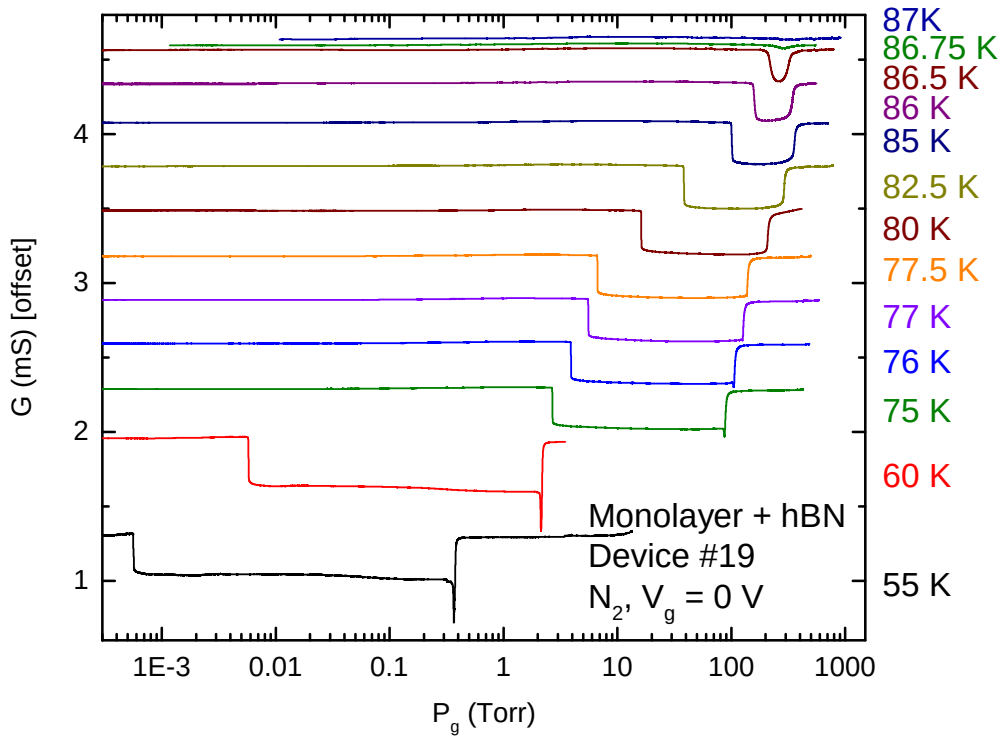

Figure B.18: Pumpout isotherms of N_2 on monolayer + hBN device #19. The hysteretic behavior in the CS phase is absent.

(a) Pumpout isotherms of Kr on monolayer + hBN device #19.

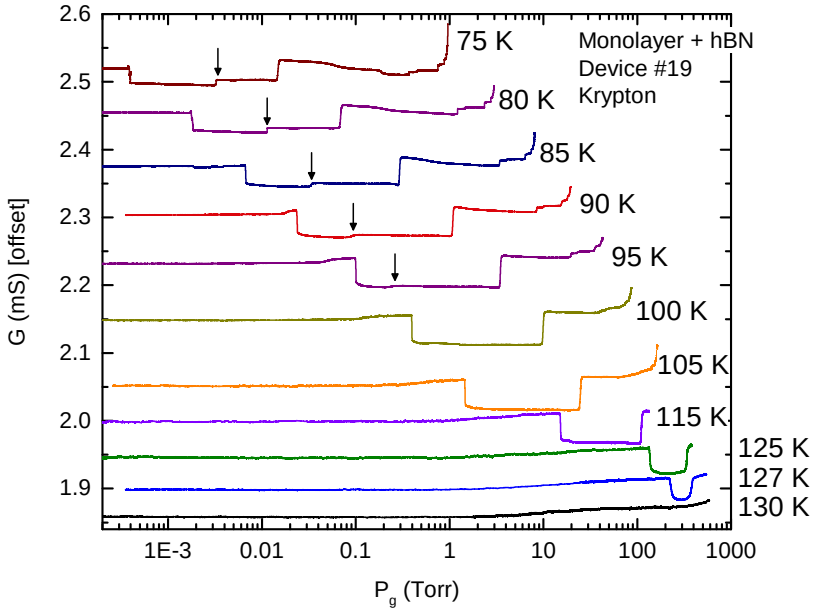

(b) Phase diagram of Kr on monolayer + hBN device #19.

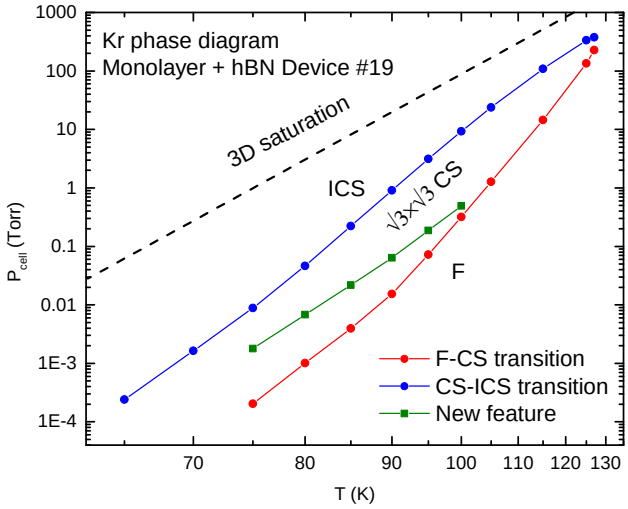

Figure B.19: The formation of the Kr CS phase results in a decrease of conductance G similar to the effect of N_2. In Kr isotherms the spike at the CS-ICS transition is absent. A step in conductance (labeled by arrow) is present while the monolayer is expected to be in the CS phase. The feature does not match the known phase transitions of the Kr monolayer on bulk graphite. At $T = 80\,\mathrm{K}$ the step is vertical, while it is continuous at $T = 85\,\mathrm{K}$. The position of the feature is plotted on a P-T phase digram in panel (b).

Appendix C

JOULE HEATING OF SUSPENDED GRAPHENE

We can raise the temperature of our suspended graphene devices through Joule heating while they are in the presence of gas at a pressure P_{cell}. During the Joule heating measurement, a DC source-drain bias V_{sd} is applied to the device, which causes the device temperature T_{device} to increase above the temperature of the cell T_{cell}. The total dissipated power in the device is $P = IV_{\text{sd}}$, but the actual location where the power dissipation occurs is unknown. The power should be dissipated in the regions of the potential drop which are not well known: the resistance of our devices is in series with the contact resistance [89]. The suspended graphene sheets are cooled as heat is conducted through their source and drain contacts. At low power it is unclear if the temperature of our suspended devices should be uniform.

As we apply a DC source-drain bias across the device we can measure the differential conductance $G_{\text{diff}} = dI/dV$ by applying a small AC source drain bias in conjunction with V_{sd}. The circuit used to perform the measurement is shown in Fig. C.1.

Employing the Joule heating technique we can either take vertical or quasi-horizontal cuts through the P-T phase diagram. First, we can measure isotherms on the device starting at a fixed cell temperature T_{cell} while applying a fixed DC bias V_{sd} to the device. The temperature of the device is higher than the cell temperature: $T_{\text{device}} > T_{\text{cell}}$. The device is exposed to a flux of gas molecules that are in equilibrium with the cell, thus they are at a lower temperature than the device surface. The effective pressure experienced by the device is then slightly higher than the cell pressure

$$P_{\text{effective}} = (T_{\text{device}}/T_{\text{cell}})^{1/2} \times P_{\text{cell}} \tag{C.1}$$

Several isotherms of Argon on a trilayer graphene device #3 with varying levels of applied

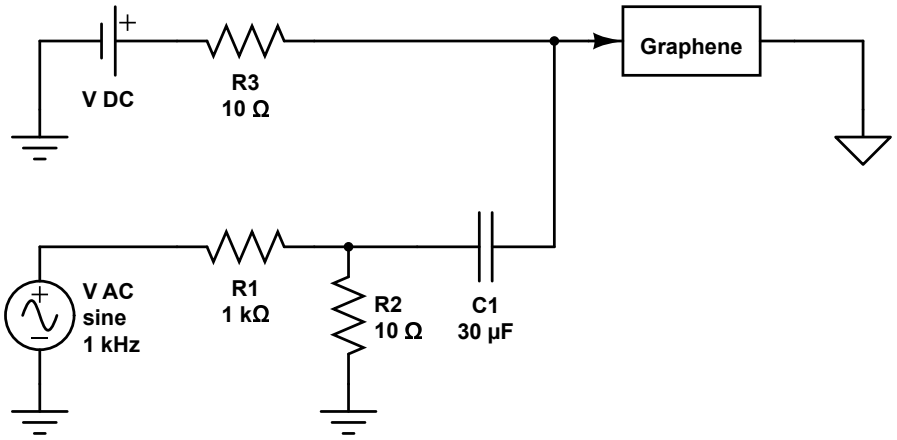

Figure C.1: The electrical circuit used for measuring Joule heating of the suspended devices. The DC voltage V_{sd} used to heat the device is supplied by a National Instruments DAC card. The AC voltage V_{AC} is produced by a lock-in amplifier. The current through the device is measured using an Ithaco 1211 current preamp.

V_{sd} are shown in Fig C.2. At low bias $V_{\mathrm{sd}} < 25\,\mathrm{mV}$ the shapes of the features present in the isotherms appear quite similar to our standard conductance isotherms (measured without any DC bias) but with their positions shifted to higher pressures due to the elevated temperature of the device. At higher V_{sd} the shapes of the features in the isotherms quickly changes: the differential conductance G_{diff} decreases at the phase transitions. The reason behind this change in behavior is unclear.

As can be seen from Fig. C.2 the feature corresponding to the Ar supercritical fluid condensation phase transition significantly broadens in the high bias isotherms. This is expected as at high temperatures the pressure range over which the fluid condenses also broadens. The features corresponding to the fluid-solid melting transition and the second layer condensation still remain sharp as a function of pressure in the high bias isotherms. This indicates that the temperature of the device T_{device} is uniform during Joule heating.

Instead of performing isotherms on the suspended device at fixed bias $V_{\mathrm{sd}} = \mathrm{const}$, we

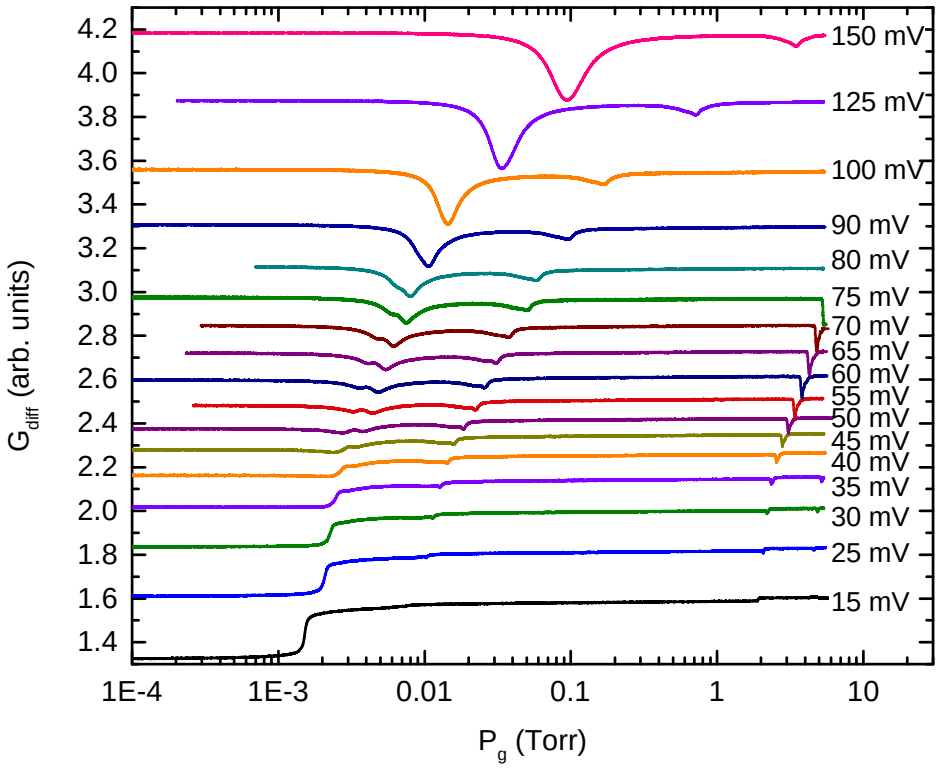

Figure C.2: Differential conductance isotherms of Argon on trilayer graphene device #3 with different levels of applied DC bias $V_{\rm sd}$. The temperature of the device increases as higher values of $V_{\rm sd}$ are applied. At low bias $V_{\rm sd} < 25\,\mathrm{mV}$ the features present appear similar to those in conductance isotherms but shifted to higher pressure.

can sweep $V_{\rm sd}$ at fixed pressure $P_{\rm cell} = \text{const}$. As the device heats up due to Joule heating an almost horizontal path is taken through the P-T phase diagram. The measurement path is not a true isobar as the effective pressure at the device surface changes according to Eq. (C.1). Such an isobar measurement performed in vacuum corresponds to the differential I-V measurement of the suspended device. Several such measurements performed at $T = 60\,\mathrm{K}$ on the trilayer device #3 in the presence of Ar are shown in Fig. C.3. Dips in the isobar measurements correspond to the known phase transitions within the Ar monolayer.

The temperature of the device can be extracted by matching the phase transitions with

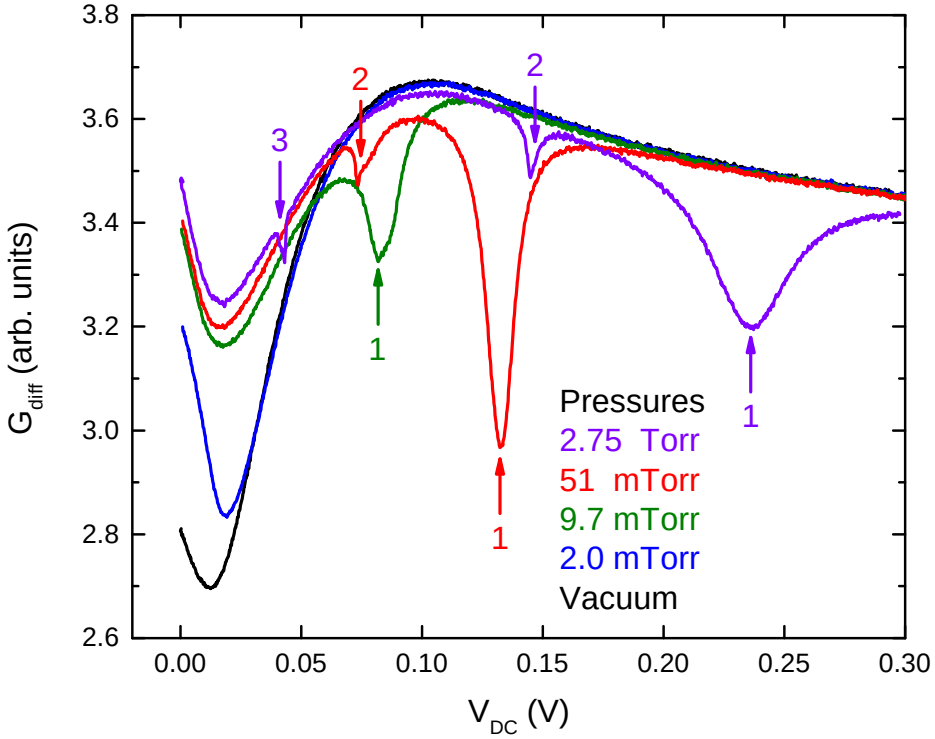

Figure C.3: Differential conductance measurements of trilayer graphene device #3 at several pressures of Ar at $T = 60\,\mathrm{K}$. At high pressures and low bias V_{sd} the device is covered with an adsorbed Ar monolayer. As V_{sd} is ramped up the temperature of the device increases. The Ar monolayer undergoes phase transitions and finally desorbs. The features (dips) in the differential I-V curves correspond to phase transitions within the adsorbed monolayer. The dip labeled 1 is due to the supercritical L-V transition. The dip labeled 2 is the incommensurate solid melting transition. The dip labeled 3 in the $P_g = 2.75\,\mathrm{Torr}$ differential I-V measurement is due to the desorption of the second layer.

the know positions of the phase boundaries on the P-T phase diagram. In the simplest model the temperature of the device should increase proportionally with power

$$T_{\mathrm{device}} = T_{\mathrm{cell}} + C \times I\,V \tag{C.2}$$

Even though the thermal conductivity of suspended graphene is known to be highly temperature dependent in the relevant temperature range [40, 64, 69], the above relation might be justified if the heating at low power is expected to occur mainly in the device contacts. By matching the nonlinear I-V isobar measurements across several different starting cell temperates, we extract constant C to be $C = 185\,\mathrm{K/mW}$ for the trilayer graphene device #3.

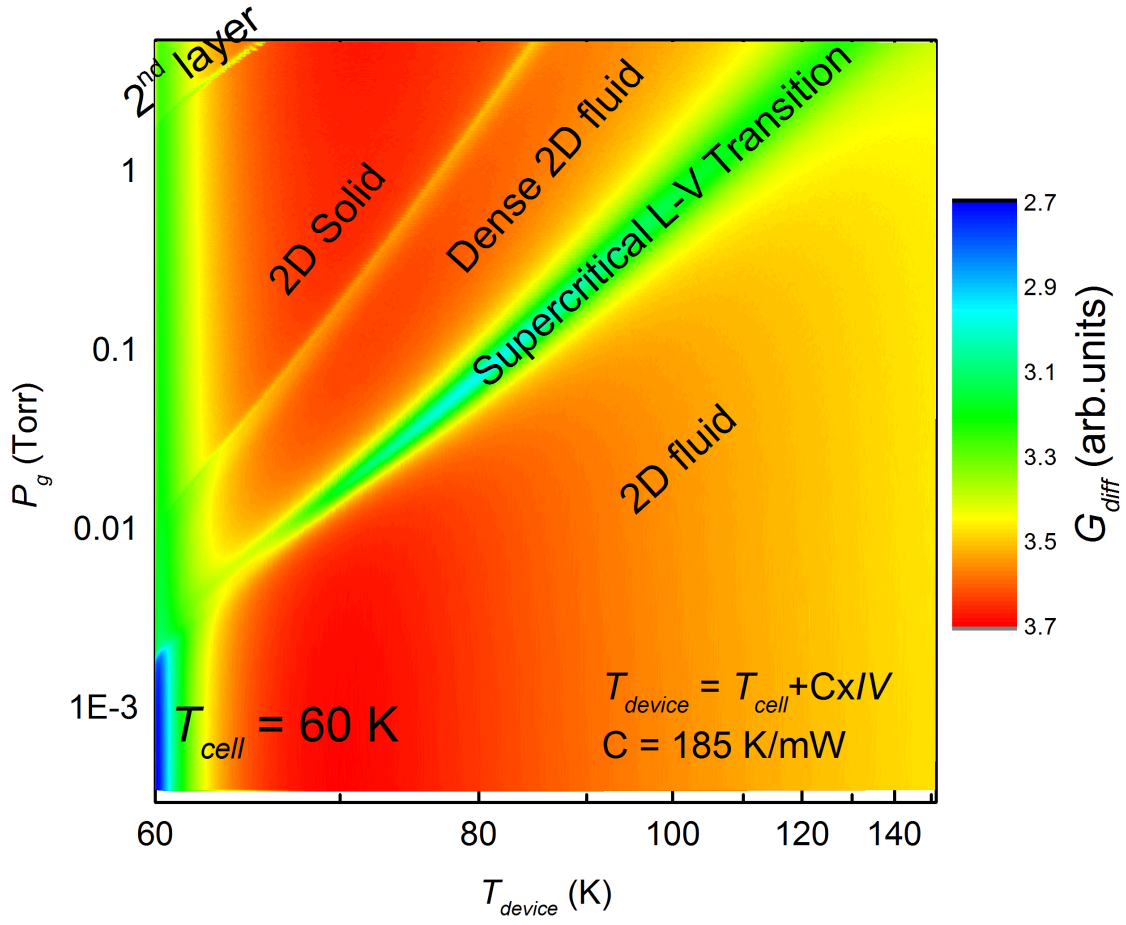

Figure C.4: A phase diagram of Ar on trilayer graphene device #3 obtained using the Joule heating technique. The temperature of the device is obtained from the total dissipated power using Eq. (C.2).

The Joule heating isobar measurements allow us to continuously map out an entire phase diagram of a particular gas, see Fig. C.4. This is done by continuously pumping gas out of the cell at the same time as isobar V_{sd} sweeps are continuously measured. The time scales for the pressure pumpout have to be much slower compared to one isobar measurement time. During the measurement shown in Fig. C.4 each isobar sweep from $V_{\mathrm{sd}} = 0\,\mathrm{V}$ to $V_{\mathrm{sd}} = 0.3\,\mathrm{V}$ to was performed over the course of approximately two minutes, while the entire pressure pumpout starting from $P_g \approx 5\,\mathrm{Torr}$ and ending at $P_g \approx 1 \times 10^{-4}\,\mathrm{Torr}$ was performed over approximately 10 h.

VITA

Boris Dzyubenko was born in Moscow, Russia in 1989. After having lived for a year and a half in Frankfurt, Germany he moved to the United States in the fall of 2000, at the age of 11. After finishing Stockdale High School in Bakersfield, CA in 2006 he attended the University of California, Los Angeles, where he obtained a B.S. in Physics in 2010. Boris Dzyubenko started his PhD work at the University of Washington in the Fall of 2010 and joined the Cobden Nanodevice Physics group in the Spring of 2011. In his free time while at UW he raced with the Husky Cycling team and was a member of the Washington Yacht Club.